TECHNISCHE UNIVERSITÄT MÜNCHEN

TUM School of Engineering and Design

Dissertation

Nonlinear modeling, identification and control of reluctance synchronous machines with analytical flux linkage prototype functions

Shih-Wei Su

TECHNISCHE UNIVERSITÄT MÜNCHEN

TUM School of Engineering and Design

Nonlinear modeling, identification and control of reluctance synchronous machines with analytical flux linkage prototype functions

Shih-Wei Su

Vollständiger Abdruck der von der TUM School of Engineering and Design der Technischen Universität München zur Erlangung eines

Doktors der Ingenieurwissenschaften (Dr.-Ing.)

genehmigten Dissertation.

Vorsitz:		Prof. Dr.sc. ETH Zürich Marcelo Lobo Heldwein
Prüfer der Dissertation:	1.	Prof. Dr.-Ing. Dr. h.c. Ralph Kennel
	2.	Prof. Dr.-Ing. habil. Christoph M. Hackl

Die Dissertation wurde am 10.10.2023 bei der Technischen Universität München eingereicht und durch die TUM School of Engineering and Design am 22.05.2024 angenommen.

This document is typeset with LaTeX/TeX.

Acknowledgment

I would like to express my heartfelt gratitude to several individuals who have significantly contributed to the completion of my doctoral dissertation.

First and foremost, I would like to thank my supervisor, Prof. Kennel, for providing a superb research environment at EAL, with many international collaborations. His unwavering support through all challenges and encouragement to pursue creativity in research projects, by granting me freedom, has been invaluable.

I am deeply grateful to my second supervisor, Prof. Hackl, who has also acted as a mentor and friend. From the beginning of my PhD journey until the end, his numerous helpful personal discussions have guided me through various stages, transforming me from a confused student to a confident researcher. Our cooperation has led to many significant achievements, none of which would have been possible without his support.

I would also like to thank Prof. Heldwein. Despite knowing each other for a short time, he has generously agreed to be the chairman of my PhD defense. His willingness to support me in this important phase of my academic career is deeply appreciated.

My sincere thanks go to my colleagues at the institute EAL & HLU at TUM and CMRES at HM: Ali, Anja, Christos, Darshan, Dehao, Eyke, Eduardo, Florian, Gean, Hanbyul, Hannes, Julien, Niklas, Qing, Stefan, Wei, Wolfgang, Xicai, Xiaonan, Yuanxiang and Yongdu. Your constant support, friendship, and the beautiful memories we've created together have made this journey unforgettable.

Finally, I would like to extend my deepest appreciation to my family and friends, especially my parents and my fiancée, Sungeun. Your support, encouragement, and companionship, especially being so far away from my hometown, have been a cornerstone of my journey. These achievements and this honor belong to you as well.

Thank you all.

Munich, July 2024 Shih-Wei Su

Contents

Abstract

This thesis discusses nonlinear control approaches of reluctance synchronous machines (RSMs) with analytical flux linkage prototype functions. Developing a high-performance RSM drive system is challenging due to the severe magnetic saturation, which may not be simply neglected as in other electrical drive systems. Hence, the machine modeling and the parameter identification, which are considered as essential tasks, are revisited at the beginning. Instead of saving the nonlinear flux linkages and differential inductances as lookup tables (LUTs), analytical flux linkage prototype functions are proposed. The features, such as low memory burden and continuous differentiablility, are attractive for applications in system identification and control algorithms. Nonlinear current controllers are developed based on the concept of the exact input/output (I/O) linearization of the current dynamics. The controller design is thus simple and independent of the nonlinear machine parameters. Moreover, a unified theory for optimal feedforward torque control (OFTC) is introduced. The optimal current references are obtained by intersecting quadrics of the machine equations and the operation strategies. Through simulative and experimental validations, the developed RSM drive system is confirmed with (i) the very high flux linkage approximation accuracy, (ii) the very fast and accurate current tracking performance and (iii) the best possible operation efficiency and the effective operation management.

Kurzzusammenfassung

Diese Arbeit behandelt nichtlineare Regelungsansätze von Reluktanzsynchronmaschinen, die analytische Prototypenfunktionen zur Berechnung der Flussverkettung nutzt. Die Berücksichtigung der nichtlinearen Flussverkettung aufgrund von starker magnetischer Sättigung ist eine Herausforderung bei der Entwicklung von leistungsfähigen Antriebssystemen mit Reluktasnzsynchronmaschinen, die im Gegensatz zu anderen Antriebssystemen nicht vernachlässigt werden darf. Daher bilden Maschinenmodellierung und -identifikation die wesentliche Basis dieser Arbeit, welche zu Beginn behandelt wird. Anstatt die nichtlinearen Flussverkettungen und die differentiellen Induktivitäten in Lookup-Tabellen zu speichern, wird vorgeschlagen, diese durch analytische Prototypenfunktionen zu berechnen. Vor allem der geringe Speicherbedarf und die stetige Differenzierbarkeit sind attraktive Eigenschaften, die bei Anwendungen zur Systemidentifikation und bei Regelungsaufgaben interessant sind. In dieser Arbeit werden nichtlineare Stromregler entwickelt, die auf dem Konzept der exakten Eingangs-/Ausgangslinearisierung (E/A-Linearisierung) der Stromdynamik basieren. Der Reglerentwurf ist somit einfach und unabhängig von den nichtlinearen Maschinenparametern. Darüber hinaus wird eine ganzheitliche Theorie für die optimale Drehmomentvorsteuerung präsentiert. Dabei sind die optimalen Sollströme das Ergebnis von Schnittpunktbestimmungen von Quadriken, welche aus Maschinengleichungen und Betriebsstrategien abgeleitet werden. Durch simulative und experimentelle Validierungen werden (i) die sehr gute Approximation der Flussverkettung, (ii) die sehr schnelle und genaue Stromnachführung und (iii) die größtmögliche Effizienz und effektive Betriebsführung des entwickelten Antriebssystems mit Relektanzsynchronmaschine bestätigt.

List of Publications

During the study at Technical University of Munich (TUM), several thesis-related publications are published in international journals and conferences. The entire doctoral program was funded by:

- the scholarship from German Academic Exchange Service (DAAD) in "Funding programme: Research Grants - Doctoral Programmes in Germany" from Oct. 2018 to Sept. 2022 and
- the employment at Chair of High-Power Converter Systems (HLU), formerly Chair of Electrical Drive Systems and Power Electronics (EAL), TUM from Oct. 2022 to Sept. 2023.

Journal publications

- S. -W. Su, C. M. Hackl, and R. Kennel, "Analytical prototype functions for flux linkage approximation in synchronous machines," *IEEE Open Journal of the Industrial Electronics Society*, vol. 3, pp. 265-282, 2022, [1].
- S. -W. Su, H. Börngen, C. M. Hackl, and R. Kennel, "Nonlinear current control of reluctance synchronous machines with analytical flux linkage prototype functions," *IEEE Open Journal of the Industrial Electronics Society*, vol. 3, pp. 582-593, 2022, [2].

Conference publications

- S. -W. Su, R. Kennel, and C. M. Hackl, "Analytical flux linkage approximation prototypes for reluctance synchronous machines," in *2020 International Symposium on Power Electronics, Electrical Drives, Automation and Motion (SPEEDAM)*, Sorrento, Italy, 2020, pp. 91-96, [3].
- S. -W. Su, N. Monzen, R. Kennel, and C. M. Hackl, "Self-identification of reluctance synchronous machines with analytical flux linkage prototype functions," in *2023 11th International Conference on Power Electronics and ECCE Asia (ICPE 2023 - ECCE Asia)*, Jeju, Korea, 2023, pp. 221-227, [4].

Nomenclature

Notation

The following mathematical symbols, functions and definitions are used:

Symbol	Description
$\mathbb{N}, \mathbb{R}, \mathbb{C}$	natural, real and complex numbers
$\mathbb{X} = \{x \vert \cdots\}$	set of feasible values for quantity x
$x := y$	x is defined as y
$x \overset{!}{=} y$	x must equal to y
$x \overset{(\#1)}{=} y$	x equals to y by invoking Eq. (#1)
$\widehat{x}$	approximation of quantity x
$\widehat{\boldsymbol{x}}$	magnitude or approximation of vector $\boldsymbol{x}$
$\overline{x}$	linearization of quantity x
$\boldsymbol{x} := (x_1, \cdots, x_n)^\top \in \mathbb{R}^n$	column vector, $n \in \mathbb{N}$ where "$^\top$" denotes "is defined as"
$\boldsymbol{0}_n := (0, \cdots, 0)^\top \in \mathbb{R}^n$	zero vector
$\boldsymbol{1}_n := (1, \cdots, 1)^\top \in \mathbb{R}^n$	unity vector
$\boldsymbol{a}^\top \boldsymbol{b} := a_1 b_1 + \cdots + a_n b_n$	scalar product of vectors $\boldsymbol{a} := (a_1, \cdots, a_n)^\top$ and $\boldsymbol{b} := (b_1, \cdots, b_n)^\top$
$\Vert\boldsymbol{x}\Vert := \sqrt{\boldsymbol{x}^\top \boldsymbol{x}} = \sqrt{x_1^2 + \cdots + x_n^2}$	Euclidean norm of $\boldsymbol{x}$
$\boldsymbol{X} \in \mathbb{R}^{n \times m}$	matrix with n rows and m columns
$\boldsymbol{A} \in \mathbb{R}^{n \times n}$	square matrix with n rows and n columns
$\boldsymbol{A}^{-1}$	inverse of square matrix $\boldsymbol{A}$ (if it exists)
$\det(\boldsymbol{A})$	determinant of square matrix $\boldsymbol{A}$
$\mathrm{diag}(a_1, \cdots, a_n) \in \mathbb{R}^{n \times n}$	diagonal matrix with entries $a_1, \cdots, a_n \in \mathbb{R}$
$\boldsymbol{I}_n := \mathrm{diag}(1, \cdots, 1) \in \mathbb{R}^{n \times n}$	identity matrix
$\boldsymbol{J} := \left[\begin{smallmatrix} 0 & -1 \\ 1 & 0 \end{smallmatrix}\right]$	rotation matrix (counter-clockwise rotation by $\frac{\pi}{2}$)
$\boldsymbol{x}$ (in X)^n	physical quantity $\boldsymbol{x}$, where each of the n elements has SI-unit X
$\wedge, \vee$	logical "and" and "or"
$f(t) \quad \circ\!\!-\!\!\bullet \quad f(s)$	Laplace transform $f(s)$ of a function $f(t)$
"s.t."	subject to (optimization with constraints)
$\mathbb{X} \cap \mathbb{Y}$	intersection of sets $\mathbb{X}, \mathbb{Y} \subset \mathbb{R}^2$

Reference frames

A signal vector $\boldsymbol{x}$ may be assigned to different reference frames, which are denoted in its superscript as $x^{\square}$:

Signal vector	**Reference frame**
$\boldsymbol{x}^{abc} := (x^a, x^b, x^c)^\top \in \mathbb{R}^3$	three-phase quantity $\boldsymbol{x}^{abc}$ in the three-phase (a,b,c)-reference frame
$\boldsymbol{x}^{\alpha\beta} := (x^\alpha, x^\beta)^\top \in \mathbb{R}^2$	two-phase quantity $\boldsymbol{x}^{\alpha\beta}$ in the stator-fixed (α,β)-reference frame
$\boldsymbol{x}^{dq} := (x^d, x^q)^\top \in \mathbb{R}^2$	two-phase quantity $\boldsymbol{x}^{dq}$ in the synchronously rotating (d,q)-reference frame

Location/component indices

A signal or parameter x may be belonged to a certain location or component, which is denoted in its subscript as $x_{\square}$:

Index	**Location/component**
"s"	stator
"r"	rotor
"m"	machine (or mechanical)
"l"	load
"pm"	permanent magnet
"re"	reluctance
"self"	self-axis
"cross"	cross-coupling
"zl"	zero locus
"reg"	region
"max"	maximum
"R"	rating
"C"	current
"V"	voltage
"dc"	dc link
"sw"	switching
"sam"	sampling
"c"	Clarke transformation
"p"	Park transformation (or pole pair, or proportional)
"ref"	reference
"pi"	proportional-integral controller
"i"	integral
"aw"	anti-windup
"CL"	closed loop
"ff"	feedforward

List of Abbreviations

Abbreviation	Definition
ADC	analog-to-digital converter
ALA	axially laminated anisotropic
ANN	artificial neural network
COP21	21st Conference of the Parties
DTC	Direct Torque Control
Dy	dysprosium
EM	electrical machine
EMF	electromotive force
EU	European Union
EV	electric vehicle
FEA	finite element analysis
FOC	Field Oriented Control
FW	field weakening
IE	International Energy
IM	induction machine
IPMSM	interior permanent magnet synchronous machine
ISR	Interrupt Service Routine
ITAE	integral time-weighted absolute error
I/O	input/output
LMA	Levenberg-Marquardt algorithm
LUT	lookup table
MC	maximum current
MEPS	minimum energy performance standard
MMF	magnetomotive force
MTPA	maximum torque per ampere
MTPC	maximum torque per current
MTPL	maximum torque per losses
MTPV	maximum torque per voltage
NaN	Not a Number
Nd	neodymium
NdFeB	neodymium iron boron

OCRC	optimal current reference computation
OFTC	optimal feedforward torque control
PI	proportional-integral
PLL	phase-locked loop
PM	permanent magnet
PMaRSM	permanent magnet assisted reluctance synchronous machine
PMSM	permanent magnet synchronous machine
PWM	pulse width modulation
QP	quadratic programming
RSM	reluctance synchronous machine
RTS	real-time system
SNR	signal-to-noise ratio
SM	synchronous machine
SPMSM	surface-mounted permanent magnet synchronous machine
SVM	space vector modulation
TLA	transversally laminated anisotropic
UNFCCC	United Nations Framework Convention on Climate Change
VSD	variable-speed drive
1D	one-dimensional
2D	two-dimensional
3D	three-dimensional

Chapter 1

Introduction

Technologies have been rapidly and widely developed since the Industrial Revolution, which have facilitated human daily life substantially. However, the extensive usage of fossil fuels for ages has resulted in climate change and energy crisis. At the 21st Conference of the Parties (COP21) in Paris on December 12, 2015, parties of the United Nations Framework Convention on Climate Change (UNFCCC) reached a milestone agreement, which is the Paris Agreement [5], to combat climate change and intensify the actions needed for a sustainable energy future. The central aim is to keep this century's global temperature rise below 2 °C, preferably to 1.5 °C, above pre-industrial levels. To achieve this goal, improving energy efficiency is a crucial mitigation solution. Electrical machines (EMs) are utilized in various applications, such as pumps, fans, compressors, transport systems and industrial processes, and hence represent the major consumption group (around 50 %) of electrical energy consumption in the world [6]. Therefore, enhancing the energy efficiency of electrical drive systems is the primary task. In recent years, reluctance synchronous machines (RSMs) [7, 8] have drawn attention from industry to their various applications due to their compact design, high efficiency and reliability.

This chapter gives an introduction to the work. In Section 1.1, its motivation is found by discussing the efficiency regulation of EMs and the current issues of rare earth material. Then the main objective of this work is defined. Section 1.2 provides a brief state-of-the-art review of the selected topics. Finally, in Section 1.3, the contributions and outline of the thesis are summarized.

1.1 Motivation and problem statement

Electrical drive systems are often too old, inefficient and oversized in the industry [9]. As a result of conservative decision-making, oversizing is a common practice that can prolong their operational lifecycles. Nevertheless, for EMs, more power losses are induced while operating at inefficient operation ranges, where they are not optimally designed for. Besides, induction machines (IMs) are still until today the majority in the market due to cost-effectiveness and well-understood technology. With advanced technologies, other machine types, such as permanent magnet synchronous machines (PMSMs) and RSMs, can outperform IMs in energy efficiency [10]. Furthermore, it is proposed in [11] to target the following four efficiency measures for electrical drive systems: (i) higher efficiency class of the machine; (ii) higher efficiency of the components; (iii) size reduction; and (iv) optimization of regulation and process. Consequently, the overall system may save up to 50 % of the energy consumption.

A well-established and globally harmonized standard is needed for EMs, which are manufactured and used worldwide [6]. For the first time in 2009, the International Electrotechnical Commission (IEC) issued the standard IEC 60034-30-1:2014 [12] defining efficiency classification for direct-on-line (grid-connected) fixed-speed machines. The standard IEC TS 60034-30-2:2016 [13] was published afterwards for converter-fed variable-speed drives (VSDs). The energy efficiency level is expressed in International Energy (IE) efficiency classes from IE1 (lowest) to IE5 (highest). These uniformly defined standards can greatly simplify the introduction of national regulations. Consequently, local machine manufacturers should release their products following the corresponding requirements and state the IE efficiency classes on the nameplates. To accelerate the introduction of highly efficient machines into the market, minimum requirements for the energy efficiency of EMs have already been implemented in several countries. In European Union (EU), the Ecodesign Directive [14] from the European Commission establishes a framework to regulate a series of energy-related products. Therefore, for all machine manufacturers and suppliers in the EU market, their products must meet the required minimum energy performance standards (MEPSs). The efficiency regulations for EMs and VSDs, as outlined in [15], encompass varying timeframes with distinct requirements. Since July 1, 2021, smaller machines (120 W-750 W) and bigger machines (750 W-1 000 kW) must meet the efficiency classes IE2 and IE3, respectively. Whereas all VSDs (120 W-1 000 kW) must reach IE2. After two years in effect, from July 1, 2023, IE4 has become compulsory for machines between 75 kW and 200 kW, which is the first one worldwide to introduce IE4 into the market. The standard efficiency class IE1 has been eliminated from the regulation and will soon be eliminated from the market. It can be speculated that IE2 will face the same fate in the near future as IE1 today, whereas IE3 and IE4 with higher efficiencies will become mainstream in the industry. Nowadays, for fixed-speed applications, IMs with IE4 are achievable by advancing in design techniques, e.g., lowering the stator and rotor copper losses. On the other hand, PMSMs and RSMs, with the absence of rotor losses, can achieve very high efficiency levels up to IE5 and also present themselves as an alternative to IMs in variable-speed applications. It is proven that the relevant standards have successfully accelerated the market penetration of energy-efficient EMs.

Rare-earth permanent magnets (PMs) [16] began a revolutionary page of EMs in the early 1980s. Their powerful magnet strength empowers PMSMs to attain higher power density and efficiency, which are desirable for many applications [17, 18]. Neodymium-iron-boron (NdFeB) PM is the most commonly used rare-earth PM, and it contains two critical rare-earth elements: neodymium (Nd) and dysprosium (Dy). Dy is added with a small amount to prevent irreversible thermal demagnetization. The availability of Nd in the earth's crust is relatively high compared to other rare-earth elements. However, several factors in political and environmental aspects have complicated the accessibility of NdFeB PMs. Due to the monopoly of the rare-earth market in specific countries and the high demand in electric vehicle (EV) and wind turbine industries, the price of rare-earth PMs is not only expensive but also volatile. In 2011, a sudden boom in the rare-earth market sent the prices of Nd and Dy rapidly up to 550 and 3 350 \$/kg, respectively, which are more than 20 times higher than the stable base prices in 2009 [16]. After hitting the peaks, they dropped as fast as how they raised and settled to the pre-bubble prices. Since EVs are urgently promoted worldwide, a massive demand for rare-earth PMs with limited supply causes inevitable and continuous price increases. In addition to the price volatility, rare-earth mining produces mountains of toxic waste with a high risk of environmental and health hazards. Hence, environmentalists are strongly opposed to it without thorough ecological protections. In order to avoid another costly risk as the 2011 price bubble and the environmental concerns, major users of rare-earth PMs must reduce the amount of usage or choose other PMs with lower magnetic performance [19, 20], e.g., ferrite magnets [21]. Alternatively, PM-free machines, such as IMs and RSMs, can also be possible solutions and are being investigated intensively.

RSMs have recently regained great interest from industry and academia [22–25], owing to the above-mentioned energy efficiency and rare-earth price instability issues. As a matter of fact, RSM is not a newly discovered technology. Kostko proposed its first topology in 1923 [26], and it was realized that the traditional simple salient-pole rotor structure leads to poor torque production capability. To conquer it, the RSM rotor must be appropriately designed with flux barriers to enhance the magnetic saliency, which can yield good torque capability as IMs. However, its applicability and acceptability were limited for decades due to the immature techniques and the dominant role of IMs. With the advent of machine design and power electronics technologies, RSM has become a promising candidate that meets high-efficiency and low-cost requirements. Its feasibility has been studied and approved in a variety of applications, for example, compressors [27], pumps [28], elevators [29, 30] and EVs [31–33]. Moreover, world-leading machine manufacturers, such as ABB, KSB and Siemens, have started mass-producing high-efficiency RSMs. Therefore, the rapid industrial acceptance of RSMs is just a matter of time.

RSMs are considered a potential competitor to other commonly used EMs due to several attractive features, including low cost, rigid structure, high energy efficiency and high torque density. Theoretically, with the identical stator geometry to IMs (and also PMSMs), their rotors can be replaced directly by a salient-type rotor to form an RSM. As a result of a complete absence of rotor copper losses, RSMs possess higher efficiency than IMs [34, 35]. Potentially, higher torque can be produced by RSMs with the same frame size. For specific applications with strict requirements on energy efficiency and power density, PMSMs must be chosen. Conversely, for applications with less stringent criteria, RSMs should be adopted to prevent using precious rare-earth PMs. As the control principle of RSMs shares much in common with PMSMs, the adaption to RSMs would not be a complex task. The rigid structure of RSMs possesses excellent overload capability. Without windings and/or PMs in the rotor, the so-called "cold rotor" [8, 25] is not subject to overheating, demagnetization and PM flyout problems. Hence, the operation under harsh environmental conditions is allowed. In addition to the robustness, the simple rotor of RSMs, composed of only stamped iron sheets, results in the cheapest technology in EMs. Not only the material cost but also the maintenance requirements can be significantly reduced, where the maintenance and repair services can be carried out conveniently in any workshops [29]. Furthermore, the inherent machine's saliency makes encoderless control schemes [36, 37] applicable down to standstill, which might further promote the use of RSMs in the future.

Along with the highlighted advantages over IMs and PMSMs, some essential issues, including machine design and control algorithms, must be dealt with to accomplish a high-performance RSM drive system. Until today, the key design challenge has always been the maximization of average torque, which remains yet to be solved. To this end, machine designers devote their attention to a major boost to the machine's magnetic saliency [38]. By increasing the number of flux barriers in the rotor, the elevated saliency can upgrade the output torque and efficiency. Some secondary effects, such as torque ripple [39] and power factor (PF) [40, 41], must be considered carefully by means of comprehensive analyses and optimizations during the design process. On the other hand, RSMs possess highly nonlinear magnetic characteristics [42–44], which must be compensated for in control to achieve the best possible drive performance. Their flux linkages and differential inductances vary considerably with currents throughout the entire operation range. Both changes are caused by magnetic saturation, which, additionally, leads to cross-coupling of direct (d-) and quadrature (q-)axes. The effectiveness of developed control algorithms, e.g., nonlinear current control strategies [45–47], optimal feedforward torque control (OFTC) [48–53] or model predictive control [54–56], is deteriorated by model and parameter uncertainties. In addition, cross-coupling inductances lead to position estimation errors in encoderless control [57–60]. As a consequence, a comprehensive flux linkage (or differential inductance) model is crucial

for modern RSM drive systems.

These above-mentioned challenges justify the slow adoption of RSMs in industrial applications, which might require a more expensive system with a higher rating and complex control algorithms. Nevertheless, it is promising to meet the tightened efficiency standards without using rare-earth PMs. Therefore, the main goal of this thesis is motivated to achieve a high-performance RSM drive system with a thorough control measure by overcoming the control difficulties as mentioned earlier, covering: (i) prototype functions to describe the magnetic nonlinearity analytically, including the magnetic saturation and cross-coupling effects; (ii) nonlinear current control to ensure excellent current dynamics throughout the complete operation range; and (iii) effective OFTC for loss minimization to achieve the best operation efficiency.

1.2 State-of-the-art

In accordance with the previously defined objective of the thesis, a brief literature review on the selected topics is given in the following.

1.2.1 Analytical prototype function

Typically, the magnetic nonlinearity of the flux linkage maps can be extracted mostly as lookup tables (LUTs) by using finite element analysis (FEA) or by conducting experiments in the laboratory. For many applications (e.g., industrial drives), FEA data from the machine manufacturers may not be available to commissioning or control engineers but—as it is required for optimal controller tuning and operation of the electrical drive system—machine identification [61–64] or self-commissioning [64, 65] must be performed to extract (at least parts of) the flux linkage maps. To compensate for the nonlinear magnetic saturation and cross-coupling effects in the real-time control system with limit-storage, analytical functions instead of LUTs are preferable. A small number of parameters usually parameterizes analytical functions. Moreover, continuity and even differentiability of such functions over the whole operation range facilitate the derivation of differential inductances or the solution of analytical optimization problems [50, 51].

Polynomial functions [66] are commonly adopted for representing the saturated flux linkages or differential inductances. Higher polynomial orders are necessary to enhance the fitting performance. Hence, a suitable polynomial order must be chosen according to the required estimation accuracy. To include the cross saturation into the models, bivariate polynomials [67–69] could be used to avoid the need to save several sets of parameters for different current regions. In [70], power functions (or so-called modified polynomial functions) with fewer parameters and a shared cross-coupling term are developed for describing the magnetic saturation of RSMs. The inverse (flux-current) relation is modeled here due to the similar curve shapes to the power function, which eases the fitting procedure. For identifying machine parameters automatically, based on [70], a self-commissioning method [71] for RSMs is developed by implementing a test injection sequence to improve the fitting process for the model. But several polynomial orders must be found to enhance the fitting results. Moreover, as the approach is not generic, the process must be repeated for each individual machine. On the other hand, a few flux linkage prototype functions do exist. For example, [55], [72], [73] or [74] introduces novel RSM flux linkage approximation prototype functions, which are also able to reproduce self-axis saturation effects. The flux linkages are modeled separately by a linear and a nonlinear part. However, in particular, for [72], several sets of parameters for different quadrature currents must be saved to cover the whole operation range. Therefore, a large number of parameters and the discontinuity of the prototype

function limit its applicability. The prototype function in [55] is continuously differentiable, but the accuracy is rather limited. For interior PMSMs (IPMSMs), a continuous prototype function is proposed in [75] to simplify the analysis of the saturation effects. But the saturation effects cannot be directly observed in the mathematical expressions due to its complexity with many reciprocal exponential functions. Furthermore, nonlinear flux maps are reduplicated by implementing artificial neural networks (ANNs) in [76]. Nevertheless, complex network structures result in complicated learning procedures and overabundant ANN parameters.

In summary, existing solutions to approximate the magnetic nonlinearity of RSMs lack physical meaning and generic structure. These flux linkage (or differential inductance) prototype functions are expressed in complicated forms with many redundant function parameters. Besides, they are feasible only on a particular machine type and cannot be adapted conveniently to other machine types, which limits their applicability.

1.2.2 Nonlinear control method

RSMs are not easy to control due to their intrinsic nonlinear behavior. The nonlinear relation between stator currents and flux linkages, caused by the magnetic saturation and cross-coupling effects, complicates the system description and controller design. Therefore, the implementation of conventional control approaches may be difficult and sophisticated.

Regarding the control of RSMs, two standard approaches are often adopted: Direct Torque Control (DTC) [77–79] and Field Oriented Control (FOC) [80–82]. DTC possesses fast torque control dynamics, while it results in a variable switching frequency and high torque ripple. On the other hand, FOC (vector control) preserves better steady-state torque response and hence higher system efficiency, but system parameters must be known, e.g., stator resistance, differential inductances and flux linkages. Adaptive current controllers [46, 83–85] are developed to ensure good current dynamics, where the proportional-integral (PI) controller parameters are updated online with the varying differential inductances of RSMs. In [83, 84], stationary and transient inductances are introduced in the system model, which leads to a more complex expression and is physically questionable. The cross-coupling is neglected in [84] to simplify the controller design; consequently, current control performance cannot be ensured in highly saturated conditions. In contrast to that, [46] proposes a nonlinear disturbance compensation method with online tracking of the flux linkages and the differential inductances, so the cross-coupling can be compensated for to achieve good current dynamics for both direct and quadrature components. In [85], the controller structure is achieved via a change of controller state variable, i.e., mapping the current to the flux linkage. Without knowing the differential inductances, the saturation effects are simply taken into account with the nonlinear flux linkages. [45] introduces a completely parameter-free control method for SMs, which guarantees tracking with prescribed asymptotic and transient control accuracy.

In [47] (in German), a nonlinear current control system, based on the concept of input/output (I/O) linearization, has been proposed for RSMs. As it is a model-based approach, the machine's parameters must be known from either FEA or experimental measurements. The I/O linearization technique from the system theory transfers a nonlinear control system to a linear system, i.e., a chain of integrators. Hence, the controller parameters can be designed conveniently with the help of conventional PI controllers and pole placement. If the actual current-dependent flux linkages and differential inductances are known and available online, an excellent current control performance over the complete operation range can be achieved.

1.2.3 Optimal operation management

In principle, the operation efficiency of RSMs can be enhanced by (i) improving machine design (hardware modification) or (ii) pursuing the best possible efficiency through OFTC (software modification). Although combining both methods leads to the best results, the former is expensive and not easily applicable except for machine designers. In contrast, the latter is economical and achievable for all machine users and, therefore, is equipped as an indispensable function for modern drive systems. The main idea of OFTC is to derive optimal current references with minimum losses while physical constraints are satisfied (e.g., current or voltage limits).

Typically, offline methods [86–88] are chosen to avoid complex calculations in the real-time system. LUTs, extracted from FEA or measurements, map the dependence between optimal currents and requested torque and thus can find the references simply. However, the construction of these LUTs is a time-consuming process and must be repeated for different machines. Conversely, solving the OFTC problem directly online is desirable, which eliminates the premade LUTs. Online methods can be categorized into two groups [89]: online-searching and loss-model approaches. Online-searching technique [90–93] (e.g., "perturb and observe") stimulates the machine with given testing signals during operation and observes the response to such stimulus to search for the optimal current references. Even though this method does not depend on the knowledge of the machine model and parameters, stability concerns arise due to its requirements of constant load torque and long search time. On the other hand, the loss-model technique is more practical. The current references can be derived analytically based on a mathematical machine model, which describes the electromechanical conversion and the losses during operation. This approach requires strictly the machine's parameters, especially the electromagnetic relationships.

Depending on the actual operation conditions, e.g., the current and voltage limitations, the angular velocity and the given target torque, the electrical drive is operated in one of the following operation strategies: (i) maximum torque per current (MTPC); (ii) field weakening (FW); (iii) maximum current (MC); and (iv) maximum torque per voltage (MTPV). The OFTC problem by means of these strategies has been widely studied and described in a significant number of publications (see, e.g., [69, 94–101] for MTPC, [95, 96, 98, 100] for MC and [95, 98, 100, 102, 103] for FW or MTPV). These four operation strategies are discussed later in detail, indicating the respective conditions and methodology.

Until recently, publications providing analytical solutions often contain simplifications, e.g., the neglection of the stator resistance or the magnetic cross-coupling, to make online calculation possible. In addition, to cover a wide speed range capability, the transition between different operation strategies, such as in [95, 98, 100], is still a subject to be further investigated. These bottlenecks have been tackled in [48–51] by proposing a unified theory for OFTC, which provides analytical solutions for all aforementioned operation strategies while the stator resistance and the magnetic saturation are considered for loss minimization. The key concept is to reformulate the optimization problems implicitly with quadrics and find the optimal solution by intersecting two respective quadrics. In [52], this approach has been extended to take both copper and iron losses into account, leading to a maximum torque per losses (MTPL) operation strategy. A novel ANN-based OFTC strategy [53] guarantees the optimal current references with high accuracy and less computational burden compared to the conventional OFTC strategies. Therefore, solving the OFTC problem by training ANN exhibits a great potential for modern drive systems but requires more assessments of its real-time applicability.

1.3 Contribution and outline

The main contributions of the thesis are:

1. Nonlinear flux linkages of the employed RSM are identified experimentally with different measurement methods.
2. Flux linkage prototype functions for RSMs and IPMSMs are developed by exploiting the intrinsic physical characteristics (such as Gaussian and sigmoid shapes) of nonlinear flux linkages instead of using polynomial functions or non-differentiable modulus (absolute value) functions; the resulting prototype functions are continuously differentiable, obey the energy conservation rule, have few parameters and can be extended in a generic and modular fashion (to meet arbitrarily high estimation accuracies).
3. Fitting procedures of the function parameters are designed in a step-by-step manner to effectively obtain an optimal parameter set with the best approximation accuracy.
4. Effectiveness, accuracy and universality of the proposed flux linkage prototype functions are evaluated with real nonlinear flux linkages (by both FEA and experimental measurements) of different machines.
5. Nonlinear I/O-linearization based current control system from [47] is adapted in order to allow for the utilization of flux linkage prototype functions instead of using LUTs.
6. Effectiveness of the proposed current control method is validated by simulation and experimental results under different testing scenarios.
7. Benefits and potential of utilizing the analytical prototype functions in closed-loop current control are confirmed by a thorough comparison between different updating approaches of the machine nonlinearities (e.g., LUTs, simplified prototype functions and proposed prototype functions).
8. Unified theory for OFTC from [50, 51] is adapted in order to allow for the utilization of flux linkage prototype functions instead of using LUTs.
9. Effectiveness of the proposed OFTC is validated by simulation and experimental results under different operation conditions.

After the introduction in this chapter, the thesis is structured as follows. Chapter 2 first introduces the machine structure and machine model of RSMs, then presents the parameter identification approaches to extract the flux linkages. Chapter 3 proposes two solutions of analytical prototype functions to approximate the nonlinear flux linkages of RSMs, and the second solution is further extended for IPMSMs. Chapter 4 develops a nonlinear current control system for RSMs based on I/O linearization, and the implementation of simulations and experiments to demonstrate the effectiveness is shown. Chapter 5 presents an analytical solution for the OFTC problem of RSMs covering all operation strategies. Finally, Chapter 6 concludes the thesis by summarizing the results and providing an outlook.

Chapter 2

Reluctance synchronous machine

Reluctance synchronous machines (RSMs) [7, 8] possess several inherently advantageous characteristics, for example, high efficiency, rigid structure and low cost. These characteristics make RSMs an attractive alternative to widely adopted induction machines (IMs) in industrial applications [10, 34, 35], which are nowadays strictly regulated by efficiency standards. Using the same stator frame from an IM, an RSM can be formed by replacing the IM rotor with a unique rotor with flux barriers. In addition, without the need of permanent magnets (PMs) in the rotor, the price instability of rare-earth materials can be prevented [19, 25]. Therefore, RSMs are believed as a promising technology for modern electrical drive systems in this century. However, control of RSMs is a challenging task. Several aspects must be considered in RSM drive systems, such as controller design (for current and speed controllers) [45–47] and operation strategies [48–51] throughout the entire operation range.

Before developing effective control methods, an introduction to RSMs is given in this chapter to have a preliminary understanding beforehand. In Section 2.1, the machine structure of RSMs is introduced together with those of other synchronous machines (SMs), so the characteristics of different SMs according to their structures can be highlighted. Afterwards, Section 2.2 gives a generic nonlinear machine model for all SMs, which is further developed to model RSMs as a linear or real nonlinear machine. In the end, in Section 2.3, different experimental approaches to identify machine parameters are introduced; moreover, their measurement results for the employed RSM are presented as examples.

2.1 Machine structure

As with all electrical machines (EMs), an RSM consists of a stator and a rotor. This section introduces various stator and rotor configurations of commonly used SMs. Then, different features of the resulting machine types, especially for RSMs, are pointed out. Besides, assembly methods for the RSM rotor are introduced.

2.1.1 Stator

According to winding distribution, the stator for SMs can be mainly categorized into two groups [22, 23]: (i) Distributed wound stator [as shown in Fig. 2.1(a)]: This technique results in stator coils with distributed and overlapping windings, and it is widely adopted for ac machines with sinusoidal currents, including IMs. (ii) Concentrated wound stator [as shown in

Fig. 2.1(b)]: This winding type encircles every single stator tooth without overlap, which leads to a much shorter length of the end turns compared to the conventional distributed winding. With the reduced size of windings, higher efficiency (due to decreased copper losses) and lower production cost (due to a more straightforward manufacturing process) can be expected. Nevertheless, high magnetomotive force (MMF) harmonic content due to the nature of winding causes some undesirable drawbacks, e.g., high torque ripple, low power factor (PF) and increased iron losses.

Recently, permanent magnet synchronous machines (PMSMs) with concentrated windings [104, 105] have been increasingly adopted in the industry, especially well suited for direct drive applications [106]. On the other hand, industrial RSMs until now solely utilize the classical distributed windings. Although developing RSMs with concentrated windings [107–109] allows for increased efficiency and torque density, it is still subject to poor torque quality, low PF and a few slot-pole combinations. Therefore, further study on this development is needed to discover its potential.

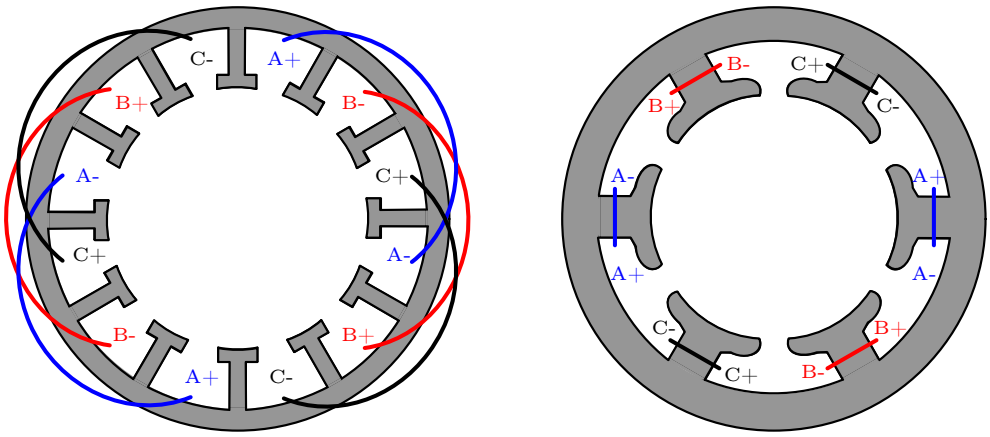

(a) (b)

Figure 2.1: Stators of SMs with: (a) distributed windings; (b) concentrated windings (based on [22, 23]).

2.1.2 Rotor

Rotor configurations of different SMs are shown in Fig. 2.2 [23, 25]: (i) surface-mounted PMSM (SPMSM) in Fig. 2.2(a); (ii) interior PMSM (IPMSM) in Fig. 2.2(b); (iii) PM-assisted RSM (PMaRSM) in Fig. 2.2(c); and (iv) transversally laminated anisotropic (TLA) RSM & axially laminated anisotropic (ALA) RSM in Fig. 2.2(d) & 2.2(e) (by two different rotor assembly approaches, which will be discussed later). Generally, direct (d-) and quadrature (q-)axes are defined according to the flux paths in the rotors, where the d-axis is always the part with higher flux linkage [25]. For PM-based machines, including SPMSM and IPMSM, the d-axis path is aligned with the PM magnetization direction. Whereas, for reluctance-based machines, including RSM and PMaRSM, the d-axis path with mainly iron material has a higher permeability; on the contrary, the q-axis path with flux barriers has a lower permeability. Note that the PM magnetization direction of PMaRSM is opposing the positive q-axis.

For SPMSM [17, 25, 27], arc-shaped PMs are mounted on the surface of a cylindrical rotor core. This forms a uniform geometry without magnetic saliency. Therefore, SPMSM is a "pure PM" machine, where its torque production is only composed of electromagnet torque component. The smooth-developed torque makes it suitable for low-speed drives [23]. To prevent PMs from

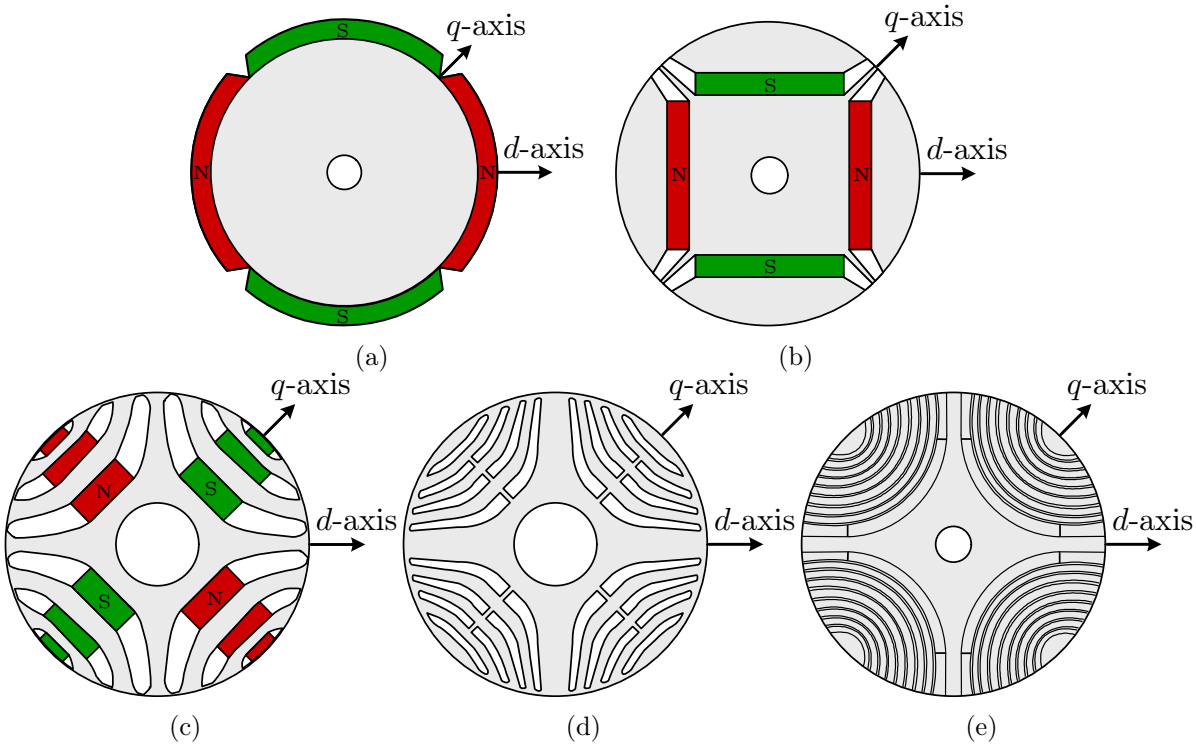

Figure 2.2: Rotors of SMs: (a) SPMSM; (b) IPMSM; (c) PMaRSM; (d) TLA RSM; (e) ALA RSM (based on [23, 25]).

detaching under centrifugal force, a stainless-steel-can [17, 27] must be equipped to cover them; however, additional eddy current losses are induced on its surface. By contrast, IPMSM [17, 25, 27] is constructed by burying PMs inside the rotor without needing a stainless-steel-can. Due to the nonuniform geometry, the resulting magnetic saliency makes it a hybrid machine containing both electromagnet and reluctance torque components. Its excellent torque production capability yields the most powerful performance among all SMs in terms of efficiency and torque density. In addition, its wide constant-power speed range eases the implementation of field-weakening control, which is desirable for traction applications [19]. Moreover, it offers machine designers a great degree of freedom to shape the rotor according to specific requirements, e.g., mechanical structure and torque versus speed characteristics.

When it comes to RSM [17, 25, 27], its rotor is made of only cavities (flux barriers) and iron without the presence of PMs. The rotor q-axis is mainly composed of flux barriers, which are equivalent to air gaps with high magnetic resistance. Thus, a permeability difference between d- and q-axis flux paths is created. Thanks to this inherently strong magnetic saliency, RSM is thus a "pure reluctance" machine relying only on reluctance torque component. Even though the efficiency of RSM cannot achieve as high as IPMSM, the simple and rigid structure is attractive for industrial applications. The excellent overload capability allows working under harsh environmental conditions without being vulnerable to the problems caused by fragile PMs, i.e., demagnetization, flyaway and short-circuit fault currents. Furthermore, the highest level of rotor saliency facilitates the implementation of saliency-based encoderless control algorithms to detect the rotor position instead of using position sensors or encoders in low-speed region or even down to standstill. To improve RSM's efficiency and PF, less-energy PMs (normally ferrite) are inserted into the flux barriers to form the rotor of PMaRSM [17, 25]. These PMs along the q-axis tend to saturate the iron bridges in the rotor, such that torque production can be effec-

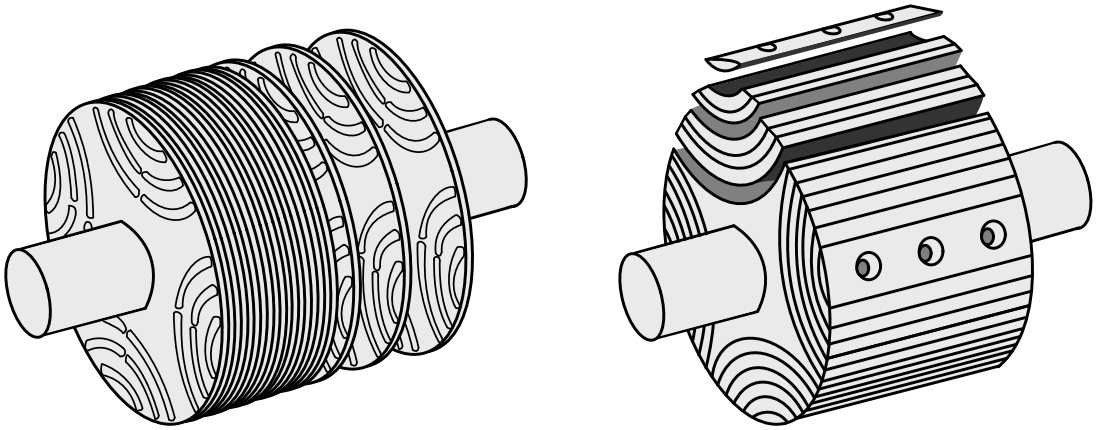

(a) (b)

Figure 2.3: Rotor assembly techniques for RSMs: (a) TLA assembly [corresponding to the TLA RSM rotor shown in Fig. 2.2(d)]; (b) ALA assembly [corresponding to the ALA RSM rotor shown in Fig. 2.2(e)] (based on [110]).

tively enhanced. Indeed, PMaRSM is an identical machine type as IPMSM, which produces both electromagnet and reluctance torque; however, for PMaRSM, the reluctance torque component accounts for a higher proportion taking advantage of its strong saliency in the rotor.

Regarding rotor assembly for RSMs, there are mainly two existing techniques forming TLA and ALA rotor geometries [110, 111]. Conventionally, the rotor can be constructed by pressing a stack of thin iron steel sheets transversally, as illustrated in Fig. 2.3(a) [corresponding to the TLA RSM rotor shown in Fig. 2.2(d)]. Each steel sheet can be produced by mechanical punching or laser cutting to remove unnecessary material. This assembling method possesses a straightforward manufacturing procedure; hence, it is widely adopted in the industry due to its suitability for mass production. As another option, as shown in Fig. 2.3(b) [corresponding to the ALA RSM rotor shown in Fig. 2.2(e)], the RSM rotor can also be assembled in axial direction using nested strips of steel with thin layers of insulation material in between. This method makes it possible to attain a higher number of flux barriers per pole in comparison with the TLA rotor, which considerably boosts the magnetic saliency. Theoretically, the ALA rotor is thus an ideal type for RSMs due to the elevated saliency. Unfortunately, additional iron losses, which arise from rotor eddy currents in the lamination, limit its efficiency [112]; more critically, the sophisticated construction hinders its acceptance for industrial production.

Despite the robustness of RSMs, the complex rotor structure results in a challenging design process with many geometrical parameters. The main focus in optimization is to derive a good torque quality with maximized averaged torque and minimized torque ripple. Apparently, shaping the rotor flux barriers to a maximum achievable saliency level is of the greatest importance [38, 113]. The key concept is to entirely block the rotor's q-axis flux while minimally affecting the d-axis flux. To this end, the influence of flux barrier number and thickness must be analyzed. The ratio between iron width and barrier width along the q-axis correlates to the rotor saturation, and it should be adequately set to yield a similar saturation extent as the stator [114]. Besides, the iron bridges (located at the end or sometimes in the middle of flux barriers) should be kept as thin as possible, as they direct additional flux through them, which does not account for torque production. However, they are purposely arranged to sustain mechanical strength without suffering from possible deformation when the rotor speed increases; therefore, the rotor structure of RSMs in high-speed applications [115] must be carefully designed. Indeed, the torque ripple,

caused mainly by slot harmonics, is one of the critical drawbacks of RSMs. Regrettably, the rotor skewing, commonly carried out for PMSMs, is insufficient to smooth the torque. To conquer it, a reasonable choice for the number of stator slots and flux barriers must be arranged, such that the flux barriers are uniformly distributed along the air gap with constant permeance [39]. Alternatively, designing an asymmetric rotor geometry [116, 117] with different flux-barrier shapes between adjacent rotor poles is also a feasible strategy, which provides adequate compensation for torque harmonics.

2.2 Machine model

After discussing the machine structure, a generic machine model based on [118, Chapter 14], applicable for all SMs (in Fig. 2.2), is introduced in this section. Based on it, nonlinear RSM modelings as a linear or (real) nonlinear machine are presented. An effective model can mathematically and analytically describe machine behavior, and it is beneficial to analyze its nonlinear characteristics and even establish a machine model in simulation. The following chapters adopt the introduced model to design nonlinear control methods. Furthermore, some critical issues in the development of a high-performance RSM drive system are summarized.

The configuration of a three-phase one-pole-pair star-connected RSM is shown in Fig. 2.4. The stator terminals U, V, W are connected to the three phases a, b, c (stator windings). For the rotor, a salient pole rotor is illustrated exemplarily. Some assumptions are made in the following derivation: (i) machine is designed symmetrically; (ii) three-phase stator windings are sinusoidally distributed; (iii) sum of the phase currents is zero at any time instant due to star-connection; (iv) harmonics are not considered; (v) mechanical losses due to friction are neglected; and (vi) iron losses due to eddy current and hysteresis effects are neglected.

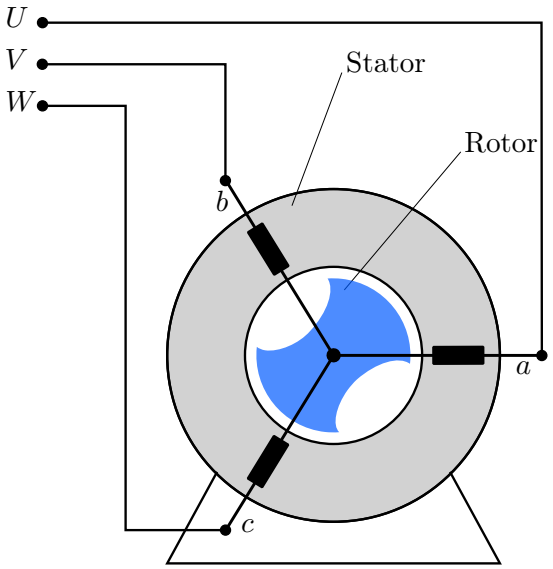

Figure 2.4: Configuration of a three-phase one-pole-pair star-connected RSM (with a salient pole rotor).

2.2.1 Generic machine model

2.2.1.1 Modeling in the (a,b,c)-reference frame

The generic nonlinear machine model for SMs in the three-phase (a,b,c)-reference frame is given by [118]

$$\left.\begin{array}{rcl} \boldsymbol{u}_{\mathrm{s}}^{abc} & = & R_{\mathrm{s}}\boldsymbol{i}_{\mathrm{s}}^{abc} + \frac{\mathrm{d}}{\mathrm{d}t}\boldsymbol{\psi}_{\mathrm{s}}^{abc}(\boldsymbol{i}_{\mathrm{s}}^{abc}, \phi_{\mathrm{m}}), \\ \frac{\mathrm{d}}{\mathrm{d}t}\omega_{\mathrm{m}} & = & \frac{1}{\Theta_{\mathrm{m}}}\big(m_{\mathrm{m}}(\boldsymbol{i}_{\mathrm{s}}^{abc}, \phi_{\mathrm{m}}) - m_{\mathrm{l}}\big), \\ \frac{\mathrm{d}}{\mathrm{d}t}\phi_{\mathrm{m}} & = & \omega_{\mathrm{m}}, \end{array}\right\} \tag{2.1}$$

where $\boldsymbol{u}_{\mathrm{s}}^{abc} := (u_{\mathrm{s}}^{a}, u_{\mathrm{s}}^{b}, u_{\mathrm{s}}^{c})^{\top}$ are the stator phase voltages (in V), $\boldsymbol{i}_{\mathrm{s}}^{abc} := (i_{\mathrm{s}}^{a}, i_{\mathrm{s}}^{b}, i_{\mathrm{s}}^{c})^{\top}$ are the stator phase currents (in A), $\boldsymbol{\psi}_{\mathrm{s}}^{abc} := (\psi_{\mathrm{s}}^{a}, \psi_{\mathrm{s}}^{b}, \psi_{\mathrm{s}}^{c})^{\top}$ are the stator flux linkages (in Vs; functions of $\boldsymbol{i}_{\mathrm{s}}^{abc}$ and the mechanical rotor angle ϕ_{m} (in rad)) and R_{s} is the stator resistance (in Ω). ω_{m} is the mechanical angular frequency (in rad/s). Furthermore, Θ_{m} is the moment of inertia (in kgm^2), m_{l} is an external load torque (in Nm),

$$m_{\mathrm{m}}(\boldsymbol{i}_{\mathrm{s}}^{abc}, \phi_{\mathrm{m}}) = n_{\mathrm{p}}(\boldsymbol{i}_{\mathrm{s}}^{abc})^{\top}\frac{1}{3}\begin{bmatrix} 1 & 1-\sqrt{3} & 1+\sqrt{3} \\ 1+\sqrt{3} & 1 & 1-\sqrt{3} \\ 1-\sqrt{3} & 1+\sqrt{3} & 1 \end{bmatrix}\boldsymbol{\psi}_{\mathrm{s}}^{abc}(\boldsymbol{i}_{\mathrm{s}}^{abc}, \phi_{\mathrm{m}}) \tag{2.2}$$

represents the (averaged) electromagnetic torque (in Nm), where n_{p} denotes the number of pole pairs.

The first equation in (2.1) demonstrates the electrical subsystem of the machine with its voltage equation. The applied stator voltage vector $\boldsymbol{u}_{\mathrm{s}}^{abc}$ must compensate for the resistance voltage drop $R_{\mathrm{s}}\boldsymbol{i}_{\mathrm{s}}^{abc}$ and the back electromotive force (EMF) $\frac{\mathrm{d}}{\mathrm{d}t}\boldsymbol{\psi}_{\mathrm{s}}^{abc}$ (i.e., the induced voltage in the machine) [118]. On the other hand, the second and third equations explain the mechanical subsystem of the machine. The difference between machine torque m_{m} and load torque m_{l} accelerates or decelerates the inertia Θ_{m} of the rotor to a certain mechanical angular velocity ω_{m}. Accordingly, the mechanical rotor angle ϕ_{m} changes during rotor movement.

2.2.1.2 Modeling in the (d,q)-reference frame

Invoking the space vector theory (as illustrated in Fig. 2.5), which is a well-known and powerful tool to describe physical quantities in three-phase systems, the presented model in the three-phase (a,b,c)-reference frame can transform into the stator-fixed or stationary (α,β)-reference frame and the arbitrarily/synchronously rotating (d,q)-reference frame [118]. Necessarily, the corresponding transformations must be implemented. Please note that as the balanced machine without the zero-sequence component is assumed, the reduced or simplified transformations will be introduced.

For a given three-phase signal vector $\boldsymbol{x}^{abc} := (x^{a}, x^{b}, x^{c})^{\top}$, which can be voltage, current or flux linkage (i.e., $x \in \{u, i, \psi\}$), the Clarke transformation and the inverse Clarke transformation can be applied to derive the signal vector $\boldsymbol{x}^{\alpha\beta} := (x^{\alpha}, x^{\beta})^{\top}$ in the stator-fixed (α,β)-reference frame and to derive $\boldsymbol{x}^{abc}$ from $\boldsymbol{x}^{\alpha\beta}$, respectively, as [118]

$$\boldsymbol{x}^{\alpha\beta} = \boldsymbol{T}_{\mathrm{c}}\boldsymbol{x}^{abc} \qquad \text{and} \qquad \boldsymbol{x}^{abc} = \boldsymbol{T}_{\mathrm{c}}^{-1}\boldsymbol{x}^{\alpha\beta}, \tag{2.3}$$

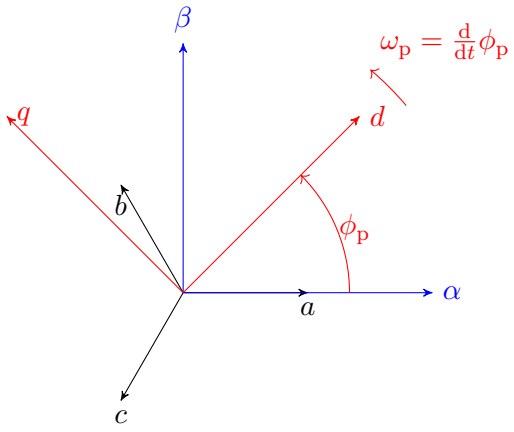

Figure 2.5: Illustration of the space vector theory.

where

$$\boldsymbol{T}_{\mathrm{c}} = \kappa \begin{bmatrix} 1 & -\frac{1}{2} & -\frac{1}{2} \\ 0 & \frac{\sqrt{3}}{2} & -\frac{\sqrt{3}}{2} \end{bmatrix} \qquad \text{and} \qquad \boldsymbol{T}_{\mathrm{c}}^{-1} = \frac{1}{\kappa} \begin{bmatrix} \frac{2}{3} & 0 \\ -\frac{1}{3} & \frac{1}{\sqrt{3}} \\ -\frac{1}{3} & -\frac{1}{\sqrt{3}} \end{bmatrix}$$

denote the Clarke transformation matrix and its inverse, respectively. The scaling factor $\kappa \in \{2/3, \sqrt{2/3}\}$ allows for an amplitude or power invariant Clarke transformation. In order to further transfer to the signal vector $\boldsymbol{x}^{dq} := (x^d, x^q)^\top$ in the synchronously rotating (d,q)-reference frame, which rotates counterclockwise by the given Park transformation angle ϕ_{p} (in rad) with respect to the (α,β)-reference frame, the Park transformation and the inverse Park transformation can be used as [118]

$$\boldsymbol{x}^{\alpha\beta} = \boldsymbol{T}_{\mathrm{p}}(\phi_{\mathrm{p}})\boldsymbol{x}^{dq} \qquad \text{and} \qquad \boldsymbol{x}^{dq} = \boldsymbol{T}_{\mathrm{p}}^{-1}(\phi_{\mathrm{p}})\boldsymbol{x}^{\alpha\beta}, \tag{2.4}$$

where

$$\boldsymbol{T}_{\mathrm{p}}(\phi_{\mathrm{p}}) = \begin{bmatrix} \cos(\phi_{\mathrm{p}}) & -\sin(\phi_{\mathrm{p}}) \\ \sin(\phi_{\mathrm{p}}) & \cos(\phi_{\mathrm{p}}) \end{bmatrix} \qquad \text{and} \qquad \boldsymbol{T}_{\mathrm{p}}^{-1}(\phi_{\mathrm{p}}) = \begin{bmatrix} \cos(\phi_{\mathrm{p}}) & \sin(\phi_{\mathrm{p}}) \\ -\sin(\phi_{\mathrm{p}}) & \cos(\phi_{\mathrm{p}}) \end{bmatrix}$$

are the Park transformation matrix and its inverse, respectively.

Transforming (2.1) through (2.3) and (2.4) by setting ϕ_{p} equivalent to the electrical rotor angle ϕ_{e} (in rad), the machine model in the rotating (d,q)-reference frame is given by [118]

$$\left.\begin{aligned} \boldsymbol{u}_{\mathrm{s}}^{dq} &= R_{\mathrm{s}}\boldsymbol{i}_{\mathrm{s}}^{dq} + \omega_{\mathrm{p}} \underbrace{\begin{bmatrix} 0 & -1 \\ 1 & 0 \end{bmatrix}}_{=\boldsymbol{T}_{\mathrm{p}}(\frac{\pi}{2})=:\boldsymbol{J}} \boldsymbol{\psi}_{\mathrm{s}}^{dq}(\boldsymbol{i}_{\mathrm{s}}^{dq}) + \tfrac{\mathrm{d}}{\mathrm{d}t}\boldsymbol{\psi}_{\mathrm{s}}^{dq}(\boldsymbol{i}_{\mathrm{s}}^{dq}), \\ \tfrac{\mathrm{d}}{\mathrm{d}t}\omega_{\mathrm{m}} &= \tfrac{1}{\Theta_{\mathrm{m}}}\big(m_{\mathrm{m}}(\boldsymbol{i}_{\mathrm{s}}^{dq}) - m_{\mathrm{l}}\big), \\ \tfrac{\mathrm{d}}{\mathrm{d}t}\phi_{\mathrm{m}} &= \omega_{\mathrm{m}}, \end{aligned}\right\} \tag{2.5}$$

where $\boldsymbol{u}_{\mathrm{s}}^{dq} := (u_{\mathrm{s}}^d, u_{\mathrm{s}}^q)^\top$ are the transformed stator voltages (in V), $\boldsymbol{i}_{\mathrm{s}}^{dq} := (i_{\mathrm{s}}^d, i_{\mathrm{s}}^q)^\top$ are the stator currents (in A) and $\boldsymbol{\psi}_{\mathrm{s}}^{dq} := (\psi_{\mathrm{s}}^d, \psi_{\mathrm{s}}^q)^\top$ are the flux linkages (in Vs; which are functions of $\boldsymbol{i}_{\mathrm{s}}^{dq}$ and stator and rotor temperature, angular velocity and rotor angle [neglected in the derivation]). The electrical angular frequency $\omega_{\mathrm{p}} = n_{\mathrm{p}}\omega_{\mathrm{m}}$ (in rad/s) synchronously rotates the (d,q)-reference

frame. Moreover, the machine torque in the (d,q)-reference frame is given by

$$m_{\mathrm{m}}(\boldsymbol{i}_{\mathrm{s}}^{dq}) = \tfrac{2}{3\kappa^2} n_{\mathrm{p}} (\boldsymbol{i}_{\mathrm{s}}^{dq})^{\top} \boldsymbol{J} \boldsymbol{\psi}_{\mathrm{s}}^{dq}(\boldsymbol{i}_{\mathrm{s}}^{dq}). \tag{2.6}$$

To distinguish between different SMs, the flux linkages can be expressed by

$$\boldsymbol{\psi}_{\mathrm{s}}^{dq}(\boldsymbol{i}_{\mathrm{s}}^{dq}) = \bar{\boldsymbol{\psi}}_{\mathrm{s}}^{dq}(\boldsymbol{i}_{\mathrm{s}}^{dq}) + \boldsymbol{\psi}_{\mathrm{pm}}^{dq} \tag{2.7}$$

where $\bar{\boldsymbol{\psi}}_{\mathrm{s}}^{dq} := (\bar{\psi}_{\mathrm{s}}^{d}, \bar{\psi}_{\mathrm{s}}^{q})^{\top}$ are stator flux linkage components due to the stator current excitation (i.e., functions of $\boldsymbol{i}_{\mathrm{s}}^{dq}$) and $\boldsymbol{\psi}_{\mathrm{pm}}^{dq} := (\psi_{\mathrm{pm}}^{d}, \psi_{\mathrm{pm}}^{q})^{\top}$ are PM flux linkage components (influenced by currents and temperature [neglected in the following derivation]). For different SMs, $\boldsymbol{\psi}_{\mathrm{pm}}^{dq}$ can be modeled generically with any PM flux linkage constant $\psi_{\mathrm{pm}} > 0$ as follows [118]

- $\boldsymbol{\psi}_{\mathrm{pm}}^{dq} = (\psi_{\mathrm{pm}}, 0)^{\top}$ for SPMSMs and IPMSMs;
- $\boldsymbol{\psi}_{\mathrm{pm}}^{dq} = (0, -\psi_{\mathrm{pm}})^{\top}$ for PMaRSMs; and
- $\boldsymbol{\psi}_{\mathrm{pm}}^{dq} = \boldsymbol{0}_2 := (0,0)^{\top}$ for RSMs.

2.2.1.3 Current dynamics

To further derive the nonlinear current dynamics of SMs, the last term of the voltage equation in (2.5) is rewritten as [118]

$$\tfrac{\mathrm{d}}{\mathrm{d}t} \boldsymbol{\psi}_{\mathrm{s}}^{dq}(\boldsymbol{i}_{\mathrm{s}}^{dq}) = \tfrac{\partial \boldsymbol{\psi}_{\mathrm{s}}^{dq}(\boldsymbol{i}_{\mathrm{s}}^{dq})}{\partial \boldsymbol{i}_{\mathrm{s}}^{dq}} \tfrac{\mathrm{d}}{\mathrm{d}t} \boldsymbol{i}_{\mathrm{s}}^{dq} = \boldsymbol{L}_{\mathrm{s}}^{dq}(\boldsymbol{i}_{\mathrm{s}}^{dq}) \tfrac{\mathrm{d}}{\mathrm{d}t} \boldsymbol{i}_{\mathrm{s}}^{dq}, \tag{2.8}$$

where the differential inductance matrix $\boldsymbol{L}_{\mathrm{s}}^{dq}$ (in H) is defined as the (partial) derivative of the flux linkages with respect to the stator currents, i.e.,

$$\boldsymbol{L}_{\mathrm{s}}^{dq}(\boldsymbol{i}_{\mathrm{s}}^{dq}) := \begin{bmatrix} \frac{\partial \psi_{\mathrm{s}}^{d}(\boldsymbol{i}_{\mathrm{s}}^{dq})}{\partial i_{\mathrm{s}}^{d}} & \frac{\partial \psi_{\mathrm{s}}^{d}(\boldsymbol{i}_{\mathrm{s}}^{dq})}{\partial i_{\mathrm{s}}^{q}} \\ \frac{\partial \psi_{\mathrm{s}}^{q}(\boldsymbol{i}_{\mathrm{s}}^{dq})}{\partial i_{\mathrm{s}}^{d}} & \frac{\partial \psi_{\mathrm{s}}^{q}(\boldsymbol{i}_{\mathrm{s}}^{dq})}{\partial i_{\mathrm{s}}^{q}} \end{bmatrix} := \begin{bmatrix} L_{\mathrm{s}}^{d}(\boldsymbol{i}_{\mathrm{s}}^{dq}) & L_{\mathrm{s}}^{dq}(\boldsymbol{i}_{\mathrm{s}}^{dq}) \\ L_{\mathrm{s}}^{qd}(\boldsymbol{i}_{\mathrm{s}}^{dq}) & L_{\mathrm{s}}^{q}(\boldsymbol{i}_{\mathrm{s}}^{dq}) \end{bmatrix}, \tag{2.9}$$

where L_{s}^{d} & L_{s}^{q} and L_{s}^{dq} & L_{s}^{qd} are the self-axis and cross-coupling differential inductances, respectively. By obeying the energy conservation rule, the reciprocity relation holds: The (differential) cross-coupling inductances must equal for all $\boldsymbol{i}_{\mathrm{s}}^{dq}$, i.e., $L_{\mathrm{s}}^{dq}(\boldsymbol{i}_{\mathrm{s}}^{dq}) = L_{\mathrm{s}}^{qd}(\boldsymbol{i}_{\mathrm{s}}^{dq})$ [118]. Finally, substituting (2.8) into (2.5) and solving for the current derivative yields the current dynamics as follows [118]

$$\tfrac{\mathrm{d}}{\mathrm{d}t} \boldsymbol{i}_{\mathrm{s}}^{dq} = \boldsymbol{L}_{\mathrm{s}}^{dq}(\boldsymbol{i}_{\mathrm{s}}^{dq})^{-1} \cdot \Big[\boldsymbol{u}_{\mathrm{s}}^{dq} - R_{\mathrm{s}} \boldsymbol{i}_{\mathrm{s}}^{dq} - \omega_{\mathrm{p}} \boldsymbol{J} \boldsymbol{\psi}_{\mathrm{s}}^{dq}(\boldsymbol{i}_{\mathrm{s}}^{dq}) \Big], \tag{2.10}$$

where the inverse of the differential inductance matrix is given by

$$\begin{aligned} \boldsymbol{L}_{\mathrm{s}}^{dq}(\boldsymbol{i}_{\mathrm{s}}^{dq})^{-1} &= \frac{1}{\det(\boldsymbol{L}_{\mathrm{s}}^{dq}(\boldsymbol{i}_{\mathrm{s}}^{dq}))} \begin{bmatrix} L_{\mathrm{s}}^{q}(\boldsymbol{i}_{\mathrm{s}}^{dq}) & -L_{\mathrm{s}}^{dq}(\boldsymbol{i}_{\mathrm{s}}^{dq}) \\ -L_{\mathrm{s}}^{qd}(\boldsymbol{i}_{\mathrm{s}}^{dq}) & L_{\mathrm{s}}^{d}(\boldsymbol{i}_{\mathrm{s}}^{dq}) \end{bmatrix} \\ &= \frac{1}{L_{\mathrm{s}}^{d}(\boldsymbol{i}_{\mathrm{s}}^{dq}) L_{\mathrm{s}}^{q}(\boldsymbol{i}_{\mathrm{s}}^{dq}) - L_{\mathrm{s}}^{dq}(\boldsymbol{i}_{\mathrm{s}}^{dq}) L_{\mathrm{s}}^{qd}(\boldsymbol{i}_{\mathrm{s}}^{dq})} \begin{bmatrix} L_{\mathrm{s}}^{q}(\boldsymbol{i}_{\mathrm{s}}^{dq}) & -L_{\mathrm{s}}^{dq}(\boldsymbol{i}_{\mathrm{s}}^{dq}) \\ -L_{\mathrm{s}}^{qd}(\boldsymbol{i}_{\mathrm{s}}^{dq}) & L_{\mathrm{s}}^{d}(\boldsymbol{i}_{\mathrm{s}}^{dq}) \end{bmatrix}. \end{aligned} \tag{2.11}$$

2.2.2 Nonlinear RSM model

Extending the generic model for SMs, two modeling examples focusing on RSMs are discussed in the following to consider the modeled machine as a linear or (real) nonlinear system.

2.2.2.1 Linear machine

In the first example, the RSM flux linkages

$$\boldsymbol{\psi}_\mathrm{s}^{dq}(\boldsymbol{i}_\mathrm{s}^{dq}) \overset{(2.7)}{=} \bar{\boldsymbol{\psi}}_\mathrm{s}^{dq}(\boldsymbol{i}_\mathrm{s}^{dq}) = \underbrace{\begin{bmatrix} l_\mathrm{s}^{d} & l_\mathrm{s}^{dq} \\ l_\mathrm{s}^{qd} & l_\mathrm{s}^{q} \end{bmatrix}}_{=:\boldsymbol{l}_\mathrm{s}^{dq}} \boldsymbol{i}_\mathrm{s}^{dq} \tag{2.12}$$

are described as an affine function of the stator currents, which consist of only the stator flux linkage components $\bar{\boldsymbol{\psi}}_\mathrm{s}^{dq}(\boldsymbol{i}_\mathrm{s}^{dq})$ in (2.7) without PM flux linkage components $\boldsymbol{\psi}_\mathrm{pm}^{dq} = \mathbf{0}_2$. The inductance matrix $\boldsymbol{l}_\mathrm{s}^{dq}$ depends on the *constant* stator inductances $l_\mathrm{s}^{d} > 0$, $l_\mathrm{s}^{q} > 0$ and the *constant* cross-coupling inductances $l_\mathrm{s}^{dq} = l_\mathrm{s}^{qd} > 0$. Hence, the flux linkages in (2.12) vary with *linear* magnetic behavior, similar to a wound core with an ideal magnetic circuit. Furthermore, the machine torque [118]

$$\begin{aligned} m_\mathrm{m}(\boldsymbol{i}_\mathrm{s}^{dq}) &\overset{(2.6)}{=} \tfrac{2}{3\kappa^2} n_\mathrm{p} (\boldsymbol{i}_\mathrm{s}^{dq})^\top \boldsymbol{J} \boldsymbol{l}_\mathrm{s}^{dq} \boldsymbol{i}_\mathrm{s}^{dq} \\ &= \underbrace{\tfrac{2}{3\kappa^2} n_\mathrm{p} (l_\mathrm{s}^{d} - l_\mathrm{s}^{q}) i_\mathrm{s}^{d} i_\mathrm{s}^{q}}_{=:m_\mathrm{re}} + \underbrace{\tfrac{2}{3\kappa^2} n_\mathrm{p} \left(l_\mathrm{s}^{dq} (i_\mathrm{s}^{q})^2 - l_\mathrm{s}^{qd} (i_\mathrm{s}^{d})^2 \right)}_{=:m_\mathrm{cross}} \end{aligned} \tag{2.13}$$

is composed of the reluctance torque m_re and the magnetic cross-coupling torque m_cross. For RSM design, the inductance difference $l_\mathrm{s}^{d} - l_\mathrm{s}^{q}$ (or division $l_\mathrm{s}^{d}/l_\mathrm{s}^{q}$, which usually refers to the saliency ratio) must be maximized to achieve high reluctance torque output.

This example is suitable for isotropic machines, e.g., SPMSMs. Due to the linear magnetic characteristics, the stator inductances $\boldsymbol{l}_\mathrm{s}^{dq}$ stay unchanged as constants during operation, and the cross-coupling saturation can normally be neglected, i.e., $l_\mathrm{s}^{dq} = l_\mathrm{s}^{qd} = 0$. Therefore, (2.12) is sufficient to present their flux linkages with a linear saturation trend. However, this example is not applicable to anisotropic machines (with magnetic saliency in their rotors), e.g., IPMSMs, PMaRSMs and RSMs. These machine types exhibit significant magnetic saturation, especially for RSMs. Hence, their stator inductances vary widely over the whole operation range and thus cannot be considered constants.

It could be argued that the modification to (2.12) with $\boldsymbol{\psi}_\mathrm{s}^{dq}(\boldsymbol{i}_\mathrm{s}^{dq}) = \boldsymbol{l}_\mathrm{s}^{dq}(\boldsymbol{i}_\mathrm{s}^{dq}) \boldsymbol{i}_\mathrm{s}^{dq}$, which is a product of the current-dependent inductance matrix $\boldsymbol{l}_\mathrm{s}^{dq}(\boldsymbol{i}_\mathrm{s}^{dq})$ and the stator current vector $\boldsymbol{i}_\mathrm{s}^{dq}$, can represent the magnetic nonlinearity of RSMs. This modeling is commonly adopted in several publications for either model simplification or user preference. Nevertheless, the problem is already stated in [47]. This modeling suffers from some disadvantages: (i) nonzero flux linkages with zero currents cannot be reproduced due to the multiplication operation, as $\boldsymbol{\psi}_\mathrm{s}^{dq}(\mathbf{0}_2) = \mathbf{0}_2$ for $\boldsymbol{i}_\mathrm{s}^{dq} = \mathbf{0}_2$; (ii) control performance may be deteriorated, e.g., a reduced controller bandwidth or even instability; and (iii) the time derivative of $\frac{\mathrm{d}}{\mathrm{d}t}\boldsymbol{\psi}_\mathrm{s}^{dq}(\boldsymbol{i}_\mathrm{s}^{dq}) = \boldsymbol{l}_\mathrm{s}^{dq} \frac{\mathrm{d}}{\mathrm{d}t}[\boldsymbol{i}_\mathrm{s}^{dq}] + \frac{\mathrm{d}}{\mathrm{d}t}[\boldsymbol{l}_\mathrm{s}^{dq}(\boldsymbol{i}_\mathrm{s}^{dq})] \boldsymbol{i}_\mathrm{s}^{dq}$ results in apparent and time-varying inductances, which both are not physically motivated. Therefore, this model is physically and mathematically problematic.

2.2.2.2 Real machine

The second example presents the *nonlinear* d-axis flux linkage $\psi_\mathrm{s}^d(\boldsymbol{i}_\mathrm{s}^{dq})$ and q-axis flux linkage $\psi_\mathrm{s}^q(\boldsymbol{i}_\mathrm{s}^{dq})$ of a real RSM as functions of the stator current vector $\boldsymbol{i}_\mathrm{s}^{dq}$. The highly nonlinear flux linkages depend on not only the d-axis current i_s^d but also the q-axis current i_s^q, leading to magnetic cross-coupling. Thus, modeling as a real machine favors covering both the magnetic saturation and cross-coupling effects. The machine torque [118]

$$m_\mathrm{m}(\boldsymbol{i}_\mathrm{s}^{dq}) = \tfrac{2}{3\kappa^2} n_\mathrm{p} (\boldsymbol{i}_\mathrm{s}^{dq})^\top \boldsymbol{J} \boldsymbol{\psi}_\mathrm{s}^{dq}(\boldsymbol{i}_\mathrm{s}^{dq}) = \tfrac{2}{3\kappa^2} n_\mathrm{p} \left(\psi_\mathrm{s}^d(i_\mathrm{s}^d, i_\mathrm{s}^q)\, i_\mathrm{s}^q - \psi_\mathrm{s}^q(i_\mathrm{s}^d, i_\mathrm{s}^q)\, i_\mathrm{s}^d \right) \tag{2.14}$$

stays as a nonlinear function depending on the stator currents $\boldsymbol{i}_\mathrm{s}^{dq}$ and the nonlinear current-dependent flux linkages $\boldsymbol{\psi}_\mathrm{s}^{dq}(\boldsymbol{i}_\mathrm{s}^{dq})$, corresponding to the generally valid torque equation in (2.6).

To model the electrical subsystem with the inclusion of the magnetic saturation, it can be categorized into two groups according to the used saturation functions [70]:

1. **Current function:** The nonlinear magnetic characteristics can be described by a current function $\boldsymbol{i}_\mathrm{s}^{dq}(\boldsymbol{\psi}_\mathrm{s}^{dq})$ using the flux linkages $\boldsymbol{\psi}_\mathrm{s}^{dq}$ as state variables. Recalling the voltage equation in (2.5), the flux linkage derivative

   $$\tfrac{\mathrm{d}}{\mathrm{d}t} \boldsymbol{\psi}_\mathrm{s}^{dq}(\boldsymbol{i}_\mathrm{s}^{dq}) = \boldsymbol{u}_\mathrm{s}^{dq} - R_\mathrm{s} \boldsymbol{i}_\mathrm{s}^{dq} - \omega_\mathrm{p} \boldsymbol{J} \boldsymbol{\psi}_\mathrm{s}^{dq}(\boldsymbol{i}_\mathrm{s}^{dq}) \tag{2.15}$$

   can be formulated, and its block diagram is illustrated in Fig. 2.6(a). Then, the electrical subsystem can be modeled accordingly by employing the nonlinear current function. Because of its straightforward structure without requiring the knowledge of the differential inductances, this model may be simpler to be built in simulation. However, available machine data expressing the magnetic nonlinearity is normally provided with the current-to-flux relation. Consequently, the inverse function to derive the desired flux-to-current relation must be additionally implemented, i.e., $\boldsymbol{i}_\mathrm{s}^{dq} = f^{-1}(\boldsymbol{\psi}_\mathrm{s}^{dq})$.

2. **Flux linkage function:** The electrical model can also be established with a nonlinear flux linkage function $\boldsymbol{\psi}_\mathrm{s}^{dq}(\boldsymbol{i}_\mathrm{s}^{dq})$ using the stator currents $\boldsymbol{i}_\mathrm{s}^{dq}$ as state variables. According to the already defined current derivative (2.10), the corresponding block diagram using the flux linkage function can be diagrammed as in Fig. 2.6(b). It can be seen that this model requires not only the flux linkages but also the differential inductances $\boldsymbol{L}_\mathrm{s}^{dq}(\boldsymbol{i}_\mathrm{s}^{dq})$ [defined in (2.9)]. The inverse differential inductances $\boldsymbol{L}_\mathrm{s}^{dq}(\boldsymbol{i}_\mathrm{s}^{dq})^{-1}$ can be derived by following (2.11). On the other hand, the inverse function required in the former model can be eliminated.

It is worth noticing that both modelings with different saturation functions can take the magnetic saturation into account properly. Therefore, they can be chosen according to user preferences and available machine information.

2.2.3 Critical issues

Following the introduced machine structure and model of RSMs, some critical issues in the development of a high-performance RSM drive system are summarized as follows:

1. **Machine design:** RSMs should be properly designed to preserve high magnetic saliency in the rotor. According to the toque equation in (2.13), without considering the saturation effects, the inductance difference $l_\mathrm{s}^d - l_\mathrm{s}^q$ or the saliency ratio $l_\mathrm{s}^d / l_\mathrm{s}^q$ should be maximized to

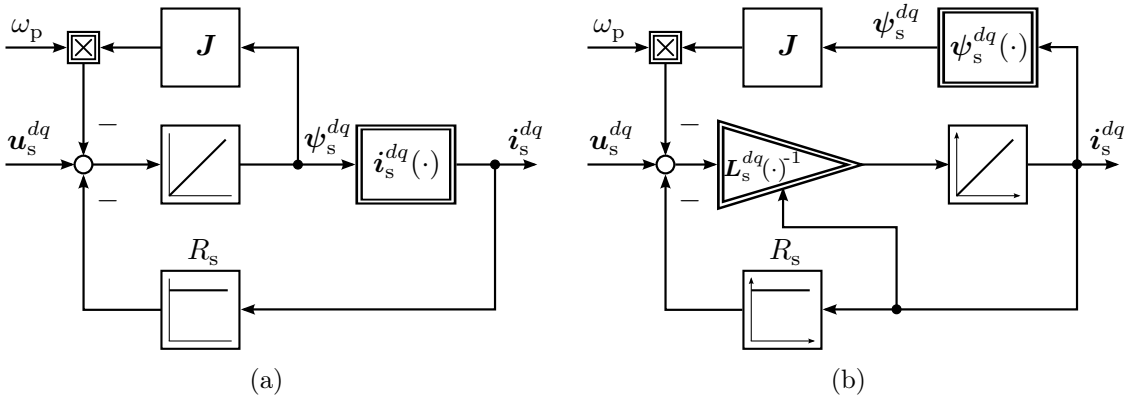

Figure 2.6: Electrical block diagrams of RSMs using different saturation functions: (a) modeling with current function; (b) modeling with flux linkage function (based on [70, 118]).

reach a maximum achievable value throughout the entire operation range [38, 113]. Hence, the developed reluctance torque can be enlarged. Both $l_\mathrm{s}^d - l_\mathrm{s}^q$ and $l_\mathrm{s}^d/l_\mathrm{s}^q$ values decrease remarkably due to the increase of the current and the frequency.

2. **System identification:** Unlike other SMs exhibiting almost linear magnetic behavior without saturation, RSMs suffer from severe parameter variation due to the magnetic saturation and cross-coupling effects. The machine parameters (e.g., stator resistance R_s, differential inductances $\boldsymbol{L}_\mathrm{s}^{dq}$ and flux linkages $\boldsymbol{\psi}_\mathrm{s}^{dq}$) vary extensively during operation, and they are influenced by not only stator currents but also temperature, angular velocity and rotor position [118]. To compensate for these nonlinearities in control algorithms and analyze the machine characteristics, the machine's parameters must be known through finite element analysis (FEA) or experimental measurements. The experimental identification methods will be further discussed in Section 2.3 with measurement results. Usually, lookup tables (LUTs) are utilized to save the identified machine parameters. At the same time, analytical prototype functions can be a good alternative with only a few function parameters, which will be introduced in Chapter 3.

3. **Controller design:** Machine model (over-)simplifications are still a common practice to ease the controller design, e.g., using constant machine parameters and/or neglecting the saturation and cross-coupling effects [84, 99]. These simplifications deteriorate the control performance significantly for nonlinear machines, e.g., RSMs. Therefore, modeling correctness is crucial for designing the current and speed controllers with good dynamic capabilities. According to the nonlinear current dynamics in (2.10), adaptive current controllers must be equipped to update the controller parameters with varying differential inductances. In Chapter 4, a nonlinear current control approach for RSMs is developed (based on [47]). With almost identical current dynamics over the complete operation range, the outer (speed and/or position) control loops can be simply designed.

4. **Current reference generation:** According to the nonlinear machine torque equation in (2.14), infinite current combinations can generate a required torque value. Hence, optimal feedforward torque control (OFTC) must be applied to obtain the most optimal d-axis current reference $i_\mathrm{s,ref}^d$ and the most optimal q-axis current reference $i_\mathrm{s,ref}^q$. A unified theory for OFTC (based on [50, 51]) covering different operation strategies can be found in Chapter 5. To achieve the best operation efficiency, maximum torque per current (MTPC) provides the optimal stator current references by minimizing copper losses (and sometimes

also iron losses) up to a certain speed. For classical MTPC (where the magnetic saturation effects are not considered), the current angle $\beta = 45°$ [1] can be set as constant in every load condition for RSMs, i.e., $i_s^d = i_s^q$. However, in reality, the optimal current angle β is greater than 45° due to the saturation effects and the iron losses, i.e., $i_s^d < i_s^q$, and it changes for different load conditions. Therefore, the MTPC trajectory should be obtained beforehand through offline tests and then compensated during operation. Alternatively, it can also be calculated online by solving the optimization problem analytically.

5. **Wide operation range:** When the machine operates higher than its rated speed, the physical constraints of drive systems may be met easily, i.e., the maximum available voltage of the inverter and the maximum stator current of the machine. In this situation, the demanded torque reference might not be feasible anymore, so the maximum producible torque should be given instead. As a consequence, extending from MTPC, other operation strategies, such as field weakening (FW) or maximum torque per voltage (MTPV), must be implemented to enable high-speed operation [50, 102, 103]. Normally, they generate the current references with a further reduced amount of i_s^d to decrease the induced voltage magnitude. Moreover, a smooth transition between different operation strategies must be ensured by a decision function or tree.

2.3 System identification

Due to the severe magnetic saturation, good machine knowledge is required for high-performance RSM drive systems. In the machine design stage, a comprehensive analysis of machine nonlinearities is conducted by means of FEA simulation. For this purpose, precise information, such as machine geometry, winding diagram and material properties, is required, which is usually available only to machine designers. Unfortunately, for commercial machines, it is common that solely key specifications on nameplates are provided. Consequently, experimental identification must be carried out on a laboratory setup to extract nonlinear machine parameters, including flux linkages and/or differential inductances.

To measure the nonlinear machine maps, traditional methods require specialized setups with power supply and data acquisition equipment, which might not be available in every laboratory. The difficulty of considering the cross-coupling limits the applicability for highly nonlinear machines, such as RSMs. In contrast, approaches using inverters are preferable, as they can cover the entire nonlinearity by a scheduled identification procedure in real-time control systems. Besides, inverters are already commonly equipped in modern electrical drive systems due to the increasing demand for variable-speed drives. According to the rotor conditions during test, these inverter-fed approaches can be mainly categorized into three groups [22, 64]: constant speed methods [62, 63], free-wheeling shaft methods [65, 72, 119] and locked-rotor methods [120, 121].

This section introduces the operation principles of two different inverter-fed identification methods, including the constant speed and free-wheeling shaft methods. Subsequently, they are

[1] The d and q current components can also be presented in the polar coordinate system, i.e., $i_s^d = I_s^{dq}\cos(\beta)$ and $i_s^q = I_s^{dq}\sin(\beta)$, where $I_s^{dq} = \|\boldsymbol{i}_s^{dq}\|$ is the stator current magnitude and $\beta = \arctan(i_s^q/i_s^d)$ is the current angle. Some publications (see, e.g., [7, 27, 81]) prefer using this presentation form for the OFTC problem, so the optimal operation point can be tuned by changing I_s^{dq} and β. Inserting these expressions into the reluctance torque in (2.13), i.e.,

$$m_{\mathrm{re}} = \tfrac{1}{3\kappa^2} n_{\mathrm{p}} (l_s^d - l_s^q)(I_s^{dq})^2 \sin(2\beta),$$

it can be seen that $\beta = 45°$ can output the maximum reluctance torque component. However, this only holds true when a linear machine is considered with constant l_s^d and l_s^q values.

implemented exemplarily to measure the flux linkages of a nonlinear 4.0 kW RSM. Then, its differential inductances can be derived by following the definition in (2.9). As the main focus here is on the magnetic characteristics, the measurement for the stator resistance is not discussed, which can be measured by a multimeter or dc/ac excitation [120].

2.3.1 Constant speed method

2.3.1.1 Operation principle

During the constant speed method, the machine under test is coupled to a prime mover to rotate with a constant speed ($\omega_\mathrm{p} \neq 0$). The speed-dependent back EMF term $\omega_\mathrm{p}\boldsymbol{J}\boldsymbol{\psi}_\mathrm{s}^{dq}$ from the voltage equation in (2.5) is the main source to derive the flux linkages. By means of the vector control with given current references $\boldsymbol{i}_\mathrm{s}^{dq} := (i_\mathrm{s,ref}^d, i_\mathrm{s,ref}^q)^\top$, the stator currents $\boldsymbol{i}_\mathrm{s}^{dq} = (i_\mathrm{s}^d, i_\mathrm{s}^q)^\top$ can be regulated steadily as constant values in the desired identification range [47]

$$\mathbb{I}(I_\mathrm{max}) := \{\, \boldsymbol{i}_\mathrm{s}^{dq} \in \mathbb{R}^2 \mid \|\boldsymbol{i}_\mathrm{s}^{dq}\| \leq I_\mathrm{max} \,\}$$

with the testing current limit I_max. Under this circumstance, the steady-state voltage equation can be obtained by neglecting the flux linkage derivative $\frac{\mathrm{d}}{\mathrm{d}t}\boldsymbol{\psi}_\mathrm{s}^{dq}$ in (2.5). Then, the flux linkages can be derived as

$$\boldsymbol{\psi}_\mathrm{s}^{dq}(\boldsymbol{i}_\mathrm{s}^{dq}) = \tfrac{1}{\omega_\mathrm{p}}\boldsymbol{J}^{-1}(\boldsymbol{u}_\mathrm{s}^{dq} - R_\mathrm{s}\boldsymbol{i}_\mathrm{s}^{dq}) \tag{2.16}$$

for the known stator resistance R_s, the measured currents $\boldsymbol{i}_\mathrm{s}^{dq}$, the measured angular velocity $\omega_\mathrm{p} = n_\mathrm{p}\omega_\mathrm{m}$ and the approximated applied voltages $\boldsymbol{u}_\mathrm{s}^{dq} \approx \boldsymbol{u}_\mathrm{s,ref}^{dq}$, where $\boldsymbol{u}_\mathrm{s,ref}^{dq} := (u_\mathrm{s,ref}^d, u_\mathrm{s,ref}^q)^\top$ are the voltage references (output from the current controllers).

2.3.1.2 Key considerations

The identified data from the constant speed method often serves as a reference to be compared with other proposed identification approaches. Under a constant rotational speed, a thorough measurement containing numerous samples can be conducted to cover both the magnetic saturation and cross-coupling effects. Consequently, the nonlinear flux linkages $\psi_\mathrm{s}^d(i_\mathrm{s}^d, i_\mathrm{s}^q)$ and $\psi_\mathrm{s}^q(i_\mathrm{s}^d, i_\mathrm{s}^q)$ can be extracted with different sets of the stator currents i_s^d and i_s^q within the given identification range $\mathbb{I}(I_\mathrm{max})$. The testing current limit I_max should be chosen with a sufficiently high value, e.g., $I_\mathrm{max} = \alpha\widehat{i}_\mathrm{s,R}$ with $\alpha \geq 1.5$ (where $\widehat{i}_\mathrm{s,R}$ is the rated current amplitude), so the machine behavior can be adequately described with the effectively obtained flux linkages [47]. In addition, the measurement can be performed under several rotational speeds or even temperatures; hence, a high degree of freedom can be achieved with this method.

Several critical issues must be considered while implementing the constant speed method:

- Controller: Parameters for current controllers must be acquired beforehand through no load tests or trial-and-error tuning, such that the stator currents can be well regulated throughout the entire measurement range.
- Data sampling: For every commanded current pair, sufficient samples [for calculation in (2.16)] must be continuously recorded for at least one rotor rotation [63]. Then, they are averaged to alleviate the effect of slot harmonics. As many current pairs must be measured to cover the whole measurement range, this results in a long-lasting identification procedure.

- Temperature: Due to the long testing period, the machine temperature will increase significantly if it is not carefully monitored and regulated to a constant level. Consequently, the identified accuracy may deteriorate. During measurements, the stator and rotor temperature should be monitored with the help of temperature sensors [122]. Alternatively, the current references can be switched to operate the tested machine between motor and generator operation modes, e.g., $(i^d_{\mathrm{s,ref}}, i^q_{\mathrm{s,ref}})$ for motor mode (to heat up) and $(i^d_{\mathrm{s,ref}}, -i^q_{\mathrm{s,ref}})$ for generator mode (to cool down) [63]. This can effectively avoid the problem of machine overheating during tests.

- Speed: Higher speed yields a good signal-to-noise ratio (SNR) with higher voltages; meanwhile, additional iron losses are induced. Therefore, a compromise between these two issues should be made. Normally, one-third of the rated mechanical speed $\omega_{\mathrm{m,R}}$ can be chosen, i.e., $\omega_{\mathrm{m}} = \frac{\omega_{\mathrm{m,R}}}{3}$ [63].

2.3.2 Self-identification method

Even though the previously introduced constant speed method is commonly adopted to identify the nonlinear flux linkages of not only RSMs but all other SMs, the time-consuming procedure and the mechanical requirements might only be valid for some applications and users. Conversely, for free-wheeling shafts, the "self-identification" [65, 71, 72, 119, 123, 124] applies a sequence of test voltages or currents to acquire nonlinear machine parameters within a short time period, while usually no further hardware modifications are needed. This is ideally suited to be included for self-commissioning, which is a desired functionality in modern electrical drive systems to start up the controlled machine successfully without knowing any system information beforehand.

The self-identification can be performed either with varying speeds or at standstill. Dynamically [119, 123], constant current references are set between motor and generator operation modes, such that the nonlinear machine maps can be extracted by calculating (2.16) during machine acceleration and deceleration. This method possesses a similar principle as the constant speed method but with dynamic rotor movement (changing speed). However, some current pairs with higher values may cause a rapid acceleration without being able to collect sufficient samples. Therefore, the admissible measurement range might be narrow, and a flywheel should be mounted to the rotor shaft to increase the moment of inertia. On the other hand, at standstill [71, 72, 124], injecting voltage and/or current test pulses into the machine under test is also feasible. This identification procedure is speedy and requires (nearly) no additional mechanical or set-up requirements and is, therefore, the preferred approach to be introduced in the following.

The introduced self-identification method is based on [4], where an effective incorporation of the flux linkage prototype functions has been demonstrated.

2.3.2.1 Operation principle

When the machine is at standstill ($\omega_{\mathrm{p}} = 0$), the back EMF term $\omega_{\mathrm{p}} \boldsymbol{J} \boldsymbol{\psi}^{dq}_{\mathrm{s}}$ in the voltage equation from (2.5) is usually neglected. Then, the flux linkage derivative $\frac{\mathrm{d}}{\mathrm{d}t}\boldsymbol{\psi}^{dq}_{\mathrm{s}}$ [the last term in (2.5)] serves as a critical component in the self-identification. Integration of the voltage signal, subtracting the resistance voltage drop from the stator voltages, can lead to the flux linkages as follows [4]

$$\boldsymbol{\psi}^{dq}_{\mathrm{s}}(\boldsymbol{i}^{dq}_{\mathrm{s}}) = \int \boldsymbol{u}^{dq}_{\mathrm{s}} - R_{\mathrm{s}} \boldsymbol{i}^{dq}_{\mathrm{s}} \, \mathrm{d}t \,. \tag{2.17}$$

For the discrete-time implementation, (2.17) can be discretized by means of the explicit Euler method, i.e.,

$$\boldsymbol{\psi}_\mathrm{s}^{dq}[n] = \boldsymbol{\psi}_\mathrm{s}^{dq}[n-1] + T_\mathrm{sam}\left(\boldsymbol{u}_\mathrm{s}^{dq}[n] - R_\mathrm{s}\boldsymbol{i}_\mathrm{s}^{dq}[n]\right)$$

with the sampling time T_sam, the known stator resistance R_s, the measured currents $\boldsymbol{i}_\mathrm{s}^{dq}$ and the voltages $\boldsymbol{u}_\mathrm{s}^{dq}$ that can be approximated by their references, i.e., $\boldsymbol{u}_\mathrm{s}^{dq}[n] \approx \boldsymbol{u}_\mathrm{s,ref}^{dq}[n-1]$. Based on this concept, the following tests must be implemented to obtain the entire flux linkage maps, including the self-axis and cross-coupling saturation effects.

2.3.2.2 Self-axis test

To extract the self-axis saturated flux linkages, voltage test sequences are applied *separately* to the d and q components. The voltage references $\boldsymbol{u}_\mathrm{s,ref}^{dq} = (u_\mathrm{s,ref}^{d}, u_\mathrm{s,ref}^{q})^\top$ can be generated by a step-like control function [4]

$$u_\mathrm{s,ref}^{d/q}[n] = \begin{cases} U_\mathrm{test}^{d/q}, & i_\mathrm{s}^{d/q}[n] \leq -I_\mathrm{max}^{d/q} \\ -U_\mathrm{test}^{d/q}, & i_\mathrm{s}^{d/q}[n] \geq I_\mathrm{max}^{d/q} \\ u_\mathrm{s,ref}^{d/q}[n-1], & \text{otherwise} \end{cases} \tag{2.18}$$

where $\boldsymbol{U}_\mathrm{test}^{dq} := (U_\mathrm{test}^{d}, U_\mathrm{test}^{q})^\top$ and $\boldsymbol{I}_\mathrm{max}^{dq} := (I_\mathrm{max}^{d}, I_\mathrm{max}^{q})^\top$ are the testing voltage amplitudes and current limits, respectively. To avoid invoking the cross-axis current, the cross-axis voltage component must be set to zero, i.e., $\boldsymbol{u}_\mathrm{s,ref}^{dq} = (\pm U_\mathrm{test}^{d}, 0)^\top$ for the d-axis test and $\boldsymbol{u}_\mathrm{s,ref}^{dq} = (0, \pm U_\mathrm{test}^{q})^\top$ for the q-axis test. Similar to a hysteresis controller, the stator current increases and decreases with the positive and negative testing voltages, respectively. When the current exceeds the corresponding limit, the polarity of the testing voltage changes. Consequently, a high-frequency square-wave voltage signal is injected into the machine under identification. The desired current-to-flux relationship can be derived from the induced stator current and the flux linkage per (2.17).

2.3.2.3 Cross-coupling test

To extract the cross-coupling saturation effects on the flux linkages, voltage test sequences are applied *simultaneously* to the d and q components. Reusing (2.18) and selecting the proper voltage amplitudes for both components, the resulting voltage references $\boldsymbol{u}_\mathrm{s,ref}^{dq} = (\pm U_\mathrm{test}^{d}, \pm U_\mathrm{test}^{q})^\top$ lead to the d-axis current i_s^{d} and the q-axis current i_s^{q} over the whole operation range. Even though the generated torque is nonzero, as i_s^{d} and i_s^{q} are nonzero during this test, the average torque is approximately zero, which prevents a dramatic acceleration of the tested machine. In addition, the pulsating torque can be filtered out to a certain extent, depending on the mechanical loading condition (the connection to the rotor shaft). However, inevitably slight rotor movement induces the back EMF, i.e., $\omega_\mathrm{p}\boldsymbol{J}\boldsymbol{\psi}_\mathrm{s}^{dq} \neq 0$. The neglection of it causes wrong voltage values in (2.17), which leads to a drift of the estimated flux linkages. Therefore, during the cross-coupling test, to derive accurate flux linkage values, the back EMF *must* be taken into account as follows [4]

$$\boldsymbol{\psi}_\mathrm{s}^{dq}(\boldsymbol{i}_\mathrm{s}^{dq}) = \int \boldsymbol{u}_\mathrm{s}^{dq} - R_\mathrm{s}\boldsymbol{i}_\mathrm{s}^{dq} - \omega_\mathrm{p}\boldsymbol{J}\boldsymbol{\psi}_\mathrm{s}^{dq}(\boldsymbol{i}_\mathrm{s}^{dq})\,\mathrm{d}t\,. \tag{2.19}$$

2.3.2.4 Key considerations

Although the constant speed method is commonly utilized to identify the flux linkages of SMs, the machine under test must be mechanically coupled to a speed-controlled load machine. Besides, the issues of machine temperature may arise due to its prolonged identification procedure. In contrast to that, these difficulties can be overcome by the introduced self-identification method at standstill, since it requires (nearly) no mechanical requirements and can be performed within a very short testing period. Furthermore, no current controllers are needed; therefore, this approach is well-suited for applications without being aware of any machine parameters.

Along with the advantages as mentioned above, some key considerations must be taken into account while applying the self-identification method:

- Testing variables: The testing voltage amplitudes $\boldsymbol{U}_{\mathrm{test}}^{dq}$ should be chosen as high as possible (close to the inverter voltage limit), such that the inaccuracies caused by incorrect stator resistance, inverter nonlinearities and measurement errors can be mitigated [72]. Due to different differential inductances for other machines, not only $\boldsymbol{U}_{\mathrm{test}}^{dq}$ but also the current limits $\boldsymbol{I}_{\mathrm{max}}^{dq}$ must be set adaptively online to increase the measurement range.
- Acquisition window: Sufficient measurement samples should be acquired during tests. However, a huge drift due to the integration in (2.17) and (2.19) must be avoided [72]. Therefore, selecting an adequate length of the acquisition window is of uttermost importance. Otherwise, an effective method to counteract the integration problem must also be considered, e.g., by cascaded low-pass filters [124].
- Rotor movement: For the q-axis and cross-coupling tests, the rotor may rotate easily due to rotor misalignment and nonzero torques, which result in inaccurate flux linkages and limited measurement range. Therefore, the rotor position required for the Park transformation should be updated by, e.g., an encoder in standard applications or encoderless position detection algorithms [72].

2.3.3 Experimental validation

Both introduced identification methods are applied to a commercial 4.0 kW RSM to obtain its nonlinear flux linkages experimentally, where its FEA data is unavailable. Its key specifications can be found in Table 3.1 (see RSM#3). Measurements are conducted in an established laboratory setup, which will be introduced elaborately in Chapter 4 (see Fig. 4.4).

2.3.3.1 Discussion (i) - constant speed

For the constant speed method, the machine under test rotates steadily at $\omega_{\mathrm{m}} = 0.3\omega_{\mathrm{m,R}} = 47.1\,\mathrm{rad/s}$ through the coupling to a speed-controlled prime mover. For the identification range $\mathbb{I}(I_{\mathrm{max}})$, the current limit I_{max} is set equal to the rated current amplitude $\widehat{i}_{\mathrm{s,R}}$ for straightforwardness, i.e., $I_{\mathrm{max}} = \widehat{i}_{\mathrm{s,R}} = 13.3\,\mathrm{A}$. A regular 51×51 grid on the current plane is created to contain all the testing current pairs with the d-axis current $i_{\mathrm{s}}^{d} \in [-9.4\,\mathrm{A}, 9.4\,\mathrm{A}]$ (step size: 0.38 A) and the q-axis current $i_{\mathrm{s}}^{q} \in [-13.3\,\mathrm{A}, 13.3\,\mathrm{A}]$ (step size: 0.53 A). A more extensive measurement range for i_{s}^{q} is made on purpose, as $i_{\mathrm{s}}^{q} > i_{\mathrm{s}}^{d}$ is normally required in MTPC and all other OFTC strategies. Note that the grid corners may be located outside the range of $\mathbb{I}(I_{\mathrm{max}})$, i.e., $\|\boldsymbol{i}_{\mathrm{s}}^{dq}\| > I_{\mathrm{max}}$, hence those points are skipped in the measurement and saved as Not a Number (NaN) values.

The identified d-axis flux linkage ψ_s^d and q-axis flux linkage ψ_s^q by using the constant speed method [through the offline calculation of (2.16)] are shown in Fig. 2.7(a) and 2.7(b) [colored surfaces], respectively. After the thorough measurement over the given current range, the acquired data with small step sizes between adjacent testing points can be presented as flux linkage maps with smooth surfaces. The severe magnetic nonlinearity of the considered RSM can be observed, since ψ_s^d and ψ_s^q saturate extremely nonlinearly throughout the entire operation range. Furthermore, taking advantage of the uniform step sizes between every current testing point, the differential inductances can be computed by numerical differentiation of the identified ψ_s^d and ψ_s^q with respect to the stator currents following the definition in (2.9). The derived d-axis differential inductance L_s^d, q-axis differential inductance L_s^q and cross-coupling differential inductances L_s^{dq} & L_s^{qd} are presented in Fig. 2.8(a), 2.8(b), 2.8(c) and 2.8(d), respectively. Apparently, the self-axis differential inductances L_s^d and L_s^q decrease considerably due to the increase of both i_s^d and i_s^q, and the cross-coupling differential inductances L_s^{dq} and L_s^{qd} also vary extensively throughout the entire operation range. Theoretically, the energy conservation rule indicates that L_s^{dq} should equal L_s^{qd} for all currents. However, in practice, a slight difference can be observed between the two inductance plots, as shown in Fig. 2.8(c) and 2.8(d). This difference may be attributed to measurement inaccuracies. Nevertheless, this variation is still acceptable since both the cross-coupling inductances exhibit similar saturation trends with values that are closely aligned.

It can be summarized that the constant speed identification method can effectively measure the nonlinear flux linkages of RSMs. Despite the time-consuming testing procedure and the mechanical requirements, a considerable amount of measurement data eventually yields flux linkage maps with smooth surfaces. Owing to the uniform nature of the measurement grid, the differential inductances can be obtained simply by numerical differentiation. Both, the identified flux linkages and differential inductances, can be saved directly as LUTs and compensated for in nonlinear control algorithms. Moreover, the extreme magnetic nonlinearities of RSMs on the flux linkages (see Fig. 2.7 [colored surfaces]) and differential inductances (see Fig. 2.8) are again confirmed from the measurement results. Therefore, modeling with constant inductances as a linear machine (as presented in Section 2.2.2.1) is inappropriate for RSMs in simulation and control design. In contrast, modeling with nonlinear flux linkages as a real machine (as introduced in Section 2.2.2.2) can properly represent the nonlinear machine behavior.

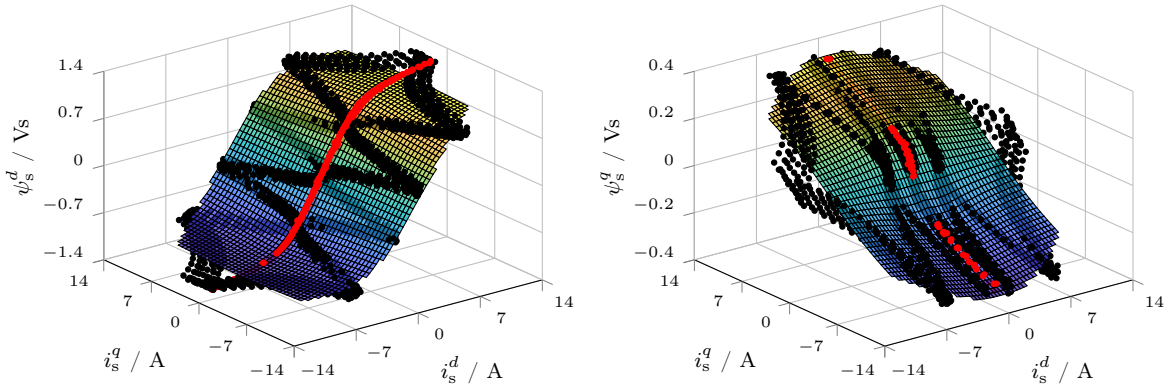

(a) (b)

Figure 2.7: Flux linkage measurement results of a 4.0 kW RSM using two different identification methods: (a) identified d-axis flux linkage ψ_s^d; (b) identified q-axis flux linkage ψ_s^q (where ψ_s^d and ψ_s^q are extracted through the constant speed method [colored surfaces] and the self-identification method by the self-axis [•] and cross-coupling [•] tests).

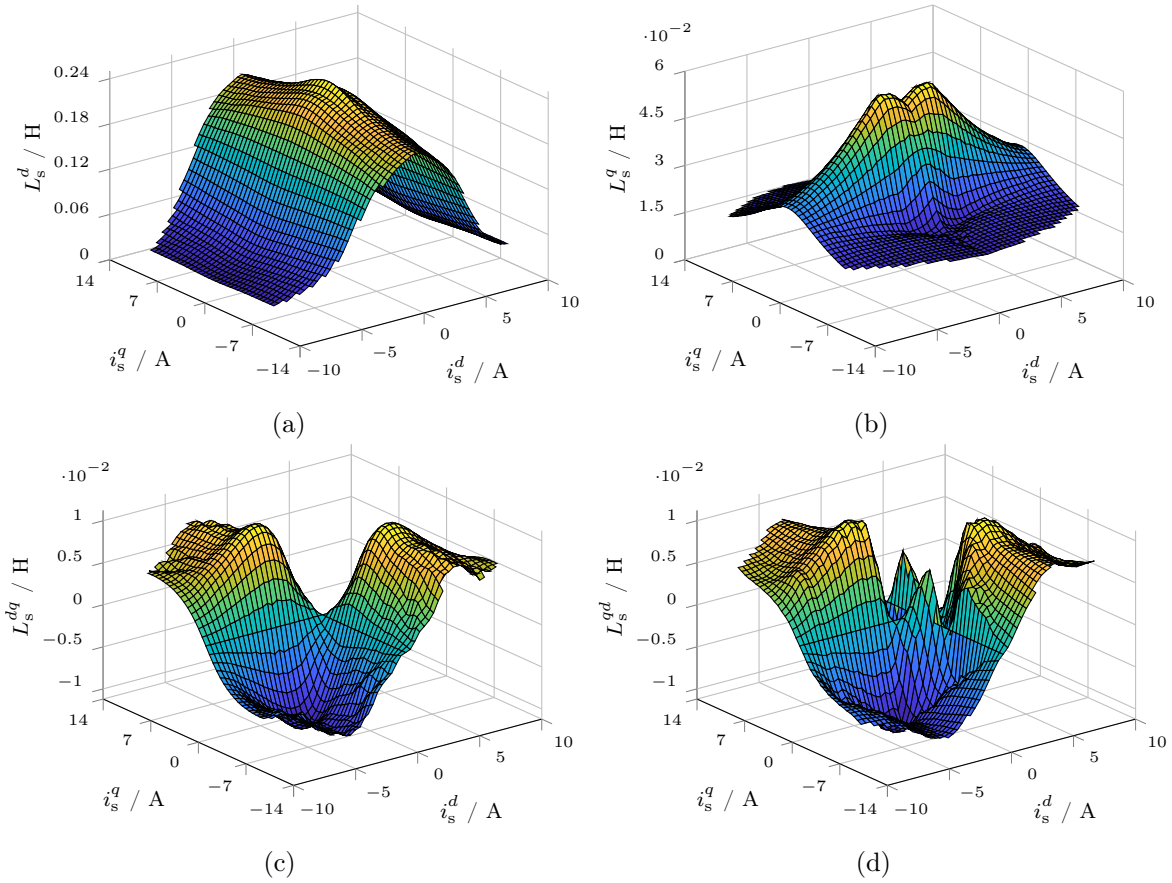

Figure 2.8: Differential inductances of a 4.0 kW RSM through numerical differentiation of the identified flux linkages by the constant speed method (as shown in Fig. 2.7 [colored surfaces]): (a) d-axis differential inductance L_s^d; (b) q-axis differential inductance L_s^q; (c) cross-coupling differential inductance L_s^{dq}; (d) cross-coupling differential inductance L_s^{qd}.

2.3.3.2 Discussion (ii) - self-identification

The self-identification method reuses the previously established setup, connecting the tested RSM to a load machine. However, only the RSM is commanded with test sequences here, whereas the load machine is in free-wheeling mode (*not controlled!*). Although mechanical coupling is not necessary for the applied approach, the resulting load increases the inertia in the mechanical subsystem, which can limit the extent of rotor movement during test. In total, *three* experimental tests at standstill, including self-axis (d- and q-axes) and cross-coupling tests, must be implemented. With the given voltage references and the measured currents, the nonlinear flux linkages can be extracted by calculating (2.17) [or by (2.19) while considering the back EMF term]. For simplicity, the testing variables in the voltage reference generation function (2.18) are selected identically for all tests, i.e., testing voltage amplitude $U_\mathrm{test} = U_\mathrm{test}^d = U_\mathrm{test}^q = 150\,\mathrm{V}$ and current limit $I_\mathrm{max} = I_\mathrm{max}^d = I_\mathrm{max}^q = 12\,\mathrm{A}$.

For the self-axis tests, the d- and q-axis testing procedures (with the voltage testing sequences) are demonstrated in Fig. 2.9 and Fig. 2.10, respectively. Both figures display the respective testing signals and responses separately, including stator voltages u_s^d & u_s^q, stator currents i_s^d & i_s^q, flux linkages ψ_s^d & ψ_s^q [computed online using (2.17)] and mechanical angular velocity ω_m. As illustrated, the acquisition window lasts *two* voltage pulse cycles for both tests, which will

normally give a sufficient number of samples for the following post-processing step. Besides, selecting an integer for the number of voltage pulses is beneficial, such that the offset, due to the (unknown) initial value of the integration, can be eliminated. The q-axis test is already completed after 17.4 ms (140 samples) in contrast to the d-axis test with 66.9 ms (536 samples). This noticeable difference is due to the smaller q-axis differential inductance L_s^q over the (almost) entire current range compared to the d-axis differential inductance L_s^d, as shown in Fig. 2.8. Due to this characteristic of RSMs, an adequate length of the acquisition window with a sufficient number of samples must be ensured (e.g., two voltage pulses are sufficient here). By extracting the resulting current responses and the calculated flux linkages from Fig. 2.9 and Fig. 2.10, the desired nonlinear current-to-flux relationship can be extracted. As a consequence, the self-saturated flux linkages ψ_s^d and ψ_s^q with zero cross-axis currents are shown in Fig. 2.7(a) and 2.7(b) [•], respectively.

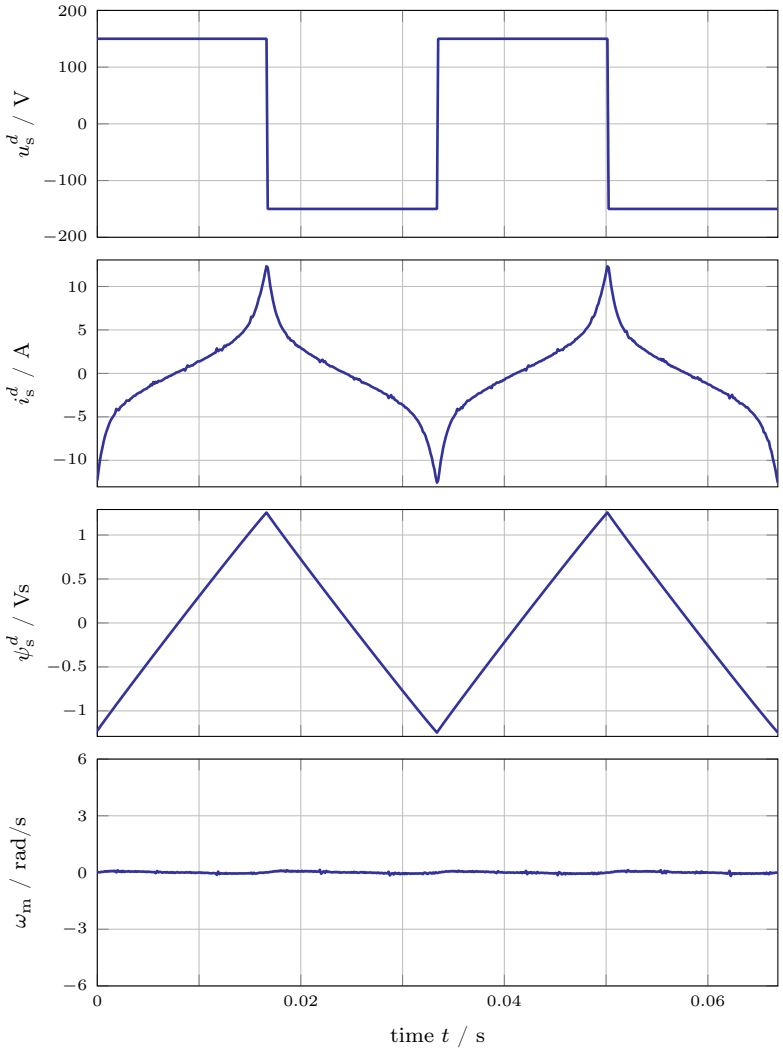

Figure 2.9: Self-axis test of the self-identification method for a 4.0 kW RSM: d-axis test.

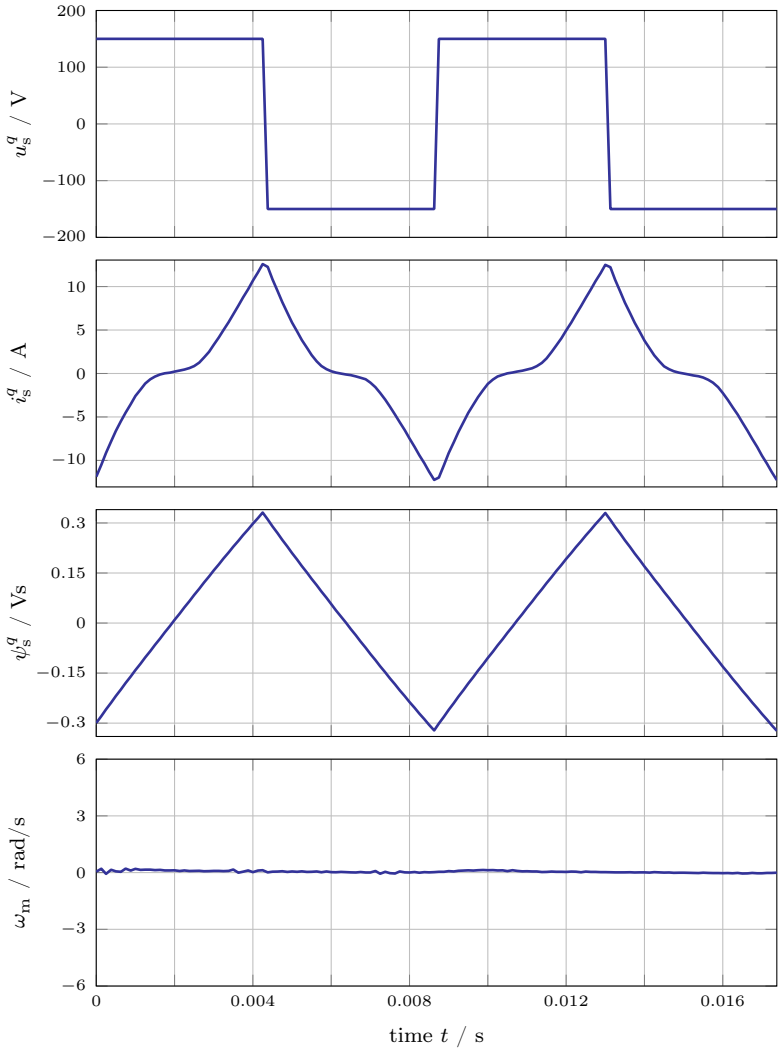

Figure 2.10: Self-axis test of the self-identification method for a 4.0 kW RSM: q-axis test.

Afterwards, for the cross-axis test, the testing procedure is illustrated in Fig. 2.11. The shown signals/quantities are identical to those shown in Fig. 2.9 and Fig. 2.10. Additionally, ψ_s^d and ψ_s^q with and without consideration of the back EMF are depicted. A longer acquisition window with *eight* d voltage pulse cycles (i.e, 267.9 ms with 2144 samples) is chosen intentionally to acquire more samples covering a wide measurement range. During the test, voltage sequences, as proposed in (2.18), are applied to both d- and q-axes at the same time. The pulsating torque is a result of the nonzero i_s^d and i_s^q. Consequently, the mechanical speed ω_m in Fig. 2.11 differs from standstill to a much greater extent in comparison to the self-axis tests in Fig. 2.9 and Fig. 2.10. This undesired rotor movement induces the speed-dependent back EMF, which is not included in the flux linkage derivation based on (2.17). As a result of these incorrect voltages, in particular, a drift in ψ_s^q [—] can be observed if (2.17) *without* considering the back EMF term is used; whereas, for ψ_s^d, the drifting problem is not so prominent.

In contrast to these rather bad estimation results, it can be seen that the compensated ψ_s^q [—] using (2.19) *with* the consideration of the back EMF term allows to suppress the integration drift very effectively and almost completely. As a result of the cross-coupling test in Fig. 2.11, the (compensated) cross-saturated flux linkages ψ_s^d and ψ_s^q are shown in Fig. 2.7(a) and 2.7(b) [•], respectively.

Finally, the entire testing procedure of the self-identification method completes within only a fraction of a second (352.2 ms). The experimentally identified flux linkages from the self-axis and cross-coupling tests (see [•] and [•] in Fig. 2.7) cover wide areas of the overall operation range and represent well the self-axis and cross-coupling saturation effects of the considered RSM. Hence, its effectiveness is confirmed. It features significant time-savings, simple implementation and standard experimental setup (no torque sensor, nor prime mover required). These properties make it a more practical and attractive approach for many applications compared to the constant speed method. Nevertheless, the extracted flux linkages with hysteresis effects scatter in the given measurement range without allowing to represent the whole flux linkage maps or at specific points (e.g., not covered by [•] and [•] points). Due to the scattered nature, saving of LUTs on a uniform grid or deriving the differential inductances is not possible. Hence, the compensation of the magnetic nonlinearity in real-time applications is not feasible yet. Therefore, post-processing tools must be utilized, e.g., by interpolation, neural network (as in [124]) or analytical prototype function (which will be demonstrated in Chapter 3).

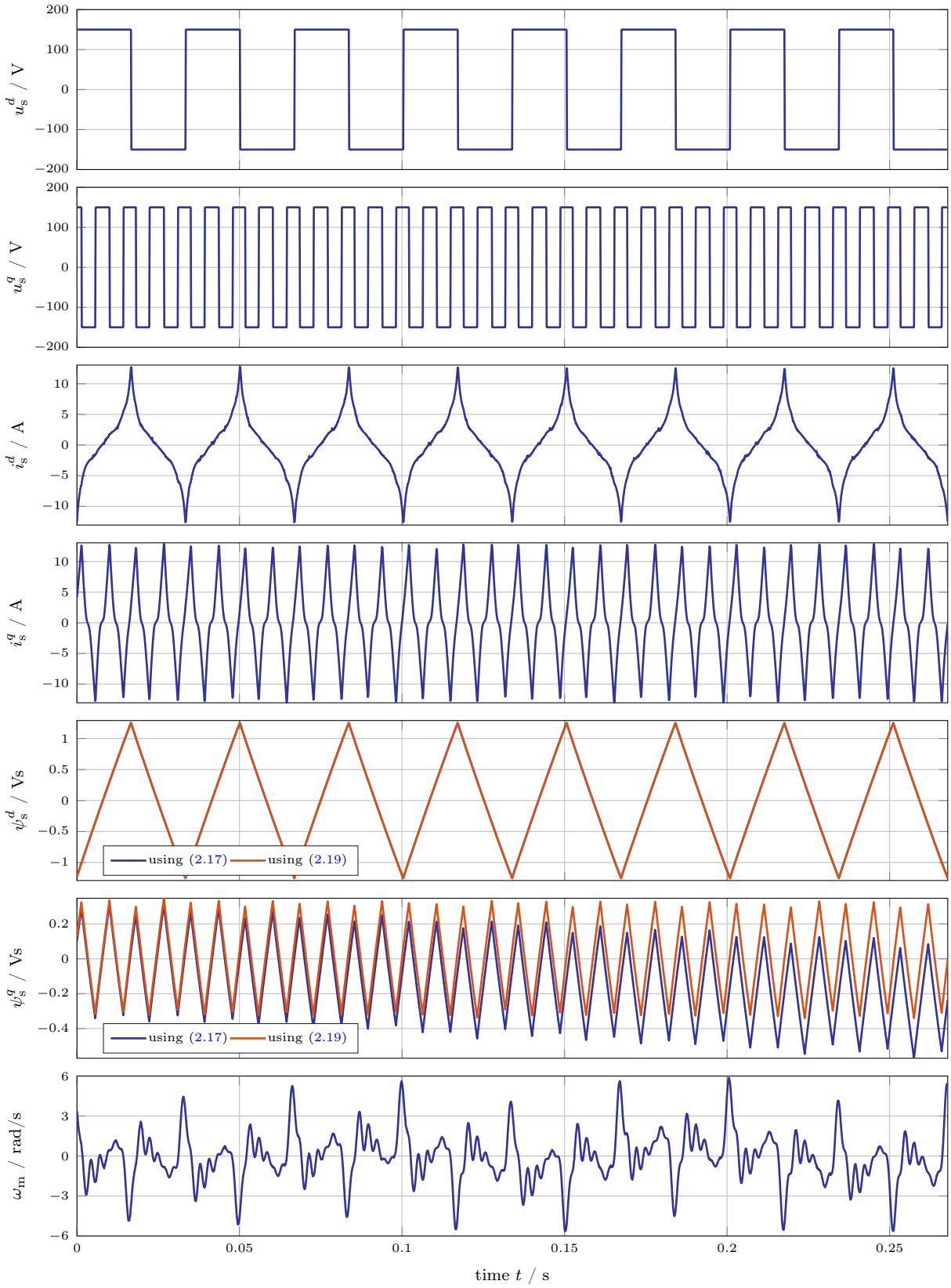

Figure 2.11: Cross-coupling test of the self-identification method for a 4.0 kW RSM where flux linkages ψ_s^d and ψ_s^q are computed *without* (using (2.17) [—]) and *with* (using (2.19) [—]) consideration of the back EMF term $\omega_p \boldsymbol{J} \boldsymbol{\psi}_s^{dq}$.

Chapter 3

Analytical flux linkage prototype functions

Physically motivated and analytical prototype functions are proposed to approximate the nonlinear flux linkages of nonlinear synchronous machines (SMs) in general, with a specific focus on reluctance synchronous machines (RSMs) and interior permanent magnet synchronous machines (IPMSMs). These analytical functions offer a significant advantage by eliminating the need for extensive lookup tables (LUTs), making them particularly beneficial for nonlinear control and optimal operation management of such machines. The proposed flux linkage prototype functions accurately replicate the nonlinear self-axis and cross-coupling saturation effects of SMs. Furthermore, their differentiability enables the straightforward derivation of analytical expressions for the differential inductances through simple differentiation of the flux linkage prototype functions. In total, two types of flux linkage prototype functions are developed. The first type is designed for "symmetric" flux linkages of RSMs and adheres the energy conservation rule. Building upon this knowledge, the second type of prototype functions is derived in order to achieve approximation flexibility necessary for SMs with permanent magnet (or electrical) excitation, where "unsymmetric" flux linkages arise due to the excitation offset. All proposed flux linkage prototype functions are continuously differentiable, obey the energy conservation rule and, as fitting results show, achieve a (very) high approximation accuracy throughout the entire operation range.

This chapter is partly based on [1], presenting more detailed derivations and thorough investigations building upon the foundational work. First, in Section 3.1, the motivation for designing prototype functions is found by observing the flux linkage and cross-coupling inductance characteristics. In Section 3.2 and Section 3.3, two different flux linkage prototype functions for RSMs are developed. Furthermore, in Section 3.4, prototype functions for IPMSMs are introduced. Eventually, in Section 3.5, a comparison between existing solutions for prototype functions is provided.

3.1 Motivation

First, the flux linkages of RSMs and IPMSMs are studied and explained, including self (direct) axis and cross (quadrature) axis saturation effects. Both real flux linkages of an RSM and an IPMSM are obtained from finite element analysis (FEA) and used as examples to observe the saturation characteristics. Then, the common saturation trends between different machine types are pointed out. Finally, the (differentiable) cross-coupling inductances are analyzed, which are

crucial for a proper design of the proposed flux linkage prototype functions.

3.1.1 Flux linkage characteristics

3.1.1.1 RSM

If iron losses are neglected, then, due to the symmetric rotor design of RSMs as shown in Fig. 2.2(d) and 2.2(e), the symmetry of the flux linkages with respect to the d-axis current i_s^d and q-axis current i_s^q implies [1, 126]

$$\left.\begin{aligned}\psi_\mathrm{s}^d(i_\mathrm{s}^d, i_\mathrm{s}^q) &= -\psi_\mathrm{s}^d(-i_\mathrm{s}^d, i_\mathrm{s}^q),\\ \psi_\mathrm{s}^q(i_\mathrm{s}^d, i_\mathrm{s}^q) &= \psi_\mathrm{s}^q(-i_\mathrm{s}^d, i_\mathrm{s}^q)\end{aligned}\right\} \tag{3.1}$$

and

$$\left.\begin{aligned}\psi_\mathrm{s}^d(i_\mathrm{s}^d, i_\mathrm{s}^q) &= \psi_\mathrm{s}^d(i_\mathrm{s}^d, -i_\mathrm{s}^q),\\ \psi_\mathrm{s}^q(i_\mathrm{s}^d, i_\mathrm{s}^q) &= -\psi_\mathrm{s}^q(i_\mathrm{s}^d, -i_\mathrm{s}^q),\end{aligned}\right\} \tag{3.2}$$

respectively. The real d-axis flux linkage ψ_s^d and q-axis flux linkage ψ_s^q of a 9.6 kW RSM are exemplarily shown in Fig. 3.1(a) and 3.1(b), respectively.

To illustrate and highlight the typical and intrinsic magnetic saturation effects of RSMs, Fig. 3.1(c) and 3.1(d) show the saturated self-axis flux linkage curves [—,—,—] extracted from the presented flux linkage maps in Fig. 3.1(a) and 3.1(b) for different cross-coupling currents. Even though flux curves in both d- and q-axes have similar trends, they illustrate different saturation effects. The d-axis flux linkage ψ_s^d saturates gradually in the higher current region after reaching the magnetic limit of the rotor laminations (e.g., iron steels). On the other hand, the q-axis flux linkage ψ_s^q saturates immediately in the lower current range, because the iron bridges located at the end of the flux barriers saturate easily; then it increases almost linearly with the current. To illustrate the typical cross-coupling saturation effects of RSMs, ψ_s^d over i_s^q and ψ_s^q over i_s^d [—,—,—] for different self-axis currents are plotted in Fig. 3.1(e) and 3.1(f), respectively. Obviously, both flux linkages are influenced by their respective cross-coupling currents. Compared to ψ_s^q, ψ_s^d is affected less by i_s^q due to the higher permeability in the d-axis flux path.

3.1.1.2 IPMSM

According to the rotor structure of IPMSMs shown in Fig. 2.2(b), the symmetry relation as in (3.2) only holds with respect to i_s^q [1, 126]. Due to the existence of PM materials in the d-axis, the flux linkage surfaces saturate asymmetrically with respect to i_s^d. In Fig. 3.2(a) and 3.2(b), the real flux linkage maps of a 3.4 kW IPMSM are shown.

Its saturated self-axis flux linkages [—,—,—] are shown in Fig. 3.2(c) and 3.2(d). ψ_s^d is the sum of stator current flux linkage $\bar{\boldsymbol{\psi}}_\mathrm{s}^{dq}(\boldsymbol{i}_\mathrm{s}^{dq})$ and PM flux linkage $\boldsymbol{\psi}_\mathrm{pm}^{dq}$ [recall (2.7)]. For positive i_s^d, it saturates gradually; in contrast, ψ_s^d for negative i_s^d (e.g., during field weakening), it decreases almost linearly. On the other hand, ψ_s^q possesses a similar saturation effect as ψ_s^d of RSMs because the flux paths are similar. Fig. 3.2(e) and 3.2(f) illustrate the cross-coupling saturation effects [—,—,—]. Additionally, ψ_s^d over i_s^q for negative i_s^d is shown in Fig. 3.3, where different trends of the cross-coupling effects for positive and negative i_s^d can be observed in contrast to those for RSMs [as illustrated in Fig. 3.2(e)]. The symmetry in (3.2) of ψ_s^d with respect to i_s^q is clearly confirmed in Fig. 3.2(e) and Fig. 3.3; meanwhile, the asymmetry of ψ_s^q with respect to i_s^d

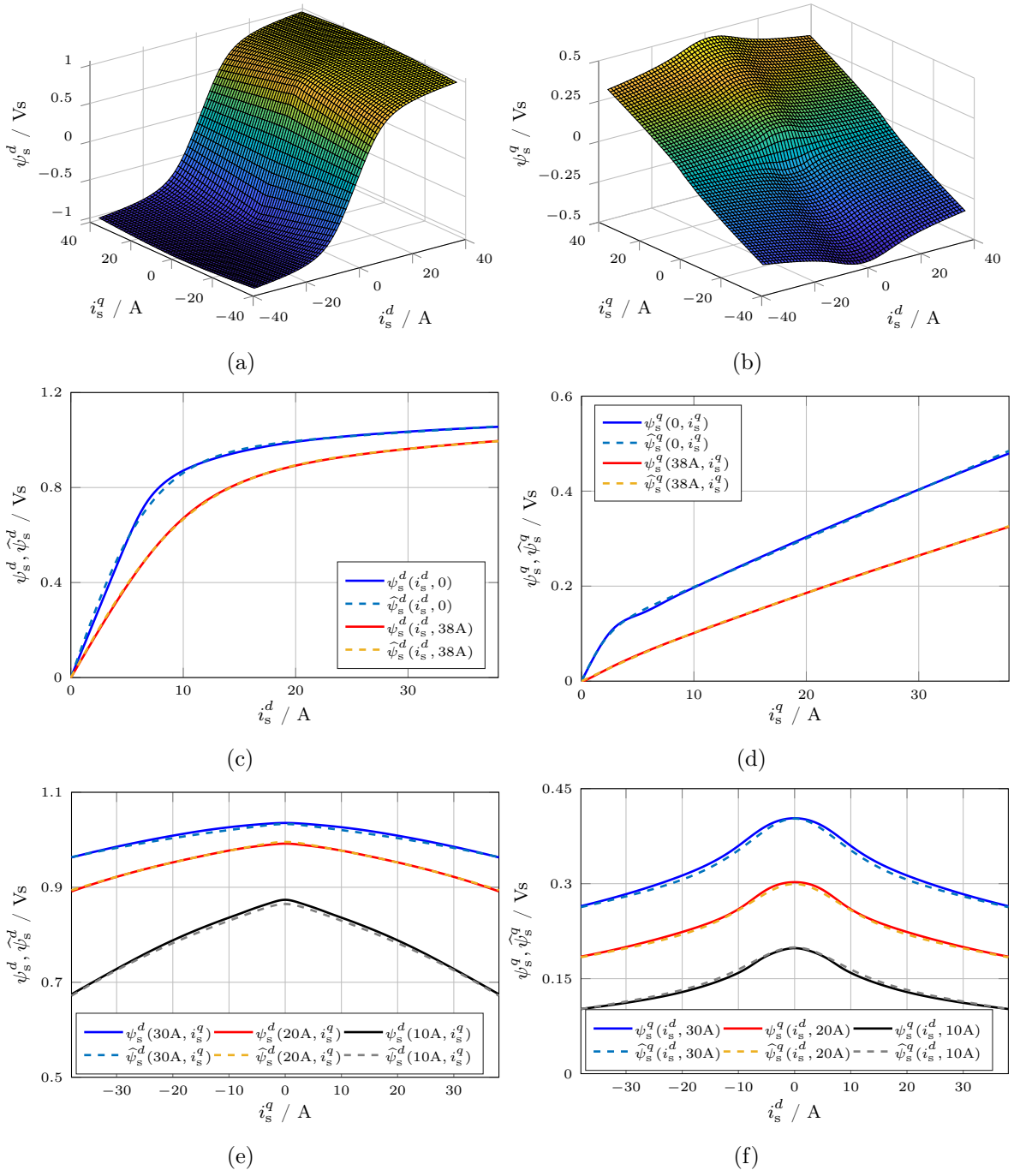

Figure 3.1: Flux linkage characteristics of a 9.6 kW RSM: (a) real d-axis flux linkage map $\psi_\mathrm{s}^d(i_\mathrm{s}^d, i_\mathrm{s}^q)$; (b) real q-axis flux linkage map $\psi_\mathrm{s}^q(i_\mathrm{s}^d, i_\mathrm{s}^q)$; (c) real and approximated self-axis d-axis flux linkages $\psi_\mathrm{s}^d(i_\mathrm{s}^d, I_\mathrm{s}^q)$ and $\widehat{\psi}_\mathrm{s}^d(i_\mathrm{s}^d, I_\mathrm{s}^q)$ for different cross-coupling currents $i_\mathrm{s}^q = I_\mathrm{s}^q$; (d) real and approximated self-axis q-axis flux linkages $\psi_\mathrm{s}^q(I_\mathrm{s}^d, i_\mathrm{s}^q)$ and $\widehat{\psi}_\mathrm{s}^q(I_\mathrm{s}^d, i_\mathrm{s}^q)$ for different cross-coupling currents $i_\mathrm{s}^d = I_\mathrm{s}^d$; (e) real and approximated cross-coupling d-axis flux linkages $\psi_\mathrm{s}^d(I_\mathrm{s}^d, i_\mathrm{s}^q)$ and $\widehat{\psi}_\mathrm{s}^d(I_\mathrm{s}^d, i_\mathrm{s}^q)$ for different self-axis currents $i_\mathrm{s}^d = I_\mathrm{s}^d$; (f) real and approximated cross-coupling q-axis flux linkages $\psi_\mathrm{s}^q(i_\mathrm{s}^d, I_\mathrm{s}^q)$ and $\widehat{\psi}_\mathrm{s}^q(i_\mathrm{s}^d, I_\mathrm{s}^q)$ for different self-axis currents $i_\mathrm{s}^q = I_\mathrm{s}^q$ (where ψ_s^d and ψ_s^q [—, —, —] represent the real flux linkages, and $\widehat{\psi}_\mathrm{s}^d$ and $\widehat{\psi}_\mathrm{s}^q$ [- - -, - - -, - - -] represent their approximations as introduced in Section 3.2).

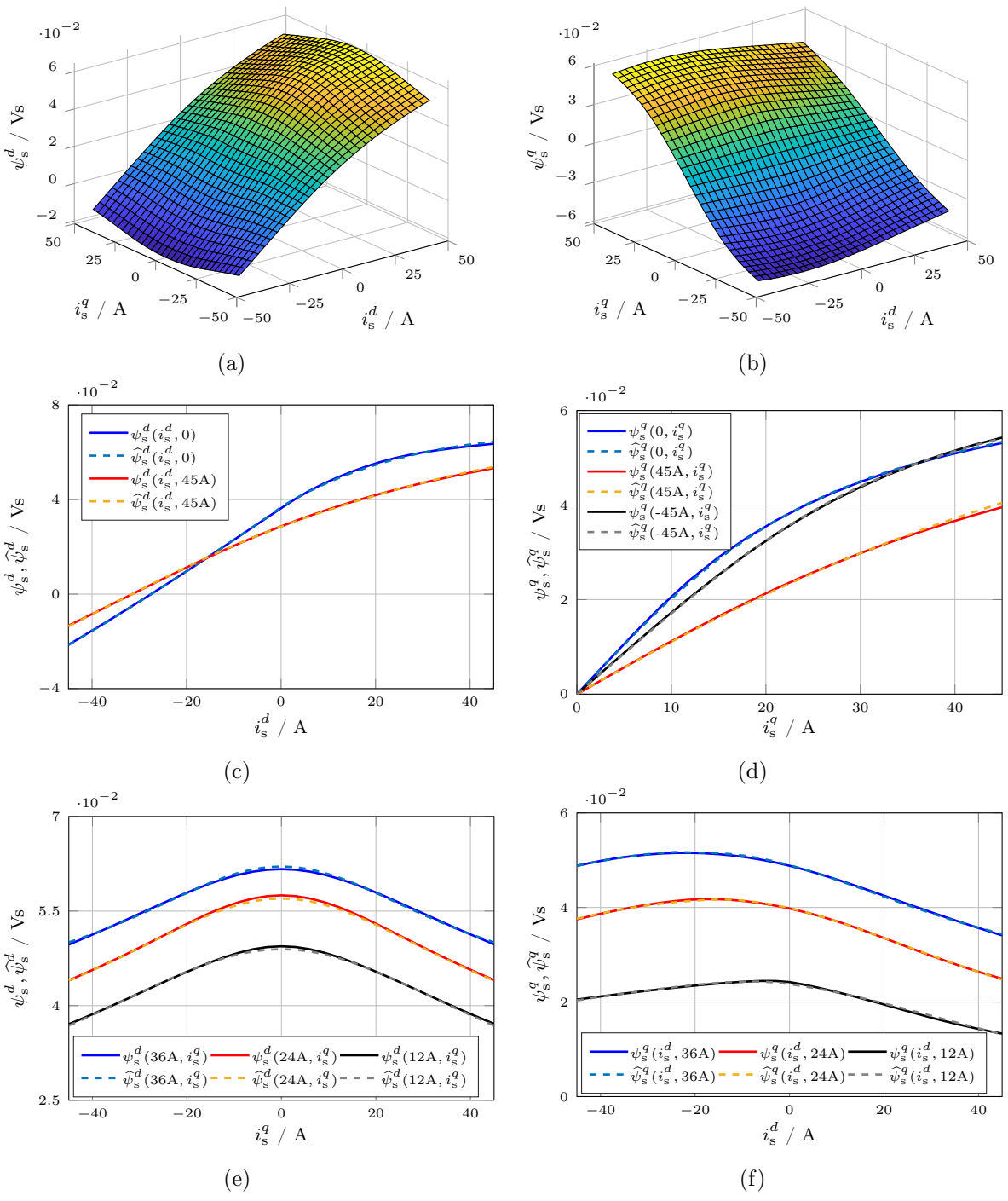

Figure 3.2: Flux linkage characteristics of a 3.4 kW IPMSM: (a) real d-axis flux linkage map $\psi_\mathrm{s}^d(i_\mathrm{s}^d, i_\mathrm{s}^q)$; (b) real q-axis flux linkage map $\psi_\mathrm{s}^q(i_\mathrm{s}^d, i_\mathrm{s}^q)$; (c) real and approximated self-axis d-axis flux linkages $\psi_\mathrm{s}^d(i_\mathrm{s}^d, I_\mathrm{s}^q)$ and $\widehat{\psi}_\mathrm{s}^d(i_\mathrm{s}^d, I_\mathrm{s}^q)$ for different cross-coupling currents $i_\mathrm{s}^q = I_\mathrm{s}^q$; (d) real and approximated self-axis q-axis flux linkages $\psi_\mathrm{s}^q(I_\mathrm{s}^d, i_\mathrm{s}^q)$ and $\widehat{\psi}_\mathrm{s}^q(I_\mathrm{s}^d, i_\mathrm{s}^q)$ for different cross-coupling currents $i_\mathrm{s}^d = I_\mathrm{s}^d$; (e) real and approximated cross-coupling d-axis flux linkages $\psi_\mathrm{s}^d(I_\mathrm{s}^d, i_\mathrm{s}^q)$ and $\widehat{\psi}_\mathrm{s}^d(I_\mathrm{s}^d, i_\mathrm{s}^q)$ for different self-axis currents $i_\mathrm{s}^d = I_\mathrm{s}^d$; (f) real and approximated cross-coupling q-axis flux linkages $\psi_\mathrm{s}^q(i_\mathrm{s}^d, I_\mathrm{s}^q)$ and $\widehat{\psi}_\mathrm{s}^q(i_\mathrm{s}^d, I_\mathrm{s}^q)$ for different self-axis currents $i_\mathrm{s}^q = I_\mathrm{s}^q$ (where ψ_s^d and ψ_s^q [——, ——, ——] represent the real flux linkages, and $\widehat{\psi}_\mathrm{s}^d$ and $\widehat{\psi}_\mathrm{s}^q$ [- - -, - - -, - - -] represent their approximations as introduced in Section 3.4).

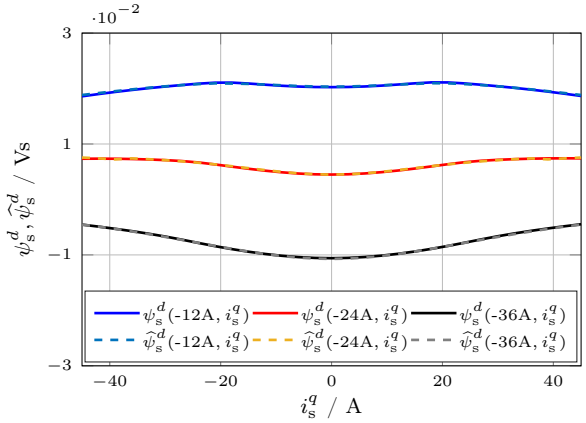

Figure 3.3: IPMSM cross-coupling d-axis flux linkages $\psi_s^d(I_s^d, i_s^q)$ and $\widehat{\psi}_s^d(I_s^d, i_s^q)$ for different self-axis currents $i_s^d = I_s^d < 0$ (where ψ_s^d [—, —, —] represents the real flux linkage and $\widehat{\psi}_s^d$ [- - -, - - -, - - -] represents its approximation as introduced in Section 3.4).

can be observed in Fig. 3.2(f). Furthermore, by comparing Fig. 3.3 with Fig. 3.2(e) and the left part in Fig. 3.2(f) with the right, it can be seen that both ψ_s^d and ψ_s^q with negative i_s^d are less affected by cross-coupling saturation effects.

3.1.1.3 Key observations for prototype function design

Several key and generic observations can be made from Fig. 3.1 (RSM) and Fig. 3.2 (IPMSM). Even though different stator and rotor designs of RSMs and IPMSMs will result in different flux linkages, their shapes will be very similar. These similarities are particularly apparent in the saturation trends in both self-axis and cross-coupling directions. Therefore, instead of fitting polynomials leading to several redundant parameters, designing physically motivated prototype functions to approximate and reflect these key observations is very meaningful.

To describe the self-axis saturation effects of the flux linkages, the sum of a hyperbolic function and a straight line [1], i.e.,

$$\psi_{s,\text{self}}^{d/q} \propto \tanh(i_s^{d/q}) + i_s^{d/q},$$

seems very well suited for RSMs [as shown in Fig. 3.1(c) & 3.1(d)] and also for IPMSMs [as illustrated in Fig. 3.2(c) & 3.2(d)]; whereas to approximate the cross-coupling saturation effects, a (shifted) bell-shaped or Gaussian-like function [1], i.e.,

$$\psi_{s,\text{cross}}^{d/q} \propto -\ln\big(\cosh(i_s^{d/q})\big) \quad \text{or} \quad \psi_{s,\text{cross}}^{d/q} \propto \exp\big(-(i_s^{d/q})^2\big),$$

seems appropriate, as illustrated in Fig. 3.1(e) & 3.1(f) for RSMs and in Fig. 3.2(e) & 3.3 for IPMSMs, respectively.

3.1.2 Cross-coupling inductance

By obeying the energy conservation rule, the well-known reciprocity relation is established, which means that mutual (differential) inductances must equal for two coupled inductors. Provided that losses are modeled separately, the reciprocity property holds true still in nonlinear synchronous

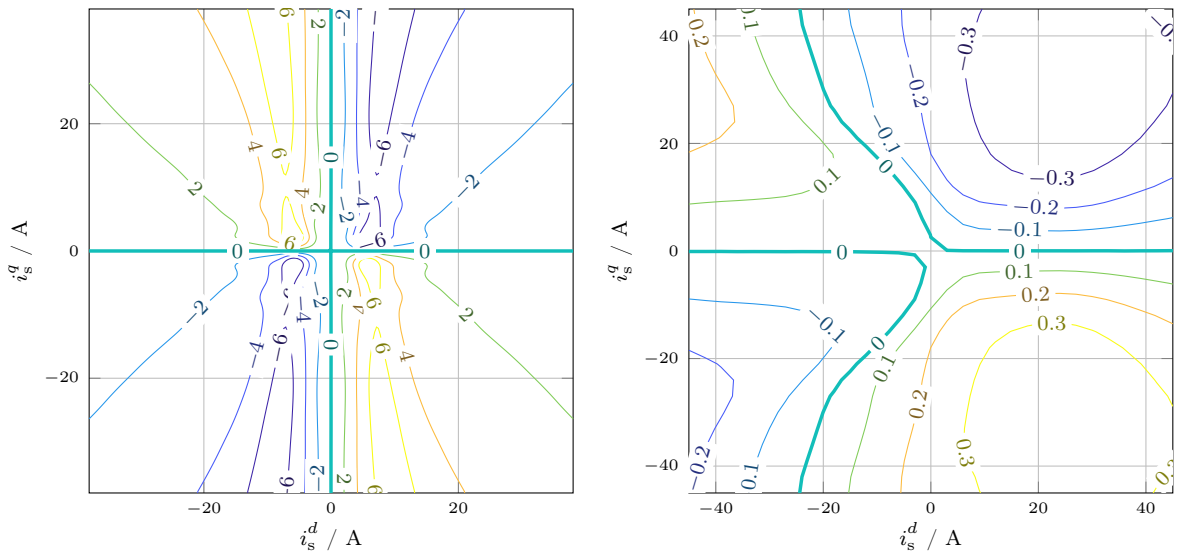

Figure 3.4: Contour plots of cross-coupling differential inductances: (a) $\mathbb{L}_s^{dq}(L)$ of RSM (in mH); (b) $\mathbb{L}_s^{dq}(L)$ of IPMSM (in mH).

machines (such as RSMs and IPMSMs) [125], i.e.,

$$L_s^{dq}(\boldsymbol{i}_s^{dq}) = L_s^{qd}(\boldsymbol{i}_s^{dq}) \text{ for all } \boldsymbol{i}_s^{dq}. \tag{3.3}$$

To illustrate the characteristic of the differential cross-coupling inductances, the contour plots

$$\mathbb{L}_s^{dq}(L) := \{\, \boldsymbol{i}_s^{dq} \in \mathbb{R}^2 \mid L_s^{dq}(\boldsymbol{i}_s^{dq}) = L_s^{qd}(\boldsymbol{i}_s^{dq}) \stackrel{!}{=} L \,\}$$

of RSM and IPMSM, where $L_s^{dq} = L_s^{qd} = L$ holds with some given value $L \in \mathbb{R}$, are plotted in Fig. 3.4(a) and 3.4(b), respectively. One can observe the following common characteristics for both machines [1, 126]:

1. $L_s^{dq} = L_s^{qd} = L > 0$ are always positive in the upper-left and lower-right regions (2nd and 4th quadrants) of the zero locus with $L = 0$ of the contour plot $\mathbb{L}_s^{dq}(0)$ (see green line [—]).

2. $L_s^{dq} = L_s^{qd} = L < 0$ are always negative in the upper-right and lower-left regions (1st and 3rd quadrants) of $\mathbb{L}_s^{dq}(0)$.

Analyzing the zero locus $\mathbb{L}_s^{dq}(0)$ with $L_s^{dq} = L_s^{qd} = 0$ (see [—] in Fig. 3.4 and [—] in Figs. 3.6 & 3.13) yields the following observations [1, 126]:

1. The zero locus $\mathbb{L}_s^{dq}(0)$ exhibits an intersection at $\boldsymbol{i}_s^{dq} = (0, 0)^\top$.

2. The zero locus $\mathbb{L}_s^{dq}(0)$ separates the contour plots $\mathbb{L}_s^{dq}(L)$ for positive and negative L.

3. On the zero locus $\mathbb{L}_s^{dq}(0)$, ψ_s^d does not change along i_s^q, and ψ_s^q does not change along i_s^d, respectively.

In Fig. 3.4(a), the zero locus $\mathbb{L}_\mathrm{s}^{dq}(0)$ of the RSM is located on the axes where $i_\mathrm{s}^q = 0$ and $i_\mathrm{s}^d = 0$, since the flux linkages of the RSM are symmetric with respect to these axes [recall (3.1) and (3.2)]. Moreover, every two adjacent quadrants have opposite signs but identical absolute values in their inductance values.

On the other hand, as shown in Fig. 3.4(b), the zero locus $\mathbb{L}_\mathrm{s}^{dq}(0)$ of the IPMSM passes through the $i_\mathrm{s}^q = 0$-axis but not through the $i_\mathrm{s}^d = 0$-axis. In the vertical direction parallel to the i_s^q-axis, it is curved and converges asymptotically to a vertical line at $i_\mathrm{s}^d \approx -24\,\mathrm{A}$ (not shown). Moreover, it is symmetric with respect to the $i_\mathrm{s}^q = 0$-axis in the second and third quadrants. In conclusion, for (I)PMSMs, due to the existence of the PM, the vertical branch of the zero locus $\mathbb{L}_\mathrm{s}^{dq}(0)$ moves from $i_\mathrm{s}^d = 0$ (as for RSMs) to a constant negative i_s^d value (e.g., $i_\mathrm{s}^d \approx -24\,\mathrm{A}$ for the considered IPMSM).

3.2 RSM flux linkage prototype function I

Now, the analytical flux linkage prototype functions of RSMs are derived. Afterwards, the fitting procedure is discussed in order to find a proper parametrization of the proposed prototype functions.

3.2.1 Analytical prototype function

As electrical machines are conservative systems, the energy during magnetization is not dissipated (if iron losses are neglected). The variation of coenergy $\Delta W_\mathrm{c}(i_\mathrm{s}^d, i_\mathrm{s}^q)$ in both axes due to the cross-coupling saturation effect must equal [43]. Hence, the RSM flux linkages can be approximated by the following analytical prototype functions [1]

$$\left.\begin{aligned}\widehat{\psi}_\mathrm{s}^d(i_\mathrm{s}^d, i_\mathrm{s}^q) &= \widehat{\psi}_\mathrm{s,self}^d(i_\mathrm{s}^d) - \widehat{\psi}_\mathrm{s,cross}^d(i_\mathrm{s}^d, i_\mathrm{s}^q),\\ \widehat{\psi}_\mathrm{s}^q(i_\mathrm{s}^d, i_\mathrm{s}^q) &= \widehat{\psi}_\mathrm{s,self}^q(i_\mathrm{s}^q) - \widehat{\psi}_\mathrm{s,cross}^q(i_\mathrm{s}^d, i_\mathrm{s}^q),\end{aligned}\right\} \tag{3.4}$$

where $\widehat{\psi}_\mathrm{s,self}^d(i_\mathrm{s}^d)$ & $\widehat{\psi}_\mathrm{s,self}^q(i_\mathrm{s}^q)$ and $\widehat{\psi}_\mathrm{s,cross}^d(i_\mathrm{s}^d, i_\mathrm{s}^q)$ & $\widehat{\psi}_\mathrm{s,cross}^q(i_\mathrm{s}^d, i_\mathrm{s}^q)$ represent *self-axis* and *cross-coupling* saturation terms, respectively. The overall flux linkages are obtained by subtracting the cross-coupling saturation terms from the self-axis saturation terms. The cross-coupling saturation terms can be modeled by the multiplication of two functions depending on only one current each, i.e.,

$$\left.\begin{aligned}\widehat{\psi}_\mathrm{s,cross}^d(i_\mathrm{s}^d, i_\mathrm{s}^q) &= F'(i_\mathrm{s}^d)G(i_\mathrm{s}^q),\\ \widehat{\psi}_\mathrm{s,cross}^q(i_\mathrm{s}^d, i_\mathrm{s}^q) &= F(i_\mathrm{s}^d)G'(i_\mathrm{s}^q),\end{aligned}\right\} \tag{3.5}$$

where $F'(i_\mathrm{s}^d) := \frac{\mathrm{d}}{\mathrm{d}i_\mathrm{s}^d}F(i_\mathrm{s}^d)$ and $G'(i_\mathrm{s}^q) := \frac{\mathrm{d}}{\mathrm{d}i_\mathrm{s}^q}G(i_\mathrm{s}^q)$ denote the respective derivatives of the functions $F(i_\mathrm{s}^d)$ and $G(i_\mathrm{s}^q)$. With the definitions in (3.4) and (3.5), an identical coenergy variation in both axes can be imposed, resulting in

$$\begin{aligned}\Delta W_\mathrm{c}(i_\mathrm{s}^d, i_\mathrm{s}^q) &= \int \Big(\underbrace{\widehat{\psi}_\mathrm{s,self}^d(i_\mathrm{s}^d) - \widehat{\psi}_\mathrm{s}^d(i_\mathrm{s}^d, i_\mathrm{s}^q)}_{=\widehat{\psi}_\mathrm{s,cross}^d(i_\mathrm{s}^d, i_\mathrm{s}^q) = F'(i_\mathrm{s}^d)G(i_\mathrm{s}^q)} \Big)\, \mathrm{d}i_\mathrm{s}^d = \int \Big(\underbrace{\widehat{\psi}_\mathrm{s,self}^q(i_\mathrm{s}^q) - \widehat{\psi}_\mathrm{s}^q(i_\mathrm{s}^d, i_\mathrm{s}^q)}_{=\widehat{\psi}_\mathrm{s,cross}^q(i_\mathrm{s}^d, i_\mathrm{s}^q) = F(i_\mathrm{s}^d)G'(i_\mathrm{s}^q)} \Big)\, \mathrm{d}i_\mathrm{s}^q\\ &= F(i_\mathrm{s}^d)G(i_\mathrm{s}^q).\end{aligned} \tag{3.6}$$

Obviously, the reciprocity property is assured by the inherent structure of the chosen analytical functions, i.e., the partial derivatives of (3.4) with respect to the cross-coupling currents which must equal, i.e.,

$$\frac{\mathrm{d}}{\mathrm{d}i_\mathrm{s}^q}\widehat{\psi}_\mathrm{s}^d(i_\mathrm{s}^d, i_\mathrm{s}^q) = \frac{\mathrm{d}}{\mathrm{d}i_\mathrm{s}^d}\widehat{\psi}_\mathrm{s}^q(i_\mathrm{s}^d, i_\mathrm{s}^q) = -F'(i_\mathrm{s}^d)G'(i_\mathrm{s}^q).$$

The RSM self-axis flux linkages in both axes for two constant cross currents are shown in Fig. 3.1(c) and 3.1(d) to illustrate the self-axis saturation characteristics. According to the key observations previously, the self-axis saturation prototype employs a hyperbolic tangent function and a linear function to mimic the saturation effect in a single axis, which means that the flux linkages are only dependent on one current (self-axis current). In view of Fig. 3.1(c) and 3.1(d) [—], the d- and q-axis self-axis saturation terms for zero cross-coupling currents are defined as follows [1]

$$\left.\begin{aligned}\widehat{\psi}_{\mathrm{s,self}}^d(i_\mathrm{s}^d) &:= \widehat{\psi}_\mathrm{s}^d(i_\mathrm{s}^d, i_\mathrm{s}^q = 0) = a_\mathrm{d1}\tanh\left(a_\mathrm{d2}i_\mathrm{s}^d\right) + a_\mathrm{d3}i_\mathrm{s}^d,\\ \widehat{\psi}_{\mathrm{s,self}}^q(i_\mathrm{s}^q) &:= \widehat{\psi}_\mathrm{s}^q(i_\mathrm{s}^d = 0, i_\mathrm{s}^q) = a_\mathrm{q1}\tanh\left(a_\mathrm{q2}i_\mathrm{s}^q\right) + a_\mathrm{q3}i_\mathrm{s}^q,\end{aligned}\right\} \tag{3.7}$$

where $a_\mathrm{d1}, a_\mathrm{d2}$ and $a_\mathrm{q1}, a_\mathrm{q2}$ affect mainly the smooth transition before the linear region, and a_d3 and a_q3 describe the slope of the linear part of the prototype functions.

Afterwards, the cross-coupling saturation terms must be found. According to the required current range of the flux linkage maps, maximum cross-coupling current constants I_d1 and I_q1 can be selected. By evaluating (3.4) at these maximum cross-coupling currents, the prototype functions simplify to

$$\left.\begin{aligned}\widehat{\psi}_\mathrm{s}^d(i_\mathrm{s}^d, i_\mathrm{s}^q = I_\mathrm{q1}) &= \widehat{\psi}_{\mathrm{s,self}}^d(i_\mathrm{s}^d) - F'(i_\mathrm{s}^d)G(I_\mathrm{q1}),\\ \widehat{\psi}_\mathrm{s}^q(i_\mathrm{s}^d = I_\mathrm{d1}, i_\mathrm{s}^q) &= \widehat{\psi}_{\mathrm{s,self}}^q(i_\mathrm{s}^q) - F(I_\mathrm{d1})G'(i_\mathrm{s}^q),\end{aligned}\right\} \tag{3.8}$$

which can be expressed with the self-axis saturation terms evaluated at I_q1 and I_d1 (as shown in Fig. 3.1(c) and 3.1(d) [—]), respectively, as [1]

$$\left.\begin{aligned}\widehat{\psi}_\mathrm{s1}^d(i_\mathrm{s}^d) &:= \widehat{\psi}_\mathrm{s}^d(i_\mathrm{s}^d, i_\mathrm{s}^q = I_\mathrm{q1}) = a_\mathrm{d4}\tanh\left(a_\mathrm{d5}i_\mathrm{s}^d\right) + a_\mathrm{d6}i_\mathrm{s}^d,\\ \widehat{\psi}_\mathrm{s1}^q(i_\mathrm{s}^q) &:= \widehat{\psi}_\mathrm{s}^q(i_\mathrm{s}^d = I_\mathrm{d1}, i_\mathrm{s}^q) = a_\mathrm{q4}\tanh\left(a_\mathrm{q5}i_\mathrm{s}^q\right) + a_\mathrm{q6}i_\mathrm{s}^q,\end{aligned}\right\} \tag{3.9}$$

where $a_\mathrm{d4}, a_\mathrm{d5}, a_\mathrm{d6}$ and $a_\mathrm{q4}, a_\mathrm{q5}, a_\mathrm{q6}$ have similar effects as the parameters defined in (3.7). Then, $\widehat{\psi}_\mathrm{s}^d(i_\mathrm{s}^d, i_\mathrm{s}^q = I_\mathrm{q1})$ and $\widehat{\psi}_\mathrm{s}^q(i_\mathrm{s}^d = I_\mathrm{d1}, i_\mathrm{s}^q)$ in (3.8) can be replaced by $\widehat{\psi}_\mathrm{s1}^d(i_\mathrm{s}^d)$ and $\widehat{\psi}_\mathrm{s1}^q(i_\mathrm{s}^q)$ from (3.9), respectively. Subsequently, the cross-coupling saturation terms $G(I_\mathrm{q1})F'(i_\mathrm{s}^d)$ and $F(I_\mathrm{d1})G'(i_\mathrm{s}^q)$ in (3.8) [as presented in Fig. 3.5(a)] can be obtained by computing the differences $\widehat{\psi}_{\mathrm{s,self}}^d(i_\mathrm{s}^d) - \widehat{\psi}_\mathrm{s1}^d(i_\mathrm{s}^d)$ and $\widehat{\psi}_{\mathrm{s,self}}^q(i_\mathrm{s}^q) - \widehat{\psi}_\mathrm{s1}^q(i_\mathrm{s}^q)$ as follows

$$\left.\begin{aligned}G(I_\mathrm{q1})F'(i_\mathrm{s}^d) &= a_\mathrm{d1}\tanh\left(a_\mathrm{d2}i_\mathrm{s}^d\right) + a_\mathrm{d3}i_\mathrm{s}^d - a_\mathrm{d4}\tanh\left(a_\mathrm{d5}i_\mathrm{s}^d\right) - a_\mathrm{d6}i_\mathrm{s}^d,\\ F(I_\mathrm{d1})G'(i_\mathrm{s}^q) &= a_\mathrm{q1}\tanh\left(a_\mathrm{q2}i_\mathrm{s}^q\right) + a_\mathrm{q3}i_\mathrm{s}^q - a_\mathrm{q4}\tanh\left(a_\mathrm{q5}i_\mathrm{s}^q\right) - a_\mathrm{q6}i_\mathrm{s}^q,\end{aligned}\right\} \tag{3.10}$$

respectively. Integration of both equations yields

$$\left.\begin{aligned}G(I_\mathrm{q1})F(i_\mathrm{s}^d) &= \frac{1}{2}(a_\mathrm{d3} - a_\mathrm{d6})(i_\mathrm{s}^d)^2 + \frac{a_\mathrm{d1}}{a_\mathrm{d2}}\ln\left(\cosh(a_\mathrm{d2}i_\mathrm{s}^d)\right) - \frac{a_\mathrm{d4}}{a_\mathrm{d5}}\ln\left(\cosh(a_\mathrm{d5}i_\mathrm{s}^d)\right),\\ F(I_\mathrm{d1})G(i_\mathrm{s}^q) &= \frac{1}{2}(a_\mathrm{q3} - a_\mathrm{q6})(i_\mathrm{s}^q)^2 + \frac{a_\mathrm{q1}}{a_\mathrm{q2}}\ln\left(\cosh(a_\mathrm{q2}i_\mathrm{s}^q)\right) - \frac{a_\mathrm{q4}}{a_\mathrm{q5}}\ln\left(\cosh(a_\mathrm{q5}i_\mathrm{s}^q)\right),\end{aligned}\right\} \tag{3.11}$$

which clearly gives continuously differentiable functions, as shown in Fig. 3.5(b).

Until now, all parts of the prototype functions are found. The cross-saturation terms $F'(i_\mathrm{s}^d)G(i_\mathrm{s}^q)$

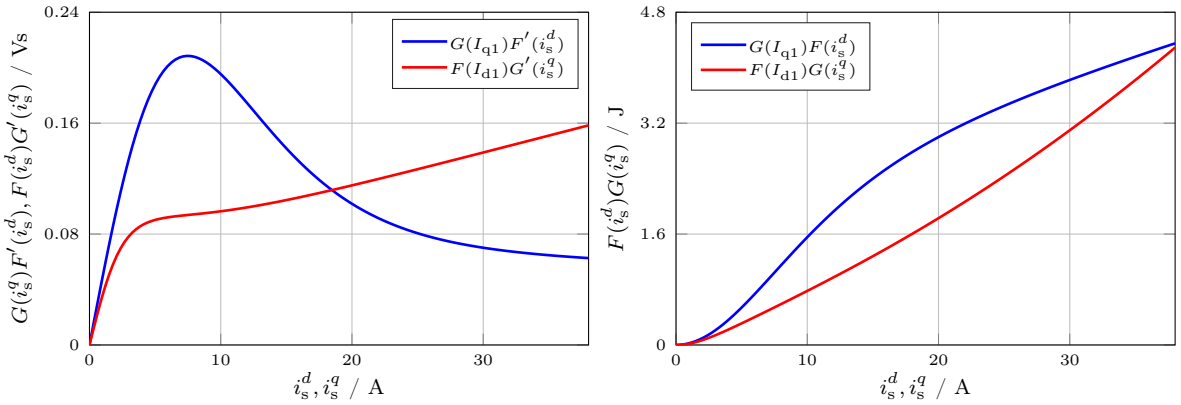

(a) (b)

Figure 3.5: Cross-coupling saturation terms of the proposed analytical flux linkage prototype functions (3.4): (a) $G(I_{q1})F'(i_s^d)$ and $F(I_{d1})G'(i_s^q)$; (b) $G(I_{q1})F(i_s^d)$ and $F(I_{d1})G(i_s^q)$ (where maximal cross-coupling current constants $I_{d1} = I_{q1} = 38$A are selected).

and $F(i_s^d)G'(i_s^q)$ can be acquired by multiplying $G(I_{q1})F'(i_s^d)$ [in (3.10)] & $F(I_{d1})G(i_s^q)$ [in (3.11)] and $F(I_{d1})G'(i_s^q)$ [in (3.10)] & $G(I_{q1})F(i_s^d)$ [in (3.11)], respectively. The entire RSM flux linkage prototype functions as in (3.4) are finally given by [1]

$$\left.\begin{aligned}\widehat{\psi}_s^d(i_s^d, i_s^q) &= \widehat{\psi}_{s,self}^d(i_s^d) - \underbrace{\frac{1}{F(I_{d1})G(I_{q1})}\Big(G(I_{q1})F'(i_s^d)\Big)\Big(F(I_{d1})G(i_s^q)\Big)}_{\overset{(3.5)}{=}\widehat{\psi}_{s,cross}^d(i_s^d,i_s^q)},\\ \widehat{\psi}_s^q(i_s^d, i_s^q) &= \widehat{\psi}_{s,self}^q(i_s^q) - \underbrace{\frac{1}{F(I_{d1})G(I_{q1})}\Big(G(I_{q1})F(i_s^d)\Big)\Big(F(I_{d1})G'(i_s^q)\Big)}_{\overset{(3.5)}{=}\widehat{\psi}_{s,cross}^q(i_s^d,i_s^q)}.\end{aligned}\right\} \tag{3.12}$$

According to the explicit form of the prototype functions (3.12) and the plotted cross-saturation terms in Fig. 3.5, it can be concluded that $F(i_s^d)$ and $G(i_s^q)$ [derived in (3.11)] describe how the cross-coupling currents affect the flux linkage values; whereas $F'(i_s^d)$ and $G'(i_s^q)$ [derived in (3.10)] control the extent of the cross-coupling saturation effect under different current levels and allow to specify the "opening width" of the bell-shaped functions $F(i_s^d)$ and $G(i_s^q)$ as is illustrated in Fig. 3.1(e) and 3.1(f). Note that all equations from (3.10) and (3.11) depend on $F(I_{d1})$ and/or $G(I_{q1})$. However, the product $F(I_{d1})G(I_{q1})$ in (3.12) can be eliminated after a successful fitting process.

3.2.2 Fitting procedure

A fitting procedure is presented, which allows to find proper (optimal) parameters of the proposed analytical flux linkage prototype function. First, in total, four functions – the self saturated terms $\widehat{\psi}_{s,self}^d(i_s^d), \widehat{\psi}_{s,self}^q(i_s^q)$ without the cross saturation effect and the terms $\widehat{\psi}_{s1}^d(i_s^d), \widehat{\psi}_{s1}^q(i_s^q)$ with the cross saturation effect – must be fitted.

To do so, the MATLAB nonlinear regression function *nlinfit* with the Levenberg-Marquardt algorithm (LMA) [127] is adopted for finding proper parameters $a_{d1}, \cdots, a_{d6}$ and $a_{q1}, \cdots, a_{q6}$ in (3.7) and (3.9). The optimal fitting parameters of the prototype functions are found by

minimizing the following four nonlinear least square problems [1]

$$\left.\begin{aligned}\min_{a_{\mathrm{d1}},a_{\mathrm{d2}},a_{\mathrm{d3}}} \sum_{j=1}^{m}\left[\psi_{\mathrm{s}}^{d}(i_{\mathrm{s},j}^{d},0)-\widehat{\psi}_{\mathrm{s,self}}^{d}(i_{\mathrm{s},j}^{d},a_{\mathrm{d1}},a_{\mathrm{d2}},a_{\mathrm{d3}})\right]^{2},\\ \min_{a_{\mathrm{q1}},a_{\mathrm{q2}},a_{\mathrm{q3}}} \sum_{k=1}^{n}\left[\psi_{\mathrm{s}}^{q}(0,i_{\mathrm{s},k}^{q})-\widehat{\psi}_{\mathrm{s,self}}^{q}(i_{\mathrm{s},k}^{q},a_{\mathrm{q1}},a_{\mathrm{q2}},a_{\mathrm{q3}})\right]^{2}\end{aligned}\right\} \tag{3.13}$$

and

$$\left.\begin{aligned}\min_{a_{\mathrm{d4}},a_{\mathrm{d5}},a_{\mathrm{d6}}} \sum_{j=1}^{m}\left[\psi_{\mathrm{s}}^{d}(i_{\mathrm{s},j}^{d},I_{\mathrm{q1}})-\widehat{\psi}_{\mathrm{s1}}^{d}(i_{\mathrm{s},j}^{d},a_{\mathrm{d4}},a_{\mathrm{d5}},a_{\mathrm{d6}})\right]^{2},\\ \min_{a_{\mathrm{q4}},a_{\mathrm{q5}},a_{\mathrm{q6}}} \sum_{k=1}^{n}\left[\psi_{\mathrm{s}}^{q}(I_{\mathrm{d1}},i_{\mathrm{s},k}^{q})-\widehat{\psi}_{\mathrm{s1}}^{q}(i_{\mathrm{s},k}^{q},a_{\mathrm{q4}},a_{\mathrm{q5}},a_{\mathrm{q6}})\right]^{2},\end{aligned}\right\} \tag{3.14}$$

where $i_{\mathrm{s},j}^{d}, i_{\mathrm{s},k}^{q}$ are the j-th and k-th current data points of the real flux linkage values ψ_{s}^{d} and ψ_{s}^{q}, which are used as references. After finding these 12 parameters, the value of coenergy variation $\Delta W_{\mathrm{c}}(I_{\mathrm{d1}},I_{\mathrm{q1}}) = F(I_{\mathrm{d1}})G(I_{\mathrm{q1}})$ can also be acquired by inputting I_{d1} and I_{q1} in (3.11), which is required to be eliminated in (3.12). Finally, the real flux linkages can be approximated by the analytical and (now) parametrized flux linkage prototype functions (3.4).

3.2.3 Approximation results

The first analytical flux linkage prototype function in (3.4) obeys the energy conservation rule and is now used to mimic the magnetic nonlinearity of an RSM. The real flux linkage maps (from FEA) of a custom-built highly nonlinear 9.6 kW RSM (Courtesy of Prof. Maarten Kamper, Stellenbosch University, ZA) are employed as references. Its parameters are collected in Table 3.1 (see RSM#1). The real flux linkage values of the RSM are used to fit the flux linkage prototypes (3.4) by obtaining an optimal parameter set for $a_{\mathrm{d1}},\cdots,a_{\mathrm{d6}}$ and $a_{\mathrm{q1}},\cdots,a_{\mathrm{q6}}$. The fitted parameters are provided in Table 3.2. Due to the symmetry of the flux linkages and the designed prototype functions, only the flux linkage samples in the first quadrant are needed for parameter fitting. The analytical prototype function directly allows to extend the approximation results to the whole operation range, including all four quadrants.

Maximal cross-coupling current constants $I_{\mathrm{d1}} = I_{\mathrm{q1}} = 38\mathrm{A}$ are selected in accordance with the desired approximation range. Ideally, the coenergy variations at the maximum currents, i.e., $\Delta W_{\mathrm{c}}(I_{\mathrm{d1}},I_{\mathrm{q1}}) = F(I_{\mathrm{d1}})G(I_{\mathrm{q1}})$, must be equal in both axes due to the energy conservation rule, as shown in (3.6). However, after fitting, $G(I_{\mathrm{q1}})F(I_{\mathrm{d1}}) = 4.35$ and $F(I_{\mathrm{d1}})G(I_{\mathrm{q1}}) = 4.29$ are obtained, which slightly differ as illustrated in Fig. 3.5(b), although both should equal according to (3.11). So their average value is used in the following. In practice, the small difference may result from numerical inaccuracies in the experimental data and the flux linkage interpolation. Nevertheless, this small difference is still acceptable for the design of the flux linkage prototype functions, as will be shown in the following.

The fitted d-axis flux linkage $\widehat{\psi}_{\mathrm{s}}^{d}$ and q-axis flux linkage $\widehat{\psi}_{\mathrm{s}}^{q}$ are shown in Fig. 3.6(a) and 3.6(b), respectively. It can be seen that both flux linkage maps possess continuous and smooth surfaces due to the continuity of the deisgned prototype functions over the entire current range. Moreover, (very) good approximation results [- - -,- - -,- - -] of the designed self-axis prototype functions (3.7) and (3.9) are confirmed in Fig. 3.1(c) and 3.1(d). On the other hand, under different conditions, Fig. 3.1(e) and 3.1(f) illustrate the capability of the proposed prototype functions to model the

Table 3.1: Key parameters of employed RSMs for fitting the proposed prototype functions.

Parameter	**Symbol**	**RSM#1** (Stellenbosch)	**RSM#2** (Stellenbosch)	**RSM#3** (ABB)
Rated power	P_{R}	9.6 kW	1.5 kW	4.0 kW
Rated speed	$\omega_{\mathrm{m,R}}$	157.1 rad/s	157.1 rad/s	157.1 rad/s
Rated torque	$m_{\mathrm{m,R}}$	61 Nm	10 Nm	25 Nm
Rated current	$\widehat{i}_{\mathrm{s,R}}$	29.7 A	5.3 A	13.3 A
Rated voltage	$\widehat{u}_{\mathrm{s,R}}$	326.6 V	326.6 V	310.3 V
Stator resistance	R_{s}	0.4 Ω	4.1 Ω	1.3 Ω
d-axis flux linkage	ψ_{s}^{d}	$[-1.06, 1.06]$ Vs	$[-1.16, 1.16]$ Vs	$[-1.15, 1.15]$ Vs
q-axis flux linkage	ψ_{s}^{q}	$[-0.48, 0.48]$ Vs	$[-0.48, 0.48]$ Vs	$[-0.35, 0.35]$ Vs
d-axis differential inductance	L_{s}^{d}	$[2.2, 115.7]$ mH	$[34.7, 382.5]$ mH	$[28.1, 249.4]$ mH
q-axis differential inductance	L_{s}^{q}	$[7.4, 46.9]$ mH	$[44.6, 199.5]$ mH	$[16.6, 57.6]$ mH
Cross-coupling differential inductance	L_{s}^{dq}	$[-8.1, 8.1]$ mH	$[-20.1, 20.1]$ mH	$[-11.2, 11.2]$ mH

Table 3.2: Fitted parameters of the proposed flux linkage prototype functions for the employed 9.6 kW RSM.

Model	**Parameters**
RSM I	$a_{\mathrm{d1}} = 0.943, a_{\mathrm{d2}} = 0.138, a_{\mathrm{d3}} = 0.003,$ $a_{\mathrm{d4}} = 0.869, a_{\mathrm{d5}} = 0.092, a_{\mathrm{d6}} = 0.003,$ $a_{\mathrm{q1}} = 0.096, a_{\mathrm{q2}} = 0.403, a_{\mathrm{q3}} = 0.010,$ $a_{\mathrm{q4}} = 0.031, a_{\mathrm{q5}} = 0.105, a_{\mathrm{q6}} = 0.008$
RSM II	$a_{\mathrm{d1}} = 0.943, a_{\mathrm{d2}} = 0.138, a_{\mathrm{d3}} = 0.003,$ $a_{\mathrm{d4}} = 0.029, a_{\mathrm{d5}} = 0.064, a_{\mathrm{d6}} = 0.223, a_{\mathrm{d7}} = 0.101,$ $a_{\mathrm{q1}} = 0.098, a_{\mathrm{q2}} = 0.464, a_{\mathrm{q3}} = 0.010,$ $a_{\mathrm{q4}} = 0.008, a_{\mathrm{q5}} = 0.084, a_{\mathrm{q6}} = 0.227, a_{\mathrm{q7}} = 0.020,$ $k_1 = 33.032, k_2 = 0.581, k_3 = 0.202, k_4 = 3.567$

cross saturation effects and to obey the reciprocity property (3.3).

To quantify the approximation (fitting) accuracy, the normalized approximation error

$$\varepsilon_{\mathrm{s}}^{d/q} := \frac{|\psi_{\mathrm{s}}^{d/q} - \widehat{\psi}_{\mathrm{s}}^{d/q}|}{\psi_{\mathrm{s,max}}^{d/q}} \cdot 100\% \tag{3.15}$$

is introduced, where $\widehat{\psi}_{\mathrm{s}}^{d}$ & $\widehat{\psi}_{\mathrm{s}}^{q}$ are the estimated flux linkages, ψ_{s}^{d} & ψ_{s}^{q} are the real flux linkages and $\psi_{\mathrm{s,max}}^{d}$ & $\psi_{\mathrm{s,max}}^{q}$ are the maximum real values of the d- and q-axis components. Fig. 3.7(a) and 3.7(b) show the normalized errors $\varepsilon_{\mathrm{s}}^{d}$ and $\varepsilon_{\mathrm{s}}^{q}$, respectively. The error plots indicate a fitting

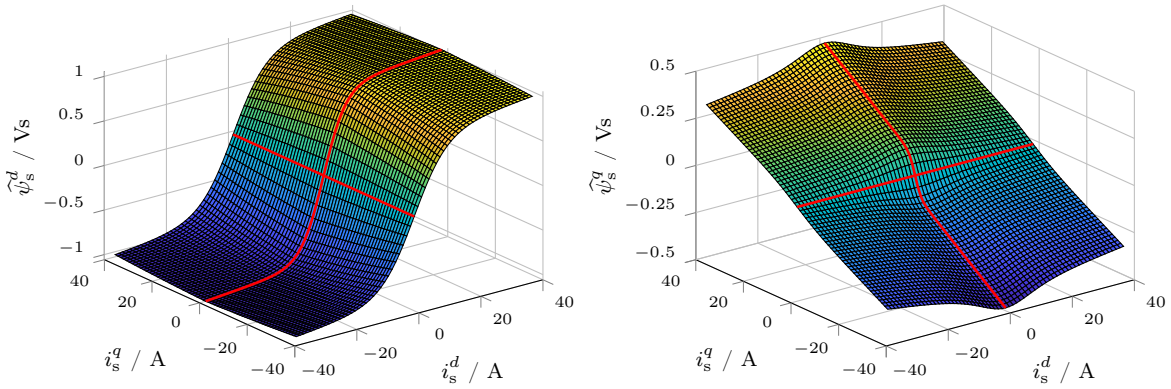

(a) (b)

Figure 3.6: Flux linkage approximation results of a 9.6 kW RSM using the proposed analytical flux linkage prototype functions (3.4): (a) fitted d-axis flux linkage $\widehat{\psi}_\mathrm{s}^d$; (b) fitted q-axis flux linkage $\widehat{\psi}_\mathrm{s}^q$; zero locus $\mathbb{L}_\mathrm{s}^{dq}(L=0)$ [—] is indicated.

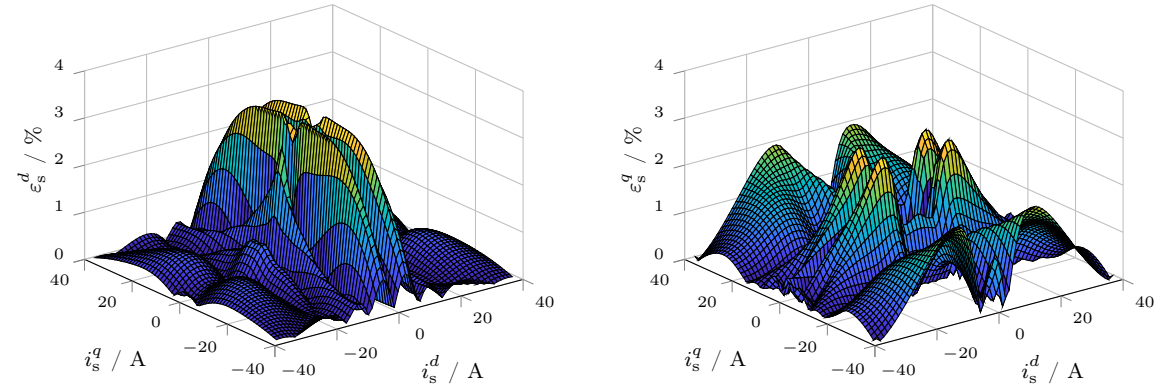

(a) (b)

Figure 3.7: Approximation errors of the proposed analytical flux linkage prototype functions (3.4) compared to the real flux linkage maps (corresponding to Fig. 3.6): (a) normalized d-axis error ε_s^d; (b) normalized q-axis error ε_s^q.

accuracy of at least 96.5 % in the whole current range; therefore, the nonlinear flux linkages of the considered RSM are properly approximated by the proposed flux linkage prototype functions (3.4).

In Fig. 3.9(a), 3.9(b) and 3.9(c), the differential inductances L_s^d, L_s^q and L_s^{dq}, computed by numerical differentiation of the real flux linkages, are shown, respectively. The approximated differential inductances $\widehat{L}_\mathrm{s}^d = \frac{\partial \widehat{\psi}_\mathrm{s}^d(\boldsymbol{i}_\mathrm{s}^{dq})}{\partial i_\mathrm{s}^d}$, $\widehat{L}_\mathrm{s}^q = \frac{\partial \widehat{\psi}_\mathrm{s}^q(\boldsymbol{i}_\mathrm{s}^{dq})}{\partial i_\mathrm{s}^q}$ and $\widehat{L}_\mathrm{s}^{dq} = \frac{\partial \widehat{\psi}_\mathrm{s}^d(\boldsymbol{i}_\mathrm{s}^{dq})}{\partial i_\mathrm{s}^q} = \frac{\partial \widehat{\psi}_\mathrm{s}^q(\boldsymbol{i}_\mathrm{s}^{dq})}{\partial i_\mathrm{s}^d}$, derived by analytical differentiation of the flux linkage prototype functions in (3.4), are shown in Fig. 3.9(d), 3.9(e) and 3.9(f), respectively. Due to the continuous differentiability of the prototype functions, well-fitted and continuous inductances are obtained, which might be used for nonlinear/adaptive current controllers (in Chapter 4) or optimal feedforward torque control (in Chapter 5).

In conclusion, the simple fitting procedure presented here results in good approximation results while solely the four self-axis functions, i.e., (3.13) and (3.14), were fitted separately instead of the entire flux linkage surfaces. Nevertheless, the prototype functions (3.4) incorporate the more complicated parts in (3.11), which is the integration of (3.10). As a consequence, an additional

fitting step, which makes use of a fitting procedure covering the whole flux linkage maps at once, seems promising but requires a relatively long convergence time and might lead to even worse fitting results (at certain current pairs). These two bottlenecks are further studied and overcome in the next sections.

3.3 RSM flux linkage prototype function II

The proposed RSM prototype function I is rather static and lacks flexibility for extension and application to other machines. Therefore, this section presents another improved RSM flux linkage prototype function from the gained knowledge. The RSM in last section is used again to assess the improved prototype function; hence, a comparison with the RSM prototype function I can be conducted. Moreover, in order to prove its generality, flux linkage maps of another two RSMs with different power ratings are approximated.

3.3.1 Analytical prototype function

To easily refer to the modified RSM model in the following derivation, the identical structures of the flux linkage prototypes as in (3.4) are reused, i.e.,

$$\left.\begin{aligned}\widehat{\psi}^d_{\mathrm{s}}(i^d_{\mathrm{s}}, i^q_{\mathrm{s}}) &= \widehat{\psi}^d_{\mathrm{s,self}}(i^d_{\mathrm{s}}) - \widehat{\psi}^d_{\mathrm{s,cross}}(i^d_{\mathrm{s}}, i^d_{\mathrm{s}}),\\ \widehat{\psi}^q_{\mathrm{s}}(i^d_{\mathrm{s}}, i^q_{\mathrm{s}}) &= \widehat{\psi}^q_{\mathrm{s,self}}(i^q_{\mathrm{s}}) - \widehat{\psi}^q_{\mathrm{s,cross}}(i^d_{\mathrm{s}}, i^q_{\mathrm{s}}),\end{aligned}\right\} \tag{3.16}$$

where $\widehat{\psi}^d_{\mathrm{s,cross}}$ and $\widehat{\psi}^q_{\mathrm{s,cross}}$ again represent cross-coupling saturation terms but now are modified to the following more general form [1]

$$\left.\begin{aligned}\widehat{\psi}^d_{\mathrm{s,cross}}(i^d_{\mathrm{s}}, i^q_{\mathrm{s}}) &= \sum_{i=1}^{n} k_i F'_i(i^d_{\mathrm{s}}) G_i(i^q_{\mathrm{s}}) = k_1 F'_1(i^d_{\mathrm{s}}) G_1(i^q_{\mathrm{s}}) + \cdots + k_n F'_n(i^d_{\mathrm{s}}) G_n(i^q_{\mathrm{s}}),\\ \widehat{\psi}^q_{\mathrm{s,cross}}(i^d_{\mathrm{s}}, i^q_{\mathrm{s}}) &= \sum_{i=1}^{n} k_i F_i(i^d_{\mathrm{s}}) G'_i(i^q_{\mathrm{s}}) = k_1 F_1(i^d_{\mathrm{s}}) G'_1(i^q_{\mathrm{s}}) + \cdots + k_n F_n(i^d_{\mathrm{s}}) G'_n(i^q_{\mathrm{s}}),\end{aligned}\right\} \tag{3.17}$$

where k_i is a cross-coupling constant, $F_i(i^d_{\mathrm{s}})$ & $G_i(i^q_{\mathrm{s}})$ describe the cross-coupling effects and $F'_i(i^d_{\mathrm{s}})$ & $G'_i(i^q_{\mathrm{s}})$ control the impact of the cross-coupling effect for different current levels of the prototype function; $F'_i(i^d_{\mathrm{s}}) := \frac{\mathrm{d}}{\mathrm{d}i^d_{\mathrm{s}}} F_i(i^d_{\mathrm{s}})$ and $G'_i(i^q_{\mathrm{s}}) := \frac{\mathrm{d}}{\mathrm{d}i^q_{\mathrm{s}}} G_i(i^q_{\mathrm{s}})$ denote the respective derivatives of the functions $F_i(i^d_{\mathrm{s}})$ and $G_i(i^q_{\mathrm{s}})$. The number n of cross-coupling saturation terms in (3.17) may be chosen arbitrarily to meet given accuracy requirements. With adequately chosen prototype terms, $n = 3$ or $n = 4$ usually gives satisfactory fitting accuracies [1].

The self-axis saturation terms $\widehat{\psi}^d_{\mathrm{s,self}}$ and $\widehat{\psi}^q_{\mathrm{s,self}}$ as introduced in (3.7) will be adopted again. The design of $\widehat{\psi}^d_{\mathrm{s,cross}}$ and $\widehat{\psi}^q_{\mathrm{s,cross}}$ is the main task now. A Gaussian function, which possesses a symmetric and bell-shaped curve, is a good candidate for describing the cross-coupling saturation effect [recall Fig. 3.1(e) and 3.1(f)]. Hence a modified Gaussian function, which is negative and shifted upward, is used here, so the flux linkages can decrease gradually from the origin due to the increase of the cross-coupling current. In order to obtain a better fitting performance, $n = 4$ is chosen; resulting four modified Gaussian functions and cross-coupling saturation terms $F_1(i^d_{\mathrm{s}}), \cdots, F_4(i^d_{\mathrm{s}})$ and $G_1(i^q_{\mathrm{s}}), \cdots, G_4(i^q_{\mathrm{s}})$, which describe how i^d_{s} affects ψ^q_{s} and how i^q_{s} affects

ψ_{s}^{d}, respectively, are chosen as [1]

$$\left.\begin{aligned} F_1(i_{\mathrm{s}}^d) &= 1 - e^{-\left(a_{\mathrm{d4}}\, i_{\mathrm{s}}^d\right)^2}, \cdots, F_4(i_{\mathrm{s}}^d) = 1 - e^{-\left(a_{\mathrm{d7}}\, i_{\mathrm{s}}^d\right)^2}, \\ G_1(i_{\mathrm{s}}^q) &= 1 - e^{-\left(a_{\mathrm{q4}}\, i_{\mathrm{s}}^q\right)^2}, \cdots, G_4(i_{\mathrm{s}}^q) = 1 - e^{-\left(a_{\mathrm{q7}}\, i_{\mathrm{s}}^q\right)^2}, \end{aligned}\right\} \tag{3.18}$$

where $a_{\mathrm{d4}}, a_{\mathrm{d5}}, a_{\mathrm{d6}}, a_{\mathrm{d7}}$ and $a_{\mathrm{q4}}, a_{\mathrm{q5}}, a_{\mathrm{q6}}, a_{\mathrm{q7}}$ control the widths of the corresponding Gaussian functions. The derivatives of (3.18) are given by

$$\left.\begin{aligned} F_1'(i_{\mathrm{s}}^d) &= 2a_{\mathrm{d4}}^2 i_{\mathrm{s}}^d e^{-(a_{\mathrm{d4}} i_{\mathrm{s}}^d)^2}, \cdots, F_4'(i_{\mathrm{s}}^d) = 2a_{\mathrm{d7}}^2 i_{\mathrm{s}}^d e^{-(a_{\mathrm{d7}} i_{\mathrm{s}}^d)^2}, \\ G_1'(i_{\mathrm{s}}^q) &= 2a_{\mathrm{q4}}^2 i_{\mathrm{s}}^q e^{-(a_{\mathrm{q4}} i_{\mathrm{s}}^q)^2}, \cdots, G_4'(i_{\mathrm{s}}^q) = 2a_{\mathrm{q7}}^2 i_{\mathrm{s}}^q e^{-(a_{\mathrm{q7}} i_{\mathrm{s}}^q)^2}. \end{aligned}\right\} \tag{3.19}$$

Note that the extent of the cross-coupling saturation effect clearly varies for different self-axis and cross-coupling currents due to the products $F_i'(i_{\mathrm{s}}^d)G_i(i_{\mathrm{s}}^q)$ and $F_i(i_{\mathrm{s}}^d)G_i'(i_{\mathrm{s}}^q)$ in (3.17).

3.3.2 Fitting procedure

For the more generic RSM flux linkage prototype function II, a modified fitting procedure must be applied. As the self-axis saturation terms $\widehat{\psi}_{\mathrm{s,self}}^{d}$ and $\widehat{\psi}_{\mathrm{s,self}}^{q}$ introduced in (3.7) are used again, also the fitting procedure to find the parameters $a_{\mathrm{d1}}, a_{\mathrm{d2}}, a_{\mathrm{d3}}$ and $a_{\mathrm{q1}}, a_{\mathrm{q2}}, a_{\mathrm{q3}}$ can be reused by solving (3.13). Afterwards, the parameters taking into account the cross-coupling saturation effect in $\widehat{\psi}_{\mathrm{s,cross}}^{d}$ and $\widehat{\psi}_{\mathrm{s,cross}}^{q}$ must be found. The flux linkage curves which contain dominant cross-coupling saturation effects must be extracted as references by subtracting the real flux linkages from the fitted self-axis saturation curves. The two d- and q-axis flux linkage terms must be fitted at the same time by solving the following minimization problem [1]

$$\begin{aligned} \min_{\boldsymbol{a}_{\mathrm{dq}}^{\mathrm{red}}} \sum_{j=1}^{m}\sum_{k=1}^{n} &\left[\psi_{\mathrm{s,cross}}^{d}(i_{\mathrm{s},j}^d, i_{\mathrm{s},k}^q) - \widehat{\psi}_{\mathrm{s,cross}}^{d}(i_{\mathrm{s},j}^d, i_{\mathrm{s},k}^q, \boldsymbol{a}_{\mathrm{dq}}^{\mathrm{red}})\right]^2 \\ &+ \left[\psi_{\mathrm{s,cross}}^{q}(i_{\mathrm{s},j}^d, i_{\mathrm{s},k}^q) - \widehat{\psi}_{\mathrm{s,cross}}^{q}(i_{\mathrm{s},j}^d, i_{\mathrm{s},k}^q, \boldsymbol{a}_{\mathrm{dq}}^{\mathrm{red}})\right]^2, \end{aligned} \tag{3.20}$$

where $\psi_{\mathrm{s,cross}}^{d}$ & $\psi_{\mathrm{s,cross}}^{q}$ are the real cross-coupling saturation flux linkage terms and

$$\boldsymbol{a}_{\mathrm{dq}}^{\mathrm{red}} = (a_{\mathrm{d4}}, a_{\mathrm{d5}}, a_{\mathrm{d6}}, a_{\mathrm{d7}}, a_{\mathrm{q4}}, a_{\mathrm{q5}}, a_{\mathrm{q6}}, a_{\mathrm{q7}}, k_1, k_2, k_3, k_4)^{\top}$$

collects the reduced number of fitting parameters as in (3.17).

In order to compensate for the induced errors by the previously separated fitting procedure and to achieve a better fitting accuracy, the already fitted parameters in $\boldsymbol{a}_{\mathrm{dq}}^{\mathrm{red}}$ are used as initial values (guesses) for another fitting iteration where self-axis *and* cross-coupling terms in (3.16) are fitted at once to find the remaining and the (globally) optimal parameters. The use of the initial values effectively shortens the convergence time of the fitting procedure. The overall minimization problem now is as follows [1]

$$\begin{aligned} \min_{\boldsymbol{a}_{\mathrm{dq}}} \sum_{j=1}^{m}\sum_{k=1}^{n} &\left[\psi_{\mathrm{s}}^{d}(i_{\mathrm{s},j}^d, i_{\mathrm{s},k}^q) - \widehat{\psi}_{\mathrm{s}}^{d}(i_{\mathrm{s},j}^d, i_{\mathrm{s},k}^q, \boldsymbol{a}_{\mathrm{dq}})\right]^2 \\ &+ \left[\psi_{\mathrm{s}}^{q}(i_{\mathrm{s},j}^d, i_{\mathrm{s},k}^q) - \widehat{\psi}_{\mathrm{s}}^{q}(i_{\mathrm{s},j}^d, i_{\mathrm{s},k}^q, \boldsymbol{a}_{\mathrm{dq}})\right]^2, \end{aligned} \tag{3.21}$$

where

$$\boldsymbol{a}_{\mathrm{dq}} = (a_{\mathrm{d1}}, \cdots, a_{\mathrm{d7}}, a_{\mathrm{q1}}, \cdots, a_{\mathrm{q7}}, k_1, k_2, k_3, k_4)^{\top}$$

incorporates now *all* fitting parameters of the flux linkage prototype functions proposed in (3.16).

3.3.3 Approximation results

3.3.3.1 Comparison with the RSM prototype function I

The real RSM introduced in the last section (see RSM#1 in Table 3.1) is reused to evaluate the second RSM flux linkage prototype function. The fitted parameters are listed in Table 3.2. As the fitting results are similar to the results obtained by the RSM flux linkage prototype function I, the approximated flux linkage maps using (3.16) are not plotted again. The normalized errors $\varepsilon_{\mathrm{s}}^{d}$ and $\varepsilon_{\mathrm{s}}^{q}$ are shown in Fig. 3.8(a) and 3.8(b), respectively. Again good fitting accuracies are feasible. In comparison to the RSM prototype function I, both $\varepsilon_{\mathrm{s}}^{d}$ and $\varepsilon_{\mathrm{s}}^{q}$ of the RSM prototype function II are reduced significantly. The cross-coupling saturation effects are approximated in a much better fashion by the four modified Gaussian functions in (3.17). Some error peaks remain but are acceptable.

Besides the flux linkages, in Fig. 3.9(g), 3.9(h) and 3.9(i), the approximated differential inductances $\widehat{L}_{\mathrm{s}}^{d}$, $\widehat{L}_{\mathrm{s}}^{q}$ and $\widehat{L}_{\mathrm{s}}^{dq}$, derived by analytical differentiation of the fitted prototype functions in (3.16), are shown. Due to the generic nature of the chosen prototype functions and the overall fitting process, the differential inductances derived from the RSM prototype function II can represent the peak-like changes of the real differential inductances better than those from the RSM prototype function I. Without any additional design of separate inductance prototype functions, the partial derivatives of the proposed flux linkage prototype functions directly allow to compute analytical approximations of the differential inductances with quite a high accuracy.

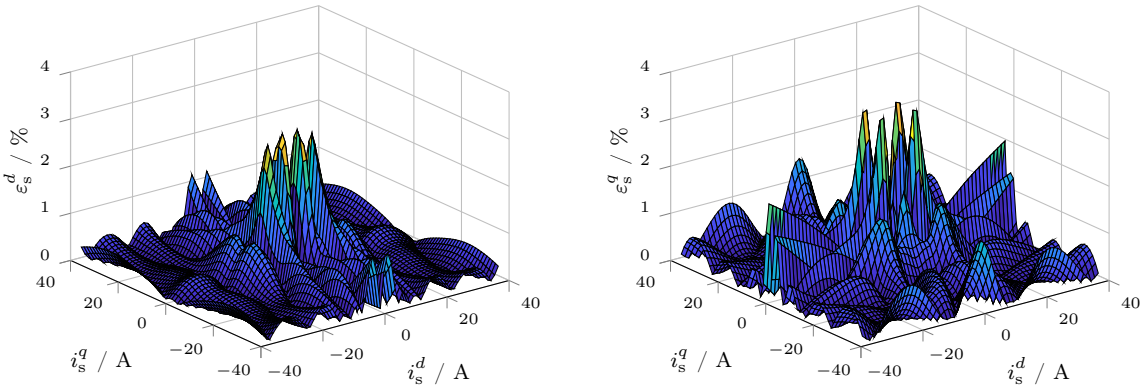

(a) (b)

Figure 3.8: Approximation errors of the proposed analytical flux linkage prototype functions (3.16) compared to the real flux linkage maps: (a) normalized d-axis error $\varepsilon_{\mathrm{s}}^{d}$; (b) normalized q-axis error $\varepsilon_{\mathrm{s}}^{q}$.

In conclusion, both proposed flux linkage approximations can present well the severe magnetic nonlinearity of RSMs, but they can be applied differently because of the different characteristics. The RSM flux model I has a simple process introducing the energy conservation rule (the reciprocity theorem), which contains only the simple (self-axis) prototype functions. On the other hand, the RSM flux model II possesses a more flexible prototype function structure, which still follows the energy conservation rule. Thanks to the general form in (3.17), the number of cross-saturation terms can be chosen arbitrarily according to the requirements induced by different applications. By consisting of not only the reused self-axis functions but also the modified Gaussian functions, the cross-saturation effect of RSMs over the whole operation range can be modeled (more) adequately.

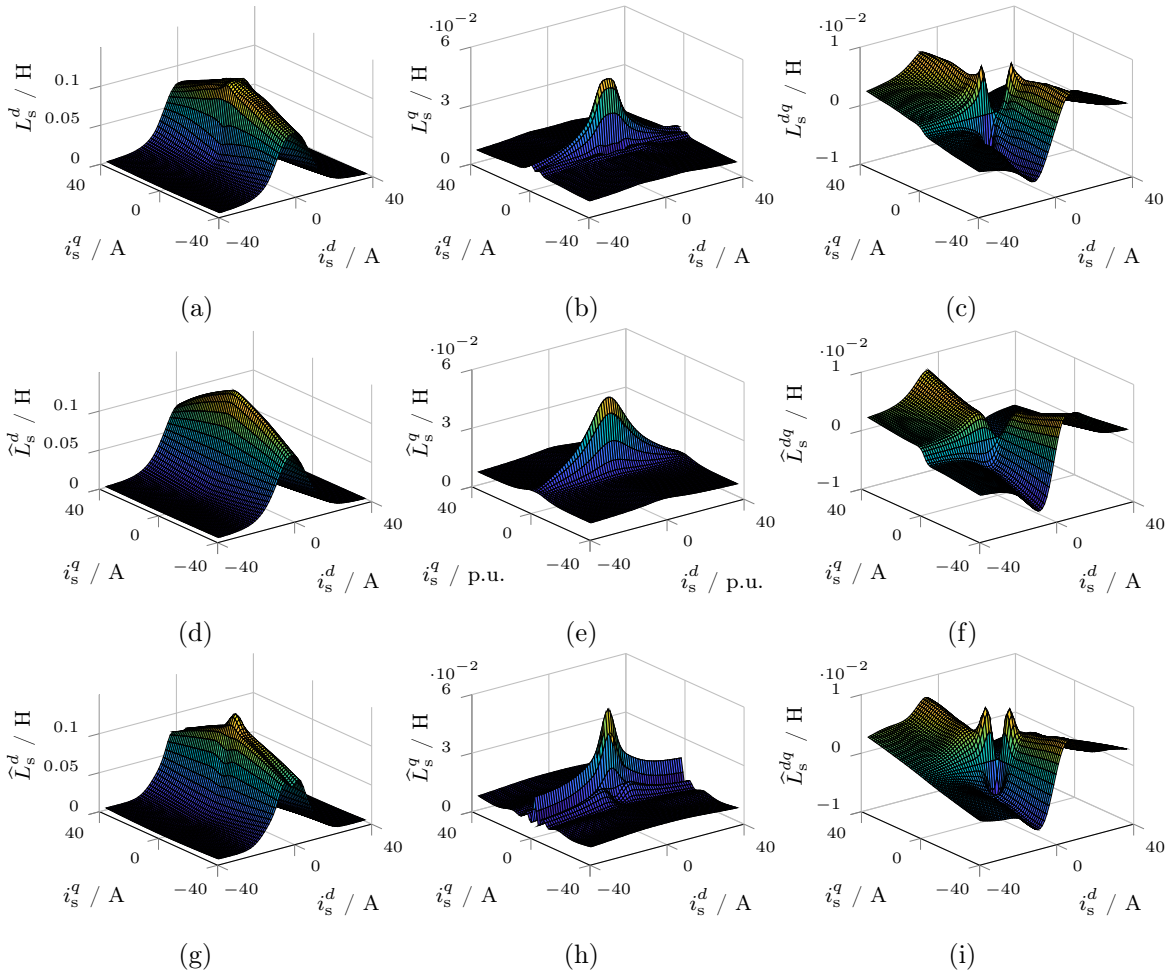

Figure 3.9: Differential inductances of the considered 9.6 kW RSM: (a) real d-axis differential inductance L_s^d; (b) real q-axis differential inductance L_s^q; (c) real cross-coupling differential inductance L_s^{dq}; (d) approximated d-axis differential inductance $\widehat{L}_\mathrm{s}^d$ derived from (3.4); (e) approximated q-axis differential inductance $\widehat{L}_\mathrm{s}^q$ derived from (3.4); (f) approximated cross-coupling differential inductance $\widehat{L}_\mathrm{s}^{dq}$ derived from (3.4); (g) approximated d-axis differential inductance $\widehat{L}_\mathrm{s}^d$ derived from (3.16); (h) approximated q-axis differential inductance $\widehat{L}_\mathrm{s}^q$ derived from (3.16); (i) approximated cross-coupling differential inductance $\widehat{L}_\mathrm{s}^{dq}$ derived from (3.16).

3.3.3.2 Universality assessment

In order to demonstrate the universality of the proposed prototype functions, more machines are employed to further evaluate the improved RSM flux linkage prototype function, including a 1.5 kW RSM (Stellenbosch University) and a 4.0 kW RSM (ABB). Their key machine parameters are collected in Table 3.1 (see RSM#2 and RSM#3, respectively). Different from the previous evaluations using FEM data, their real d-axis flux linkage ψ_s^d and q-axis flux linkage ψ_s^q are experimentally identified by the introduced identification approaches in Chapter 2. For the 1.5 kW RSM, its flux linkages are measured under a constant speed at $\omega_\mathrm{m} = 0.3\omega_\mathrm{m,R}$ (measurement results not shown). Due to the limitation of the machine's maximum stator current, a current measurement range is prescribed, i.e., $\|\boldsymbol{i}_\mathrm{s}^{dq}\| \leq 9.0\,\mathrm{A}$. Whereas, for the 4.0 kW RSM, not only the constant speed method ($\omega_\mathrm{m} = 0.3\omega_\mathrm{m,R}$ and $\|\boldsymbol{i}_\mathrm{s}^{dq}\| \leq 13.3\,\mathrm{A}$) but also the self-identification method at standstill are applied (see [colored surfaces] by the constant speed method and [•] & [•] by the self-identification method in Fig. 2.7).

In total, *three* sets of data (i.e., one for the 1.5 kW RSM and two for the 4.0 kW RSM) are employed as fitting references to fit the developed flux linkage prototype functions (3.16). For the cross-coupling saturation terms $\widehat{\psi}_\mathrm{s,cross}^d$ and $\widehat{\psi}_\mathrm{s,cross}^q$ in (3.17), $n = 3$ is chosen for all fittings, which results in three modified Gaussian functions and 15 function parameters in the optimal parameter set

$$\boldsymbol{a}_\mathrm{dq} = (a_\mathrm{d1}, \cdots, a_\mathrm{d6}, a_\mathrm{q1}, \cdots, a_\mathrm{q6}, k_1, k_2, k_3)^\top.$$

The fitted parameters of the employed 1.5 kW and 4.0 kW RSMs are collected in Table 3.3 and Table 3.4, respectively. Compared to the previously evaluated 9.6 kW RSM ($n = 4$ chosen with 18 parameters in $\boldsymbol{a}_\mathrm{dq}$), fewer Gaussian functions are required to achieve a satisfactory approximation performance. This can be the result of (i) the smaller current measurement ranges and (ii) the influenced magnetic characteristics during the machine manufacturing process (e.g., cutting) [22, Chapter 4], i.e., less severe cross-coupling saturation effects.

First, two fittings from different machines are evaluated using the data sets from the constant speed method, which yields flux linkage maps with a uniform grid as fitting references (see, e.g., [colored surfaces] in Fig. 2.7 for the utilized 4.0 kW RSM). For the 1.5 kW RSM, the fitting results using the flux linkage prototype functions (3.16) are shown in Fig. 3.10. The fitted flux linkages $\widehat{\psi}_\mathrm{s}^d$ & $\widehat{\psi}_\mathrm{s}^q$ and the normalized errors ε_s^d & ε_s^q are shown in Fig. 3.10(a) & 3.10(b) and Fig. 3.10(c) & 3.10(d), respectively. Both error plots exhibit (very) excellent fitting results with less than 1.4 % errors throughout both d- and q-axis flux linkage surfaces. Moreover, by analytical differentiation, the approximated differential inductances $\widehat{L}_\mathrm{s}^d$, $\widehat{L}_\mathrm{s}^q$ and $\widehat{L}_\mathrm{s}^{dq}$ can be derived simply, and they are also plotted in Fig. 3.10(e), 3.10(f) and 3.10(g), respectively.

For the 4.0 kW RSM, the fitting results are shown in Fig. 3.11, including the same quantities as in Fig. 3.10. Again, both error plots ε_s^d and ε_s^q illustrate a good fitting performance with less than 1.0 % errors over the (almost) entire current operation range, except two high peak errors (3.4 %) in ε_s^q. In addition to the high approximation accuracy, the flux linkage prototype functions also allow for correct extrapolation for both, approximated flux linkages *and* differential inductances, outside the fitted current range (i.e., four corners of the uniform measurement grid) with appropriate output values and smooth surfaces, as illustrated in Fig. 3.10 and Fig. 3.11.

Now, by means of the self-identification method, the obtained data points of the flux linkages of the considered 4.0 kW RSM are used to fit (3.16). From Fig. 2.7, the extracted flux linkages ψ_s^d and ψ_s^q from the measurements are reshown in Fig. 3.12(a) and 3.12(b) [•] & [•], respectively. These scattered data points as references may lead to a more challenging fitting. Again, in Fig. 3.12(a) and 3.12(b) [colored surfaces], the fitted flux linkages $\widehat{\psi}_\mathrm{s}^d$ and $\widehat{\psi}_\mathrm{s}^q$ are presented, re-

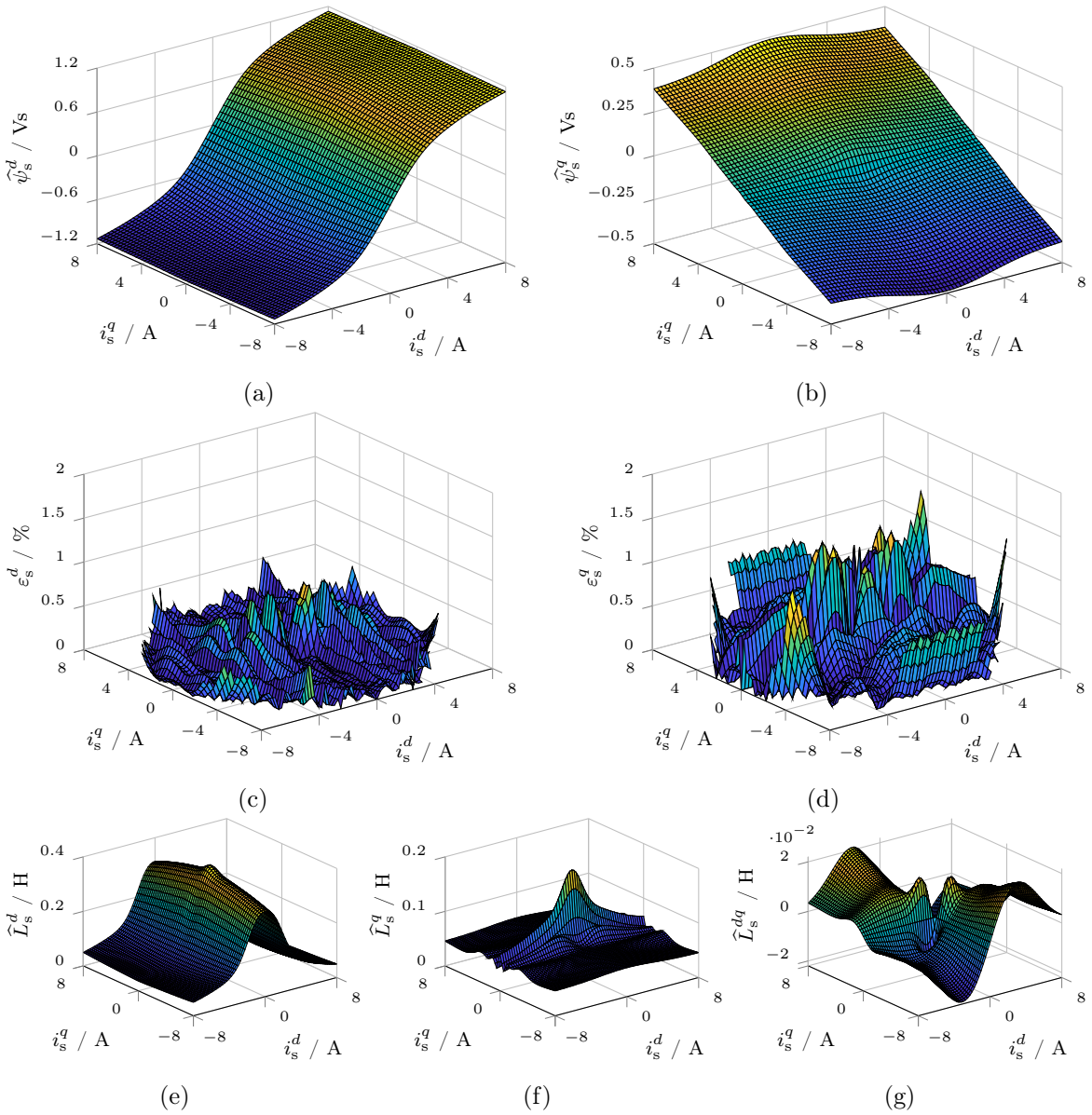

Figure 3.10: Flux linkage approximation results of a 1.5 kW RSM (constant speed) using the flux linkage prototype functions (3.16): (a) fitted d-axis flux linkage $\widehat{\psi}_\mathrm{s}^d$; (b) fitted q-axis flux linkage $\widehat{\psi}_\mathrm{s}^q$; (c) normalized d-axis error ε_s^d; (d) normalized q-axis error ε_s^q; (e) approximated d-axis differential inductance $\widehat{L}_\mathrm{s}^d$; (f) approximated q-axis differential inductance $\widehat{L}_\mathrm{s}^q$; (g) approximated cross-coupling differential inductance $\widehat{L}_\mathrm{s}^{dq}$.

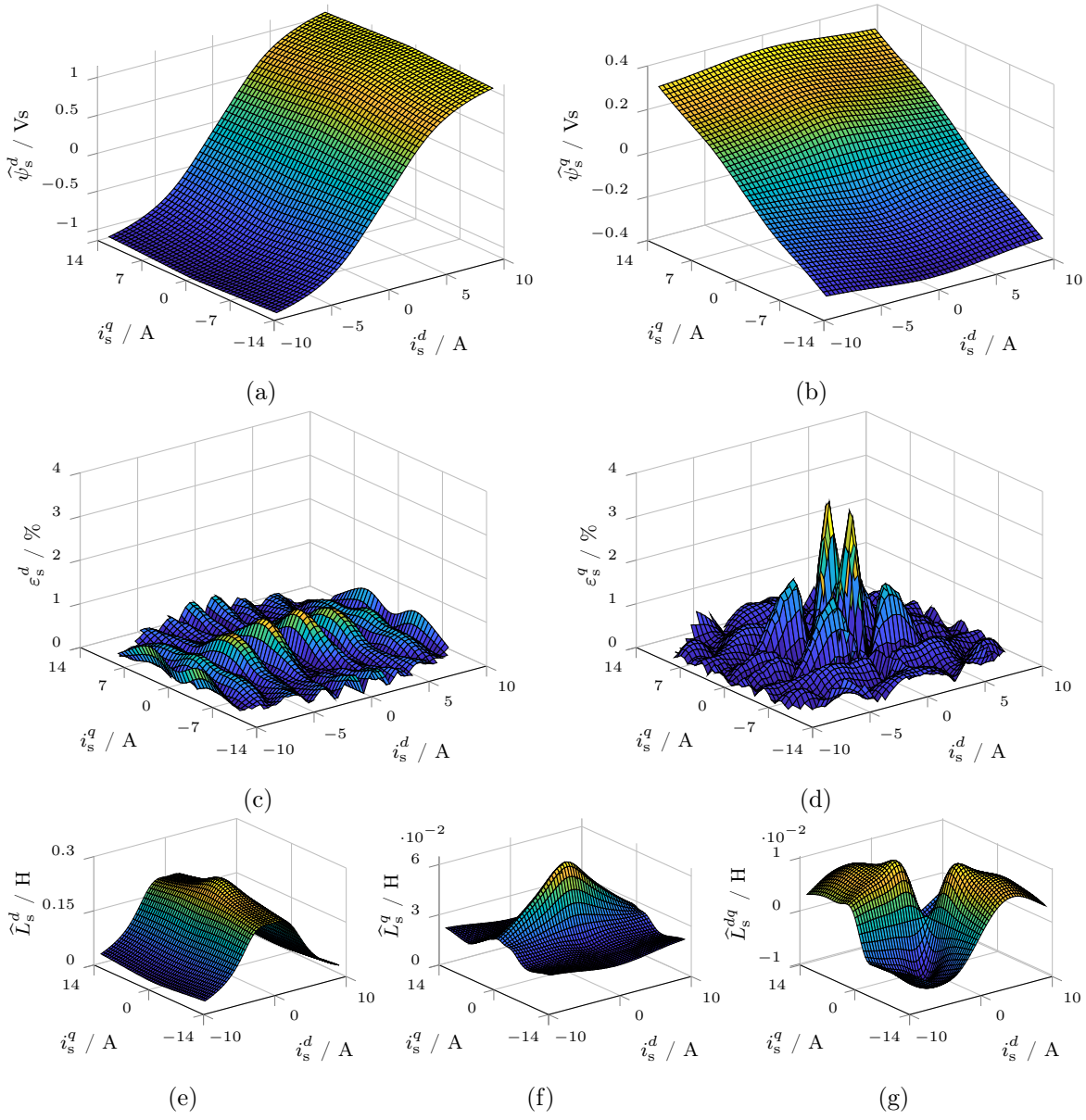

Figure 3.11: Flux linkage approximation results of a 4.0 kW RSM (constant speed) using the flux linkage prototype functions (3.16): (a) fitted d-axis flux linkage $\widehat{\psi}_\mathrm{s}^d$; (b) fitted q-axis flux linkage $\widehat{\psi}_\mathrm{s}^q$; (c) normalized d-axis error ε_s^d; (d) normalized q-axis error ε_s^q; (e) approximated d-axis differential inductance $\widehat{L}_\mathrm{s}^d$; (f) approximated q-axis differential inductance $\widehat{L}_\mathrm{s}^q$; (g) approximated cross-coupling differential inductance $\widehat{L}_\mathrm{s}^{dq}$.

Table 3.3: Fitted parameters of the proposed flux linkage prototype functions (3.16) for the considered 1.5 kW RSM by the constant speed identification method.

Model	**Parameters**
RSM II	$a_{\mathrm{d1}} = 0.889, a_{\mathrm{d2}} = 0.401, a_{\mathrm{d3}} = 0.034,$ $a_{\mathrm{d4}} = 0.226, a_{\mathrm{d5}} = 0.670, a_{\mathrm{d6}} = 0.163,$ $a_{\mathrm{q1}} = 0.061, a_{\mathrm{q2}} = 2.175, a_{\mathrm{q3}} = 0.053,$ $a_{\mathrm{q4}} = 0.058, a_{\mathrm{q5}} = 1.174, a_{\mathrm{q6}} = 0.448,$ $k_1 = 2.495, k_2 = 0.024, k_3 = 0.117$

Table 3.4: Fitted parameters of the proposed flux linkage prototype functions (3.16) for the considered 4.0 kW RSM by different identification approaches (constant speed and self-identification methods).

Model	**Parameters**
RSM II (constant speed)	$a_{\mathrm{d1}} = 1.190, a_{\mathrm{d2}} = 0.213, a_{\mathrm{d3}} = 2.791e\text{-}4,$ $a_{\mathrm{d4}} = 0.146, a_{\mathrm{d5}} = 0.098, a_{\mathrm{d6}} = 0.380,$ $a_{\mathrm{q1}} = 0.121, a_{\mathrm{q2}} = 0.393, a_{\mathrm{q3}} = 0.017,$ $a_{\mathrm{q4}} = 0.084, a_{\mathrm{q5}} = 0.322, a_{\mathrm{q6}} = 0.223,$ $k_1 = 0.953, k_2 = 0.126, k_3 = 0.091$
RSM II (self-identification)	$a_{\mathrm{d1}} = 1.083, a_{\mathrm{d2}} = 0.233, a_{\mathrm{d3}} = 0.013,$ $a_{\mathrm{d4}} = 0.202, a_{\mathrm{d5}} = 0.088, a_{\mathrm{d6}} = 0.357,$ $a_{\mathrm{q1}} = 0.099, a_{\mathrm{q2}} = 1.139, a_{\mathrm{q3}} = 0.018,$ $a_{\mathrm{q4}} = 0.056, a_{\mathrm{q5}} = 0.207, a_{\mathrm{q6}} = 0.518,$ $k_1 = 0.769, k_2 = 0.388, k_3 = 0.084$

spectively. Both fitted flux linkage maps are (almost) identical to the dotted reference samples. They are continuously differentiable with smooth surfaces. Transferring those scattered data points to the flux linkage surfaces allows a complete presentation of the magnetic saturation and cross-coupling effects of the RSM. Due to the generic nature of the prototype functions, additional interpolation is not needed for the scattered samples obtained from the self-identification. Note that the approximation errors are not plotted, as it may lead to an unfair assessment by utilizing the scattered fitting references from the extracted flux linkages with hysteresis effects. Furthermore, with the identical parameter set $\boldsymbol{a}_{\mathrm{dq}}$, the approximated differential inductances $\widehat{L}_{\mathrm{s}}^{d}$, $\widehat{L}_{\mathrm{s}}^{q}$ and $\widehat{L}_{\mathrm{s}}^{dq}$ are shown in Fig. 3.12(c), 3.12(d) and 3.12(e), respectively. The analytical differentiation of (3.16) can be performed conveniently thanks to its continuous differentiability. Contrastly, for the extracted flux linkage samples from the self-identification (see [•] & [•] in Fig. 3.12(a) and 3.12(b)), their scattered nature prohibits numerical differentiation (normally used for LUTs) to derive the differential inductances.

For the identical machine (4.0 kW RSM), by utilizing the fitting references from the different identification approaches, the fitted optimal parameter sets $\boldsymbol{a}_{\mathrm{dq}}$ using the prototype functions (3.16) are collected in Table 3.4. They can be compared with each other to further examine their effectiveness. It can be seen that all fitted function parameters correspond with similar values except for the self-axis parameters a_{d3} and a_{q2}. For a_{d3}, it is relatively small (close to zero) for the constant speed method as a result of the smaller measurement range for ψ_{s}^{d} (as shown in Fig. 2.7(a) [colored surface]), such that the self-saturated ψ_{s}^{d} does not enter the

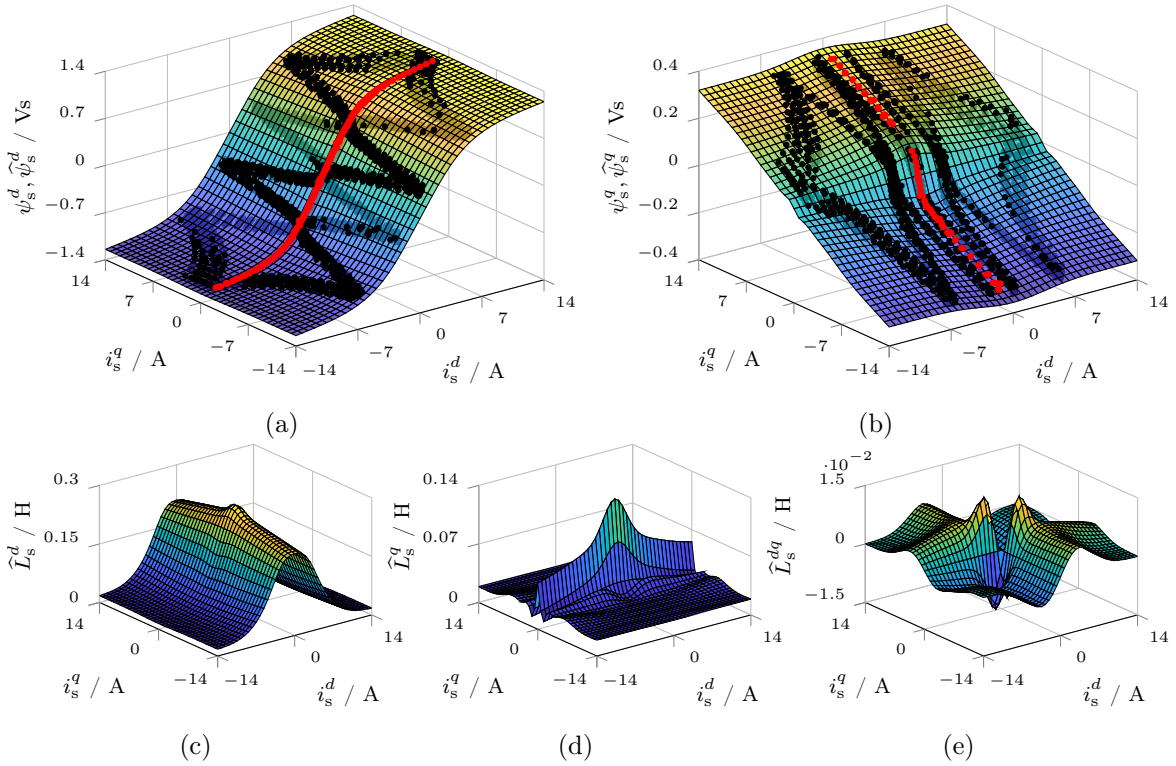

Figure 3.12: Flux linkage approximation results of a 4.0 kW RSM (self-identification) using the flux linkage prototype functions (3.16): (a) real and fitted d-axis flux linkages ψ_s^d and $\widehat{\psi}_\mathrm{s}^d$; (b) real and fitted q-axis flux linkages ψ_s^q and $\widehat{\psi}_\mathrm{s}^q$; (c) approximated d-axis differential inductance $\widehat{L}_\mathrm{s}^d$; (d) approximated q-axis differential inductance $\widehat{L}_\mathrm{s}^q$; (e) approximated cross-coupling differential inductance $\widehat{L}_\mathrm{s}^{dq}$ (where ψ_s^d and ψ_s^q [•] & [•] represent the real flux linkages extracted by the self-identification, and $\widehat{\psi}_\mathrm{s}^d$ and $\widehat{\psi}_\mathrm{s}^q$ [colored surfaces] represent their approximations by the prototype functions).

saturated linear region entirely. Again, a_q2 for the self-identification method is comparatively higher. In Fig. 2.7(b), comparing the extracted ψ_s^q per both identification methods, ψ_s^q by the self-identification (see [•] & [•]) possesses an extremely fast transition to the linear region. This results in a greater (approximated) q-axis differential inductance $\widehat{L}_\mathrm{s}^q$ in the low current area, as shown in Fig. 3.12(d). Despite these minor differences, both fitted flux linkage prototype functions by different identification approaches still provide satisfactory approximation performances by accurately representing the self-axis and cross-coupling saturation effects.

For parameters other than a_d3 and a_q2, a slight difference exists between the two parameter sets; this may be induced due to different speeds during tests, i.e., at standstill for the self-identification method and under a constant speed for the constant speed method. The influence of the rotational speed on the flux linkage measurement is worth further studying in future research.

In summary, the developed RSM flux linkage prototype function II demonstrated its applicability in common use by fitting *three* RSMs with different power ratings from different identification approaches (FEM and experimental measurements). In the case of fittings using flux linkage maps with a uniform grid (i.e., by FEA and the constant speed method), all approximation results achieved excellent accuracies with at least 96.0 % in the whole current operation range. Additionally, the previously addressed issues of scattered data in Chapter 2 were overcome by combining

the self-identification and the prototype functions. The natural inter-/extrapolation capability was hence confirmed due to the physically motivated and analytical prototype functions. As a consequence, the developed prototype functions can serve as a powerful post-processing tool based on few (scattered) data points.

3.4 IPMSM flux linkage prototype function

Now, analytical flux linkage prototype functions for IPMSMs are presented. Due to the existence of the PM flux linkage, an offset is introduced, and the asymmetry of the flux linkages increases. Therefore, developing analytical prototype functions for IPMSMs covering the whole operation range becomes more difficult. In this section, the developed RSM model II is adopted but further modified to accommodate the IPMSM's difficulties.

3.4.1 Analytical prototype function

In [128], the same approach presented with the RSM model I has been applied to PM-assisted RSM (PMaRSM). It is stated that the flux linkages must be modeled separately into two parts when the d-axis (aligned to PM flux) current i_s^d is positive or negative. Compared to PMaRSMs, IPMSMs have higher PM flux linkage values. Its cross-coupling flux linkage curves change throughout the whole current domain, especially when i_s^d is negative. As shown in Fig. 3.4(b), the part of the zero locus $\mathbb{L}_\mathrm{s}^{dq}(L=0)$ [—] parallel to the vertical q-axis converges gradually to a constant negative i_s^d-value of $-24\,\mathrm{A}$. This prevents the RSM model I from being applicable to IPMSMs, because a rectangular region must be defined for deriving the varying coenergy values. Therefore, the flux linkage surfaces must be divided into at least *four* regions, and separate prototype functions must be derived for each region. Hence, the method proposed in [128] is more complicated and impractical for IPMSMs.

The RSM flux model II possesses a greater flexibility; therefore, it is chosen and extended for IPMSMs in the following. As shown in Fig. 3.4(b), different saturation effects on the left and right sides of the vertical zero locus $\mathbb{L}_\mathrm{s}^{dq}(L=0)$ can be observed. The values of the differential inductance L_s^{dq} on the left side are smaller than those on the right side. Thus, due to this "twisted" characteristic of the zero locus $\mathbb{L}_\mathrm{s}^{dq}(L=0)$ and different saturation extents between both sides, the flux linkage surfaces of IPMSMs are cut along the vertical (d-) direction of the zero locus $\mathbb{L}_\mathrm{s}^{dq}(L=0)$ into *two* parts only and modeled separately (see Regions 1 & 2 in Fig. 3.13) [1].

In the first region (reg1), i.e., Region 1 in Fig. 3.13, which is located in the right part of the zero locus $\mathbb{L}_\mathrm{s}^{dq}(L=0)$, the IPMSM flux linkages can be approximated by [1]

$$\left.\begin{aligned}\widehat{\psi}_{\mathrm{s,reg1}}^{d}(i_\mathrm{s}^d, i_\mathrm{s}^q) &= \widehat{\psi}_{\mathrm{s,self1}}^{d}(i_\mathrm{s}^d) - \widehat{\psi}_{\mathrm{s,cross1}}^{d}(i_\mathrm{s}^d, i_\mathrm{s}^q),\\ \widehat{\psi}_{\mathrm{s,reg1}}^{q}(i_\mathrm{s}^d, i_\mathrm{s}^q) &= \widehat{\psi}_{\mathrm{s,self1}}^{q}(i_\mathrm{s}^q) - \widehat{\psi}_{\mathrm{s,cross1}}^{q}(i_\mathrm{s}^d, i_\mathrm{s}^q),\end{aligned}\right\} \tag{3.22}$$

where $\widehat{\psi}_{\mathrm{s,self1}}^{d}$ & $\widehat{\psi}_{\mathrm{s,self1}}^{q}$ and $\widehat{\psi}_{\mathrm{s,cross1}}^{d}$ & $\widehat{\psi}_{\mathrm{s,cross1}}^{q}$ are the self-axis and cross-coupling saturation terms in the first region. Note that the prototype subfunctions $\widehat{\psi}_{\mathrm{s,cross1}}^{d}$ and $\widehat{\psi}_{\mathrm{s,cross1}}^{q}$ have a similar structure as those defined in (3.17).

The IPMSM self-axis flux linkage curves for both axes are shown in Fig. 3.2(c) and 3.2(d). Their similarity in the saturation trends with those of RSMs is obvious and motivates for the reuse and adaption of the RSM prototype functions. Hence, the self-axis saturation terms in (3.22)

can be expressed similarly as follows [1]

$$\left.\begin{aligned}\widehat{\psi}^{d}_{\mathrm{s,self1}}(i^{d}_{\mathrm{s}}) &= a_{\mathrm{d1}}\tanh\Big(a_{\mathrm{d2}}(i^{d}_{\mathrm{s}}-a_{\mathrm{d3}})\Big),\\ \widehat{\psi}^{q}_{\mathrm{s,self1}}(i^{q}_{\mathrm{s}}) &= a_{\mathrm{q1}}\tanh\left(a_{\mathrm{q2}}i^{q}_{\mathrm{s}}\right)+a_{\mathrm{q3}}i^{q}_{\mathrm{s}}.\end{aligned}\right\} \tag{3.23}$$

For $\widehat{\psi}^{d}_{\mathrm{s,self1}}$, the linear function in (3.7) is replaced by a horizontal shift by a_{d3} in the hyperbolic tangent function to take the PM flux linkage (offset) additionally into account. For $\widehat{\psi}^{q}_{\mathrm{s,self1}}$, which means $\widehat{\psi}^{q}_{\mathrm{s}}(i^{d}_{\mathrm{s}}=I_{\mathrm{zl}},i^{q}_{\mathrm{s}})$, I_{zl} changes along the zero locus $\mathbb{L}^{dq}_{\mathrm{s}}(L=0)$ [recall Fig. 3.4(b) and Fig. 3.13]. (3.7) can be reused directly due to the symmetric rotor structure along the q-axis.

For the IPMSM cross-saturation effects, as shown in Fig. 3.2(e) & 3.2(f) and Fig. 3.3, the modified Gaussian function prototypes in (3.18) can be reused as well. However, the maximum or minimum values of ψ^{q}_{s} over i^{d}_{s} occur at negative i^{d}_{s}-values and move gradually to constant asymptote, which can be seen in Fig. 3.2(f) and Fig. 3.4(b). Therefore, in $\widehat{\psi}^{q}_{\mathrm{s,cross1}}$, $F_1,\cdots,F_{\mathrm{n}}$ describe how i^{d}_{s} affects ψ^{q}_{s} and must be shifted horizontally along the d-axis. Due to less nonlinearities compared to RSMs, the cross-coupling prototype functions can be built with $n=2$ and are given by [1]

$$\left.\begin{aligned}F_1(i^{d}_{\mathrm{s}}) &= 1-e^{-\left(a_{\mathrm{d4}}(i^{d}_{\mathrm{s}}-a_{\mathrm{d5}})\right)^2},\ F_2(i^{d}_{\mathrm{s}}) = 1-e^{-\left(a_{\mathrm{d6}}(i^{d}_{\mathrm{s}}-a_{\mathrm{d7}})\right)^2},\\ G_1(i^{q}_{\mathrm{s}}) &= 1-e^{-(a_{\mathrm{q4}}i^{q}_{\mathrm{s}})^2},\ G_2(i^{q}_{\mathrm{s}}) = 1-e^{-(a_{\mathrm{q5}}i^{q}_{\mathrm{s}})^2},\end{aligned}\right\} \tag{3.24}$$

where a_{d5} and a_{d7} shift the functions horizontally, and the other parameters affect the cross-coupling saturation. The differential terms F_1',F_2' and G_1',G_2' can be easily derived.

In the second region (reg2), i.e., Region 2 in Fig. 3.13, which is located in the left part of the zero locus $\mathbb{L}^{dq}_{\mathrm{s}}(L=0)$, the flux linkages can be modeled by [1]

$$\left.\begin{aligned}\widehat{\psi}^{d}_{\mathrm{s,reg2}}(i^{d}_{\mathrm{s}},i^{q}_{\mathrm{s}}) &= \widehat{\psi}^{d}_{\mathrm{s,self2}}(i^{d}_{\mathrm{s}})-\widehat{\psi}^{d}_{\mathrm{s,cross2}}(i^{d}_{\mathrm{s}},i^{q}_{\mathrm{s}}),\\ \widehat{\psi}^{q}_{\mathrm{s,reg2}}(i^{d}_{\mathrm{s}},i^{q}_{\mathrm{s}}) &= \widehat{\psi}^{q}_{\mathrm{s,self1}}(i^{q}_{\mathrm{s}})-\widehat{\psi}^{q}_{\mathrm{s,cross2}}(i^{d}_{\mathrm{s}},i^{q}_{\mathrm{s}}),\end{aligned}\right\} \tag{3.25}$$

which are composed of self-axis $\widehat{\psi}^{d}_{\mathrm{s,self2}}$ & $\widehat{\psi}^{q}_{\mathrm{s,self1}}$ and cross-coupling $\widehat{\psi}^{d}_{\mathrm{s,cross2}}$ & $\widehat{\psi}^{q}_{\mathrm{s,cross2}}$ saturation terms. Both, $\widehat{\psi}^{d}_{\mathrm{s,cross2}}$ and $\widehat{\psi}^{q}_{\mathrm{s,cross2}}$, possess the identical structure as those in (3.17).

Due to the shared contour lines along the zero locus $\mathbb{L}^{dq}_{\mathrm{s}}(L=0)$, $\widehat{\psi}^{q}_{\mathrm{s,self1}}$ from the first region can be reused in (3.25). In contrast to that, $\widehat{\psi}^{d}_{\mathrm{s,self2}}$ must be modeled separately in the second region. Instead of shifting the function as $\widehat{\psi}^{d}_{\mathrm{s,self1}}$ in (3.23), an offset is added in order to achieve a better fitting performance, because ψ^{d}_{s} does only saturate slowly for negative i^{d}_{s} (almost linear behavior). Hence, it is approximated by [1]

$$\widehat{\psi}^{d}_{\mathrm{s,self2}}(i^{d}_{\mathrm{s}}) = a_{\mathrm{d8}}\tanh\left(a_{\mathrm{d9}}i^{d}_{\mathrm{s}}\right)+a_{\mathrm{d10}} \tag{3.26}$$

where a_{d8} and a_{d9} represent the gradual saturation and allow for a smooth transition between the saturated regions, and a_{d10} represents the PM flux linkage offset in the d-direction. By following the same ideas as introduced in (3.24), the cross-saturation terms (for $n=2$) can be modeled as

$$\left.\begin{aligned}F_3(i^{d}_{\mathrm{s}}) &= 1-e^{-\left(a_{\mathrm{d11}}(i^{d}_{\mathrm{s}}-a_{\mathrm{d5}})\right)^2},\ F_4(i^{d}_{\mathrm{s}}) = 1-e^{-\left(a_{\mathrm{d12}}(i^{d}_{\mathrm{s}}-a_{\mathrm{d7}})\right)^2},\\ G_3(i^{q}_{\mathrm{s}}) &= 1-e^{-(a_{\mathrm{q6}}i^{q}_{\mathrm{s}})^2},\ G_4(i^{q}_{\mathrm{s}}) = 1-e^{-(a_{\mathrm{q7}}i^{q}_{\mathrm{s}})^2},\end{aligned}\right\} \tag{3.27}$$

where $a_{\mathrm{d}11}, a_{\mathrm{d}12}$ and $a_{\mathrm{q}6}, a_{\mathrm{q}7}$ control the opening widths of the Gaussian functions. The horizontal shifts $a_{\mathrm{d}5}$ and $a_{\mathrm{d}7}$ in (3.24) are reused here, as the maximum or minimum cross-coupling flux linkages always occur at the shared contour lines between the first and second regions. After computing the derivative terms of (3.27), all the required prototype functions for the IPMSM flux linkage approximation are found.

3.4.2 Fitting procedure

Due to the asymmetry of the IPMSM flux linkage surfaces, its analytical prototype functions are modeled by two separate parts. Therefore, the procedure, which is similar for the RSM flux model II, is invoked and adjusted for the fitting process of self- and cross-coupling saturation terms in both regions. For the self-saturation terms in (3.23) and (3.26), the corresponding parameters must be found by solving the following minimization problems [1]

$$\left.\begin{aligned} &\min_{a_{\mathrm{d}1},a_{\mathrm{d}2},a_{\mathrm{d}3}} \sum_{j=1}^{m} \left[\psi_{\mathrm{s}}^{d}(i_{\mathrm{s},j}^{d}, 0) - \widehat{\psi}_{\mathrm{s,self1}}^{d}(i_{\mathrm{s},j}^{d}, a_{\mathrm{d}1}, a_{\mathrm{d}2}, a_{\mathrm{d}3})\right]^2, \\ &\min_{a_{\mathrm{q}1},a_{\mathrm{q}2},a_{\mathrm{q}3}} \sum_{k=1}^{n} \left[\psi_{\mathrm{s}}^{q}(I_{\mathrm{zl}}, i_{\mathrm{s},k}^{q}) - \widehat{\psi}_{\mathrm{s,self1}}^{q}(i_{\mathrm{s},k}^{q}, a_{\mathrm{q}1}, a_{\mathrm{q}2}, a_{\mathrm{q}3})\right]^2 \end{aligned}\right\} \tag{3.28}$$

and

$$\min_{a_{\mathrm{d}8},a_{\mathrm{d}9},a_{\mathrm{d}10}} \sum_{j=1}^{m} \left[\psi_{\mathrm{s}}^{d}(i_{\mathrm{s},j}^{d}, 0) - \widehat{\psi}_{\mathrm{s,self2}}^{d}(i_{\mathrm{s},j}^{d}, a_{\mathrm{d}8}, a_{\mathrm{d}9}, a_{\mathrm{d}10})\right]^2. \tag{3.29}$$

Afterwards, the reference samples of the cross-coupling saturation surfaces can be obtained according to (3.22) and (3.25). For both regions, the cross-coupling saturation terms with shared parameters can be fitted by minimizing

$$\begin{aligned} \min_{\boldsymbol{a}_{\mathrm{dq}1}} \sum_{j=1}^{m}\sum_{k=1}^{n} &\left[\psi_{\mathrm{s,cross1}}^{d}(i_{\mathrm{s},j}^{d}, i_{\mathrm{s},k}^{q}) - \widehat{\psi}_{\mathrm{s,cross1}}^{d}(i_{\mathrm{s},j}^{d}, i_{\mathrm{s},k}^{q}, \boldsymbol{a}_{\mathrm{dq}1})\right]^2 \\ &+ \left[\psi_{\mathrm{s,cross1}}^{q}(i_{\mathrm{s},j}^{d}, i_{\mathrm{s},k}^{q}) - \widehat{\psi}_{\mathrm{s,cross1}}^{q}(i_{\mathrm{s},j}^{d}, i_{\mathrm{s},k}^{q}, \boldsymbol{a}_{\mathrm{dq}1})\right]^2 \end{aligned} \tag{3.30}$$

and

$$\begin{aligned} \min_{\boldsymbol{a}_{\mathrm{dq}2}} \sum_{j=1}^{m}\sum_{k=1}^{n} &\left[\psi_{\mathrm{s,cross2}}^{d}(i_{\mathrm{s},j}^{d}, i_{\mathrm{s},k}^{q}) - \widehat{\psi}_{\mathrm{s,cross2}}^{d}(i_{\mathrm{s},j}^{d}, i_{\mathrm{s},k}^{q}, \boldsymbol{a}_{\mathrm{dq}2})\right]^2 \\ &+ \left[\psi_{\mathrm{s,cross2}}^{q}(i_{\mathrm{s},j}^{d}, i_{\mathrm{s},k}^{q}) - \widehat{\psi}_{\mathrm{s,cross2}}^{q}(i_{\mathrm{s},j}^{d}, i_{\mathrm{s},k}^{q}, \boldsymbol{a}_{\mathrm{dq}2})\right]^2, \end{aligned} \tag{3.31}$$

where $\psi_{\mathrm{s,cross1}}^{d}$ & $\psi_{\mathrm{s,cross1}}^{q}$ and $\psi_{\mathrm{s,cross2}}^{d}$ & $\psi_{\mathrm{s,cross2}}^{q}$ are the references of cross-coupling flux surfaces in the first and second regions. The parameter vectors

$$\boldsymbol{a}_{\mathrm{dq}1} = (a_{\mathrm{d}4}, a_{\mathrm{d}5}, a_{\mathrm{d}6}, a_{\mathrm{d}7}, a_{\mathrm{q}4}, a_{\mathrm{q}5}, k_1, k_2)^{\top}$$

and

$$\boldsymbol{a}_{\mathrm{dq}2} = (a_{\mathrm{d}5}, a_{\mathrm{d}7}, a_{\mathrm{d}11}, a_{\mathrm{d}12}, a_{\mathrm{q}6}, a_{\mathrm{q}7}, k_3, k_4)^{\top}$$

comprise all fitting parameters of the cross-coupling saturation terms.

Using the obtained parameters above as initial values, the entire analytical functions in (3.22) and (3.25) are now fitted at once in the final fitting step. Consequently, not only the approximation

errors due to the separate fitting in the previous steps can be compensated for, but also the shared parameters $a_{\mathrm{q1}}, a_{\mathrm{q2}}, a_{\mathrm{q3}}$ as in (3.23) and $a_{\mathrm{d5}}, a_{\mathrm{d7}}$ as in (3.24) and (3.27) which are used in both regions can be fitted together to achieve globally optimal values. The final IPMSM flux linkage prototype function parameter set can be obtained by minimizing the following optimization problem [1]

$$\begin{aligned}\min_{\boldsymbol{a}_{\mathrm{dq}}} \sum_{j=1}^{m}\sum_{k=1}^{n} &\left[\psi^{d}_{\mathrm{s,reg1}}(i^{d}_{\mathrm{s},j}, i^{q}_{\mathrm{s},k}) - \widehat{\psi}^{d}_{\mathrm{s,reg1}}(i^{d}_{\mathrm{s},j}, i^{q}_{\mathrm{s},k}, \boldsymbol{a}_{\mathrm{dq}})\right]^2 \\ &+\left[\psi^{q}_{\mathrm{s,reg1}}(i^{d}_{\mathrm{s},j}, i^{q}_{\mathrm{s},k}) - \widehat{\psi}^{q}_{\mathrm{s,reg1}}(i^{d}_{\mathrm{s},j}, i^{q}_{\mathrm{s},k}, \boldsymbol{a}_{\mathrm{dq}})\right]^2 \\ +\sum_{f=1}^{x}\sum_{h=1}^{y} &\left[\psi^{d}_{\mathrm{s,reg2}}(i^{d}_{\mathrm{s},f}, i^{q}_{\mathrm{s},h}) - \widehat{\psi}^{d}_{\mathrm{s,reg2}}(i^{d}_{\mathrm{s},f}, i^{q}_{\mathrm{s},h}, \boldsymbol{a}_{\mathrm{dq}})\right]^2 \\ &+\left[\psi^{q}_{\mathrm{s,reg2}}(i^{d}_{\mathrm{s},f}, i^{q}_{\mathrm{s},h}) - \widehat{\psi}^{q}_{\mathrm{s,reg2}}(i^{d}_{\mathrm{s},f}, i^{q}_{\mathrm{s},h}, \boldsymbol{a}_{\mathrm{dq}})\right]^2,\end{aligned} \tag{3.32}$$

where $\psi^{d}_{\mathrm{s,reg1}}$ & $\psi^{q}_{\mathrm{s,reg1}}$ and $\psi^{d}_{\mathrm{s,reg2}}$ & $\psi^{q}_{\mathrm{s,reg2}}$ are the reference flux linkages in the first and second regions and $(i^{d}_{\mathrm{s},j}, i^{q}_{\mathrm{s},k})$ are the j-th and k-th current data points of the first region, and $(i^{d}_{\mathrm{s},f}, i^{q}_{\mathrm{s},h})$ are the f-th and h-th current data points of the second region. The overall parameter vector

$$\boldsymbol{a}_{\mathrm{dq}} = (a_{\mathrm{d1}}, \cdots, a_{\mathrm{d12}}, a_{\mathrm{q1}}, \cdots, a_{\mathrm{q7}}, k_1, \cdots, k_4)^{\top}$$

consists of 23 fitting parameters in total for d- and q-axis flux linkage prototype functions.

3.4.3 Approximation results

In order to evaluate the developed IPMSM flux linkage prototype functions, the real flux maps (from FEA) of a 3.4 kW IPMSM are employed as references. Its parameters are listed in Table 3.5. Its real flux linkages are used to fit the analytical flux linkage prototype functions in (3.22) and (3.25) and to obtain the optimal parameters $a_{\mathrm{d1}}, \cdots, a_{\mathrm{d12}}$, $a_{\mathrm{q1}}, \cdots, a_{\mathrm{q7}}$ and $k_1, \cdots, k_4$. These fitted parameters are collected in Table 3.6. Due to the existence of a permanent magnet, the IPMSM flux linkage maps are separated into the two regions (Regions 1 & 2 in Fig. 3.13) of the zero locus $\mathbb{L}^{dq}_{\mathrm{s}}(L = 0)$ and modeled separately.

The approximated IPMSM d-axis flux linkage $\widehat{\psi}^{d}_{\mathrm{s}}$ and q-axis flux linkage $\widehat{\psi}^{q}_{\mathrm{s}}$ are shown in Fig. 3.13(a) and 3.13(b), respectively. Its smooth surfaces confirm the continuity and differentiability of the proposed prototype functions. Instead of showing the surfaces of Regions 1 & 2 separately, they are merged to form the entire flux linkage approximations $\widehat{\psi}^{d}_{\mathrm{s}}$ and $\widehat{\psi}^{q}_{\mathrm{s}}$, respectively. The shared boundaries (contour lines) of the zero locus $\mathbb{L}^{dq}_{\mathrm{s}}(L = 0)$ [—] between the first and second regions are shown. Furthermore, the approximated IPMSM flux linkages [- - -,- - -,- - -] plotted in Fig. 3.2(c), 3.2(d), 3.2(e) & 3.2(f) and Fig. 3.3 confirm the outstanding fitting accuracy of the self-axis and cross-coupling saturation terms.

The normalized errors $\varepsilon^{d}_{\mathrm{s}}$ and $\varepsilon^{q}_{\mathrm{s}}$ are shown in Fig. 3.14(a) and 3.14(b), respectively. In both error plots, a very good fitting accuracy with less than 1.7 % approximation errors over the whole current operation range is achieved. Therefore, the effectiveness of the developed analytical flux linkage prototype functions for IPMSMs with proper separation is confirmed.

The differential inductances L^{d}_{s}, L^{q}_{s} and L^{dq}_{s} computed by the real IPMSM flux linkages are presented in Fig. 3.15(a), 3.15(b) and 3.15(c), respectively. In Fig. 3.15(d), 3.15(e) and 3.15(f), the approximated differential inductances $\widehat{L}^{d}_{\mathrm{s}}$, $\widehat{L}^{q}_{\mathrm{s}}$ and $\widehat{L}^{dq}_{\mathrm{s}}$, obtained by analytical differentiation of the flux linkage prototype functions in (3.22) and (3.25), are shown. For $\widehat{L}^{d}_{\mathrm{s}}$, bumpy parts in

the map near the shared boundary can be seen due to the slightly different values at the border of the two regions. In general, with higher flux linkage approximation accuracy, the approximated differential inductances of IPMSM match the real differential inductances much better than those of the RSM approximation.

Table 3.5: Key parameters of employed IPMSM for fitting the proposed prototype functions.

Parameter	**Symbol**	**IPMSM**
Rated power	P_R	3.4 kW
Rated speed	$\omega_\mathrm{m,R}$	576.0 rad/s
Rated torque	$m_\mathrm{m,R}$	6 Nm
Rated current	$\widehat{i}_\mathrm{s,R}$	35.0 A
Rated voltage	$\widehat{u}_\mathrm{s,R}$	130.0 V
Stator resistance	R_s	0.2 Ω
d-axis flux linkage	ψ_s^d	$[-21.4, 63.6]$ mVs
q-axis flux linkage	ψ_s^q	$[-56.4, 56.4]$ mVs
d-axis differential inductance	L_s^d	$[0.20, 1.34]$ mH
q-axis differential inductance	L_s^q	$[0.42, 2.13]$ mH
Cross-coupling differential inductance	L_s^{dq}	$[-0.38, 0.38]$ mH

Table 3.6: Fitted parameters of the proposed flux linkage prototype functions (3.22) and (3.25) for the employed 3.4 kW IPMSM.

Model	**Parameters**
IPMSM	$a_\mathrm{d1} = 0.070, a_\mathrm{d2} = 0.023, a_\mathrm{d3} = -25.404,$ $a_\mathrm{d4} = 0.021, a_\mathrm{d5} = -21.080, a_\mathrm{d6} = 0.012,$ $a_\mathrm{d7} = -0.938, a_\mathrm{d8} = 0.157, a_\mathrm{d9} = 0.009,$ $a_\mathrm{d10} = 0.037, a_\mathrm{d11} = 0.020, a_\mathrm{d12} = 0.048,$ $a_\mathrm{q1} = 0.048, a_\mathrm{q2} = 0.042, a_\mathrm{q3} = 2.285e\text{-}4,$ $a_\mathrm{q4} = 0.018, a_\mathrm{q5} = 0.039, a_\mathrm{q6} = 0.026, a_\mathrm{q7} = 0.052,$ $k_1 = 1.156, k_2 = 0.597, k_3 = 0.680, k_4 = 0.066$

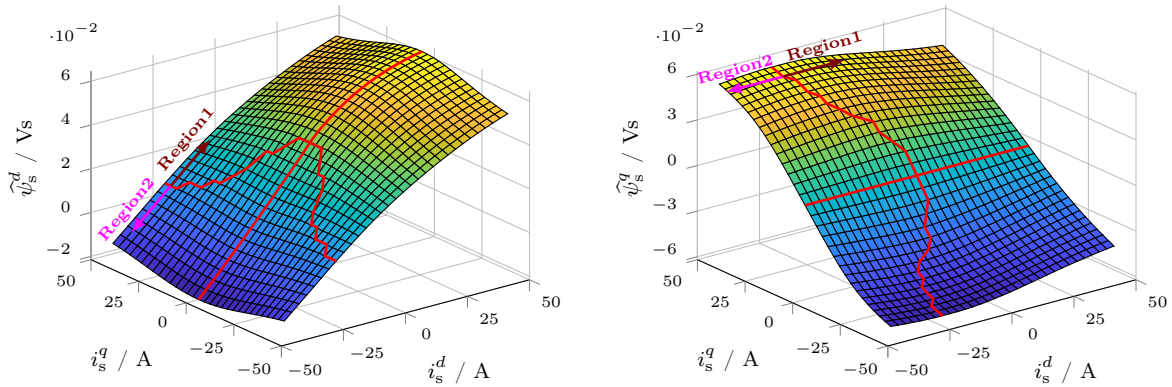

(a) (b)

Figure 3.13: Flux linkage approximation results of a 3.4 kW IPMSM using the proposed analytical flux linkage prototype functions (3.22) and (3.25): (a) fitted d-axis flux linkage $\widehat{\psi}_s^d$; (b) fitted q-axis flux linkage $\widehat{\psi}_s^q$; zero locus $\mathbb{L}_s^{dq}(L=0)$ [—] is indicated.

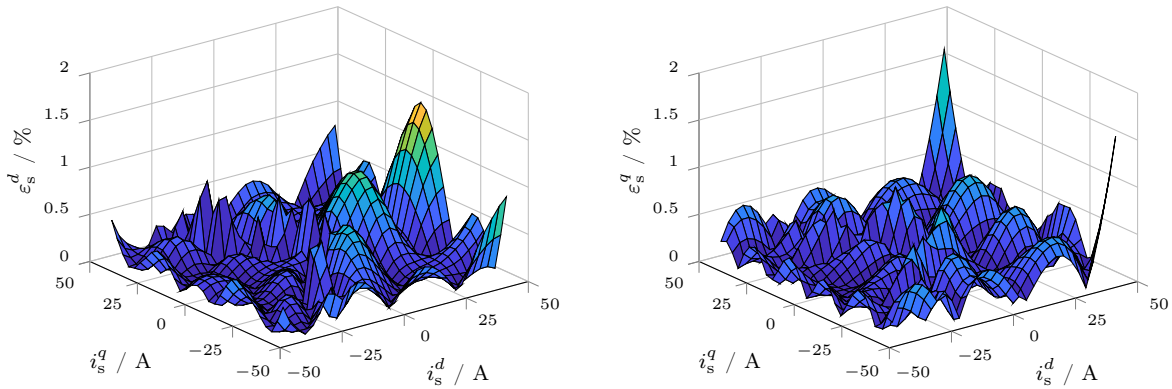

(a) (b)

Figure 3.14: Approximation errors of the proposed analytical flux linkage prototype functions (3.22) and (3.25) compared to the real flux linkage maps (corresponding to Fig. 3.13): (a) normalized d-axis error ε_s^d; (b) normalized q-axis error ε_s^q.

3.5 Discussion and comparison with other approximation methods

This section discusses and compares important aspects of prototype functions used in the literature in order to show the potential of the developed flux linkage prototype functions. In Table 3.7, a comparison of key characteristics/properties of different prototype functions is shown. The checkmark (✓) indicates that the characteristic/property is covered, whereas the cross (×) indicates that the characteristic/property is *not* covered in the respective publication.

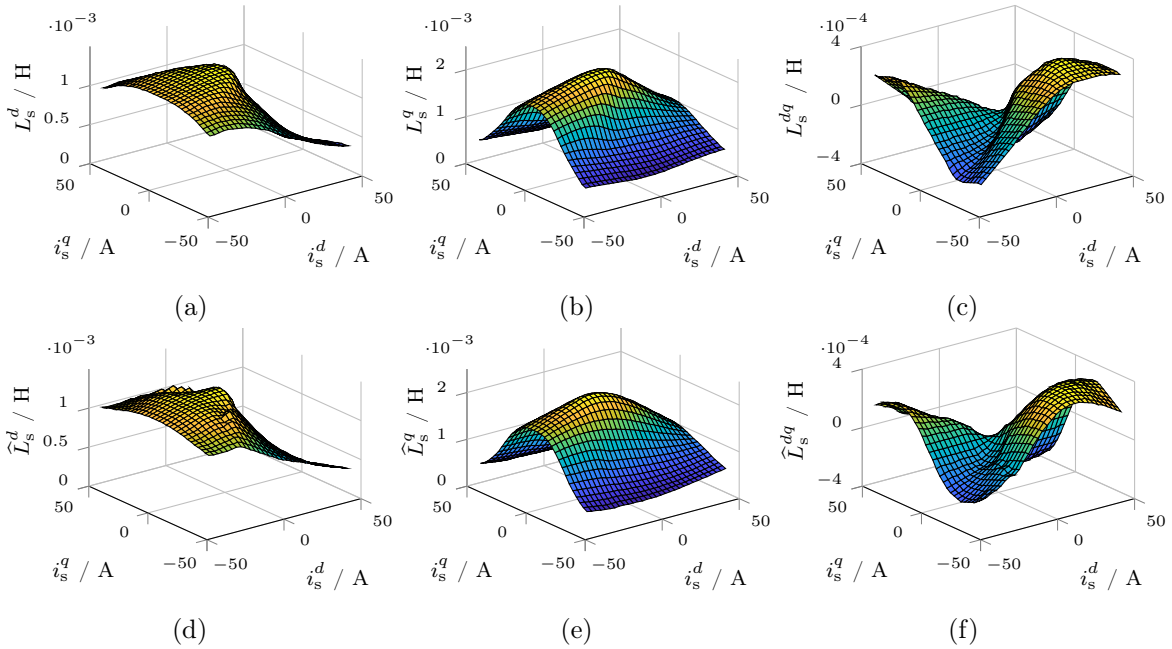

Figure 3.15: Differential inductances of the considered 3.4 kW IPMSM: (a) real d-axis differential inductance L_s^d; (b) real q-axis differential inductance L_s^q; (c) real cross-coupling differential inductance L_s^{dq}; (d) approximated d-axis differential inductance $\widehat{L}_\mathrm{s}^d$ derived from (3.22) and (3.25); (e) approximated q-axis differential inductance $\widehat{L}_\mathrm{s}^q$ derived from (3.22) and (3.25); (f) approximated cross-coupling differential inductance $\widehat{L}_\mathrm{s}^{dq}$ derived from (3.22) and (3.25).

Table 3.7: Comparison of key characteristics/properties of different prototype functions found in literature.

Method	**Flux linkage maps**	**Energy conservation**	**Differentiability**	**Over-range capability**	**Extensibility**
Current bivariate polynomial [67]	×	✓	×	✓	✓
Modified power function [70, 71]	×	✓	×	✓	×
High-order polynomial [66]	× (1D)	×	(✓)	×	✓
Piece-wise function [72]	× (1D)	×	×	✓	×
Flux bivariate polynomial [68]	✓	×	✓	×	×
Flux Prototype [73]	✓	✓	×	✓	×
ANN training [76]	✓	×	✓	×	✓
Prototypes in this chapter	✓	✓	✓	✓	✓

1. **Flux linkage maps:** Current maps $\boldsymbol{i}_\mathrm{s}^{dq}(\boldsymbol{\psi}_\mathrm{s}^{dq})$, which use the flux linkages as state variables, are more common [67, 70, 71] than flux linkage maps. The flux-to-current curves saturate similarly as a polynomial with an odd power number. This property of the current maps motivates for the widespread utilization of polynomials as prototype functions. However, the machine's stator currents are measured in almost every application. Therefore, flux linkage maps $\boldsymbol{\psi}_\mathrm{s}^{dq}(\boldsymbol{i}_\mathrm{s}^{dq})$ are more practical. In both [66, 72], one-dimensional (1D) flux linkage curves (lines), i.e., $\psi_\mathrm{s}^{d}(i_\mathrm{s}^{d})$ and $\psi_\mathrm{s}^{q}(i_\mathrm{s}^{q})$, are developed. Therefore, the two-dimensional (2D) flux linkage maps (surfaces) cannot be represented by *one* function each. They can only be approximated line by line for different but constant cross-coupling currents (which requires LUT-like interpolation methods). In contrast, 2D flux linkage prototype functions, dependent on both d- and q-axis currents, are developed in [68, 73, 76]. Rather simple bivariate quadratic polynomial functions are utilized to approximate the flux linkages of PMSMs in [68]; however, due to their low equation order, the functions require a separate fitting for each of the four quadrants and are not applicable for highly nonlinear RSMs. In [73], by designing a prototype function for the coenergy variation, then flux linkage prototypes for RSMs are derived subsequently. Its insufficient fitting accuracy can be seen in the differential inductance plots with unnatural and unsmooth surfaces. Artificial neural networks (ANNs) [76] result in the most complex and recursively defined mathematical expressions, which cause a high computational burden similar to LUT-based methods. Compared to the above-mentioned methods, the proposed flux linkage prototype functions can easily be applied, e.g., (i) to compensate for machine nonlinearities, (ii) to implement nonlinear/adaptive current controllers or (iii) optimal feedforward torque control.

2. **Energy conservation:** With the consideration of energy conservation (reciprocity rule), the proposed prototype functions can directly represent physical properties and reduce the number of required parameters for fitting by sharing common parameters along both axes. In Table 3.7, it can be seen that only current prototype functions consider the reciprocity rule. In contrast to that, other available flux linkage prototype functions, such ANNs [76] or flux bivariate polynomials [68], do not obey it and thus require a larger number of parameters to approximate the entire flux linkage maps, except for [73]. The 7th-order polynomials proposed in [66] allow to approximate the self-axis flux linkage curves of SPMSMs (which possess an almost linear magnetic behavior without saturation), but different cross-coupling current constants must be found to achieve an acceptable fitting accuracy over the whole current range. Nevertheless, a two-dimensional function is not obtained, so the reciprocity rule is violated.

3. **Differentiability (with respect to the self-axis and cross-coupling currents)**: To simplify the fitting process, prototype functions often approximate the non-saturated regions and the saturated regions separately and/or contain non-differentiable absolute values and sign functions of the currents [70–73] and, therefore, are not globally continuously differentiable. Moreover, all approaches which approximate the currents as functions of the flux linkages (current maps) [67, 70, 71] are not differentiable with respect to the currents. Furthermore, the flux linkage prototype functions proposed in [66, 72] are composed of several segments with different cross-coupling current sets. Besides, single-variant polynomials as in [66] can only be seen as quasi-differentiable (with respect to the self-axis current), and differential cross-coupling inductances cannot be derived as an analytical differentiation is not feasible (with respect to the cross-coupling current). Consequently, discontinuous functions are obtained which do not allow to analytically derive or compute (continuously) differential inductances. ANNs [76] (with Gaussian-like activation functions) or flux bivariate polynomials [68] are clearly continuously differentiable. However,

both do not allow to represent the physically meaningful differential inductances properly, as the reciprocity rule does not hold. The proposed flux linkage prototype functions are globally continuously differentiable due to their physics-based design.

4. **Over-range (extrapolation) capability:** The fitting with power functions [70, 71], polynomials [66–68], piece-wise continuous functions [72] or ANNs [76] usually requires many parameters to minimize the approximation error globally. Nevertheless, the resulting and parametrized prototype functions may produce severe inaccuracies or even oscillations, when the input currents are outside the range of the used fitting samples or training data. Conversely, if the proposed prototype functions are appropriately designed, these problems will not arise. For example, the developed flux linkage prototype functions allow for correct extrapolation for both, approximated flux linkages *and* differential inductances, outside the fitted current range, which is not (directly) feasible with other existing solutions. Moreover, they can even be employed in post-processing for any parameter identification methods, owing to the natural inter-/extrapolation capability.

5. **Extensibility:** The proposed physically motivated prototype functions are capable of approximating flux linkages of all types of synchronous machines, as their generic design is based on physical and intrinsic magnetic properties of real flux linkages. Power functions [70, 71], polynomials [66–68], piece-wise continuous functions [72] or ANNs [76] cannot cover different machine types as easily as many redundant parameters must be fitted. For example, in [67], current bivariate polynomials must be extended by a constant to cover the offset effect due to permanent magnets in IPMSMs. However, only two quadrants with positive i_s^d are considered; hence, not the full operation range is covered. The available methods are not as practical as the proposed generic function prototypes, when the flux linkages of different SMs should be approximated with one type of prototype functions.

In summary, in contrast to the proposed prototype functions, the existing flux linkage (or current) prototype functions are often expressed in complicated forms and lack of generic expressions to cover all relevant physical properties of real flux linkages (see above). To overcome this bottleneck, the physically motivated and analytical flux linkage prototype functions were developed being capable of approximating the flux linkages of any SM in an intrinsic and generic form. The proposed continuously differentiable prototype functions can represent typical magnetic saturation effects very well. Moreover, the differential inductances can be easily computed by computing the respective partial derivatives analytically. Finally, thanks to the consideration of energy conservation, the developed prototype functions have physical meaning and make redundant parameters obsolete.

Chapter 4

Nonlinear current control

Based on [47], a nonlinear current control system of reluctance synchronous machines (RSMs) is developed in combination with analytical flux linkage prototype functions. For highly nonlinear machines, such as RSMs, the magnetic characteristics change significantly throughout the whole operation range due to saturation and cross-coupling effects. Consequently, it is essential to adapt the current controller tuning online in order to achieve a fast and accurate tracking performance [46, 83–85]. The proposed current controllers are derived based on the system theoretic concept of the exact input/output (I/O) linearization of the current dynamics. Therefore, the nonlinear control system is simplified to an integrator which, in combination of proportional-integral (PI) controllers, can be tuned by means of pole placement similar to a phase-locked loop (PLL). For I/O linearization and control, the magnetic saturation and cross-coupling effects in the flux linkages and the differential inductances must be considered, which is done by the utilization of analytical flux linkage prototype functions instead of lookup tables (LUTs). As already demonstrated in the preceding chapter, the introduced flux linkage prototype functions possess a very high approximation accuracy, continuity and differentiability over the entire operation range. The performance of the developed nonlinear current control system is validated by both, simulation and experimental results, for a highly nonlinear RSM. The results underpin the very fast and accurate tracking performance of the nonlinear I/O control system.

In this chapter, the introduced nonlinear current control system is based on [47], which has been combined with the flux linkage prototype functions for the first time in [2]. In Section 4.1, the control problem and objective of the nonlinear current control system are first stated. After that, in Section 4.2, a nonlinear controller design based on I/O linearization is presented. In Section 4.3, the implementation for simulations and experiments is introduced. Eventually, in Section 4.4, both simulative and experimental results are provided to prove the effectiveness of the proposed method.

4.1 Problem statement

The control objective of the nonlinear current controllers is stable, fast and accurate tracking of stator currents $\boldsymbol{i}_\mathrm{s}^{dq} := (i_\mathrm{s}^d, i_\mathrm{s}^q)^\top$ for given current references $\boldsymbol{i}_\mathrm{s,ref}^{dq} := (i_\mathrm{s,ref}^d, i_\mathrm{s,ref}^q)^\top$ (e.g., obtained by optimal feedforward torque control methods, which will be introduced in the next chapter). Moreover, in order to allow for a simple design of the outer (speed and/or position) control loops, the closed-loop current dynamics must be identical throughout the whole operation range.

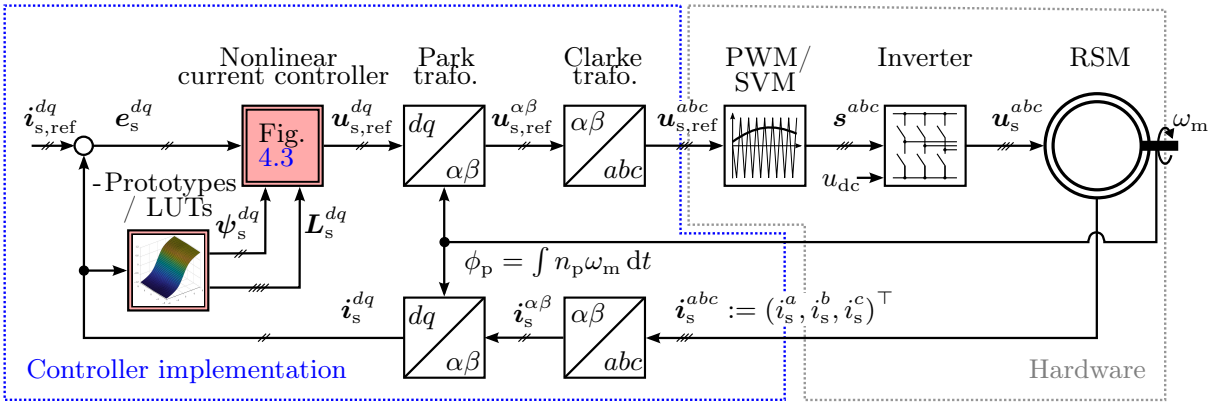

Figure 4.1: Block diagram of the proposed current control system for RSMs with flux linkage prototype functions or LUTs (based on Fig. 6.44 in [47]).

Recalling from (2.10), the nonlinear current dynamics of RSMs is given by

$$\tfrac{\mathrm{d}}{\mathrm{d}t}\boldsymbol{i}_\mathrm{s}^{dq} = \boldsymbol{L}_\mathrm{s}^{dq}(\boldsymbol{i}_\mathrm{s}^{dq})^{-1} \cdot \Big[\boldsymbol{u}_\mathrm{s}^{dq} - R_\mathrm{s}\boldsymbol{i}_\mathrm{s}^{dq} - \omega_\mathrm{p}\boldsymbol{J}\boldsymbol{\psi}_\mathrm{s}^{dq}(\boldsymbol{i}_\mathrm{s}^{dq})\Big], \tag{4.1}$$

where it is coupled due to the inverse inductance $L_\mathrm{s}^{dq}(\boldsymbol{i}_\mathrm{s}^{dq})^{-1}$ but also due to the back electromotive force (EMF) term $\omega_\mathrm{p}\boldsymbol{J}\boldsymbol{\psi}_\mathrm{s}^{dq}(\boldsymbol{i}_\mathrm{s}^{dq})$. To alleviate the highly nonlinear characteristics of RSMs, a current control method based on the input-output linearization is proposed and will be explained thoroughly in the upcoming section.

The block diagram of the proposed nonlinear current control system for RSMs is illustrated in Fig. 4.1. The controller implementation is done in the reduced synchronously rotating (d,q)-reference frame. The nonlinear current controller block is highlighted with shaded double frames, referred to as the controller structure to be presented (as shown in Fig. 4.3), or replaced by other effective current control methods. Not only current control errors $\boldsymbol{e}_\mathrm{s}^{dq} := \boldsymbol{i}_\mathrm{s,ref}^{dq} - \boldsymbol{i}_\mathrm{s}^{dq}$ but also flux linkages $\boldsymbol{\psi}_\mathrm{s}^{dq}$ and differential inductances $\boldsymbol{L}_\mathrm{s}^{dq}$ must be provided, so the controllers can output the voltage references $\boldsymbol{u}_\mathrm{s,ref}^{dq} := (u_\mathrm{s,ref}^d, u_\mathrm{s,ref}^q)^\top$. Then, the generated references $\boldsymbol{u}_\mathrm{s,ref}^{dq}$ are transformed by the inverse Park and Clarke transformation in order to obtain the voltage references in the (α,β)-reference frame and in the (a,b,c)-reference frame, respectively, i.e., $\boldsymbol{u}_\mathrm{s,ref}^{\alpha\beta} := (u_\mathrm{s,ref}^\alpha, u_\mathrm{s,ref}^\beta)^\top$ and $\boldsymbol{u}_\mathrm{s,ref}^{abc} := (u_\mathrm{s,ref}^a, u_\mathrm{s,ref}^b, u_\mathrm{s,ref}^c)^\top$. With the help of pulse width modulation (PWM) or space vector modulation (SVM), these voltage references can be converted into the required pulse pattern $\boldsymbol{s}^{abc} := (s^a, s^b, s^c)^\top \in \{0,1\}^3$ for the voltage source inverter, such that the three-phase stator voltages $\boldsymbol{u}_\mathrm{s}^{abc} := (u_\mathrm{s}^a, u_\mathrm{s}^b, u_\mathrm{s}^c)^\top$ of RSM are produced according to the desired references $\boldsymbol{u}_\mathrm{s,ref}^{abc}$. The three-phase stator currents $\boldsymbol{i}_\mathrm{s}^{abc} := (i_\mathrm{s}^a, i_\mathrm{s}^b, i_\mathrm{s}^c)^\top$ and the mechanical angle ϕ_m of RSM are fed back for the controller implementation. With the Park transformation angle ϕ_p, the currents $\boldsymbol{i}_\mathrm{s}^{abc}$ are transformed into the currents $\boldsymbol{i}_\mathrm{s}^{dq}$ in the (d,q)-reference frame.

In order to achieve the defined control objective, a few considerations must be taken into account while developing the nonlinear current control system:

1. The modeling correctness must be ensured in accordance with the revisited machine model and current dynamics in Chapter 2. Inappropriate model simplification, e.g., assuming constant machine parameters and/or neglecting the magnetic saturation and cross-coupling effects, may lead to unsatisfactory control performance.

2. Resistance R_s and flux linkages $\boldsymbol{\psi}_\mathrm{s}^{dq} := (\psi_\mathrm{s}^d, \psi_\mathrm{s}^q)^\top$ [which can be obtained by finite element

analysis (FEA) or measurements] must be known, as a model-based control method will be developed. In addition, at least two phases of the stator currents $\boldsymbol{i}_\mathrm{s}^{abc}$, mechanical angle ϕ_m and mechanical angular velocity ω_m are available for feedback.

3. Nonlinear current-dependent flux linkages $\boldsymbol{\psi}_\mathrm{s}^{dq}(\boldsymbol{i}_\mathrm{s}^{dq})$ are continuously differentiable functions of the stator currents $\boldsymbol{i}_\mathrm{s}^{dq}$, so the differential inductances $\boldsymbol{L}_\mathrm{s}^{dq}(\boldsymbol{i}_\mathrm{s}^{dq})$ can be derivable. For the implementation in simulations and experiments, the flux linkages of the employed RSM are further augmented with various rotational speeds. Their position or temperature dependence is neglected.

4. Nonlinear machine characteristics can be stored either in LUTs or represented by analytical prototype functions (introduced in Chapter 3), which are again highlighted with shaded double frames in Fig. 4.1.

4.2 Current controller design

In this section, the nonlinear controller design based on exact input-output (I/O) linearization and the tuning of the PI controller with anti-windup are discussed. After I/O linearization, the PI controller design is independent of the nonlinear machine parameters.

4.2.1 PI controller with anti-windup

It is well-known that PI(D) controllers may encounter integral windup due to actuator saturation of the plant. This causes large overshoots and/or oscillations in the closed-loop system response. To prevent the windup problem, a simple and effective anti-windup method utilizing conditional integration [129] is applied. A compact state-space description of the PI controller with anti-windup is given by [47]

$$\left.\begin{aligned} \tfrac{\mathrm{d}}{\mathrm{d}t}\boldsymbol{\xi}_\mathrm{i}^{dq} &= f_\mathrm{aw}(\widehat{u}, \boldsymbol{u}_\mathrm{s,pi}^{dq})\boldsymbol{e}_\mathrm{s}^{dq}, \\ \boldsymbol{u}_\mathrm{s,pi}^{dq}(\boldsymbol{e}_\mathrm{s}^{dq}) &= \boldsymbol{K}_\mathrm{p}^{dq}\boldsymbol{e}_\mathrm{s}^{dq} + \boldsymbol{K}_\mathrm{i}^{dq}\boldsymbol{\xi}_\mathrm{i}^{dq}, \end{aligned}\right\} \tag{4.2}$$

with PI controller outputs $\boldsymbol{u}_\mathrm{s,pi}^{dq} := (u_\mathrm{s,pi}^d, u_\mathrm{s,pi}^q)^\top$ [functions of the tracking errors $\boldsymbol{e}_\mathrm{s}^{dq} := (e_\mathrm{s}^d, e_\mathrm{s}^q)^\top$], integral actions $\boldsymbol{\xi}_\mathrm{i}^{dq} := (\xi_\mathrm{i}^d, \xi_\mathrm{i}^q)^\top$ of the PI controllers and the proportional $\boldsymbol{K}_\mathrm{p}^{dq} \in \mathbb{R}^{2\times 2}$ and integral $\boldsymbol{K}_\mathrm{i}^{dq} \in \mathbb{R}^{2\times 2}$ gain matrices. In the case of current control, the tracking errors

$$\boldsymbol{e}_\mathrm{s}^{dq} := \boldsymbol{i}_\mathrm{s,ref}^{dq} - \boldsymbol{i}_\mathrm{s}^{dq}$$

are defined by the difference between the current references $\boldsymbol{i}_\mathrm{s,ref}^{dq} = (i_\mathrm{s,ref}^d, i_\mathrm{s,ref}^q)^\top$ and the real currents $\boldsymbol{i}_\mathrm{s}^{dq} = (i_\mathrm{s}^d, i_\mathrm{s}^q)^\top$. Moreover, the anti-windup decision function [47]

$$f_\mathrm{aw}(\widehat{u}, \boldsymbol{u}_\mathrm{s,pi}^{dq}) = \begin{cases} 1, & \|\boldsymbol{u}_\mathrm{s,pi}^{dq}\| < \widehat{u} \\ 0, & \|\boldsymbol{u}_\mathrm{s,pi}^{dq}\| \geq \widehat{u} \end{cases} \tag{4.3}$$

stops the integration in (4.2) if the controller output $\boldsymbol{u}_\mathrm{s,pi}^{dq}$ exceeds the admissible voltage magnitude $\widehat{u}$. According to the applied modulation scheme, for PWM, the voltage threshold of the inverter is half of the dc link voltage u_dc, i.e., $\widehat{u} = \frac{u_\mathrm{dc}}{2}$; whereas, for SVM, it is $\widehat{u} = \frac{u_\mathrm{dc}}{\sqrt{3}}$.

4.2.2 Basic concept

The basic idea of the I/O linearization is to transform the nonlinear current dynamics of RSMs in (4.1) into a simple integrator [47], i.e.,

$$\frac{\mathrm{d}}{\mathrm{d}t}\boldsymbol{i}_{\mathrm{s}}^{dq} = \boldsymbol{u}_{\mathrm{s,pi}}^{dq}(\boldsymbol{e}_{\mathrm{s}}^{dq}) \qquad \circ\!\!-\!\!\bullet \qquad i_{\mathrm{s}}^{d/q}(s) = \tfrac{1}{s}u_{\mathrm{s,pi}}^{d/q}(s) \tag{4.4}$$

whose virtual inputs correspond to the outputs of the current PI controllers $\boldsymbol{u}_{\mathrm{s,pi}}^{dq}$. To realize (4.4), a nonlinear feedforward and decoupling of the current dynamics are necessary (see Section 4.2.3).

Neglecting the inverter dynamics and the PI controller nonlinearity [due to the anti-windup decision function in (4.3)], the closed-loop current control systems (as shown in Fig. 4.2) consisting of the integrator as in (4.4) and the PI controller in (4.2) become, for both d- and q-axis current components, second order systems of the following form

$$F_{\mathrm{CL}}^{d/q}(s) := \frac{i_{\mathrm{s}}^{d/q}(s)}{i_{\mathrm{s,ref}}^{d/q}(s)} = \frac{k_{\mathrm{p}}^{d/q}s + k_{\mathrm{i}}^{d/q}}{s^2 + k_{\mathrm{p}}^{d/q}s + k_{\mathrm{i}}^{d/q}}. \tag{4.5}$$

Proportional gains $k_{\mathrm{p}}^{d/q}$ and integral gains $k_{\mathrm{i}}^{d/q}$ can be tuned by pole placement according to the given desired closed-loop polynomial

$$\chi_{\mathrm{ref}}^{d/q}(s) = s^2 + 2D^{d/q}\omega_0^{d/q}s + (\omega_0^{d/q})^2, \tag{4.6}$$

where damping $D^{d/q} > 0$ and eigenfrequency $\omega_0^{d/q}$ for d and q components are free design parameters.

A comparison of the coefficients of the desired polynomial in (4.6) and in the denominator of the closed-loop transfer function (4.5), i.e.,

$$\chi_{\mathrm{CL}}^{d/q}(s) = s^2 + k_{\mathrm{p}}^{d/q}s + k_{\mathrm{i}}^{d/q}, \tag{4.7}$$

eventually leads to the following tuning rules [47]:

- for given eigenfrequencies $\omega_0^{d/q}$ (in terms of the d- and q-axis bandwidths) and dampings $D^{d/q}$, the controller parameters are obtained as follows

$$k_{\mathrm{p}}^{d/q} = 2D^{d/q}\omega_0^{d/q} \quad \wedge \quad k_{\mathrm{i}}^{d/q} = (\omega_0^{d/q})^2, \tag{4.8}$$

- for given proportional gains $k_{\mathrm{p}}^{d/q} > 0$ (as large as possible) *and* dampings $D^{d/q}$, the integral gains become

$$k_{\mathrm{i}}^{d/q} = (\omega_0^{d/q})^2 \overset{(4.8)}{=} \left(\frac{k_{\mathrm{p}}^{d/q}}{2D^{d/q}}\right)^2. \tag{4.9}$$

Normally, an identical choice for d and q components is sufficient, i.e., $k_{\mathrm{p}} = k_{\mathrm{p}}^{d} = k_{\mathrm{p}}^{q}$ and $k_{\mathrm{i}} = k_{\mathrm{i}}^{d} = k_{\mathrm{i}}^{q}$. Therefore, the controller parameters in (4.2) can be derived with the form of diagonal matrix

$$\boldsymbol{K}_{\mathrm{p}}^{dq} := \begin{bmatrix} k_{\mathrm{p}} & 0 \\ 0 & k_{\mathrm{p}} \end{bmatrix} \quad \wedge \quad \boldsymbol{K}_{\mathrm{i}}^{dq} := \begin{bmatrix} k_{\mathrm{i}} & 0 \\ 0 & k_{\mathrm{i}} \end{bmatrix}, \tag{4.10}$$

i.e., $\boldsymbol{K}_{\mathrm{p}}^{dq} = k_{\mathrm{p}}\boldsymbol{I}_2$ and $\boldsymbol{K}_{\mathrm{i}}^{dq} = k_{\mathrm{i}}\boldsymbol{I}_2$.

4.2.3 Controller structure

The overall controller structure of the nonlinear current control with I/O linearization is given by [47]

$$\boldsymbol{u}_{\mathrm{s,ref}}^{dq} = \underbrace{\boldsymbol{L}_{\mathrm{s}}^{dq}(\boldsymbol{i}_{\mathrm{s}}^{dq}) \cdot \boldsymbol{u}_{\mathrm{s,pi}}^{dq}(\boldsymbol{e}_{\mathrm{s}}^{dq})}_{\text{nonlinear decoupling and PI controller}} + \underbrace{\boldsymbol{u}_{\mathrm{s,ff}}^{dq}(\omega_{\mathrm{p}}, \boldsymbol{i}_{\mathrm{s}}^{dq})}_{\text{nonlinear feedforward}} \tag{4.11}$$

and is illustrated in Fig. 4.3 with the stator voltage references $\boldsymbol{u}_{\mathrm{s,ref}}^{dq} = (u_{\mathrm{s,ref}}^{d}, u_{\mathrm{s,ref}}^{q})^{\top}$ and the feedforward terms $\boldsymbol{u}_{\mathrm{s,ff}}^{dq} := (u_{\mathrm{s,ff}}^{d}, u_{\mathrm{s,ff}}^{q})^{\top}$. It consists of two parts: (i) the product of the differential inductance matrix $\boldsymbol{L}_{\mathrm{s}}^{dq}(\boldsymbol{i}_{\mathrm{s}}^{dq})$ in (2.9) and the PI controller output $\boldsymbol{u}_{\mathrm{s,pi}}^{dq}(\boldsymbol{e}_{\mathrm{s}}^{dq})$ in (4.2) and (ii) the additive but nonlinear feedforward term

$$\boldsymbol{u}_{\mathrm{s,ff}}^{dq}(\omega_{\mathrm{p}}, \boldsymbol{i}_{\mathrm{s}}^{dq}) = R_{\mathrm{s}}\boldsymbol{i}_{\mathrm{s}}^{dq} + \omega_{\mathrm{p}}\boldsymbol{J}\boldsymbol{\psi}_{\mathrm{s}}^{dq}(\boldsymbol{i}_{\mathrm{s}}^{dq}). \tag{4.12}$$

Both parts require an online adaption of the nonlinear flux linkages $\psi_{\mathrm{s}}^{d}(\boldsymbol{i}_{\mathrm{s}}^{dq})$ and $\psi_{\mathrm{s}}^{q}(\boldsymbol{i}_{\mathrm{s}}^{dq})$ and the differential inductances $L_{\mathrm{s}}^{d}(\boldsymbol{i}_{\mathrm{s}}^{dq})$, $L_{\mathrm{s}}^{q}(\boldsymbol{i}_{\mathrm{s}}^{dq})$ and $L_{\mathrm{s}}^{dq}(\boldsymbol{i}_{\mathrm{s}}^{dq})$ $[= L_{\mathrm{s}}^{qd}(\boldsymbol{i}_{\mathrm{s}}^{dq})]$, which can be stored in LUTs or represented by prototype functions (see Chapter 3).

With sufficiently high switching frequencies and if inverter nonlinearities and voltage drop on the cables are negligible, the inverter output can be seen as (approximately) equivalent to the stator voltage vector $\boldsymbol{u}_{\mathrm{s}}^{dq}$ at the machine's terminals, i.e., $\boldsymbol{u}_{\mathrm{s}}^{dq} \approx \boldsymbol{u}_{\mathrm{s,ref}}^{dq}$. Under this assumption, the exact I/O linearization of the current dynamics in (4.1) can be achieved by means of the controller structure in (4.11), as it compensates the additive disturbance terms in the current dynamics (4.1) with the help of the feedforward term in (4.12) and achieves a decoupling of the d and q current components by means of the multiplication $L_{\mathrm{s}}^{dq}(\boldsymbol{i}_{\mathrm{s}}^{dq}) \cdot \boldsymbol{u}_{\mathrm{s,pi}}^{dq}(\boldsymbol{e}_{\mathrm{s}}^{dq})$. As a result, inserting (4.11) with (4.12) into (4.1) finally yields (4.4) as [47]

$$\frac{\mathrm{d}}{\mathrm{d}t}\boldsymbol{i}_{\mathrm{s}}^{dq} \overset{(4.1),(4.11)}{=} \boldsymbol{L}_{\mathrm{s}}^{dq}(\boldsymbol{i}_{\mathrm{s}}^{dq})^{-1} \cdot \left[\boldsymbol{L}_{\mathrm{s}}^{dq}\boldsymbol{u}_{\mathrm{s,pi}}^{dq} + \boldsymbol{u}_{\mathrm{s,ff}}^{dq} - R_{\mathrm{s}}\boldsymbol{i}_{\mathrm{s}}^{dq} - \omega_{\mathrm{p}}\boldsymbol{J}\boldsymbol{\psi}_{\mathrm{s}}^{dq}(\boldsymbol{i}_{\mathrm{s}}^{dq})\right] \overset{(4.12)}{=} \boldsymbol{u}_{\mathrm{s,pi}}^{dq}.$$

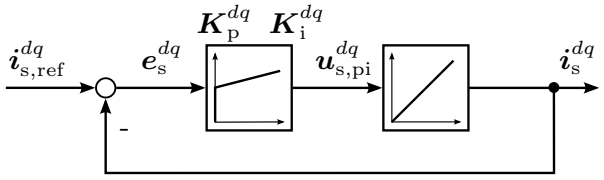

Figure 4.2: Block diagram of the closed-loop current control system with I/O linearization [47].

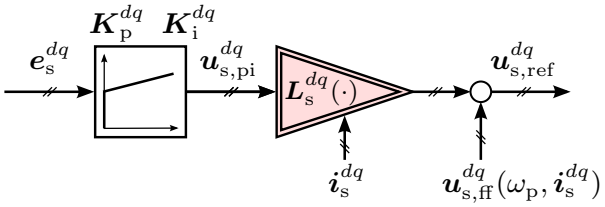

Figure 4.3: Controller structure (4.11) of the nonlinear current controllers with I/O linearization [47].

4.3 Implementation

In order to validate the effectiveness of the proposed nonlinear control methods for RSMs, including the nonlinear current control system and the optimal feedforward torque control (in the upcoming chapter), simulative and experimental platforms are constructed. According to the block diagram shown in Fig. 4.1, the fundamental structure of a current control system is implemented for both simulations and experiments.

4.3.1 Simulation

Machine model (2.5) is built in the rotating (d,q)-reference frame. To include the magnetic saturation, it is structured with the flux linkage saturation function, as shown in Fig. 2.6(b). Instead of utilizing the available flux linkage data (per measurements) by saving as LUTs, the developed flux linkage prototype functions are employed due to the proven high approximation accuracy. Moreover, together with only a few number of function parameters, the natural extrapolation capability ensures effective outputs of flux linkage values, even when the current inputs are outside the measurement range. Whereas this is not feasible with LUTs, as those stored Not a Number (NaN) values outside the measurement range may cause a sudden stop or error in simulation.

Regarding the controller implementation, the nonlinear PI controllers (4.2) and also the controller structure (4.11) with I/O linearization are implemented in the (d,q)-reference frame. In order to yield a similar simulation scenario as real-time operation, the PI controllers (4.2) with anti-windup (4.3) are discretized by means of the bilinear transform, which offers a more robust performance than the commonly used forward Euler method.

The implemented regularly sampled and symmetrical SVM applies the required pulse pattern $\boldsymbol{s}^{abc}$ to the voltage source inverter according to the desired references $\boldsymbol{u}^{dq}_{\mathrm{s,ref}}$. Besides, the inverter model is established in the stator fixed (α,β)-reference frame (for more details, see, e.g., [118, Chapter 14]).

4.3.2 Experiment

The laboratory setup, as depicted in Fig. 4.4, consists of the following fundamental components:

- **RSM (A):** A 4.0 kW ABB RSM is employed as the machine under test. It is mechanically coupled to a prime mover. An incremental encoder is mounted at the machine end, so the rotor position ϕ_{m} and the angular velocity ω_{m} are available for the implemented control system. In Chapter 2, its nonlinear flux linkages and differential inductances have been identified (as shown in Fig. 2.7 and Fig. 2.8), which must be compensated for to achieve a satisfactory drive performance.
- **Load machine (B):** A SEW permanent magnet synchronous machine (PMSM) with a higher rating and also equipment of an encoder serves as the prime mover. In order to reserve high flexibility for experiments, the real-time system (RTS) controls not only the tested RSM but also the PMSM. Consequently, depending on the testing scenarios for the machine under test, the prime mover is able to offer either a steady load torque or a constant speed rotation.
- **Torque sensor (C):** A torque sensor is installed between the coupling of two equipped machines. Hence, the developed machine torque m_{m} and the mechanical power are available during test.

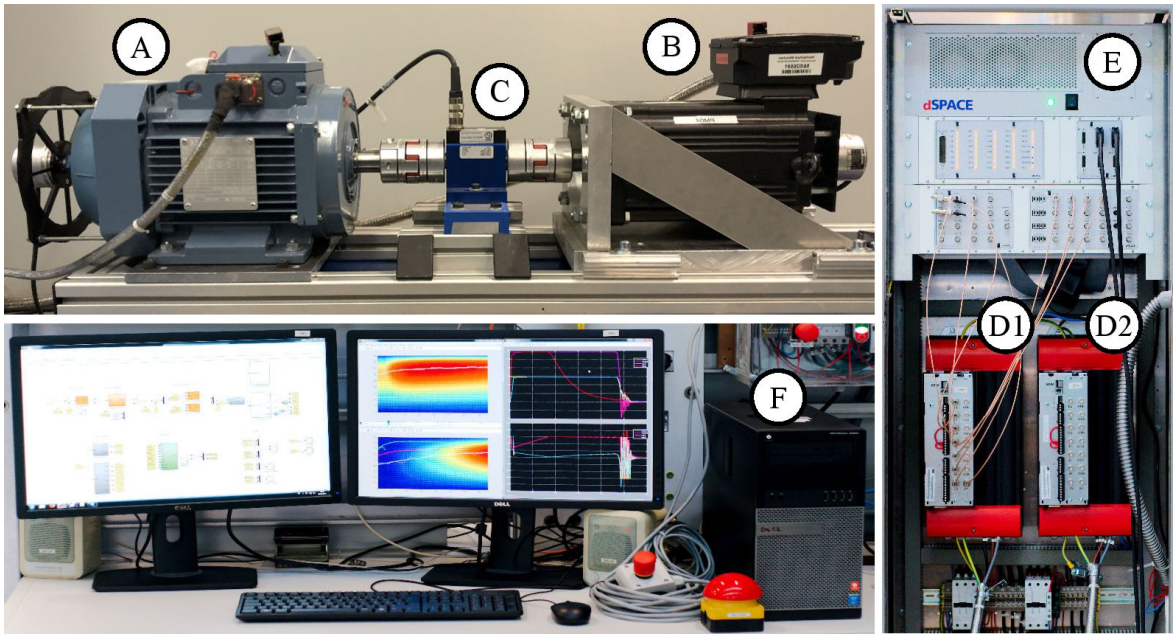

Figure 4.4: Laboratory setup comprising (A) RSM, (B) load machine, (C) torque sensor, (D1 & D2) inverter, (E) real-time system and (F) host PC.

- **Inverter (D1 & D2):** Two SEW inverters are adopted to power both machines separately, and they are connected in a back-to-back configuration that shares the common dc link. With the built-in sensors in the inverters, the respective machine currents $\boldsymbol{i}_{\mathrm{s}}^{abc}$ and the dc link voltage u_{dc} are measured. Instead of supplying the power directly via a three-phase rectifier from the grid, a commercial dc power source is utilized to provide a stable and adjustable dc link voltage.
- **Real-time system (E):** A dSPACE RTS with processor board DS1007 and other I/O boards [e.g., for PWM, encoder and analog-to-digital converter (ADC)] is utilized. It runs the control routine from the developed control approaches and generates the required pulse patterns $\boldsymbol{s}^{abc}$ to the respective inverters.
- **Host PC (F):** A host PC is connected to RTS via an Ethernet cable to build real-time applications of the developed control algorithms. The custom-built platform runs with the required software (i.e., MATLAB/Simulink RCPHIL R2019b and dSPACE ControlDesk 6.2) for rapid prototyping, data acquisition and online evaluation.

4.4 Simulative and experimental validation

In this section, both simulations and experiments are conducted in order to demonstrate the effectiveness of the proposed nonlinear current control system using flux linkage prototype functions for RSMs. It has been proved in Chapter 3 that the developed flux linkage prototype functions can present the magnetic saturation of RSMs well. Notably, the RSM flux linkage prototype function II [i.e., (3.16) introduced in Section 3.3] yields better flexibility and universality; thus, it is chosen to be applied here. In order to acquire a higher fitting accuracy, the number of cross-coupling saturation terms $n = 3$ is chosen, leading to a total of 15 function parameters in (3.16). As a consequence, the nonlinear current controllers (4.2) with the concept

Table 4.1: Key parameters of laboratory setup, implementation and control system for simulations and experiments.

RSM	**Symbol**	**Value**
Rated power	P_{R}	4.0 kW
Pole pair	n_{p}	2
Rated speed	$\omega_{\mathrm{m,R}}$	157.1 rad/s
Rated torque	$m_{\mathrm{m,R}}$	25 Nm
Rated current	$\widehat{i}_{\mathrm{s,R}}$	13.3 A
Rated voltage	$\widehat{u}_{\mathrm{s,R}}$	310.3 V
Stator resistance	R_{s}	1.3 Ω
Inertia	Θ_{m}	6.9×10^{-3} kgm^2
Inverter		
dc link voltage	u_{dc}	700.0 V
Switching frequency	$f_{\mathrm{sw}} = 1/T_{\mathrm{sw}}$	8.0 kHz
Sampling frequency	$f_{\mathrm{sam}} = 1/T_{\mathrm{sam}}$	8.0 kHz
Voltage limit (SVM)	$\widehat{u} = u_{\mathrm{dc}}/\sqrt{3}$	404.1 V
Nonlinear current control system		
Damping	$D = D^d = D^q$	1.25
Eigenfrequency	$\omega_0 = \omega_0^d = \omega_0^q$	1×10^3 Hz
Proportional gain	$k_{\mathrm{p}} = k_{\mathrm{p}}^d = k_{\mathrm{p}}^q$	2.5×10^3 s^{-1}
Integral gain	$k_{\mathrm{i}} = k_{\mathrm{i}}^d = k_{\mathrm{i}}^q$	1×10^6 s^{-2}

of the exact I/O linearization (4.4) and the flux linkage prototype functions (3.16) are implemented in MATLAB/Simulink and at laboratory setup. The block diagram of the implemented control system is shown in Fig. 4.1. Key parameters of laboratory setup, implementation and controllers for simulations and experiments are collected in Table 4.1. Note that *no filters* are used for the current measurements, such that the control performance can be illustrated and validated as close as possible to the theoretical controller design introduced in the last section. Hence, the measured signals in the following exhibit noticeable noise. Nevertheless, the controller performance is still acceptable with stable and fast tracking over the entire operation range.

Note that the employed 4.0 kW ABB RSM here is adopted from one of the listed RSMs in Table 3.1 (see RSM#3), where its nonlinear flux linkages have been identified in Chapter 2 and approximated with the flux linkage prototype functions in Chapter 3. Furthermore, by means of the constant speed identification method, flux linkage maps are extracted under *ten* different rotational speeds, i.e., $\omega_{\mathrm{m}} = \alpha\omega_{\mathrm{m,R}}$ with $\alpha = 0.1, 0.2, \cdots, 1$. Then, they are fitted separately with the prototype functions, which lead to ten sets of function parameters in total. Since the approximated flux linkages $\widehat{\psi}_{\mathrm{s}}^d(i_{\mathrm{s}}^d, i_{\mathrm{s}}^q)$ and $\widehat{\psi}_{\mathrm{s}}^q(i_{\mathrm{s}}^d, i_{\mathrm{s}}^q)$, which are functions of the currents, possess continuity over the whole current range and require only a linear interpolation to acquire flux linkages between two speeds.

For the *identical* current reference trajectories, the control performance is evaluated by *three* scenarios throughout the whole operation range, i.e., $\|\boldsymbol{i}_{\mathrm{s}}^{dq}\| \leq 11.3\,\mathrm{A}$:

- Operation at idle speed (see simulation [—] and measurement [—] results in Fig. 4.5);
- Operation at constant speed (see simulation [—] and measurement [—] results in Fig. 4.7); and
- Comparison of the control performance during operation while flux linkages and differential inductances are updated using LUTs [—], simplified prototype functions [—] and the proposed flux linkage prototype functions in (3.16) [—] (see respective measurement results in Fig. 4.9).

In order to ease the legibility of Fig. 4.5 and Fig. 4.7, both simulation and measurement results are merged and depicted with the overall duration of the assigned current pattern, including direct currents $i_{\mathrm{s,ref}}^{d}$ & i_{s}^{d}, quadrature currents $i_{\mathrm{s,ref}}^{q}$ & i_{s}^{q}, norm of the control input $\|\boldsymbol{u}_{\mathrm{s,ref}}^{dq}\|$ (& inverter voltage limit $\widehat{u}$) and mechanical angular velocity ω_{m}. Whereas Fig. 4.6(a) & 4.6(b) and Fig. 4.8(a) & 4.8(b) illustrate the same quantities as Fig. 4.5 and Fig. 4.7 but over a smaller time interval (zoomed versions).

4.4.1 Scenario (i) - idle speed

In this test scenario, only the employed RSM under test is controlled with the developed nonlinear current control system. By contrast, the load machine is *not* controlled. Its mechanical angular velocity is thus not kept constant and, on the contrary, will change due to the applied RSM torque. This produces time-varying disturbances, e.g., counter voltages, which must be compensated for dynamically by the proposed current control system.

For a chosen current reference over the whole operation range, the simulation results [—] and the measurement results [—] are shown in Fig. 4.5 with the entire operation at idle speed and Fig. 4.6 with a smaller timer interval. For the mechanical subsystem, there is an apparent difference between the simulated and measured mechanical angular velocities ω_{m}, owing to the inaccurate inertia in the low-speed region and the neglection of friction in the simulative machine model. However, despite the distinctive acceleration and deceleration rates, their phenomenons due to the developed RSM torque are appropriately interpreted. On the other hand, for the electrical subsystem, it can be seen that simulation and measurement results coincide very well. Thus, the machine's nonlinearities are correctly considered by means of the designed flux linkage prototype functions in the realistic simulation model.

The control performance of the proposed current control system at idle speed is confirmed by its fast and very accurate reference tracking capability. Especially, the good decoupling behavior in Fig. 4.5, when d or q current is at a high steady-state value, the other component can rapidly follow a jump of the respective reference value. For both d and q components, an (almost) identical transient behavior with similar rise and settling times is ensured. As a consequence, the outer control loops can be easily designed based on simple approximations of the closed-loop current dynamics.

4.4.2 Scenario (ii) - constant speed

Unlike the former test scenario at idle speed, the load machine is speed-controlled to rotate the RSM constantly at half the rated speed $\omega_{\mathrm{m,R}}$, i.e., $\omega_{\mathrm{m}} = 0.5\,\omega_{\mathrm{m,R}} = 78.5\,\mathrm{rad/s}$.

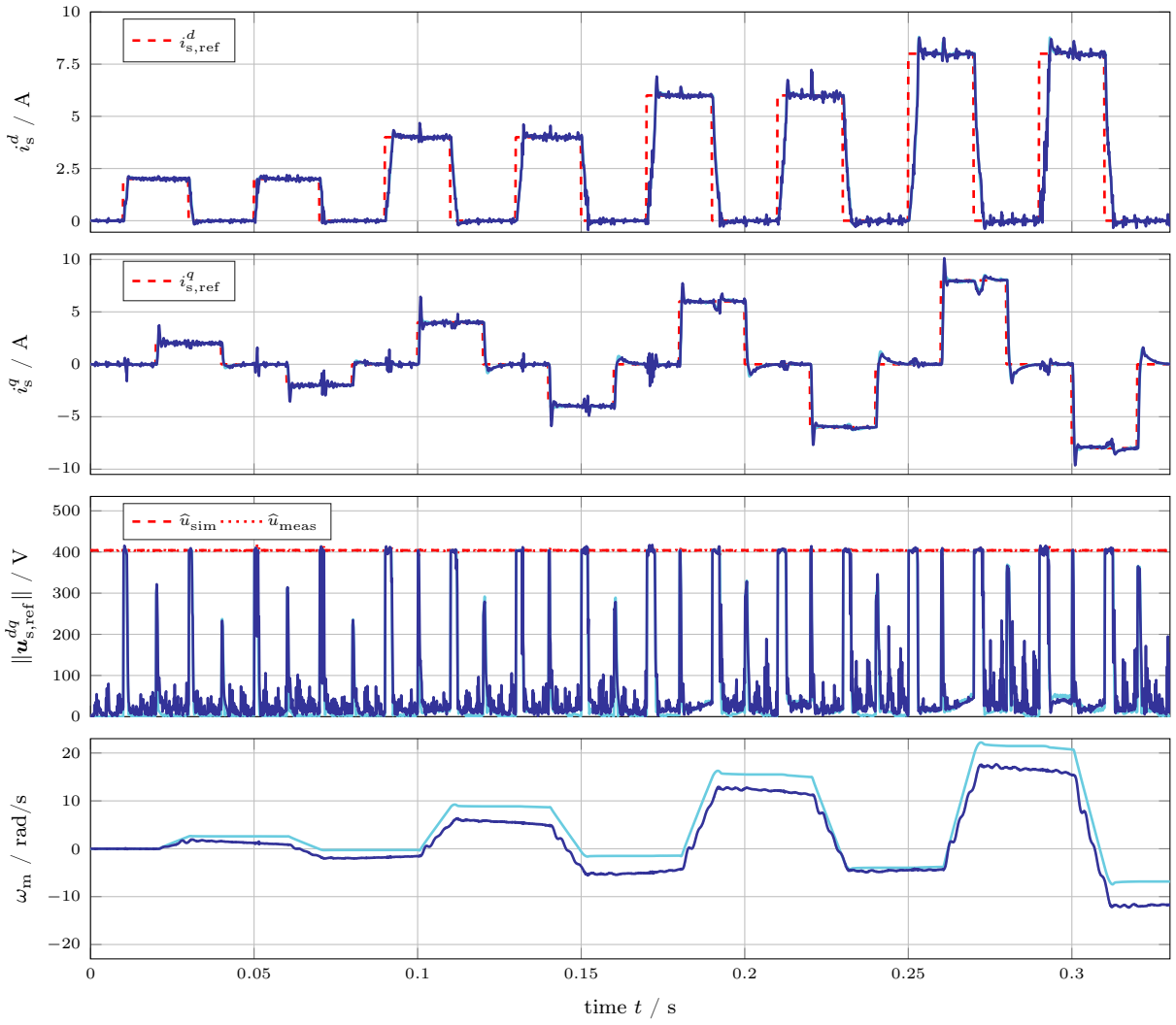

Figure 4.5: Simulation results [—] and measurement results [—] at idle speed of the nonlinear current control (4.11) with I/O linearization for the RSM using the flux linkage prototype functions (3.16).

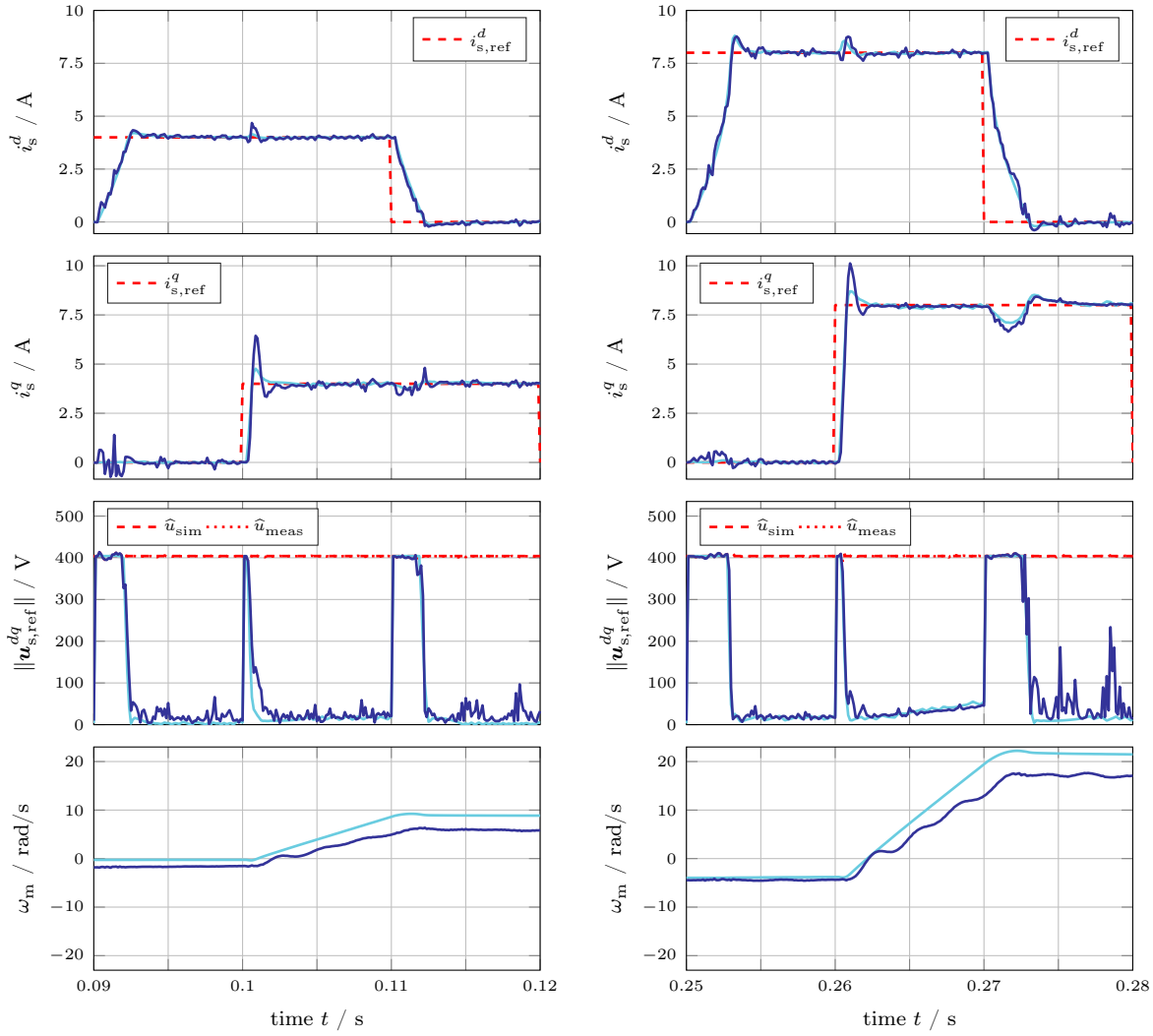

Figure 4.6: Zoomed plots of Fig. 4.5 over a smaller time interval: (a) zoom 1; (b) zoom 2.

For the identical current reference, the simulation results [—] and the measurement results [—] are shown in Fig. 4.7 with the entire operation at (almost) constant speed and Fig. 4.8 with a smaller timer interval. Simulation and measurement results match nicely for both the electrical and mechanical subsystems in this test scenario. However, it can be seen that higher current ripples are induced on the measured q-axis current i_s^q due to slot harmonics [101, 114], which are not considered in the simulation model. As shown in Fig. 4.8(a) and 4.8(b), after the $i_{\mathrm{s,ref}}^q$ reference changes at $t = 0.1, 0.26\,\mathrm{s}$, some periodic oscillations appear on i_s^q during steady-state, i.e., 18-th order of the current harmonics. Regarding the control performance, good steady-state and transient responses are maintained. Compared to scenario (i) at idle speed, longer settling times and a poorer decoupling behavior with larger current drops can be observed due to the higher back EMF voltages at constant speed.

Due to the severe magnetic saturation of RSMs, the flux linkages saturate and thus the differential inductances vary notably with the applied stator currents throughout the entire operation range, as shown in Fig. 2.7 and Fig. 2.8, respectively. The developed nonlinear current controllers based on I/O linearization effectively alleviate the effects of the machine's nonlinearities. The excellent control performance (including steady-state, dynamic and decoupling behavior) is confirmed in the idle and constant speed scenarios. By means of the introduced controller structure (4.11), the differential inductance matrix $\boldsymbol{L}_\mathrm{s}^{dq}$ allows for (i) direct and quite accurate decoupling and (ii) compensation of the magnetic nonlinearities. Moreover, using the flux linkage prototype functions (3.16) makes memory-expensive LUTs obsolete and allows for a meaningful extrapolation.

It can be concluded that the system knowledge is of key importance and can be put to full effect with the proposed control strategy; therefore, the control performance of nonlinear RSMs can be significantly improved.

4.4.3 Scenario (iii) - comparison

To show the potential of the utilization of prototype functions in the control system, measurement results at idle speed [identical to scenario (i)] are shown in Fig. 4.9 where the flux linkages $\boldsymbol{\psi}_\mathrm{s}^{dq}$ and the differential inductances $\boldsymbol{L}_\mathrm{s}^{dq}$ of the RSM [in the controller structure (4.11)] are compensated for and updated in different ways by:

- *six* three-dimensional (3D) LUTs (functions of i_s^d, i_s^q and ω_m) with 51×51×10 supporting points and linear interpolation method [—];
- *simplified* prototype functions without considering the cross-coupling effects [—] (i.e., $\widehat{\psi}_\mathrm{s}^d(i_\mathrm{s}^d) = \widehat{\psi}_{\mathrm{s,self}}^d(i_\mathrm{s}^d)$ & $\widehat{\psi}_\mathrm{s}^q(i_\mathrm{s}^q) = \widehat{\psi}_{\mathrm{s,self}}^q(i_\mathrm{s}^q)$ in (3.7) and $\widehat{L}_\mathrm{s}^{dq} = \widehat{L}_\mathrm{s}^{qd} = 0$); and
- proposed flux linkage prototype functions (3.16) [—] (as presented in Fig. 3.11).

Note that all approaches are augmented with not only the stator currents but also *ten* different angular velocities. For the solutions using prototype functions, interpolated values between two available speed indexes are computed online from the already fitted prototype functions under various speeds.

Although different controller tunings might lead to different control performances, the tuning is kept identical for all approaches in order to achieve a fair comparison of the control performances and different compensation methods. Moreover, it is important to note that, due to the exact I/O-linearization approach, a more aggressive tuning will not lead to, e.g., a better decoupling

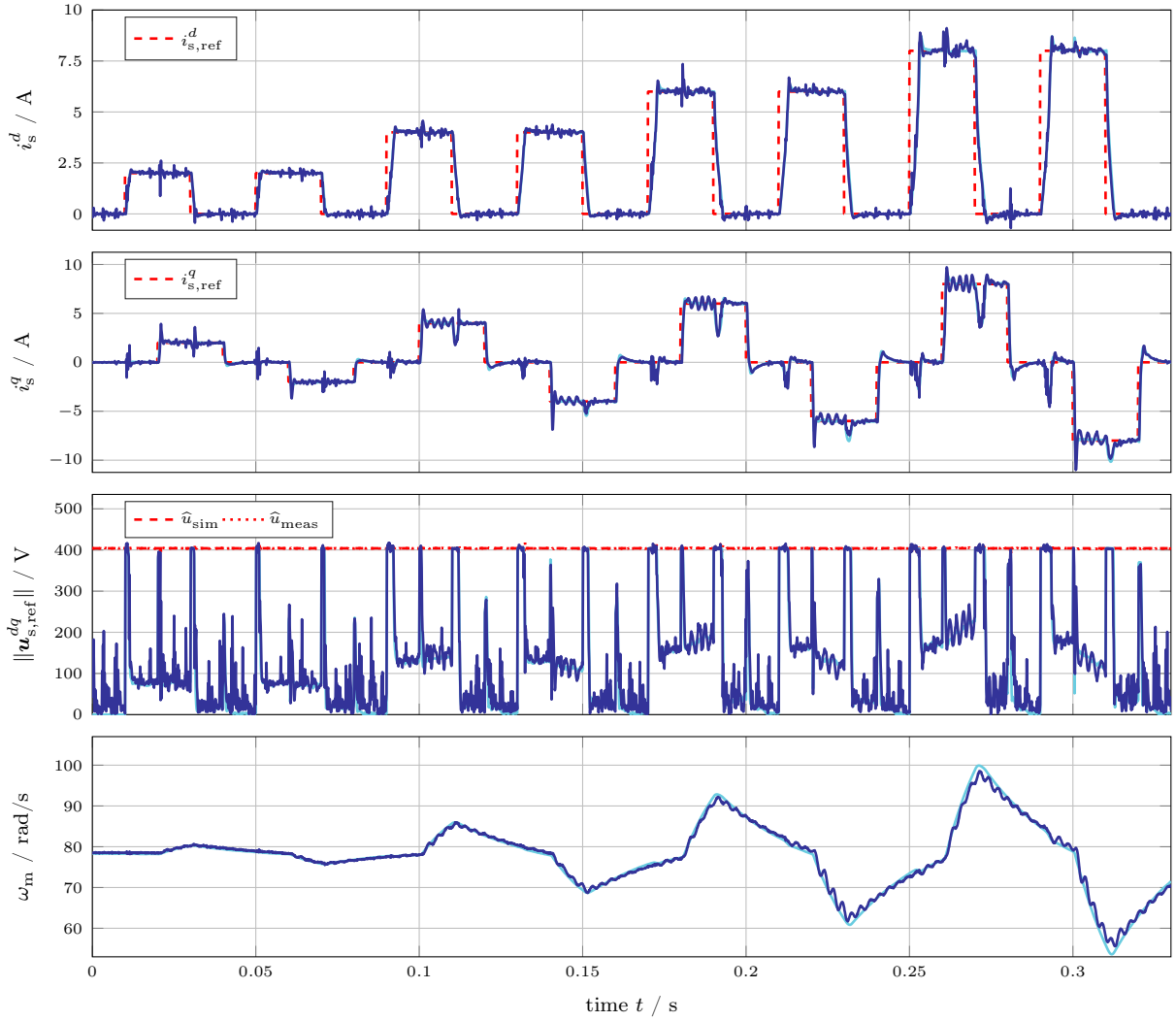

Figure 4.7: Simulation results [—] and measurement results [—] at (almost) constant speed $\omega_{\mathrm{m}} = 78.5\,\mathrm{rad/s}$ of the nonlinear current control (4.11) with I/O linearization for the RSM using the flux linkage prototype functions (3.16).

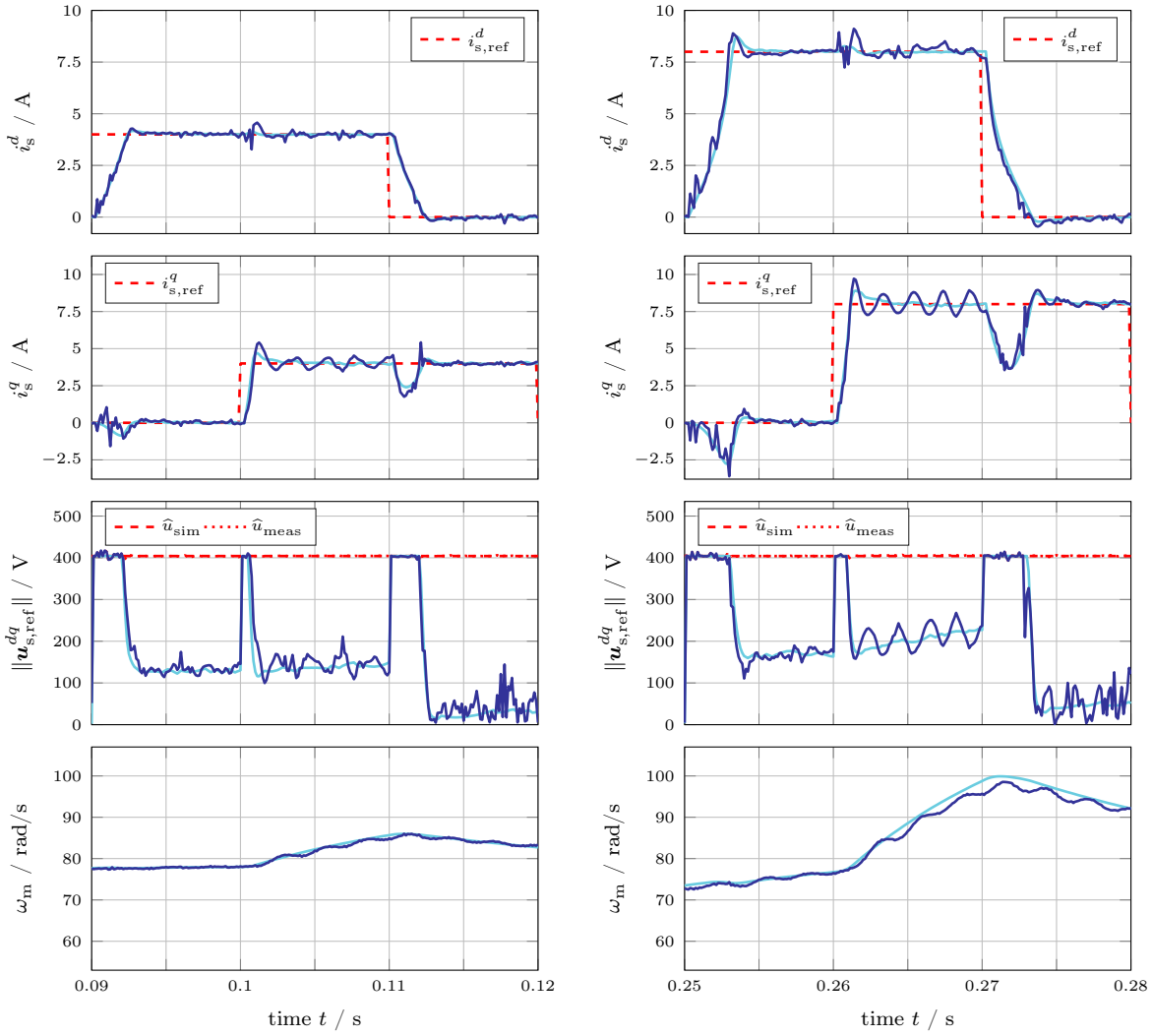

Figure 4.8: Zoomed plots of Fig. 4.7 over a smaller time interval: (a) zoom 1; (a) zoom 2.

performance. The control performance is mostly affected by precise system knowledge requiring high-resolution LUTs or well-fitted flux linkage prototype functions considering magnetic saturation *and* cross-coupling effects.

In Fig. 4.9, it can be observed that the results using LUTs or the proposed prototype functions as in (3.16), both considering cross-coupling effects, are similar and lead to a very good control and decoupling performance. Direct current i_s^d and quadrature current i_s^q are decoupled and track the reference steps very quickly and accurately. In contrast to that, when solely the simplified prototype functions *without* consideration of the cross-coupling effects are used, the decoupling performance is significantly deteriorated, particularly at $t = 0.02, 0.06\,\mathrm{s}$ for i_s^q. Whereas rise time and steady-state performances are similar to the other two approaches. In conclusion, the magnetic saturation and cross-coupling effects must be taken into account in the nonlinear current control system design to achieve an improved and decoupled control performance.

For further comparisons of the measurement results in Fig. 4.9, Table 4.2 lists several parameters of the different nonlinear current control algorithms that were evaluated by (i) the integral time-weighted absolute error (ITAE) performance measure

$$\mathrm{ITAE}^{d/q}(e_\mathrm{s}^{d/q}, 0, t_\mathrm{end}) := \int_0^{t_\mathrm{end}} \tau |e_\mathrm{s}^{d/q}(\tau)| \,\mathrm{d}\tau$$

for both d and q components and $t_\mathrm{end} = 0.07\,\mathrm{s}$; (ii) (average) data update time T_upd in an Interrupt Service Routine (ISR), including LUT index searching, interpolation or prototype function calculation; and (iii) number of required floating-point variables (parameters) saved in the memory. As already observed in Fig. 4.9, a similar control performance on i_s^d is attained by different compensation methods with close ITAE^d values. Apparently, using the simplified prototype functions results in the worst control performance on i_s^q with the highest value for ITAE^q. However, the shortest update time and the least memory are needed. Only six parameters are required for the self-axis saturation functions (3.7) under ten different speeds, i.e., 60 variables in total. When it comes to the comparison between LUTs and flux linkage prototype functions (3.16), the ITAE values when using (3.16) are slightly higher but as good as when high-resolution LUTs are used. Using the prototype functions (3.16) requires longer data update time due to the chosen hyperbolic and (modified) Gaussian functions, i.e., 1.2 % time increase in a single interrupt. Whereas –most importantly– the stored amount of data (variables/parameters) can be significantly reduced to only 150 parameters in contrast to 156060 when LUTs are used. The saved storage can therefore be utilized to compensate for further nonlinear effects such as inverter nonlinearities or iron losses.

For storage-limited (e.g., electromotive or industrial) applications, only one-dimensional (1D) or two-dimensional (2D) LUTs with small sizes are normally allowed to be equipped. This is different from the adopted implementation here using high-resolution 3D LUTs. As stated in [2], where somewhat smaller LUTs with 20×20 data points are used for the same current control method, undesired oscillations (i.e., current ripples) and a deteriorated control performance (i.e., poor ITAE values) may be resulted from insufficient supporting points of saved LUTs and/or inaccurate inter-/extrapolation of LUTs.

In summary, the potential of using flux linkage prototype functions in control is confirmed by simulation and measurement results. With high approximation accuracy and continuous differentiability, the (fitted) flux linkages and (approximated) differential inductances can be utilized directly in the proposed current control scheme and make LUTs obsolete. Apart from that, the prototype functions can also be used to compensate for machine parameters in optimal feedforward torque control, which will be presented in the upcoming chapter.

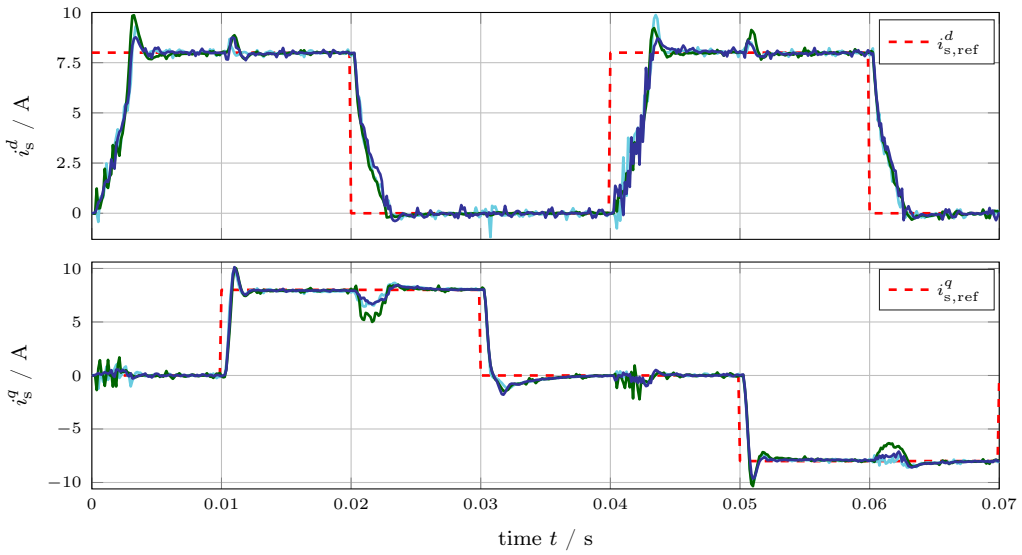

Figure 4.9: Measurement results at idle speed of the nonlinear current control (4.11) with I/O linearization for the RSM using: (i) six LUTs [—]; (ii) simplified prototype functions [—]; and (iii) the flux linkage prototype functions (3.16) [—].

Table 4.2: Comparison of integral time-weighted absolute error (ITAE), data update time T_{upd} in an ISR and memory (required floating-point variable numbers) by different compensation methods (corresponding to Fig. 4.9).

Method	**ITAE^d** (µAs)	**ITAE^q** (µAs)	**T_{upd}** (µs)	**Memory** (variable)
Six LUTs	1699.9	969.6	2.0	156060
Simplified prototype functions	1732.4	1250.4	1.2	60
Flux linkage prototype functions (3.16)	1785.4	995.5	3.5	150

Chapter 5

Optimal feedforward torque control

A unified theory for optimal feedforward torque control (OFTC) of synchronous machines (SMs) is introduced based on [50, 51] with application on reluctance synchronous machines (RSMs) utilizing analytical flux linkage prototype functions. The optimal current references are derived analytically to ensure the best possible operation performance in different operation strategies, including maximum torque per current [MTPC, which is also known as maximum torque per ampere (MTPA)], field weakening (FW), maximum current (MC) and maximum torque per voltage (MTPV). As a consequence, numerical approaches (by only approximating the solutions) can be replaced. The principal concept of OFTC is to (i) reformulate machine equations (i.e., voltage, torque and constraints) and all operation strategies as quadrics via online linearization and (ii) solve the resulting optimization problems by looking for the intersection point of two respective quadrics. A decision tree is designed and equipped to guarantee excellent operation management and a smooth transition between different operation strategies. Furthermore, the magnetic saturation and cross-coupling effects, which are especially non-negligible in OFTC for RSMs, are taken into account and compensated for using the developed flux linkage prototype functions in Chapter 3. As already proved in the last chapter, the nonlinear current control system by the prototype functions achieves similar performance as lookup tables (LUTs). At the same time, the required memory is significantly reduced. The effectiveness and applicability of the developed OFTC are confirmed by measurement results for a highly nonlinear RSM.

In this chapter, the introduced unified theory for OFTC is based on [50, 51], and it is applied intently to RSMs with the flux linkage prototype functions for the first time. In Section 5.1, the OFTC problem is formulated, and a possible solution is proposed. In Section 5.2, various machine equations with quadratic expression forms are derived. Subsequently, in Section 5.3, all operation strategies and the analytical solutions for them are presented. Lastly, in Section 5.4, experimental results with different scenarios are provided.

5.1 Problem statement

The developed machine torque of RSMs is given by

$$m_{\mathrm{m}}(\boldsymbol{i}_{\mathrm{s}}^{dq}) = \tfrac{2}{3\kappa^2} n_{\mathrm{p}} (\boldsymbol{i}_{\mathrm{s}}^{dq})^{\top} \boldsymbol{J} \boldsymbol{\psi}_{\mathrm{s}}^{dq}(\boldsymbol{i}_{\mathrm{s}}^{dq}) = \tfrac{2}{3\kappa^2} n_{\mathrm{p}} \left(\psi_{\mathrm{s}}^{d}(i_{\mathrm{s}}^{d}, i_{\mathrm{s}}^{q})\, i_{\mathrm{s}}^{q} - \psi_{\mathrm{s}}^{q}(i_{\mathrm{s}}^{d}, i_{\mathrm{s}}^{q})\, i_{\mathrm{s}}^{d} \right), \tag{5.1}$$

recalling from (2.14). Apparently, there are infinite current pairs (direct current i_{s}^{d} and quadrature current i_{s}^{q}) to produce a single torque value. Therefore, an appropriate current pair must

be chosen in accordance with operation conditions and requirements. For isotropic permanent magnet synchronous machines (PMSMs), i_s^d may be conveniently set to zero or a constant value due to the almost linear magnetic behavior. However, in the case of RSMs, both i_s^d and i_s^q must be nonzero and alter considerably over the whole operation range, owing to the extremely nonlinear magnetic characteristics.

Due to safety reasons during operation, stator voltage vector $\boldsymbol{u}_\mathrm{s}^{dq}$ and current vector $\boldsymbol{i}_\mathrm{s}^{dq}$ should not exceed their maximum magnitudes $\widehat{u}_\mathrm{max}$ and $\widehat{i}_\mathrm{max}$, respectively. Hence, the following operation constraints must be followed at any time instant [51], i.e.,

$$\|\boldsymbol{u}_\mathrm{s}^{dq}\|^2 = (u_\mathrm{s}^d)^2 + (u_\mathrm{s}^q)^2 \leq \widehat{u}_\mathrm{max}^2 \qquad \text{and} \qquad \|\boldsymbol{i}_\mathrm{s}^{dq}\|^2 = (i_\mathrm{s}^d)^2 + (i_\mathrm{s}^q)^2 \leq \widehat{i}_\mathrm{max}^2. \tag{5.2}$$

Normally, the maximum voltage magnitude $\widehat{u}_\mathrm{max}$ is equal to the voltage threshold of the inverter, which depends on the dc link voltage and the implemented modulation technique. On the other hand, the maximum current magnitude $\widehat{i}_\mathrm{max}$ can be set equivalent to the machine's rated current, although it is usually allowed to surpass the rated current for a short time period.

After realizing the nonlinearity of the RSM torque and also the operation constraints, the main objective of OFTC can be defined: for a given torque reference $m_\mathrm{m,ref}$, to obtain optimal and analytical solutions of the current references $\boldsymbol{i}_\mathrm{s,ref}^{dq} := (i_\mathrm{s,ref}^d, i_\mathrm{s,ref}^q)^\top$ for all operation strategies (MTPC, FW, MC and MTPV). To this end, the optimization problem [51]

$$\begin{aligned} \boldsymbol{i}_\mathrm{s,ref}^{dq} := \ & \arg\max_{\boldsymbol{i}_\mathrm{s}^{dq} \in \mathbb{S}} \ -f(\boldsymbol{i}_\mathrm{s}^{dq}) \quad \text{s.t.} \\ & \|\boldsymbol{u}_\mathrm{s}^{dq}\| \leq \widehat{u}_\mathrm{max}, \ \|\boldsymbol{i}_\mathrm{s}^{dq}\| \leq \widehat{i}_\mathrm{max}, \ |m_\mathrm{m}| \leq |m_\mathrm{m,ref}| \text{ and } \operatorname{sign}(m_\mathrm{m,ref}) = \operatorname{sign}(m_\mathrm{m}) \end{aligned} \tag{5.3}$$

with three inequality constraints and one equality constraint must be solved online. The first two constraints lay the feasible set $\mathbb{S}$ according to the voltage and current limits in (5.2). Additionally, the developed machine torque should not exceed its reference, and their signs must coincide. The cost function $f(\boldsymbol{i}_\mathrm{s}^{dq})$ should be designed according to the aims of the respective operation strategies, e.g., $f(\boldsymbol{i}_\mathrm{s}^{dq}) = \|\boldsymbol{i}_\mathrm{s}^{dq}\|^2$ for MTPC (for more details, see Section 5.3). An analytical solution of the optimal current references

$$\boldsymbol{i}_\mathrm{s,ref}^{dq}(m_\mathrm{m,ref}, \widehat{u}_\mathrm{max}, \widehat{i}_\mathrm{max}, \omega_\mathrm{p}) = \begin{pmatrix} i_\mathrm{s,ref}^d(m_\mathrm{m,ref}, \widehat{u}_\mathrm{max}, \widehat{i}_\mathrm{max}, \omega_\mathrm{p}) \\ i_\mathrm{s,ref}^q(m_\mathrm{m,ref}, \widehat{u}_\mathrm{max}, \widehat{i}_\mathrm{max}, \omega_\mathrm{p}) \end{pmatrix}, \tag{5.4}$$

as functions of torque reference $m_\mathrm{m,ref}$, maximum voltage $\widehat{u}_\mathrm{max}$, maximum current $\widehat{i}_\mathrm{max}$ and electrical angular frequency ω_p, can be derived as an outcome of the optimization problem in (5.3). Consequently, the proposed solution can provide optimal and analytical solutions in all operation strategies, which typically cannot be achieved with other existing methods.

The overall OFTC problem is solved by optimal current reference computation (OCRC) to generate both d and q current references, as shown in Fig. 5.1 [corresponding to (5.4)]. Then, current control system (e.g., the nonlinear current control system with input/output linearization introduced in Chapter 4) can be augmented with OCRC, i.e., handing over the generated current references by OCRC to any underlying current controllers. Therefore, a high-performance RSM drive system can be finally achieved with good current tracking and operation management.

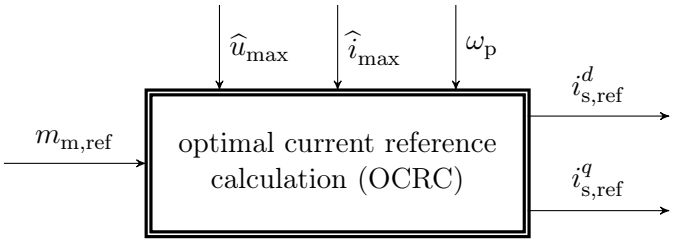

Figure 5.1: Optimal current references $\boldsymbol{i}^{dq}_{\mathrm{s,ref}} = (i^{d}_{\mathrm{s,ref}}, i^{q}_{\mathrm{s,ref}})^{\top}$ for given torque reference $m_{\mathrm{m,ref}}$, voltage constraint $\widehat{u}_{\max}$, current constraint $\widehat{i}_{\max}$ and actual electrical frequency ω_{p} (based on [50]).

5.2 Machine quadrics

In line with the concept presented in [50], machine torque and operation constraints are reformulated implicitly as quadrics (quadratic surfaces) in the following form

$$\mathbb{Q}_{\mathrm{A}}(\boldsymbol{i}^{dq}_{\mathrm{s}}) := \{\, \boldsymbol{i}^{dq}_{\mathrm{s}} \in \mathbb{R}^2 \mid \underbrace{(\boldsymbol{i}^{dq}_{\mathrm{s}})^{\top}\boldsymbol{A}\boldsymbol{i}^{dq}_{\mathrm{s}} + 2\boldsymbol{a}^{\top}\boldsymbol{i}^{dq}_{\mathrm{s}} + \alpha}_{=:q_{\mathrm{A}}(\boldsymbol{i}^{dq}_{\mathrm{s}})} = 0 \,\}, \tag{5.5}$$

where

$$\boldsymbol{A} = \boldsymbol{A}^{\top} := \begin{bmatrix} a_{11} & a_{12} \\ a_{12} & a_{22} \end{bmatrix} \in \mathbb{R}^{2\times 2},\ \boldsymbol{a} := \begin{pmatrix} a_1 \\ a_2 \end{pmatrix} \in \mathbb{R}^2 \ \text{ and } \alpha \in \mathbb{R}.$$

Consequently, the upcoming subsections derive the implicit forms of torque hyperbola, voltage ellipse (elliptical area) and current circle (circular area). This will pave the way for the analytical solutions of the current references in the OFTC problem. Besides, the machine nonlinearities are taken into account by means of online linearization.

5.2.1 Flux linkage linearization

As already thoroughly discovered in the previous chapters, due to the magnetic saturation and cross-coupling effects of RSMs, the resulting machine nonlinearities on flux linkages $\boldsymbol{\psi}^{dq}_{\mathrm{s}}(\boldsymbol{i}^{dq}_{\mathrm{s}})$ (see Fig. 5.2), torque $m_{\mathrm{m}}(\boldsymbol{i}^{dq}_{\mathrm{s}})$ (see Fig. 5.3) and also differential inductances $\boldsymbol{L}^{dq}_{\mathrm{s}}(\boldsymbol{i}^{dq}_{\mathrm{s}})$ are more severe than other SMs. Thus, they cannot be neglected in control algorithms, which can be saved by LUTs or represented with prototype functions. In order to take these nonlinearities into consideration for the proposed OFTC approach, they can be linearized around an arbitrary operation point $\overline{\boldsymbol{x}} := \overline{\boldsymbol{i}}^{dq}_{\mathrm{s}}$. Different quantities can be linearized by the first- or second-order Taylor series expansion.

For a vector-valued function $\boldsymbol{f}(\boldsymbol{x})$, its first-order approximation around the operation point $\overline{\boldsymbol{x}}$ is given by [51]

$$\boldsymbol{f}(\boldsymbol{x}) \approx \boldsymbol{f}(\overline{\boldsymbol{x}}) + \left.\frac{\mathrm{d}\boldsymbol{f}(\boldsymbol{x})}{\mathrm{d}\boldsymbol{x}^{\top}}\right|_{\overline{\boldsymbol{x}}} \cdot (\boldsymbol{x} - \overline{\boldsymbol{x}})\,. \tag{5.6}$$

Accordingly, at the operation point $\overline{\boldsymbol{i}}^{dq}_{\mathrm{s}}$, the nonlinear flux linkage vector can be approximated

as [51]

$$\begin{aligned}\boldsymbol{\psi}_\mathrm{s}^{dq}(\boldsymbol{i}_\mathrm{s}^{dq}) &\approx \underbrace{\boldsymbol{\psi}_\mathrm{s}^{dq}(\bar{\boldsymbol{i}}_\mathrm{s}^{dq})}_{=:\bar{\boldsymbol{\psi}}_\mathrm{s}^{dq}} + \underbrace{\left.\frac{\mathrm{d}\boldsymbol{\psi}_\mathrm{s}^{dq}(\boldsymbol{i}_\mathrm{s}^{dq})}{\mathrm{d}\boldsymbol{i}_\mathrm{s}^{dq}}\right|_{\bar{\boldsymbol{i}}_\mathrm{s}^{dq}}}_{=:\bar{\boldsymbol{L}}_\mathrm{s}^{dq}} \cdot \big(\underbrace{\boldsymbol{i}_\mathrm{s}^{dq} - \bar{\boldsymbol{i}}_\mathrm{s}^{dq}}_{=:\Delta\boldsymbol{i}_\mathrm{s}^{dq}}\big) \\ &\approx \bar{\boldsymbol{\psi}}_\mathrm{s}^{dq} + \bar{\boldsymbol{L}}_\mathrm{s}^{dq}\,\Delta\boldsymbol{i}_\mathrm{s}^{dq}\end{aligned} \tag{5.7}$$

for the upcoming derivations (quantities evaluated at the operation point are denoted with overline, i.e., $\bar{\boldsymbol{\psi}}_\mathrm{s}^{dq}$ and $\bar{\boldsymbol{L}}_\mathrm{s}^{dq}$ at $\bar{\boldsymbol{i}}_\mathrm{s}^{dq}$), where the differential inductance matrix

$$\bar{\boldsymbol{L}}_\mathrm{s}^{dq} := \left.\begin{bmatrix} \frac{\partial\psi_\mathrm{s}^{d}}{\partial i_\mathrm{s}^{d}} & \frac{\partial\psi_\mathrm{s}^{d}}{\partial i_\mathrm{s}^{q}} \\ \frac{\partial\psi_\mathrm{s}^{q}}{\partial i_\mathrm{s}^{d}} & \frac{\partial\psi_\mathrm{s}^{q}}{\partial i_\mathrm{s}^{q}} \end{bmatrix}\right|_{\bar{\boldsymbol{i}}_\mathrm{s}^{dq}} := \begin{bmatrix} \bar{L}_\mathrm{s}^{d} & \bar{L}_\mathrm{s}^{dq} \\ \bar{L}_\mathrm{s}^{qd} & \bar{L}_\mathrm{s}^{q} \end{bmatrix} = (\bar{\boldsymbol{L}}_\mathrm{s}^{dq})^\top > 0 \tag{5.8}$$

is symmetric (i.e., $\bar{L}_\mathrm{s}^{dq} = \bar{L}_\mathrm{s}^{qd}$) and positive definite. Through the linearization in (5.7), an affine approximation with offset $\bar{\boldsymbol{\psi}}_\mathrm{s}^{dq}$ and tangential surface $\bar{\boldsymbol{L}}_\mathrm{s}^{dq}\Delta\boldsymbol{i}_\mathrm{s}^{dq}$ can be obtained.

In Fig. 5.2, flux linkage linearization is demonstrated exemplarily for the nonlinear flux linkages of a 4.0 kW RSM. Without suffering from limited measurement range, fitted flux linkages using the RSM flux linkage prototype function II (see Chapter 3) are utilized instead, owing to its high accuracy and differentiable continuity. The fitted d-axis flux linkage $\widehat{\psi}_\mathrm{s}^{d}$ and q-axis flux linkage $\widehat{\psi}_\mathrm{s}^{q}$ are shown with colored surfaces in Fig. 5.2(a) and 5.2(b) [retrieved from Fig. 3.11(a) and 3.11(b)], respectively. By means of the flux linkage linearization (5.7), the resulting tangential surfaces [■] for both d and q components at the operation point $\bar{\boldsymbol{i}}_\mathrm{s}^{dq}$ [■] are presented.

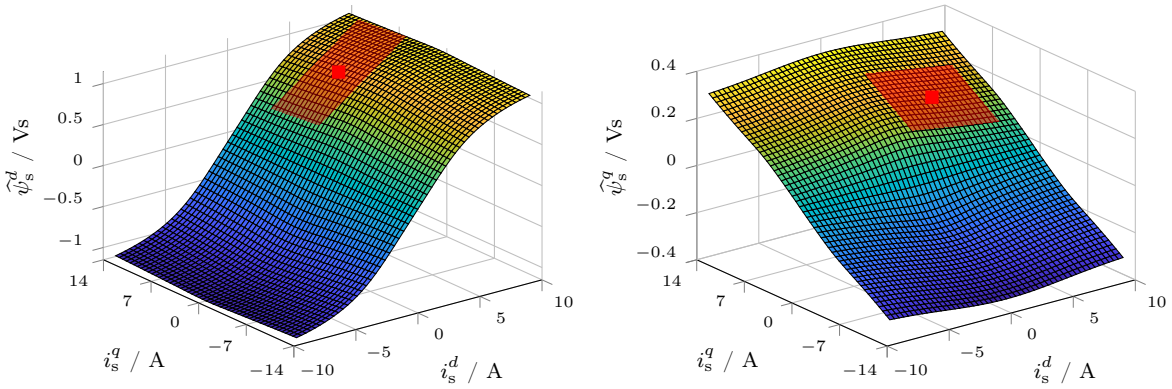

(a) (b)

Figure 5.2: Flux linkage linearization of a 4.0 kW RSM: (a) d-axis flux linkage $\widehat{\psi}_\mathrm{s}^{d}$; (b) q-axis flux linkage $\widehat{\psi}_\mathrm{s}^{q}$ (where $\widehat{\psi}_\mathrm{s}^{d}$ and $\widehat{\psi}_\mathrm{s}^{q}$ are the fitted flux linkages [colored surfaces] by the flux linkage prototype functions, and the linearization (5.7) results in tangential surfaces [■] at $\bar{\boldsymbol{i}}_\mathrm{s}^{dq}$ [■]).

5.2.2 Torque hyperbola

In addition to the flux linkages, the nonlinear machine torque and the voltage limit must also be linearized. As they are both scalar quantities and a more accurate second-order approximation is to be made, a general linearization of scalar function is briefly discussed here. For a scalar function [51]

$$f(\boldsymbol{x}) := \boldsymbol{g}(\boldsymbol{x})^\top \boldsymbol{M}\boldsymbol{h}(\boldsymbol{x}) \tag{5.9}$$

with an arbitrary matrix $\boldsymbol{M} \in \mathbb{R}^{n\times m}$ and two continuously differentiable functions $\boldsymbol{g}(\boldsymbol{x}) \in \mathbb{R}^n$ & $\boldsymbol{h}(\boldsymbol{x}) \in \mathbb{R}^m$, the first derivative (gradient) and approximated second derivative (symmetric Hessian matrix) can be derived as

$$\left(\frac{\mathrm{d}f(\boldsymbol{x})}{\mathrm{d}\boldsymbol{x}}\right)^\top = \boldsymbol{h}(\boldsymbol{x})^\top \boldsymbol{M}^\top \left[\frac{\mathrm{d}\boldsymbol{g}(\boldsymbol{x})}{\mathrm{d}\boldsymbol{x}^\top}\right] + \boldsymbol{g}(\boldsymbol{x})^\top \boldsymbol{M} \left[\frac{\mathrm{d}\boldsymbol{h}(\boldsymbol{x})}{\mathrm{d}\boldsymbol{x}^\top}\right]$$

and

$$\left[\frac{\mathrm{d}^2 f(\boldsymbol{x})}{\mathrm{d}\boldsymbol{x}\mathrm{d}\boldsymbol{x}^\top}\right] \approx \left[\frac{\mathrm{d}\boldsymbol{h}(\boldsymbol{x})^\top}{\mathrm{d}\boldsymbol{x}}\right] \boldsymbol{M}^\top \left[\frac{\mathrm{d}\boldsymbol{g}(\boldsymbol{x})}{\mathrm{d}\boldsymbol{x}^\top}\right] + \left[\frac{\mathrm{d}\boldsymbol{g}(\boldsymbol{x})^\top}{\mathrm{d}\boldsymbol{x}}\right] \boldsymbol{M} \left[\frac{\mathrm{d}\boldsymbol{h}(\boldsymbol{x})}{\mathrm{d}\boldsymbol{x}^\top}\right],$$

respectively, where $\frac{\mathrm{d}}{\mathrm{d}\boldsymbol{x}}\left[\frac{\mathrm{d}\boldsymbol{g}(\boldsymbol{x})}{\mathrm{d}\boldsymbol{x}^\top}\right]$ and $\frac{\mathrm{d}}{\mathrm{d}\boldsymbol{x}}\left[\frac{\mathrm{d}\boldsymbol{h}(\boldsymbol{x})}{\mathrm{d}\boldsymbol{x}^\top}\right]$ are neglected in the second derivative (for more details, see [51]). Applying Taylor series expansion to $f(\boldsymbol{x})$ in (5.9), its second-order approximation

$$f(\boldsymbol{x}) \approx f(\overline{\boldsymbol{x}}) + \left(\frac{\mathrm{d}f(\boldsymbol{x})}{\mathrm{d}\boldsymbol{x}}\bigg|_{\overline{\boldsymbol{x}}}\right)^\top (\boldsymbol{x}-\overline{\boldsymbol{x}}) + \tfrac{1}{2}(\boldsymbol{x}-\overline{\boldsymbol{x}})^\top \left[\frac{\mathrm{d}^2 f(\boldsymbol{x})}{\mathrm{d}\boldsymbol{x}\mathrm{d}\boldsymbol{x}^\top}\bigg|_{\overline{\boldsymbol{x}}}\right] (\boldsymbol{x}-\overline{\boldsymbol{x}}) \tag{5.10}$$

at the operation point $\overline{\boldsymbol{x}}$ can be obtained.

Now, the linearization (5.10) can be applied to the machine torque in (5.1) by selecting $\boldsymbol{x} = \boldsymbol{g}(\boldsymbol{x}) = \boldsymbol{i}_\mathrm{s}^{dq}$, $f(\boldsymbol{x}) = m_\mathrm{m}(\boldsymbol{i}_\mathrm{s}^{dq})$, $\boldsymbol{M} = \boldsymbol{J}$ and $\boldsymbol{h}(\boldsymbol{x}) = \boldsymbol{\psi}_\mathrm{s}^{dq}(\boldsymbol{i}_\mathrm{s}^{dq})$. This leads to the approximation of the machine torque [51]

$$\begin{aligned}
m_\mathrm{m}(\boldsymbol{i}_\mathrm{s}^{dq}) \overset{(5.1)}{=} & \tfrac{2}{3\kappa^2} n_\mathrm{p} (\boldsymbol{i}_\mathrm{s}^{dq})^\top \boldsymbol{J} \boldsymbol{\psi}_\mathrm{s}^{dq}(\boldsymbol{i}_\mathrm{s}^{dq}) \\
\overset{(5.10),(5.7)}{\approx} & \underbrace{\tfrac{2}{3\kappa^2} n_\mathrm{p} (\overline{\boldsymbol{i}}_\mathrm{s}^{dq})^\top \boldsymbol{J} \overline{\boldsymbol{\psi}}_\mathrm{s}^{dq}}_{=:\overline{m}_\mathrm{m}} \\
& + 2 \underbrace{\tfrac{1}{3\kappa^2} n_\mathrm{p} \left[(\overline{\boldsymbol{\psi}}_\mathrm{s}^{dq})^\top \boldsymbol{J}^\top + (\overline{\boldsymbol{i}}_\mathrm{s}^{dq})^\top \boldsymbol{J} \overline{\boldsymbol{L}}_\mathrm{s}^{dq}\right]}_{=:\overline{\boldsymbol{m}}^\top} (\boldsymbol{i}_\mathrm{s}^{dq} - \overline{\boldsymbol{i}}_\mathrm{s}^{dq}) \\
& + (\boldsymbol{i}_\mathrm{s}^{dq} - \overline{\boldsymbol{i}}_\mathrm{s}^{dq})^\top \underbrace{\tfrac{1}{3\kappa^2} n_\mathrm{p} \left[(\overline{\boldsymbol{L}}_\mathrm{s}^{dq})^\top \boldsymbol{J}^\top + \boldsymbol{J} \overline{\boldsymbol{L}}_\mathrm{s}^{dq}\right]}_{=:\overline{\boldsymbol{M}}} (\boldsymbol{i}_\mathrm{s}^{dq} - \overline{\boldsymbol{i}}_\mathrm{s}^{dq}) \\
\approx & \ \overline{m}_\mathrm{m} + 2\,\overline{\boldsymbol{m}}^\top \Delta \boldsymbol{i}_\mathrm{s}^{dq} + (\Delta \boldsymbol{i}_\mathrm{s}^{dq})^\top \overline{\boldsymbol{M}} \Delta \boldsymbol{i}_\mathrm{s}^{dq}
\end{aligned} \tag{5.11}$$

as a quadratic function at the operation point depending on the stator currents $\boldsymbol{i}_\mathrm{s}^{dq}$, the operation currents $\overline{\boldsymbol{i}}_\mathrm{s}^{dq}$ and the difference $\Delta \boldsymbol{i}_\mathrm{s}^{dq} = \boldsymbol{i}_\mathrm{s}^{dq} - \overline{\boldsymbol{i}}_\mathrm{s}^{dq}$. In Fig. 5.3, the nonlinear machine torque $m_\mathrm{m}(\boldsymbol{i}_\mathrm{s}^{dq})$ of the considered 4.0 kW RSM is illustrated in colored surface with the linearized torque via (5.11) (tangential surface [■]). Besides, a torque reference $m_\mathrm{m,ref}$ [■] is exemplarily given and shown.

Subsequent to torque linearization, the torque hyperbola can be formulated as a quadric in (5.5) with the linearized machine torque (5.11). According to the torque constraint in the optimization problem (5.3), the developed machine torque must equal the torque reference, i.e., $m_\mathrm{m} \overset{!}{=} m_\mathrm{m,ref}$. Following this definition, the approximated torque hyperbola (as presented in Fig. 5.4 [—]) can be obtained as follows

$$\boxed{\overline{\mathbb{T}}(m_\mathrm{m,ref}) := \{\, \boldsymbol{i}_\mathrm{s}^{dq} \in \mathbb{R}^2 \mid (\boldsymbol{i}_\mathrm{s}^{dq})^\top \overline{\boldsymbol{T}} \boldsymbol{i}_\mathrm{s}^{dq} + 2\overline{\boldsymbol{t}}^\top \boldsymbol{i}_\mathrm{s}^{dq} + \overline{\tau}(m_\mathrm{m,ref}) = 0 \,\}} \tag{5.12}$$

with the following matrix, vector and scalar

$$\left.\begin{aligned}
\overline{\boldsymbol{T}} &:= \begin{bmatrix} \bar{t}_{11} & \bar{t}_{12} \\ \bar{t}_{12} & \bar{t}_{22} \end{bmatrix} := \overline{\boldsymbol{M}} = \overline{\boldsymbol{T}}^{\top}, \\
\bar{\boldsymbol{t}} &:= \begin{pmatrix} \bar{t}_1 \\ \bar{t}_2 \end{pmatrix} := \left(\overline{\boldsymbol{m}}^{\top} - (\bar{\boldsymbol{i}}_{\mathrm{s}}^{dq})^{\top} \overline{\boldsymbol{M}} \right)^{\top}, \\
\overline{\tau}(m_{\mathrm{m,ref}}) &:= \overline{m}_{\mathrm{m}} - 2\overline{\boldsymbol{m}}^{\top} \bar{\boldsymbol{i}}_{\mathrm{s}}^{dq} + (\bar{\boldsymbol{i}}_{\mathrm{s}}^{dq})^{\top} \overline{\boldsymbol{M}}\, \bar{\boldsymbol{i}}_{\mathrm{s}}^{dq} - m_{\mathrm{m,ref}}.
\end{aligned}\right\} \tag{5.13}$$

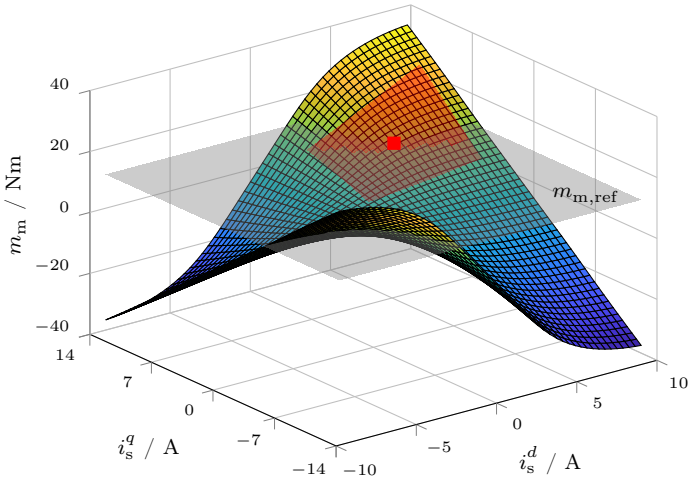

Figure 5.3: Torque linearization of a 4.0 kW RSM (where m_{m} represents the nonlinear machine torque [colored surface] with a given torque reference $m_{\mathrm{m,ref}}$ [▭], and the linearization (5.11) results in tangential surface [▭] at $\bar{\boldsymbol{i}}_{\mathrm{s}}^{dq}$ [▪]).

5.2.3 Voltage ellipse

In the introduced OFTC problem, the steady-state operation is considered with the simplified voltage equation

$$\boldsymbol{u}_{\mathrm{s}}^{dq} = R_{\mathrm{s}} \boldsymbol{i}_{\mathrm{s}}^{dq} + \omega_{\mathrm{p}} \boldsymbol{J} \boldsymbol{\psi}_{\mathrm{s}}^{dq}(\boldsymbol{i}_{\mathrm{s}}^{dq}), \tag{5.14}$$

where the flux linkage derivative $\frac{\mathrm{d}}{\mathrm{d}t} \boldsymbol{\psi}_{\mathrm{s}}^{dq}(\boldsymbol{i}_{\mathrm{s}}^{dq})$ in the electrical subsystem in (2.5) is neglected. This assumption is justified, as the torque reference normally changes much slower than the (well-tuned) current dynamics.

With the help of assigning $\boldsymbol{x} = \boldsymbol{i}_\mathrm{s}^{dq}$, $f(\boldsymbol{x}) = \|\boldsymbol{u}_\mathrm{s}^{dq}(\boldsymbol{i}_\mathrm{s}^{dq})\|^2$, $\boldsymbol{M} = \boldsymbol{I}_2$ and $\boldsymbol{g}(\boldsymbol{x}) = \boldsymbol{h}(\boldsymbol{x}) =$ (5.14), the squared norm of the steady-state voltage $\|\boldsymbol{u}_\mathrm{s}^{dq}\|^2$ can be linearized through the quadratic approximation (5.10). One obtains [51]

$$
\begin{aligned}
\|\boldsymbol{u}_\mathrm{s}^{dq}(\boldsymbol{i}_\mathrm{s}^{dq})\|^2 \overset{(5.14)}{=} & \left(R_\mathrm{s}\boldsymbol{i}_\mathrm{s}^{dq} + \omega_\mathrm{p}\boldsymbol{J}\boldsymbol{\psi}_\mathrm{s}^{dq}(\boldsymbol{i}_\mathrm{s}^{dq})\right)^\top \boldsymbol{I}_2 \left(R_\mathrm{s}\boldsymbol{i}_\mathrm{s}^{dq} + \omega_\mathrm{p}\boldsymbol{J}\boldsymbol{\psi}_\mathrm{s}^{dq}(\boldsymbol{i}_\mathrm{s}^{dq})\right) \\
\overset{(5.10),(5.7)}{\approx} & \underbrace{(\overline{R}_\mathrm{s}\bar{\boldsymbol{i}}_\mathrm{s}^{dq} + \overline{\omega}_\mathrm{p}\boldsymbol{J}\overline{\boldsymbol{\psi}}_\mathrm{s}^{dq})^\top \boldsymbol{I}_2 (\overline{R}_\mathrm{s}\bar{\boldsymbol{i}}_\mathrm{s}^{dq} + \overline{\omega}_\mathrm{p}\boldsymbol{J}\overline{\boldsymbol{\psi}}_\mathrm{s}^{dq})}_{=:\|\overline{\boldsymbol{u}}_\mathrm{s}^{dq}\|^2} \\
& + 2\underbrace{(\overline{\boldsymbol{u}}_\mathrm{s}^{dq})^\top (\overline{R}_\mathrm{s}\boldsymbol{I}_2 + \overline{\omega}_\mathrm{p}\boldsymbol{J}\overline{\boldsymbol{L}}_\mathrm{s}^{dq})}_{=:\overline{\boldsymbol{u}}^\top}(\boldsymbol{i}_\mathrm{s}^{dq} - \bar{\boldsymbol{i}}_\mathrm{s}^{dq}) \\
& + (\boldsymbol{i}_\mathrm{s}^{dq} - \bar{\boldsymbol{i}}_\mathrm{s}^{dq})^\top \underbrace{(\overline{R}_\mathrm{s}\boldsymbol{I}_2 + \overline{\omega}_\mathrm{p}\boldsymbol{J}\overline{\boldsymbol{L}}_\mathrm{s}^{dq})^\top (\overline{R}_\mathrm{s}\boldsymbol{I}_2 + \overline{\omega}_\mathrm{p}\boldsymbol{J}\overline{\boldsymbol{L}}_\mathrm{s}^{dq})}_{=:\overline{\boldsymbol{U}}}(\boldsymbol{i}_\mathrm{s}^{dq} - \bar{\boldsymbol{i}}_\mathrm{s}^{dq}) \\
\approx & \|\overline{\boldsymbol{u}}_\mathrm{s}^{dq}\|^2 + 2\,\overline{\boldsymbol{u}}^\top \Delta\boldsymbol{i}_\mathrm{s}^{dq} + (\Delta\boldsymbol{i}_\mathrm{s}^{dq})^\top \overline{\boldsymbol{U}}\Delta\boldsymbol{i}_\mathrm{s}^{dq}.
\end{aligned}
\tag{5.15}
$$

Inserting (5.15) into the voltage constraint in (5.2), the approximated voltage elliptical area can be described implicitly as a quadratic surface as

$$
\overline{\mathbb{V}}(\widehat{u}_\mathrm{max}) := \{\, \boldsymbol{i}_\mathrm{s}^{dq} \in \mathbb{R}^2 \mid (\boldsymbol{i}_\mathrm{s}^{dq})^\top \overline{\boldsymbol{V}}\boldsymbol{i}_\mathrm{s}^{dq} + 2\overline{\boldsymbol{v}}^\top \boldsymbol{i}_\mathrm{s}^{dq} + \overline{\nu}(\widehat{u}_\mathrm{max}) \leq 0 \,\}. \tag{5.16}
$$

Furthermore, its boundary, the approximated voltage ellipse (as illustrated in Fig. 5.4 [—]), is given by

$$
\boxed{\partial\overline{\mathbb{V}}(\widehat{u}_\mathrm{max}) := \{\, \boldsymbol{i}_\mathrm{s}^{dq} \in \mathbb{R}^2 \mid (\boldsymbol{i}_\mathrm{s}^{dq})^\top \overline{\boldsymbol{V}}\boldsymbol{i}_\mathrm{s}^{dq} + 2\overline{\boldsymbol{v}}^\top \boldsymbol{i}_\mathrm{s}^{dq} + \overline{\nu}(\widehat{u}_\mathrm{max}) = 0 \,\},} \tag{5.17}
$$

where

$$
\left.
\begin{aligned}
\overline{\boldsymbol{V}} &:= \begin{bmatrix} \overline{v}_{11} & \overline{v}_{12} \\ \overline{v}_{12} & \overline{v}_{22} \end{bmatrix} := \overline{\boldsymbol{U}} = \overline{\boldsymbol{V}}^\top, \\
\overline{\boldsymbol{v}} &:= \begin{pmatrix} \overline{v}_1 \\ \overline{v}_2 \end{pmatrix} := \left(\overline{\boldsymbol{u}}^\top - (\bar{\boldsymbol{i}}_\mathrm{s}^{dq})^\top \overline{\boldsymbol{U}}\right)^\top, \\
\overline{\nu}(\widehat{u}_\mathrm{max}) &:= \|\overline{\boldsymbol{u}}_\mathrm{s}^{dq}\|^2 - 2\overline{\boldsymbol{u}}^\top \bar{\boldsymbol{i}}_\mathrm{s}^{dq} + (\bar{\boldsymbol{i}}_\mathrm{s}^{dq})^\top \overline{\boldsymbol{U}}\,\bar{\boldsymbol{i}}_\mathrm{s}^{dq} - \widehat{u}_\mathrm{max}^2.
\end{aligned}
\right\} \tag{5.18}
$$

5.2.4 Current circle

The current constraint in (5.2) can also be reformulated implicitly as a quadric by [51]

$$
\mathbb{I}(\widehat{i}_\mathrm{max}) := \{\, \boldsymbol{i}_\mathrm{s}^{dq} \in \mathbb{R}^2 \mid (\boldsymbol{i}_\mathrm{s}^{dq})^\top \boldsymbol{I}_2 \boldsymbol{i}_\mathrm{s}^{dq} - \widehat{i}_\mathrm{max}^2 \leq 0 \,\}, \tag{5.19}
$$

which describes the maximum admissible current circular area in the current plane. Similar to the voltage ellipse, the boundary of (5.19), the current circle (as shown in Fig. 5.4 [—]), is given by

$$
\boxed{\partial\mathbb{I}(\widehat{i}_\mathrm{max}) := \{\, \boldsymbol{i}_\mathrm{s}^{dq} \in \mathbb{R}^2 \mid (\boldsymbol{i}_\mathrm{s}^{dq})^\top \boldsymbol{I}_2 \boldsymbol{i}_\mathrm{s}^{dq} - \widehat{i}_\mathrm{max}^2 = 0 \,\}.} \tag{5.20}
$$

Different from the previously introduced torque hyperbola and voltage ellipse, the current circle is not linearized per (5.10) and, therefore, stays fixed for all operation points. The maximum current $\widehat{i}_\mathrm{max}$ decides the radius of the current circle and changes for different machines; moreover, it may be adapted online in accordance with the machine temperature during operation.

5.3 Operation strategies

With the derived machine quadrics, it has been proposed in [50] in the sense of a unified theory of the optimal torque control problem: (i) The general but nonlinear optimization problem (5.3) with constraints can be approximated as a quadratic optimization problem [or called quadratic programming (QP)] with a quadratic equality constraint, i.e.,

$$\begin{aligned} \boldsymbol{i}_{\mathrm{s,ref}}^{dq} := \ \arg\max_{\boldsymbol{i}_{\mathrm{s}}^{dq}\in\overline{\mathbb{S}}} \ & -\Big(\underbrace{(\boldsymbol{i}_{\mathrm{s}}^{dq})^{\top}\boldsymbol{A}\boldsymbol{i}_{\mathrm{s}}^{dq}+2\boldsymbol{a}^{\top}\boldsymbol{i}_{\mathrm{s}}^{dq}+\alpha}_{=:q_{\mathrm{A}}(\boldsymbol{i}_{\mathrm{s}}^{dq})}\Big) \\ \text{s.t.} \ & \underbrace{(\boldsymbol{i}_{\mathrm{s}}^{dq})^{\top}\boldsymbol{B}\boldsymbol{i}_{\mathrm{s}}^{dq}+2\boldsymbol{b}^{\top}\boldsymbol{i}_{\mathrm{s}}^{dq}+\beta}_{=:q_{\mathrm{B}}(\boldsymbol{i}_{\mathrm{s}}^{dq})}=0, \end{aligned} \tag{5.21}$$

where $\boldsymbol{A},\boldsymbol{B}\in\mathbb{R}^{2\times2}$, $\boldsymbol{a},\boldsymbol{b}\in\mathbb{R}^{2}$ and $\alpha,\beta\in\mathbb{R}$ describe the quadratic forms $q_{\mathrm{A}}(\boldsymbol{i}_{\mathrm{s}}^{dq})$ and $q_{\mathrm{B}}(\boldsymbol{i}_{\mathrm{s}}^{dq})$, respectively, and follow the definitions in (5.5). The approximated feasible set $\overline{\mathbb{S}}\subset\mathbb{S}$ is a subset of the original feasible set $\mathbb{S}$. (ii) Then, the quadratic optimization problem (5.21) can be solved analytically by means of the Lagrangian formalism. (iii) Eventually, the analytical solution of the optimal current references

$$\boxed{\boldsymbol{i}_{\mathrm{s,ref}}^{dq}=\boldsymbol{i}_{\mathrm{s,X}}^{dq}:=\mathbb{Q}_{\mathrm{A}}(\boldsymbol{i}_{\mathrm{s}}^{dq})\cap\mathbb{Q}_{\mathrm{B}}(\boldsymbol{i}_{\mathrm{s}}^{dq}) \quad \text{for X}\in\{\text{MTPC, FW, MC, MTPV}\}} \tag{5.22}$$

can be obtained in all operation strategies by finding the optimal intersection point of two respective quadrics $\mathbb{Q}_{\mathrm{A}}(\boldsymbol{i}_{\mathrm{s}}^{dq})$ and $\mathbb{Q}_{\mathrm{B}}(\boldsymbol{i}_{\mathrm{s}}^{dq})$, which can be computed analytically by looking for the roots of a fourth-order polynomial.

This section discusses the operation strategies, including MTPC, FW, MC and MTPV, in detail with their respective optimization problems and solutions. In order to better illustrate different operation strategies, Fig. 5.4 presents them separately for different mechanical angular velocities ω_{m} from low to high and a fixed torque reference $m_{\mathrm{m,ref}}=0.5m_{\mathrm{m,R}}$ with

- torque hyperbola $\overline{\mathbb{T}}(m_{\mathrm{m,ref}})$ [—],
- voltage ellipse $\partial\overline{\mathbb{V}}(\widehat{u}_{\mathrm{max}})$ [—],
- current circle $\partial\mathbb{I}(\widehat{i}_{\mathrm{max}})$ [—],
- admissible current area $\overline{\mathbb{S}}$ [ ],
- MTPC hyperbola $\overline{\mathbb{MTPC}}$ [—],
- MTPV hyperbola $\overline{\mathbb{MTPV}}$ [—] and
- respective optimal current references $\boldsymbol{i}_{\mathrm{s,ref}}^{dq}$ [★].

Note that the voltage and current constraints are selected exemplarily identical to the machine rating, i.e., $\widehat{u}_{\mathrm{max}}=\widehat{u}_{\mathrm{s,R}}$ and $\widehat{i}_{\mathrm{max}}=\widehat{i}_{\mathrm{s,R}}$ (see Table 4.1). Furthermore, operation management between all operation strategies for a wide-range operation is introduced.

5.3.1 Maximum torque per current (MTPC)

For low to medium speed range, where the voltage constraint in (5.2) is not critical, MTPC dominates the operation of the machine in the OFTC problem. Its goal is to achieve the best machine efficiency by minimizing the copper losses $p_{\mathrm{s,Cu,L}}:=\frac{2}{3\kappa^2}R_{\mathrm{s}}\|\boldsymbol{i}_{\mathrm{s}}^{dq}\|^2$, while following the

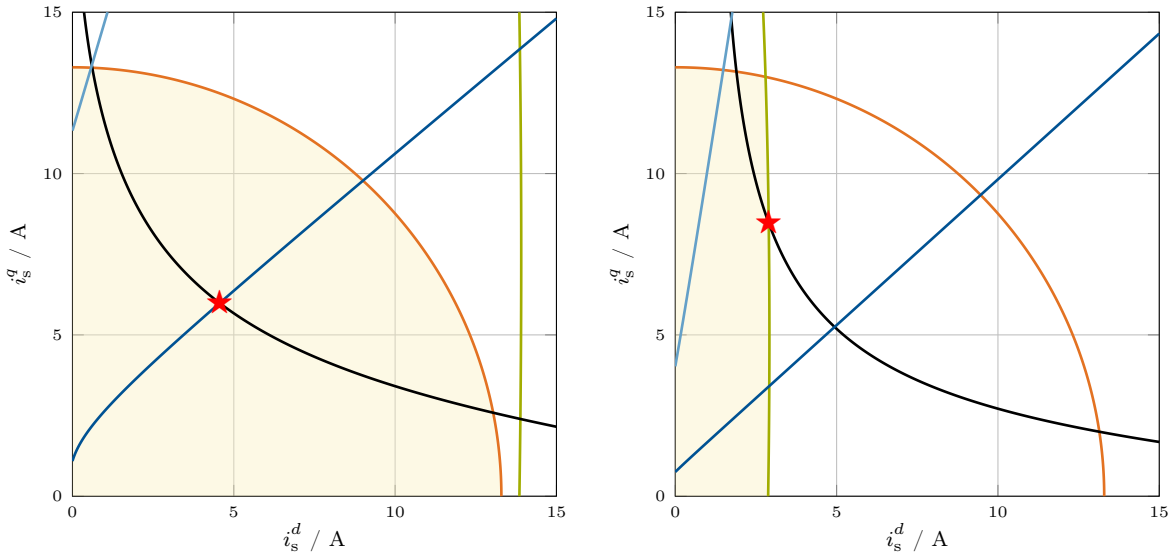

(a) MTPC at $\omega_m = 0.5\omega_{m,R}$

(b) FW at $\omega_m = 1.5\omega_{m,R}$

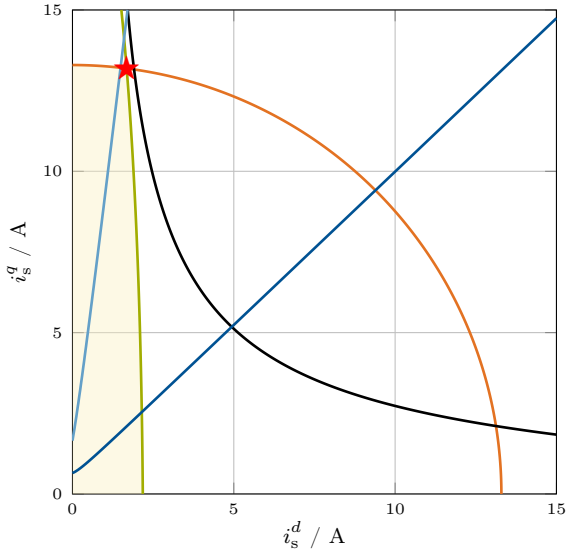

(c) MC at $\omega_m = 2\omega_{m,R}$

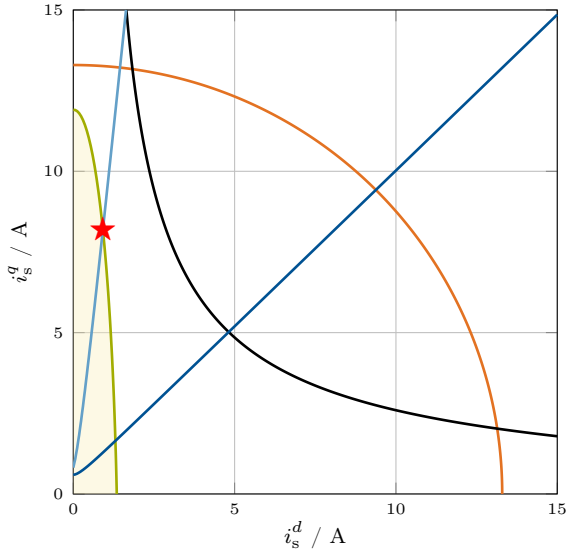

(d) MTPV at $\omega_m = 3\omega_{m,R}$

Figure 5.4: Current loci for different operation strategies with different speeds ω_m and a fixed torque reference $m_{m,ref} = 0.5m_{m,R}$: (a) MTPC at $\omega_m = 0.5\omega_{m,R}$; (b) FW at $\omega_m = 1.5\omega_{m,R}$; (c) MC at $\omega_m = 2\omega_{m,R}$; (d) MTPV at $\omega_m = 3\omega_{m,R}$ (where $\overline{\mathbb{T}}(m_{m,ref})$ [—], $\partial\overline{\mathbb{V}}(\widehat{u}_{max})$ [—], $\partial\mathbb{I}(\widehat{i}_{max})$ [—], $\overline{\mathbb{S}}$ [ ], $\overline{\mathbb{MTPC}}$ [—], $\overline{\mathbb{MTPV}}$ [—] and $\boldsymbol{i}_{s,ref}^{dq}$ [★]).

current constraint in (5.2). The general MTPC optimization problem is formulated as follows [51]

$$\boldsymbol{i}_{s,ref}^{dq} := \arg\max_{\boldsymbol{i}_s^{dq} \in \mathbb{S}} \; -\|\boldsymbol{i}_s^{dq}\|^2 \quad \text{s.t.} \quad m_m(\boldsymbol{i}_s^{dq}) \stackrel{!}{=} m_{m,ref}. \tag{5.23}$$

The squared current magnitude, which is proportional to the copper losses, should be minimized under the nonlinear torque equality constraint. Furthermore, with the help of the approximated torque hyperbola (5.12), the nonlinear MTPC optimization problem (5.23) can be approximated

as a quadratic optimization problem

$$\boldsymbol{i}_{\mathrm{s,ref}}^{dq} := \arg\max_{\boldsymbol{i}_{\mathrm{s}}^{dq}\in\overline{\mathbb{S}}} -(\boldsymbol{i}_{\mathrm{s}}^{dq})^{\top}\boldsymbol{I}_2\boldsymbol{i}_{\mathrm{s}}^{dq} \quad \text{s.t.} \quad \underbrace{(\boldsymbol{i}_{\mathrm{s}}^{dq})^{\top}\overline{\boldsymbol{T}}\boldsymbol{i}_{\mathrm{s}}^{dq} + 2\overline{\boldsymbol{t}}^{\top}\boldsymbol{i}_{\mathrm{s}}^{dq} + \overline{\tau}(m_{\mathrm{m,ref}})}_{\overset{(5.12)}{\approx} m_{\mathrm{m}}(\boldsymbol{i}_{\mathrm{s}}^{dq}) - m_{\mathrm{m,ref}}} = 0 \tag{5.24}$$

by following the form of (5.21). The approximated feasible set

$$\overline{\mathbb{S}} := \overline{\mathbb{V}}(\widehat{u}_{\max}) \cap \mathbb{I}(\widehat{i}_{\max}) \subset \mathbb{S} \tag{5.25}$$

is the intersection surface, as illustrated in Fig. 5.4 [ ], of approximated voltage elliptical area $\overline{\mathbb{V}}(\widehat{u}_{\max})$ and current circular area $\mathbb{I}(\widehat{i}_{\max})$.

The solution of the approximated MTPC optimization problem (5.24), the MTPC hyperbola (as shown in Fig. 5.4 [—]), can be expressed again as a quadric [51]

$$\boxed{\overline{\mathbb{MTPC}} := \{\, \boldsymbol{i}_{\mathrm{s}}^{dq} \in \mathbb{R}^2 \mid (\boldsymbol{i}_{\mathrm{s}}^{dq})^{\top}\overline{\boldsymbol{M}}_{\mathrm{C}}\boldsymbol{i}_{\mathrm{s}}^{dq} + 2\overline{\boldsymbol{m}}_{\mathrm{C}}^{\top}\boldsymbol{i}_{\mathrm{s}}^{dq} + \overline{\mu}_{\mathrm{C}} = 0 \,\},} \tag{5.26}$$

where

$$\left.\begin{aligned} \overline{\boldsymbol{M}}_{\mathrm{C}} = \overline{\boldsymbol{M}}_{\mathrm{C}}^{\top} &:= \begin{bmatrix} \overline{t}_{12} & \frac{1}{2}(\overline{t}_{22} - \overline{t}_{11}) \\ \frac{1}{2}(\overline{t}_{22} - \overline{t}_{11}) & -\overline{t}_{12} \end{bmatrix}, \\ \overline{\boldsymbol{m}}_{\mathrm{C}} &:= \tfrac{1}{2}\begin{pmatrix} \overline{t}_2 \\ -\overline{t}_1 \end{pmatrix}, \\ \overline{\mu}_{\mathrm{C}} &:= 0 \end{aligned}\right\} \tag{5.27}$$

are dependent on the corresponding entries of the torque matrix $\overline{\boldsymbol{T}}$ and the torque vector $\overline{\boldsymbol{t}}$ in (5.13). By applying the Lagrangian formalism to (5.24), the implicit form as a quadric in (5.26) and the explicit expressions in (5.27) are obtained (for the detailed derivation, see Appendix 2 in [50]). Similarly, this derivation can also be performed for the MTPV strategy to achieve its implicit form and explicit expressions.

For the MTPC operation strategy, the optimal current reference vector [51]

$$\boxed{\boldsymbol{i}_{\mathrm{s,MTPC}}^{dq} := \overline{\mathbb{MTPC}} \cap \overline{\mathbb{T}}(m_{\mathrm{m,ref}})} \tag{5.28}$$

is the intersection point, as shown in Fig. 5.4(a) (marked by [★]), of approximated MTPC hyperbola $\overline{\mathbb{MTPC}}$ [—] and approximated torque hyperbola $\overline{\mathbb{T}}(m_{\mathrm{m,ref}})$ [—]. The intersection of these two previously formulated quadrics can be found by the analytical determination of intersection point (for more details, see [50]).

5.3.2 Field weakening (FW)

For increasing speeds or a reduced voltage limit, the voltage ellipse $\partial\overline{\mathbb{V}}(\widehat{u}_{\max})$ shrinks. As a consequence, the loss-minimizing intersection of MTPC hyperbola $\overline{\mathbb{MTPC}}$ and torque hyperbola $\overline{\mathbb{T}}(m_{\mathrm{m,ref}})$ may not be located anymore within the feasible set $\overline{\mathbb{S}}$ [ ], as shown in Fig. 5.4(b). In this case, the machine should be operated in the FW operation strategy to reach the desired torque reference $m_{\mathrm{m,ref}}$, and still comply with the voltage constraint. For the FW strategy, its operation point [51]

$$\boxed{\boldsymbol{i}_{\mathrm{s,FW}}^{dq} := \partial\overline{\mathbb{V}}(\widehat{u}_{\max}) \cap \overline{\mathbb{T}}(m_{\mathrm{m,ref}})} \tag{5.29}$$

is defined as the intersection point, as shown in Fig. 5.4(b) [★], of approximated voltage ellipse $\partial\overline{\mathbb{V}}(\widehat{u}_{\max})$ [—] and approximated torque hyperbola $\overline{\mathbb{T}}(m_{\mathrm{m,ref}})$ [—].

By comparing Fig. 5.4(b) with Fig 5.4(a) (with a constant voltage limit), the speed dependency of the approximated voltage elliptical area $\overline{\mathbb{V}}(\widehat{u}_{\max})$ and ellipse $\partial\overline{\mathbb{V}}(\widehat{u}_{\max})$ can be observed. Due to the speed increase, $\partial\overline{\mathbb{V}}(\widehat{u}_{\max})$ [—] shifts extensively leftward (in the direction of negative d current), which implies a reduced admissible voltage area. This influence can also be seen in Fig. 5.4(c) and 5.4(d) with even higher speeds.

5.3.3 Maximum current (MC)

To operate the machine at its current limit with further increasing speeds, the MC strategy should be implemented to produce the maximum feasible torque. This results in the nonlinear MC optimization problem [51]

$$\boldsymbol{i}_{\mathrm{s,ref}}^{dq} := \arg\max_{\boldsymbol{i}_{\mathrm{s}}^{dq}\in\mathbb{S}} \operatorname{sign}(m_{\mathrm{m,ref}}) m_{\mathrm{m}}(\boldsymbol{i}_{\mathrm{s}}^{dq}), \tag{5.30}$$

which can also be approximated as a quadratic optimization problem

$$\boldsymbol{i}_{\mathrm{s,ref}}^{dq} := \arg\max_{\boldsymbol{i}_{\mathrm{s}}^{dq}\in\overline{\mathbb{S}}} \operatorname{sign}(m_{\mathrm{m,ref}}) \Big(\underbrace{(\boldsymbol{i}_{\mathrm{s}}^{dq})^{\top}\overline{\boldsymbol{T}}\boldsymbol{i}_{\mathrm{s}}^{dq} + 2\overline{\boldsymbol{t}}^{\top}\boldsymbol{i}_{\mathrm{s}}^{dq} + \overline{\tau}(m_{\mathrm{m,ref}})}_{\overset{(5.12)}{\approx} m_{\mathrm{m}}(\boldsymbol{i}_{\mathrm{s}}^{dq}) - m_{\mathrm{m,ref}}} \Big). \tag{5.31}$$

The approximated feasible set $\overline{\mathbb{S}}$ is identical to (5.25), which is the intersection surface of current circular area $\mathbb{I}(\widehat{i}_{\max})$ and approximated voltage elliptical area $\overline{\mathbb{V}}(\widehat{u}_{\max})$. Due to these constraints of the admissible solution, the optimal current references [51]

$$\boxed{\boldsymbol{i}_{\mathrm{s,MC}}^{dq} := \partial\mathbb{I}(\widehat{i}_{\max}) \cap \partial\overline{\mathbb{V}}(\widehat{u}_{\max})} \tag{5.32}$$

are defined for the MC operation strategy. The intersection, as shown in Fig. 5.4(c) [★], is obtained by intersecting the current circle $\partial\mathbb{I}(\widehat{i}_{\max})$ [—] and the approximated voltage ellipse $\partial\overline{\mathbb{V}}(\widehat{u}_{\max})$ [—].

5.3.4 Maximum torque per voltage (MTPV)

For even higher speeds, the voltage constraint in (5.2) becomes more critical during operation. The MTPV strategy should be implemented, although the desired torque reference $m_{\mathrm{m,ref}}$ cannot be reached anymore. Its objective is to develop the maximum feasible torque with the still available voltage. Therefore, the resulting MTPV optimization problem [51]

$$\boldsymbol{i}_{\mathrm{s,ref}}^{dq} := \arg\max_{\boldsymbol{i}_{\mathrm{s}}^{dq}\in\mathbb{S}} -\|\boldsymbol{u}_{\mathrm{s}}^{dq}(\boldsymbol{i}_{\mathrm{s}}^{dq})\|^2 \quad \text{s.t.} \quad m_{\mathrm{m}}(\boldsymbol{i}_{\mathrm{s}}^{dq}) \overset{!}{=} m_{\mathrm{m,ref}}. \tag{5.33}$$

can be formulated by minimizing the squared voltage magnitude for a given torque reference. Again, this general but nonlinear optimization problem can be approximated as a quadratic

optimization problem as

$$\begin{aligned} \boldsymbol{i}_{\mathrm{s,ref}}^{dq} := \arg\max_{\boldsymbol{i}_{\mathrm{s}}^{dq}\in\overline{\mathbb{S}}} & -\Big(\underbrace{(\boldsymbol{i}_{\mathrm{s}}^{dq})^{\top}\overline{\boldsymbol{V}}\boldsymbol{i}_{\mathrm{s}}^{dq}+2\overline{\boldsymbol{v}}^{\top}\boldsymbol{i}_{\mathrm{s}}^{dq}+\overline{\nu}(\widehat{u}_{\max})}_{\overset{(5.17)}{\approx}\|\boldsymbol{u}_{\mathrm{s}}^{dq}(\boldsymbol{i}_{\mathrm{s}}^{dq})\|^2-\widehat{u}_{\max}^2}\Big) \\ \text{s.t. } & \underbrace{(\boldsymbol{i}_{\mathrm{s}}^{dq})^{\top}\overline{\boldsymbol{T}}\boldsymbol{i}_{\mathrm{s}}^{dq}+2\overline{\boldsymbol{t}}^{\top}\boldsymbol{i}_{\mathrm{s}}^{dq}+\overline{\tau}(m_{\mathrm{m,ref}})}_{\overset{(5.12)}{\approx}m_{\mathrm{m}}(\boldsymbol{i}_{\mathrm{s}}^{dq})-m_{\mathrm{m,ref}}}=0 \end{aligned} \tag{5.34}$$

with the help of the approximated voltage ellipse and the approximated torque hyperbola. Its solution, the MTPV hyperbola (as shown in Fig. 5.4 [—]), can be described implicitly as a quadric [51]

$$\boxed{\overline{\mathbb{MTPV}} := \{\ \boldsymbol{i}_{\mathrm{s}}^{dq}\in\mathbb{R}^2 \mid (\boldsymbol{i}_{\mathrm{s}}^{dq})^{\top}\overline{\boldsymbol{M}}_{\mathrm{V}}\boldsymbol{i}_{\mathrm{s}}^{dq}+2\overline{\boldsymbol{m}}_{\mathrm{V}}^{\top}\boldsymbol{i}_{\mathrm{s}}^{dq}+\overline{\mu}_{\mathrm{V}}=0\ \},} \tag{5.35}$$

where

$$\left.\begin{aligned} \overline{\boldsymbol{M}}_{\mathrm{V}} = \overline{\boldsymbol{M}}_{\mathrm{V}}^{\top} &:= \begin{bmatrix} \overline{v}_{11}\overline{t}_{12}-\overline{v}_{12}\overline{t}_{11} & \frac{1}{2}(\overline{v}_{11}\overline{t}_{22}-\overline{v}_{22}\overline{t}_{11}) \\ \frac{1}{2}(\overline{v}_{11}\overline{t}_{22}-\overline{v}_{22}\overline{t}_{11}) & \overline{v}_{12}\overline{t}_{22}-\overline{v}_{22}\overline{t}_{12} \end{bmatrix}, \\ \overline{\boldsymbol{m}}_{\mathrm{V}} &:= \frac{1}{2}\begin{pmatrix} \overline{v}_{11}\overline{t}_{2}+\overline{v}_{1}\overline{t}_{12}-\overline{v}_{12}\overline{t}_{1}-\overline{v}_{2}\overline{t}_{11} \\ \overline{v}_{12}\overline{t}_{2}+\overline{v}_{1}\overline{t}_{22}-\overline{v}_{22}\overline{t}_{1}-\overline{v}_{2}\overline{t}_{12} \end{pmatrix}, \\ \overline{\mu}_{\mathrm{V}} &:= \overline{v}_{1}\overline{t}_{2}-\overline{v}_{2}\overline{t}_{1} \end{aligned}\right\} \tag{5.36}$$

depend on the entries of defined matrices and vectors in (5.13) and (5.18).

For the MTPV operation strategy, the optimal current reference vector [51]

$$\boxed{\boldsymbol{i}_{\mathrm{s,MTPV}}^{dq} := \overline{\mathbb{MTPV}}\cap\partial\overline{\mathbb{V}}(\widehat{u}_{\max})} \tag{5.37}$$

is the intersection point, as shown in Fig. 5.4(d) [★], of approximated MTPV hyperbola $\overline{\mathbb{MTPV}}$ [—] and approximated voltage ellipse $\partial\overline{\mathbb{V}}(\widehat{u}_{\max})$ [—].

5.3.5 Operation management

After discussing all operation strategies (MTPC, FW, MC and MTPV), an effective operation management is introduced based on [51, 52], i.e., the decision tree presented in Fig. 5.5. Since it is not known in advance, which is the most suitable strategy for the actual operation point. By means of the decision tree, the optimal operation strategy can be determined online during machine operation; furthermore, a smooth transition between different strategies can also be ensured. The introduced decision tree is composed of the following steps in order: initialization, computation, limitation and decision.

Initially, conditions and parameters at the actual operation point are updated as input variables from measurements and by LUTs/prototype functions, i.e., $\overline{\boldsymbol{i}}_{\mathrm{s}}^{dq}$, $\overline{\omega}_{\mathrm{p}}$, $\overline{R}_{\mathrm{s}}$, $\overline{\boldsymbol{\psi}}_{\mathrm{s}}^{dq}$, $\overline{\boldsymbol{L}}_{\mathrm{s}}^{dq}$, torque reference $m_{\mathrm{m,ref}}$ and limits $\widehat{u}_{\max}$ & $\widehat{i}_{\max}$. In the second step, the matrices, vectors and constants in the relevant quadrics can be calculated, e.g., $\overline{\boldsymbol{T}}$, $\overline{\boldsymbol{t}}$ & $\overline{\tau}(m_{\mathrm{m,ref}})$ of the torque hyperbola $\overline{\mathbb{T}}(m_{\mathrm{m,ref}})$ and $\overline{\boldsymbol{V}}$, $\overline{\boldsymbol{v}}$ & $\overline{\nu}(\widehat{u}_{\max})$ of the voltage ellipse $\partial\overline{\mathbb{V}}(\widehat{u}_{\max})$. Besides, the maximum feasible machine torque [51]

$$m_{\mathrm{m,max}} := m_{\mathrm{m}}(\boldsymbol{i}_{\mathrm{s,MTPC,max}}^{dq}) \quad \text{with} \quad \boldsymbol{i}_{\mathrm{s,MTPC,max}}^{dq} := \overline{\mathbb{MTPC}}\cap\partial\mathbb{I}(\widehat{i}_{\max}) \tag{5.38}$$

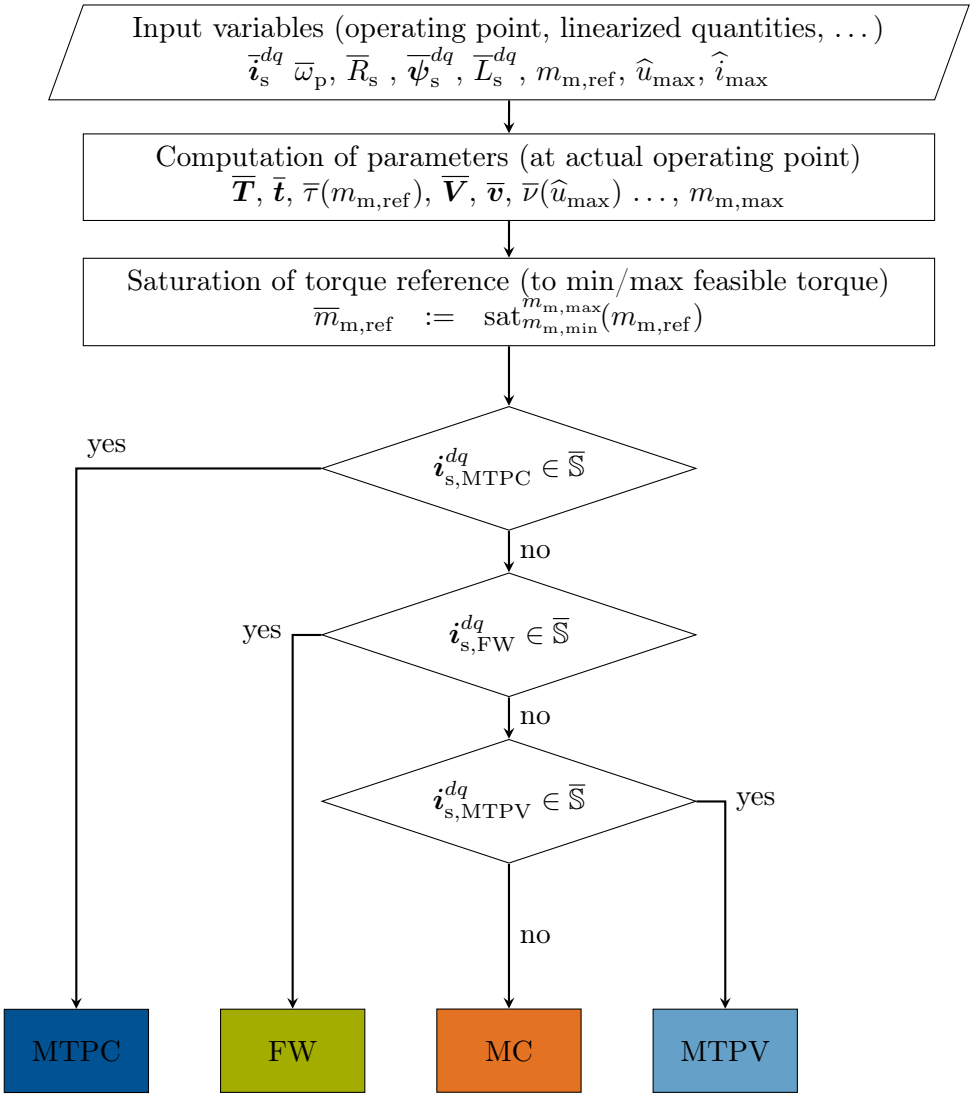

Figure 5.5: Decision tree for optimal operation management (based on [52]).

is also calculated, which is the developed torque at the intersection $\boldsymbol{i}^{dq}_{\mathrm{s,MTPC,max}}$ of MTPC hyperbola and current circle. Afterwards, in the third step, the given torque reference $m_{\mathrm{m,ref}}$ must be limited by a saturation function

$$\overline{m}_{\mathrm{m,ref}} := \mathrm{sat}_{m_{\mathrm{m,max}}}(m_{\mathrm{m,ref}}) := \begin{cases} m_{\mathrm{m,ref}}, & m_{\mathrm{m,ref}} \leq m_{\mathrm{m,max}} \\ m_{\mathrm{m,max}}, & m_{\mathrm{m,ref}} > m_{\mathrm{m,max}} \end{cases} \tag{5.39}$$

based on the updated $m_{\mathrm{m,max}}$. Such that an unreasonable torque reference (i.e., $m_{\mathrm{m,ref}} \gg m_{\mathrm{m,max}}$) and also (generated) excessive current references (i.e., $\|\boldsymbol{i}^{dq}_{\mathrm{s,ref}}\| \gg \widehat{i}_{\mathrm{max}}$) can be prevented. If necessary, only when $m_{\mathrm{m,ref}} > m_{\mathrm{m,max}}$, some already calculated quadratic parameters [which are related to $m_{\mathrm{m,ref}}$, e.g., $\overline{\tau}(m_{\mathrm{m,ref}})$ in $\overline{\mathbb{T}}(m_{\mathrm{m,ref}})$] from the previous calculation step must be recalculated. After the torque reference is limited, with all the updated quadratic parameters, the intersections $\boldsymbol{i}^{dq}_{\mathrm{s,X}}$ for X $\in$ {MTPC, FW, MC, MTPV} of two respective quadrics can be obtained in the upcoming step.

In the final step, the most suitable operation strategy will be selected, eventually resulting in

the optimal current references. First, the MTPC current references $\boldsymbol{i}^{dq}_{\mathrm{s,MTPC}}$ are calculated. If they are located within the feasible region, i.e., $\boldsymbol{i}^{dq}_{\mathrm{s,MTPC}} \in \overline{\mathbb{S}}$, MTPC is chosen. As the first priority, the MTPC strategy ensures the best possible operation efficiency, such that the additional calculations of other strategies can be avoided. If $\boldsymbol{i}^{dq}_{\mathrm{s,MTPC}}$ are located outside the feasible region, then the FW current references $\boldsymbol{i}^{dq}_{\mathrm{s,FW}}$ are calculated. If $\boldsymbol{i}^{dq}_{\mathrm{s,FW}} \in \overline{\mathbb{S}}$, the FW strategy is applied. If not, in the last conditional branch, the MTPV current references $\boldsymbol{i}^{dq}_{\mathrm{s,MTPV}}$ are computed and checked whether they are located inside the feasible region, i.e., $\boldsymbol{i}^{dq}_{\mathrm{s,MTPV}} \in \overline{\mathbb{S}}$. If yes, MTPV is selected; otherwise, MC is the final remaining option.

5.4 Experimental validation

As a final step, the theoretical derivations for the OFTC problem are validated by experiments in the concluding section. It has been proved in the previous chapter that both simulation and measurement results match well in the nonlinear current control system. To focus intently on the real-time capability of the developed method, only measurement results are provided here. On the established laboratory setup with a 4.0 kW RSM (see Fig. 4.4), the optimal current reference computation (OCRC, as presented in Fig. 5.1) with the decision tree (as illustrated in Fig. 5.5) is implemented. The generated optimal current references are fed into the developed nonlinear current controllers based on input/output linearization (see Fig. 4.1). Instead of using LUTs, the magnetic saturation is taken into account in OFTC by the designed flux linkage prototype functions. Consequently, at each control instant, the nonlinear flux linkages and differential inductances of the employed RSM can be compensated for through the prototype functions in both OCRC and the nonlinear current controllers.

In order to cover all the introduced operation strategies in OFTC completely, the effectiveness of the developed OCRC is assessed by *three* different scenarios:

- Operation at constant speed with *only* MTPC (see measurement results in Fig. 5.6);
- Start-up procedure with *all* operation strategies by setting a low voltage limit (see measurement results in Fig. 5.8); and
- Start-up procedure with different operation strategies *without* MTPV by setting a high voltage limit (see measurement results in Fig. 5.10).

Moreover, the corresponding current loci of the computed current references are illustrated separately in Figs. 5.7, 5.9 and 5.11. Note that the settings and parameters for the three test scenarios are slightly different, and they are provided and explained in detail in the following subsections.

5.4.1 Scenario (i) - MTPC

In this test scenario, the tested RSM is current-controlled; in contrast, the load machine is speed-controlled to rotate the RSM constantly at half of the rated speed $\omega_{\mathrm{m,R}}$, i.e., $\omega_{\mathrm{m}} = 0.5\omega_{\mathrm{m,R}} = 78.5\,\mathrm{rad/s}$. For the RSM, a time-varying torque reference (ramping up from zero to 19 Nm in 1 s) is assigned to the OCRC, which provides the required current references for the nonlinear current controllers. The voltage and current limits are chosen as $\widehat{u}_{\max} = 404.1\,\mathrm{V}$ (identical to the inverter voltage limit $\widehat{u} = \frac{u_{\mathrm{dc}}}{\sqrt{3}}$) and $\widehat{i}_{\max} = 10.0\,\mathrm{A}$, respectively, with sufficiently high values to stay in the MTPC strategy.

In Fig. 5.6, measurement results [—] in time series are depicted, including (from top to bottom) direct currents $i^d_{\mathrm{s,ref}}$ & i^d_{s}, quadrature currents $i^q_{\mathrm{s,ref}}$ & i^q_{s} and machine torques $m_{\mathrm{m,ref}}$ & m_{m} (& load torque m_{l} measured by the equipped torque sensor), where m_{m} is the online linearized torque via (5.11). Due to the ramping torque reference, the current references $i^d_{\mathrm{s,ref}}$ and $i^q_{\mathrm{s,ref}}$ gradually increase along the MTPC locus. The actual stator currents in both components are well regulated along their references utilizing the nonlinear current controllers. As a consequence, all torque references are feasible and can be produced by the machine.

Additionally, the current locus of the optimal current references by the MTPC strategy, i.e., $\boldsymbol{i}^{dq}_{\mathrm{s,ref}} = \boldsymbol{i}^{dq}_{\mathrm{s,MTPC}}$, is shown in Fig. 5.7 (corresponding to Fig. 5.6). It can be observed that the loss-minimizing MTPC trajectory does not follow the classical MTPC trajectory for RSMs (i.e., $i^d_{\mathrm{s}} = i^q_{\mathrm{s}}$), where a linear magnetic property is assumed. Owing to the severe magnetic saturation of RSMs, the d current component must be reduced with the increase of the torque values, i.e., $i^d_{\mathrm{s,MTPC}} < i^q_{\mathrm{s,MTPC}}$. Hence, the best possible operation efficiency can be ensured when the employed RSM is not highly saturated. Moreover, the magnetic nonlinearities on the flux linkages and differential inductances are presented by the physically designed and motivated flux linkage prototype functions for RSMs. Therefore, using the prototype functions makes LUTs entirely obsolete in the OFTC problem.

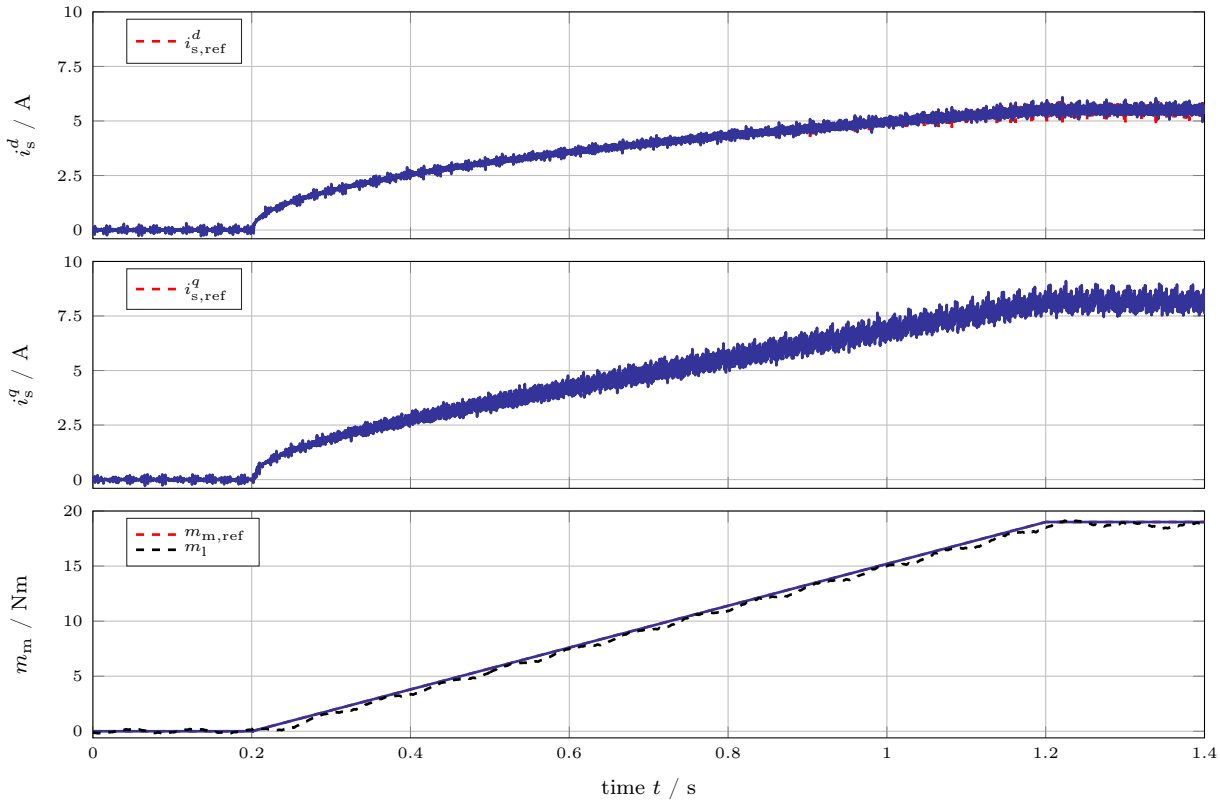

Figure 5.6: Measurement results [—] in time series with MTPC at constant speed $\omega_{\mathrm{m}} = 78.5\,\mathrm{rad/s}$ for a ramping torque reference from zero to 19 Nm.

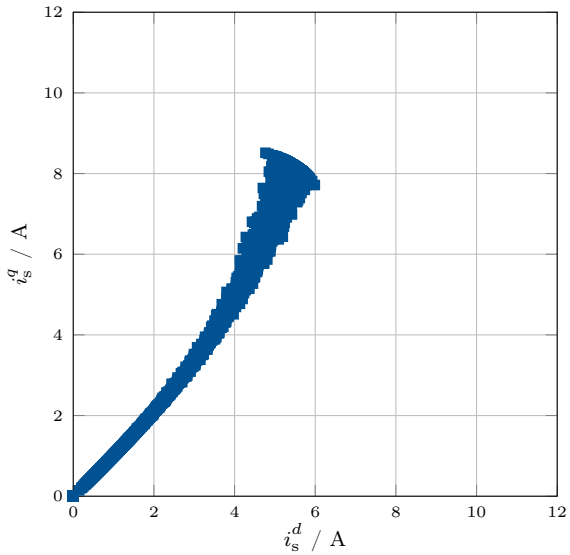

Figure 5.7: Current locus of MTPC (corresponding to Fig. 5.6).

5.4.2 Scenario (ii) - all operation strategies

In the second test scenario, the roles of two equipped machines in the laboratory setup are switched reversely from the previous scenario. The RSM under test is speed-controlled by augmenting with an outer-loop speed controller, which outputs the required torque reference for the OCRC. A start-up procedure is executed by giving a step change on the speed reference $\omega_{\mathrm{m,ref}}$ from zero to 200.0 rad/s. Note that the speed controller is set less aggressively, so the speed overshoot can be more prominent. Conversely, the current-controlled load machine provides a constant load torque $m_{\mathrm{l}} \approx 4\,\mathrm{Nm}$. To include all operation strategies through the start-up procedure, the voltage limit is reduced virtually to $\widehat{u}_{\max} = 0.4\widehat{u} = 161.7\,\mathrm{V}$ in the OCRC, where the inverter voltage limit $\widehat{u}$ stays unchanged (see the system specifications in Table 4.1).

The measurement in Fig. 5.8 demonstrates the wide speed range and smooth transitions between all operation strategies with different background colors, such as MTPC [■], MC [■], MTPV [■] and FW [■]. Its measurement results [—] in time series are illustrated, including $i_{\mathrm{s,ref}}^d$ & i_{s}^d, $i_{\mathrm{s,ref}}^q$ & i_{s}^q, norm of the stator voltages $\|\boldsymbol{u}_{\mathrm{s,ref}}^{dq}\|$ (& voltage limit $\widehat{u}_{\max}$), mechanical angular velocities $\omega_{\mathrm{m,ref}}$ & ω_{m} and torques $m_{\mathrm{m,ref}}$ & m_{m} & m_{l}.

In the beginning ($t < 0.1\,\mathrm{s}$), the machine is at standstill under a constant load torque. As the operation constraints are not critical in the low-speed range, the MTPC strategy [■] is in charge of providing the optimal current references $\boldsymbol{i}_{\mathrm{s,MTPC}}^{dq}$ by intersecting MTPC and torque hyperbolas, i.e., $\overline{\mathbb{MTPC}} \cap \overline{\mathbb{T}}(m_{\mathrm{m,ref}})$. At $t = 0.1\,\mathrm{s}$, the speed reference jumps to 200.0 rad/s, so the machine starts accelerating. Shortly after the reference change, the torque reference, output by the speed controller, exceeds the maximum feasible machine torque due to the current limit. Hence, until $t = 0.16\,\mathrm{s}$, as the current limit is already reached, the machine torque is limited at $m_{\mathrm{m}} = m_{\mathrm{m,max}} \approx 19.5\,\mathrm{Nm}$ (not shown) by the torque saturation function (5.39).

At $t = 0.16\,\mathrm{s}$, the voltage limit is also approached due to the increasing speed, where the current limit is already reached in the middle of the previous strategy. Consequently, the active operation strategy is switched to the MC strategy [■]. Its optimal current references $\boldsymbol{i}_{\mathrm{s,MC}}^{dq}$ are obtained from the intersection of current circle and voltage ellipse, i.e., $\partial\mathbb{I}(\widehat{i}_{\max}) \cap \partial\overline{\mathbb{V}}(\widehat{u}_{\max})$. Owing to

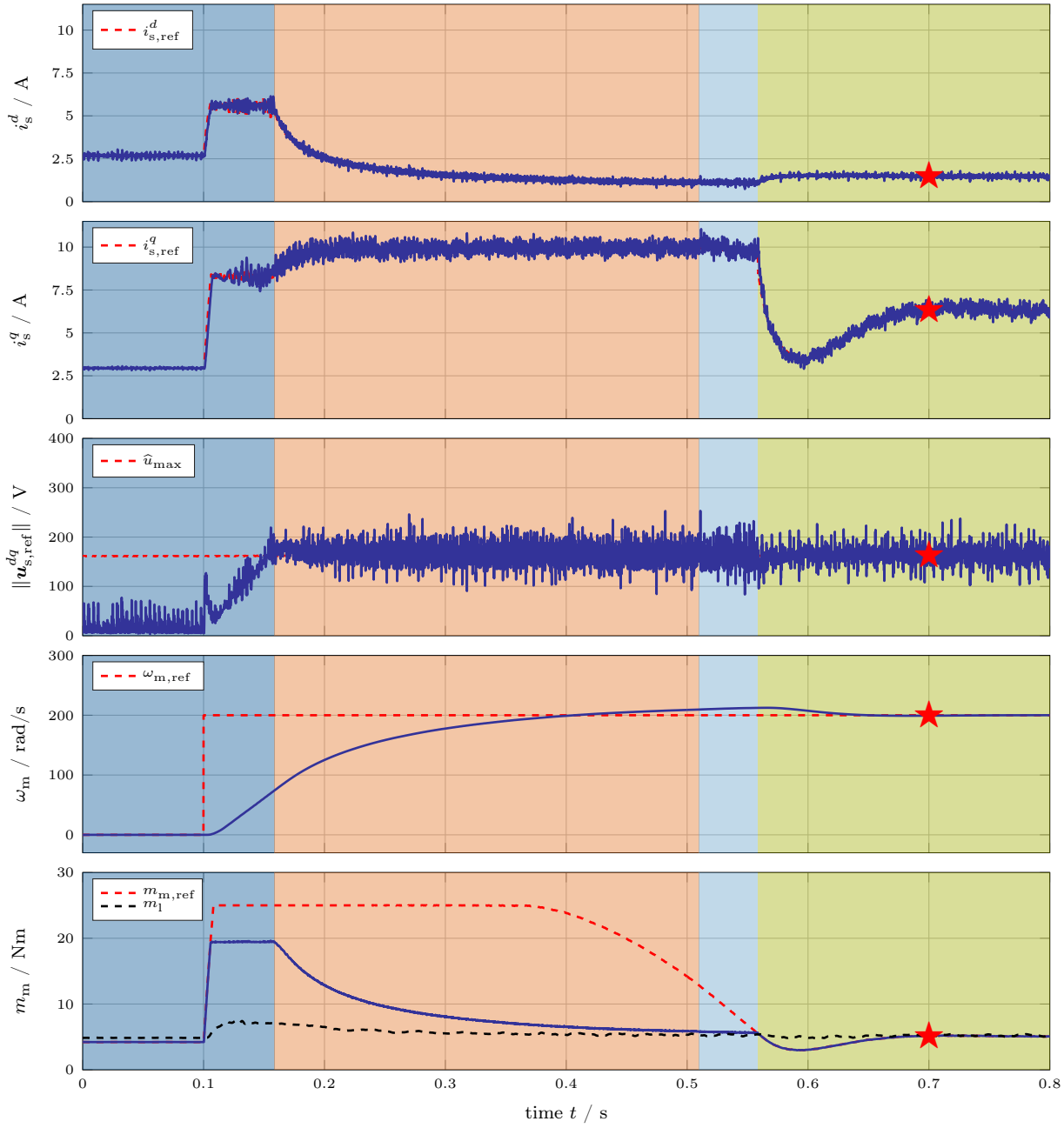

Figure 5.8: Measurement results [—] in time series with all operation strategies, such as MTPC [■], MC [■], MTPV [■] and FW [■], during the start-up procedure by setting the voltage limit $\widehat{u}_{\max} = 161.7\,\mathrm{V}$ under a constant load torque $m_{\mathrm{l}} \approx 4\,\mathrm{Nm}$.

the continuously increasing speed, the maximum possible torque is developed by the shrinking voltage ellipse along the current circle, where the given torque reference is not reachable anymore. As shown in Fig. 5.8, the d current component $i_{\mathrm{s,MC}}^{d}$ decreases considerably, so the desired speed can be achieved at $t = 0.41\,\mathrm{s}$ with a following speed overshoot.

For $t \in [0.51\,\mathrm{s}, 0.56\,\mathrm{s}]$, the MTPV strategy [■] is applied during the speed overshoot. With further higher speed, the voltage constraint becomes more critical. The optimal current references $\boldsymbol{i}_{\mathrm{s,MTPV}}^{dq}$ by intersecting MTPV hyperbola and voltage ellipse [i.e., $\overline{\mathbb{MTPV}} \cap \partial\overline{\mathbb{V}}(\widehat{u}_{\max})$] provide the maximum feasible machine torque. Although the desired torque reference given by the speed

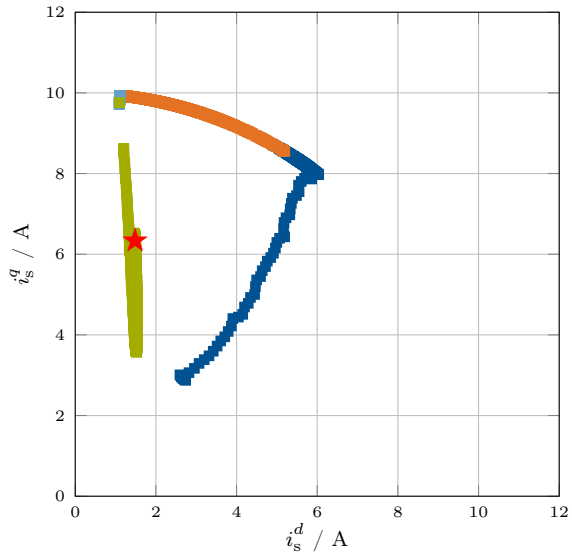

Figure 5.9: Current locus of all operation strategies, including $\boldsymbol{i}_{\mathrm{s,MTPC}}^{dq}$ [■], $\boldsymbol{i}_{\mathrm{s,MC}}^{dq}$ [■], $\boldsymbol{i}_{\mathrm{s,MTPV}}^{dq}$ [■] and $\boldsymbol{i}_{\mathrm{s,FW}}^{dq}$ [■] (& final operation point [★]), by setting the voltage limit $\widehat{u}_{\max} = 161.7\,\mathrm{V}$ (corresponding to Fig. 5.8).

controller is still not achievable.

Ultimately, acceleration is no more required, so the remaining torque reference compensates for only the load torque $m_{\mathrm{l}} = m_{\mathrm{m,ref}} = m_{\mathrm{m}}$. From $t = 0.56\,\mathrm{s}$, the FW strategy [■] is active until the end. Its resulting current references $\boldsymbol{i}_{\mathrm{s,FW}}^{dq}$ are the intersection of voltage ellipse and torque hyperbola, i.e., $\partial\overline{\mathbb{V}}(\widehat{u}_{\max}) \cap \overline{\mathbb{T}}(m_{\mathrm{m,ref}})$. The entire start-up procedure completes at $t = 0.7\,\mathrm{s}$ [★] with the desired speed and constant currents. It is successfully attained with smooth transitions between different strategies thanks to the designed operation management, as presented in Fig. 5.5. Moreover, all operation strategies introduced in Section 5.3 are sequentially implemented in the following order: MTPC → MC → MTPV → FW.

Corresponding to Fig. 5.8, the current locus of the optimal current references throughout the start-up scenario is presented in Fig. 5.9 for all operation strategies, including $\boldsymbol{i}_{\mathrm{s,MTPC}}^{dq}$ [■], $\boldsymbol{i}_{\mathrm{s,MC}}^{dq}$ [■], $\boldsymbol{i}_{\mathrm{s,MTPV}}^{dq}$ [■] and $\boldsymbol{i}_{\mathrm{s,FW}}^{dq}$ [■] (& final operation point [★]). The MTPC current references $\boldsymbol{i}_{\mathrm{s,MTPC}}^{dq}$ begin at $(2.69\,\mathrm{A}, 2.94\,\mathrm{A})$ as the starting point and move along the MTPC locus (i.e., the trajectory of $\boldsymbol{i}_{\mathrm{s,MTPC}}^{dq}$) until the current circle. Following that, the MC current references $\boldsymbol{i}_{\mathrm{s,MC}}^{dq}$ are provided by shifting leftward along the current circle. After entering the high-speed region, the voltage constraint becomes more crucial; hence, the MTPV current references $\boldsymbol{i}_{\mathrm{s,MTPV}}^{dq}$ are generated. Subsequently, with the significantly decreased torque reference, the FW current references $\boldsymbol{i}_{\mathrm{s,FW}}^{dq}$ are given until the endpoint, and the final operation point [★] is located at $(1.49\,\mathrm{A}, 6.33\,\mathrm{A})$.

As already pointed out in the previous scenario for MTPC, the d current component i_{s}^{d} must be reduced with the increase of torque in order to minimize the operation losses. In Fig. 5.9, it can be clearly seen that i_{s}^{d} should be further decreased in the MC, MTPV and FW strategies after MTPC. Furthermore, the optimal current operation point moves along the operation constraints in the high-speed range, e.g., intersecting the (leftward) shrinking voltage ellipse on the current circle for the MC strategy.

5.4.3 Scenario (iii) - different operation strategies without MTPV

Similar to test scenario (ii), the start-up procedure is reexamined in this subsection to confirm the effectiveness of OFTC under different conditions. The identical laboratory setup is utilized. Furthermore, also for the test procedure, a speed reference change from zero speed to 200.0 rad/s is given under a constant load torque $m_\mathrm{l} \approx 4\,\mathrm{Nm}$. However, different from the previous scenario, the voltage limit is virtually enhanced to $\widehat{u}_\mathrm{max} = 0.7\widehat{u} = 282.9\,\mathrm{V}$ in the developed OCRC.

In Fig. 5.10, the measurement results [—] are presented with the same quantities as in Fig. 5.8. The active operation strategies in different time zones are again highlighted with varying colors of background, i.e., MTPC [■], MC [■] and FW [■].

Initially ($t < 0.2\,\mathrm{s}$), the employed RSM begins with the MTPC strategy [■] at standstill under a constant load torque. As shown in Fig. 5.10, the machine torque reaches its maximum $m_\mathrm{m,max} \approx 19.5\,\mathrm{Nm}$, shortly after the speed reference jump at $t = 0.1\,\mathrm{s}$. Due to the raised voltage constraint, the saturated torque reference stays longer compared to scenario (ii).

At $t = 0.2\,\mathrm{s}$, the voltage limit approaches. Not only the current constraint but also the voltage constraint are now violated. Consequently, the MC strategy [■] must be applied by intersecting the current circle and the voltage ellipse. Such that the maximum possible torque can be produced, although the given torque reference (by the speed controller) is not achievable anymore.

For $t \in [0.24\,\mathrm{s}, 0.27\,\mathrm{s}]$, the FW strategy [■] becomes active. Since the machine speed has almost reached the desired speed value, no more acceleration torque is required anymore. Thus, the gradually reducing torque reference is now producible by the RSM with field weakening mode.

From $t = 0.27\,\mathrm{s}$, as a result of the shrinking currents and voltages, the MTPC strategy [■] regains control and remains in charge until the end of the test scenario. The final operation point [★] is reached at $t = 0.39\,\mathrm{s}$, and the machine speed stays constant. The complete start-up procedure is successfully accomplished by utilizing the following operation strategies: MTPC → MC → FW → MTPC. Compared to scenario (ii), the desired speed value is achieved in a much shorter time owing to the enhanced voltage constraint. Moreover, the MTPV strategy is *not* applied because the shrinking voltage ellipse has no intersections with the MTPV hyperbola.

Corresponding to Fig. 5.10, the current locus of the optimal current references is illustrated in Fig. 5.11, covering $\boldsymbol{i}^{dq}_\mathrm{s,MTPC}$ [■], $\boldsymbol{i}^{dq}_\mathrm{s,MC}$ [■] and $\boldsymbol{i}^{dq}_\mathrm{s,FW}$ [■] (& final operation point [★]). Similar to the previous scenario in Fig. 5.9, the MTPC current references $\boldsymbol{i}^{dq}_\mathrm{s,MTPC}$ share a (nearly) identical locus before meeting the current circle (i.e., the current limit). After approaching the current circle, the voltage ellipse shrinks gradually due to the speed increase. Then, the MC current references $\boldsymbol{i}^{dq}_\mathrm{s,MC}$ are provided by intersecting the current circle and the voltage ellipse. In this scenario, the MC locus has a relatively shorter path on the current circle, as the further reduced d current component is not necessary due to the sufficient voltages in this scenario. Afterwards, the torque reference is reduced and affordable by the employed RSM, so the FW current references $\boldsymbol{i}^{dq}_\mathrm{s,FW}$ are provided. Starting from the current circle, $\boldsymbol{i}^{dq}_\mathrm{s,FW}$ travel downward along the (already shrunk) voltage ellipse with the decreasing torque. Eventually, the final operation point is located again on the MTPC locus.

In conclusion, the developed OFTC for RSMs guarantees the maximum (both speed and load) operation range capability. In total, *three* scenarios (from Section 5.4.1 to Section 5.4.3) were implemented to validate the effectiveness of the proposed OFTC on the considered RSM under different circumstances. By means of the OCRC (as shown in Fig. 5.1), the optimal current references are acquired analytically online in accordance with actual operation conditions. Besides, the operation management (as presented in Fig. 5.5) ensures a suitable selection of operation

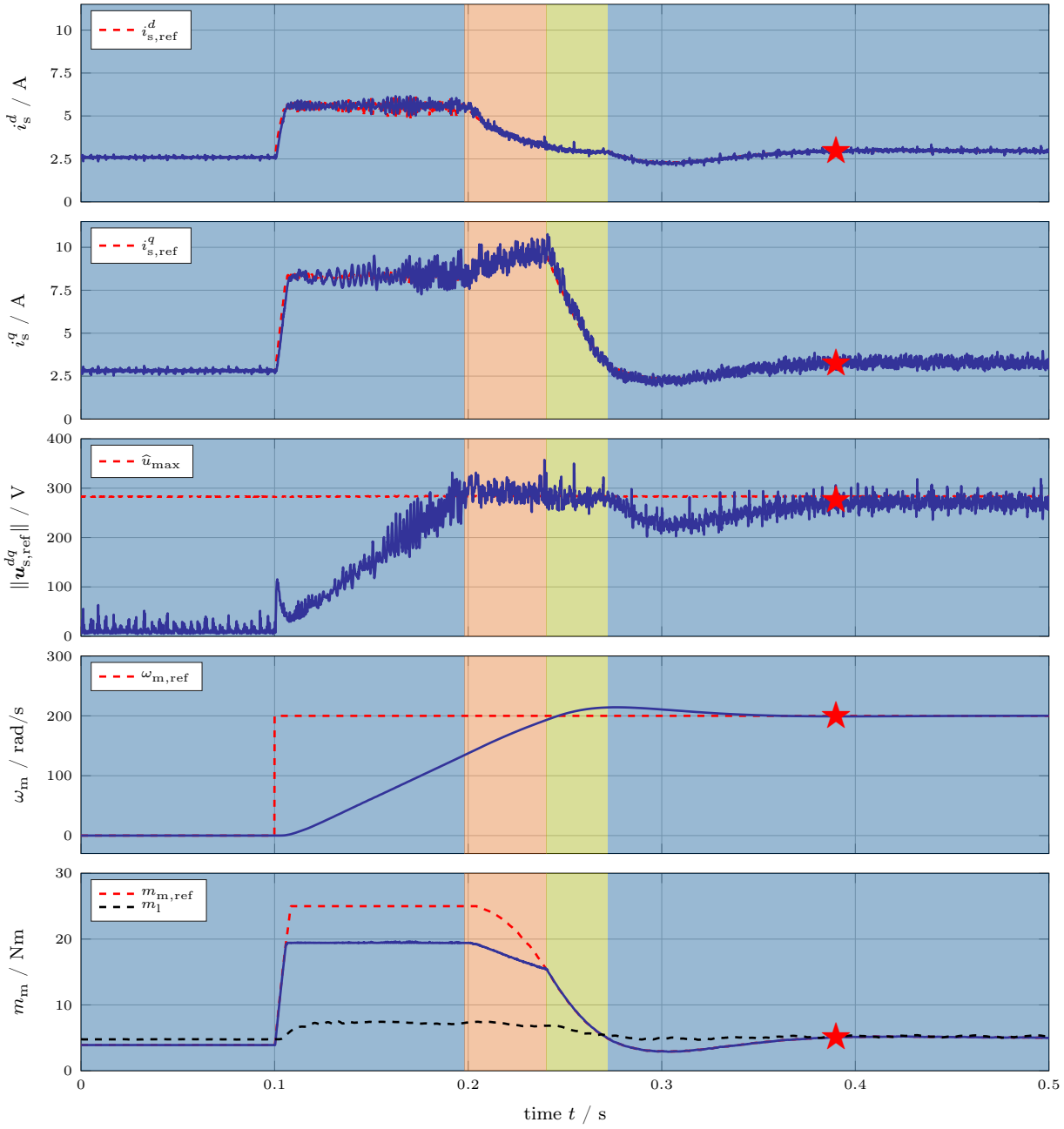

Figure 5.10: Measurement results [—] in time series with different operation strategies without MTPV, such as MTPC [■], MC [■] and FW [■], during the start-up procedure by setting the voltage limit $\widehat{u}_{\mathrm{max}} = 282.9\,\mathrm{V}$ under a constant load torque $m_{\mathrm{l}} \approx 4\,\mathrm{Nm}$.

strategies and a smooth transition between different strategies. Moreover, the magnetic nonlinearities of RSMs are taken into account in OFTC by means of the analytical flux linkage prototype functions. Therefore, at each control instant, the approximated flux linkages and differential inductances through the prototype functions can be effectively compensated for in not only the discussed OFTC problem but also the nonlinear current control system (in Chapter 4).

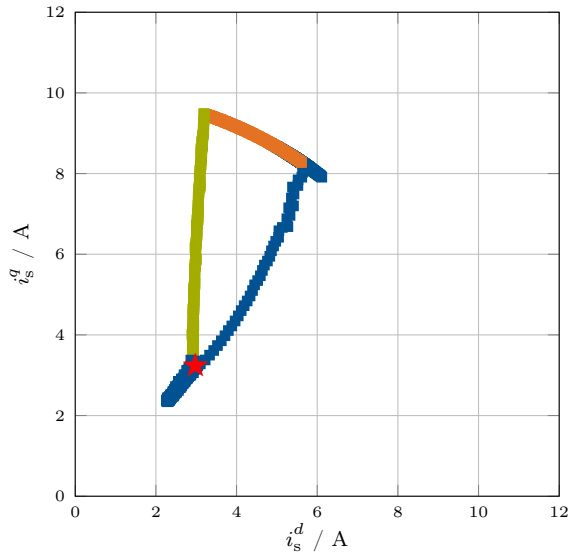

Figure 5.11: Current locus of different operation strategies, including $\boldsymbol{i}_{\mathrm{s,MTPC}}^{dq}$ [■], $\boldsymbol{i}_{\mathrm{s,MC}}^{dq}$ [■] and $\boldsymbol{i}_{\mathrm{s,FW}}^{dq}$ [■] (& final operation point [★]), by setting the voltage limit $\widehat{u}_{\mathrm{max}} = 282.9\,\mathrm{V}$ (corresponding to Fig. 5.10).

Chapter 6

Conclusion

This thesis conducted a comprehensive study on reluctance synchronous machines (RSMs), including modeling, identification, simulation and advanced control. Hence, a high-performance RSM drive system can be achieved with excellent dynamic capability and high efficiency, which are nowadays highly demanded in various occasions. In the following paragraphs, the accomplished results in this work are summarized, and a brief outlook is given.

In Chapter 2, a thorough introduction to RSMs was provided, covering machine structure, modeling and identification. Due to the unique rotor structure, i.e., without the use of windings and permanent magnets, the excellent potential for industrial applications has been recognized. However, the magnetic nonlinearity is more severe than other synchronous machines (SMs), which requires a complex control system to properly handle its effects. As a consequence, machine modeling and identification are essential tasks for RSMs and should serve as bases in the development of control algorithms. A generic machine model for SMs, including electrical and mechanical subsystems, was introduced, which can be further extended to model a simplified linear RSM or a real nonlinear RSM. Besides, critical points for developing an RSM drive system were pointed out. To identify the machine parameters experimentally, the constant speed and self-identification methods were discussed with their principles and implementations. Both approaches were applied to identify the flux linkages of a real RSM, and it was proved that they could both effectively obtain the desired data over the given measurement range.

In Chapter 3, analytical flux linkage prototype functions were presented, which allow to generically approximate the nonlinear flux linkages of RSMs and interior permanent magnet synchronous machines (IPMSMs). Due to their continuity and differentiability over the whole current range, the analytical prototype functions are very beneficial to ease the analysis of machine characteristics and to use them in real-world applications, such as advanced nonlinear control, operation management or self-commissioning. Three flux linkage prototype functions are presented; all obey the energy conservation rule. First, a prototype function was proposed for the modeling of RSM flux linkages. It has a simple and intuitive structure, and only a few parameters need to be fitted. Then, a second RSM flux linkage prototype function was developed based on the first approach in order to provide a higher flexibility and to achieve a better fitting accuracy. The number of cross-saturation terms can be chosen arbitrarily according to the requirements induced by different applications. At the end, an analytical flux linkage prototype function for IPMSMs was developed based on the second RSM flux model. Due to the asymmetric saturation effects in IPMSMs, the flux linkage surfaces must be (i) separated into two regions along a curved line in the d-direction of the zero locus of the differential inductances and (ii) modeled separately. The parameters of the prototype function of both regions are obtained by an effective

fitting process. Finally, all three flux linkage prototype functions were validated against real flux linkages of three RSMs and an IPMSM showing very high approximation accuracies.

The proposed flux linkage prototype functions are: (i) physically motivated and designed to describe the self-axis and cross-coupling saturation effects; (ii) continuously differentiable throughout the whole operation range; (iii) avoiding the need of many and redundant parameters; (iv) naturally capable of inter-/extrapolation; and (v) applicable for both RSMs and IPMSMs. These advantages can facilitate the implementation of more sophisticated control algorithms in the real-time system, which was demonstrated afterward on the control for RSMs.

In Chapter 4, a nonlinear current control system for RSMs with input/output (I/O) linearization and analytical flux linkage prototype functions was proposed. Based on the idea of I/O linearization [47], the nonlinear control system can be simplified to an integrator for both current components. Hence, the proportional-integral (PI) controller design is independent of the machine parameters and can be tuned simply by pole placement. For the designed controller structure, the nonlinear flux linkages and differential inductances must be updated online at each sampling instant. To do so, analytical flux linkage prototype functions with few parameters were utilized instead of lookup tables (LUTs). Thanks to their excellent fitting accuracies, the approximated flux linkages and differential inductances can be used directly. Finally, the presented nonlinear current controllers for RSMs were validated by simulations and at a laboratory setup. Simulation and measurement results matched nicely and illustrated the good control performance: The closed-loop current dynamics were shown to have (i) fast and accurate current reference tracking capabilities and (ii) an (almost) identical closed-loop response over the entire operation range. In addition, by comparing different solutions for making the machine parameters available to the control system, the full advantages of the flux linkage prototype functions were confirmed, as a (very) good control performance and much lower memory requirements in the real-time system are achieved.

In Chapter 5, an analytical solution for the optimal feedforward torque control (OFTC) problem of RSMs was presented (based on [50, 51]) by applying analytical flux linkage prototype functions. The optimal current references are obtained to guarantee efficiency improvement and operation performance through different operation strategies: maximum torque per current (MTPC), field weakening (FW), maximum current (MC) and maximum torque per voltage (MTPV). All machine equations and operation strategies were reformulated in quadratic form by means of online linearization, and then the optimal current references can be derived by intersecting two respective quadrics. The operation management (i.e., a decision tree) was proposed to ensure the most optimal selection and a smooth transition between different strategies. Moreover, analytical flux linkage prototype functions were employed to compensate for the nonlinear flux linkages and differential inductances. Therefore, the entire RSM control system successfully made LUTs obsolete in the OFTC problem and for the nonlinear current control method. Measurement results for different test scenarios were conducted to validate the effectiveness of the implemented OFTC at a laboratory setup. It was confirmed that the developed control method possesses: (i) a real-time capability; (ii) an effective generation of the optimal current references for all conditions; and (iii) a complete (both load and speed) operation range with a smooth transition between all operation strategies.

In conclusion, a thorough measure to develop a high-performance RSM drive system was presented. It was realized that the magnetic nonlinearity of RSMs must be handled appropriately to achieve the best possible drive performance in spite of their numerous advantages. To this end, the analytical flux linkage prototype functions were proposed to present the magnetic saturation effects including the cross-coupling. Owing to the great potential and meaning in real-time

applications, they were utilized to facilitate the implementation of system identification, nonlinear/adaptive current control and OFTC (efficiency improvement and operation management).

Based on the achieved results and gained knowledge in this work, future work comprises the following directions:

- Iron losses: Machine performance is also influenced by iron losses, which were not considered in the adopted machine model. They are highly nonlinear and dependent on both stator currents and speed. The modeling and identification approaches of iron losses should be studied and carried out, and then they can be considered in the control of RSMs. For example, in the OFTC problem, both the copper and iron losses can be minimized online to achieve even better efficiency (as was shown in [51, 52]).

- Comprehensive prototype function: Nonlinear flux linkages are, in reality, functions of current, speed, position and temperature. However, they are only current-dependent in the used model and the designed flux linkage prototype functions. These multiple factors should be firstly considered and extracted from the identification, and then they can be augmented in the prototype functions. Consequently, a more comprehensive manner to describe the magnetic nonlinearity can be obtained.

- Self-commissioning: A desirable functionality in modern electrical drive systems to start up the employed machine successfully without being aware of any system knowledge in advance. It typically comprises self-identification, auto-tuning and self-sensing (encoderless control). For the self-identification, it was demonstrated in this work to identify the nonlinear flux linkages of RSMs. Moreover, it was combined with the prototype functions to yield an entire representation of the magnetic nonlinearity. The future self-identification should eliminate the encoder, which was equipped to compensate for the incorrect voltage values due to the inevitable rotor movement. Once this fundamental part is completed, it serves as a basis and supports the other two functions. For example, the obtained machine information can be used to tune controller parameters in auto-tuning and to compensate for the position estimation errors in self-sensing.

Bibliography

[1] S.-W. Su, C. M. Hackl, and R. Kennel, "Analytical prototype functions for flux linkage approximation in synchronous machines," *IEEE Open J. Ind. Electron. Soc.*, vol. 3, pp. 265–282, 2022.

[2] S.-W. Su, H. Börngen, C. M. Hackl, and R. Kennel, "Nonlinear current control of reluctance synchronous machines with analytical flux linkage prototype functions," *IEEE Open J. Ind. Electron. Soc.*, vol. 3, pp. 582–593, 2022.

[3] S.-W. Su, R. Kennel, and C. M. Hackl, "Analytical flux linkage approximation prototypes for reluctance synchronous machines," in *Proc. IEEE SPEEDAM*, pp. 91–96, 2020.

[4] S.-W. Su, N. Monzen, R. Kennel, and C. M. Hackl, "Self-identification of reluctance synchronous machines with analytical flux linkage prototype functions," in *Proc. IEEE ICPE - ECCE Asia*, pp. 221–227, 2023.

[5] "Paris agreement," United Nations, Tech. Rep., Dec. 2015.

[6] P. Waide and C. U. Brunner, "Energy-efficiency policy opportunities for electric motor-driven systems," *IEA Energy Papers*, no. 7, May 2011.

[7] T. Lipo, "Synchronous reluctance machines-a viable alternative for ac drives?" *Electric Machines and Power Systems*, vol. 19, pp. 659–671, Nov. 1991.

[8] A. Vagati, "The synchronous reluctance solution: a new alternative in ac drives," in *Proc. IEEE IECON*, pp. 1–13, 1994.

[9] B. Weis, B. Leprettre, M. Patra, N. Hanigovszki, P. Holm, T. Schuman, M. Könen, N. Bidstrup, and K. Anderson, "Increasing the energy savings of motor applications: The extended product approach," in *Energy Efficiency in Motor Systems*, P. Bertoldi, Ed., pp. 37–52. Cham: Springer International Publishing, 2021.

[10] A. T. de Almeida, F. J. T. E. Ferreira, and G. Baoming, "Beyond induction motors—technology trends to move up efficiency," *IEEE Trans. Ind. Appl.*, vol. 50, no. 3, pp. 2103–2114, May/June 2014.

[11] R. Phillips, "Programme for in-depth analyses of electric motor systems in industry (pro-analysys)," in *Energy Efficiency in Motor Systems*, P. Bertoldi, Ed., pp. 147–163. Cham: Springer International Publishing, 2021.

[12] *Rotating electrical machines - Part 30-1: Efficiency classes of line operated AC motors (IE code)*, IEC 60034-30-1:2014, 2014.

[13] *Rotating electrical machines - Part 30-2: Efficiency classes of variable speed AC motors (IE code)*, IEC TS 60034-30-2:2016, 2016.

[14] "Directive 2009/125/EC of the european parliament and of the council of 21 October 2009 establishing a framework for the setting of ecodesign requirements for energy-related products," *OJEU*, Oct. 2009.

[15] "Commission regulation (EU) 2019/1781 of 1 October 2019 laying down ecodesign requirements for electric motors and variable speed drives pursuant to directive 2009/125/EC of the european parliament and of the council, amending regulation (EC) No 641/2009 with regard to ecodesign requirements for glandless standalone circulators and glandless circulators integrated in products and repealing commission regulation (EC) No 640/2009," *OJEU*, Oct. 2019.

[16] J. M. D. Coey, "Perspective and prospects for rare earth permanent magnets," *Engineering*, vol. 6, no. 2, pp. 119 – 131, 2020.

[17] S. Morimoto, "Trend of permanent magnet synchronous machines," *IEEJ Trans. Electr. Electron. Eng.*, vol. 2, no. 2, pp. 101 – 108, Mar. 2007.

[18] J. Kolehmainen and J. Ikäheimo, "Motors with buried magnets for medium-speed applications," *IEEE Trans. Energy Convers.*, vol. 23, no. 1, pp. 86–91, Mar. 2008.

[19] T. Jahns, "Getting rare-earth magnets out of ev traction machines: A review of the many approaches being pursued to minimize or eliminate rare-earth magnets from future ev drivetrains," *IEEE Electrif. Mag.*, vol. 5, no. 1, pp. 6–18, Mar. 2017.

[20] B. Poudel, E. Amiri, P. Rastgoufard, and B. Mirafzal, "Toward less rare-earth permanent magnet in electric machines: A review," *IEEE Trans. Magn.*, vol. 57, no. 9, pp. 1–19, Sept. 2021.

[21] S. Morimoto, S. Ooi, Y. Inoue, and M. Sanada, "Experimental evaluation of a rare-earth-free pmasynrm with ferrite magnets for automotive applications," *IEEE Trans. Ind. Electron.*, vol. 61, no. 10, pp. 5749–5756, Oct. 2014.

[22] G. Pellegrino, T. Jahns, N. Bianchi, W. Soong, and F. Cupertino, *The Rediscovery of Synchronous Reluctance and Ferrite Permanent Magnet Motors.* Springer Cham, 2016.

[23] C.-M. Liaw, J.-H. Zhuang, S.-W. Su, K.-W. Hu, and G. V. Kumar, "Driving control technologies of new high-efficient motors," in *Applied Electromechanical Devices and Machines for Electric Mobility Solutions*, A. El-Shahat and M. Ruba, Eds., ch. 8. Rijeka: IntechOpen, 2019.

[24] N. Bianchi, C. Babetto, and G. Bacco, *Synchronous Reluctance Machines: Analysis, optimization and applications*, ser. Energy Engineering. Institution of Engineering and Technology, 2021.

[25] M. Murataliyev, M. Degano, M. Di Nardo, N. Bianchi, and C. Gerada, "Synchronous reluctance machines: A comprehensive review and technology comparison," *Proc. IEEE*, vol. 110, no. 3, pp. 382–399, Mar. 2022.

[26] J. K. Kostko, "Polyphase reaction synchronous motors," *J. Amer. Inst. Electr. Eng.*, vol. 42, no. 11, pp. 1162–1168, Nov. 1923.

[27] H. Murakami, Y. Honda, H. Kiriyama, S. Morimoto, and Y. Takeda, "The performance comparison of spmsm, ipmsm and synrm in use as air-conditioning compressor," in *Proc. IEEE IAS*, pp. 840–845, 1999.

[28] T. Ahonen, J. Tamminen, and J. Montonen, "Comparison of electric motor types for realising an energy efficient pumping system," in *Proc. IEEE EPE*, pp. 1–9, 2014.

[29] J. Schörner, "Vorschläge zur Verringerung von Kosten und Energieverbrauch bei geregelten Seilaufzug-Antrieben," *Lift Report*, vol. 46, no. 6, pp. 4–16, 2020.

[30] P. Ragazzo, S. Ferrari, G. Dilevrano, L. Beatrici, C. Girardi, and G. Pellegrino, "Synchronous reluctance machines with and without ferrite assistance for lifting systems," in *Proc. IEEE IEMDC*, pp. 1–7, 2023.

[31] J. Malan and M. J. Kamper, "Performance of a hybrid electric vehicle using reluctance synchronous machine technology," *IEEE Trans. Ind. Appl.*, vol. 37, no. 5, pp. 1319–1324, Sept./Oct. 2001.

[32] N. Bianchi, S. Bolognani, E. Carraro, M. Castiello, and E. Fornasiero, "Electric vehicle traction based on synchronous reluctance motors," *IEEE Trans. Ind. Appl.*, vol. 52, no. 6, pp. 4762–4769, Nov./Dec. 2016.

[33] B. Ban, S. Stipetić, and M. Klanac, "Synchronous reluctance machines: Theory, design and the potential use in traction applications," in *Proc. IEEE EDPE*, pp. 177–188, 2019.

[34] H. Kärkkäinen, L. Aarniovuori, M. Niemelä, J. Pyrhönen, and J. Kolehmainen, "Technology comparison of induction motor and synchronous reluctance motor," in *Proc. IEEE IECON*, pp. 2207–2212, 2017.

[35] A. Rassolkin, H. Heidari, A. Kallaste, T. Vaimann, J. P. Acedo, and E. Romero-Cadaval, "Efficiency map comparison of induction and synchronous reluctance motors," in *Proc. IEEE IWED*, pp. 1–4, 2019.

[36] J.-I. Ha, S.-J. Kang, and S.-K. Sul, "Position-controlled synchronous reluctance motor without rotational transducer," *IEEE Trans. Ind. Appl.*, vol. 35, no. 6, pp. 1393–1398, Nov./Dec. 1999.

[37] H. W. De Kock, M. J. Kamper, and R. M. Kennel, "Anisotropy comparison of reluctance and pm synchronous machines for position sensorless control using hf carrier injection," *IEEE Trans. Power Electron.*, vol. 24, no. 8, pp. 1905–1913, Aug. 2009.

[38] D. A. Staton, T. J. E. Miller, and S. E. Wood, "Maximising the saliency ratio of the synchronous reluctance motor," *IEE Proc.-Electr. Power Appl.*, vol. 140, no. 4, pp. 249–259, July 1993.

[39] A. Vagati, M. Pastorelli, G. Francheschini, and S. C. Petrache, "Design of low-torque-ripple synchronous reluctance motors," *IEEE Trans. Ind. Appl.*, vol. 34, no. 4, pp. 758–765, July/Aug. 1998.

[40] T. Matsuo and T. A. Lipo, "Rotor design optimization of synchronous reluctance machine," *IEEE Trans. Energy Convers.*, vol. 9, no. 2, pp. 359–365, June 1994.

[41] S. Stipetic, D. Zarko, and N. Cavar, "Adjustment of rated current and power factor in a synchronous reluctance motor optimally designed for maximum saliency ratio," *IEEE Trans. Ind. Appl.*, vol. 56, no. 3, pp. 2481–2490, May/June 2020.

[42] A. Vagati, M. Pastorelli, and G. Franceschini, "High-performance control of synchronous reluctance motors," *IEEE Trans. Ind. Appl.*, vol. 33, no. 4, pp. 983–991, July/Aug. 1997.

[43] A. Vagati, M. Pastorelli, F. Scapino, and G. Franceschini, "Impact of cross saturation in synchronous reluctance motors of the transverse-laminated type," *IEEE Trans. Ind. Appl.*, vol. 36, no. 4, pp. 1039–1046, July/Aug. 2000.

[44] T. Lubin, H. Razik, and A. Rezzoug, "Magnetic saturation effects on the control of a synchronous reluctance machine," *IEEE Trans. Energy Convers.*, vol. 17, no. 3, pp. 356–362, Sept. 2002.

[45] C. M. Hackl, "Current pi-funnel control with anti-windup for synchronous machines," in *Proc. IEEE CDC*, pp. 1997–2004, 2015.

[46] C. M. Hackl, M. J. Kamper, J. Kullick, and J. Mitchell, "Current control of reluctance synchronous machines with online adjustment of the controller parameters," in *Proc. IEEE ISIE*, pp. 153–160, 2016.

[47] C. M. Hackl, J. Kullick, and P. Landsmann, "Nichtlineare Stromregelverfahren für Reluktanz-Synchronmaschinen," in *Elektrische Antriebe – Regelung von Antriebssystemen*, D. Schröder and J. Böcker, Eds. Springer-Verlag, 2021.

[48] H. Eldeeb, C. M. Hackl, J. Kullick, and L. Horlbeck, "Analytical solutions for the optimal reference currents for mtpc/mtpa, mtpv and mtpf control of anisotropic synchronous machines," in *Proc. IEEE IEMDC*, pp. 1–6, 2017.

[49] C. M. Hackl, J. Kullick, H. Eldeeb, and L. Horlbeck, "Analytical computation of the optimal reference currents for mtpc/mtpa, mtpv and mtpf operation of anisotropic synchronous machines considering stator resistance and mutual inductance," in *Proc. IEEE EPE ECCE*, pp. 1–10, 2017.

[50] H. Eldeeb, C. M. Hackl, L. Horlbeck, and J. Kullick, "A unified theory for optimal feedforward torque control of anisotropic synchronous machines," *Int. J. Control*, vol. 91, no. 10, pp. 2273–2302, 2018.

[51] C. M. Hackl, J. Kullick, and N. Monzen, "Optimale Betriebsführung von nichtlinearen Synchronmaschinen," in *Elektrische Antriebe – Regelung von Antriebssystemen*, D. Schröder and J. Böcker, Eds. Springer-Verlag, 2021.

[52] C. Hackl, J. Kullick, and N. Monzen, "Generic loss minimization for nonlinear synchronous machines by analytical computation of optimal reference currents considering copper and iron losses," in *Proc. IEEE ICIT*, pp. 1348–1355, 2021.

[53] M. A. Buettner, N. Monzen, and C. M. Hackl, "Artificial neural network based optimal feedforward torque control of interior permanent magnet synchronous machines: A feasibility study and comparison with the state-of-the-art," *Energies*, vol. 15, no. 5, 2022.

[54] S. Wendel, P. Karamanakos, P. Gebhardt, A. Dietz, and R. Kennel, "Flux linkage-based direct model predictive current control for synchronous machines," *IEEE Trans. Power Electron.*, vol. 36, no. 12, pp. 14 237–14 256, Dec. 2021.

[55] A. Zanelli, J. Kullick, H. M. Eldeeb, G. Frison, C. M. Hackl, and M. Diehl, "Continuous control set nonlinear model predictive control of reluctance synchronous machines," *IEEE Trans. Control Syst. Technol.*, vol. 30, no. 1, pp. 130–141, Jan. 2022.

[56] R. Surus, L. J. Niewiara, T. Tarczewski, and L. M. Grzesiak, "Finite control set model predictive current control for reluctance synchronous motor," in *Proc. IEEE PEMC*, pp. 235–242, 2022.

[57] P. Guglielmi, M. Pastorelli, and A. Vagati, "Impact of cross-saturation in sensorless control of transverse-laminated synchronous reluctance motors," *IEEE Trans. Ind. Electron.*, vol. 53, no. 2, pp. 429–439, Apr. 2006.

[58] P. Landsmann, J. Jung, M. Kramkowski, P. Stolze, D. Paulus, and R. Kennel, "Lowering injection amplitude in sensorless control by means of current oversampling," in *Proc. IEEE SLED*, pp. 1–6, 2012.

[59] S. Kuehl, P. Landsmann, and R. M. Kennel, "Compensating angle estimation errors caused by magnetic saturation in anisotropy-based sensorless control schemes," in *Proc. IEEE SLED*, pp. 1–6, 2012.

[60] D. Paulus, P. Landsmann, and R. Kennel, "General arbitrary injection approach for synchronous machines," in *Proc. IEEE SLED/PRECEDE*, pp. 1–6, 2013.

[61] K. Yahia, D. Matos, J. O. Estima, and A. J. M. Cardoso, "Modeling synchronous reluctance motors including saturation, iron losses and mechanical losses," in *Proc. IEEE SPEEDAM*, pp. 601–606, 2014.

[62] K. M. Rahman and S. Hiti, "Identification of machine parameters of a synchronous motor," *IEEE Trans. Ind. Appl.*, vol. 41, no. 2, pp. 557–565, Mar./Apr. 2005.

[63] E. Armando, R. I. Bojoi, P. Guglielmi, G. Pellegrino, and M. Pastorelli, "Experimental identification of the magnetic model of synchronous machines," *IEEE Trans. Ind. Appl.*, vol. 49, no. 5, pp. 2116–2125, Sept./Oct. 2013.

[64] S. A. Odhano, P. Pescetto, H. A. A. Awan, M. Hinkkanen, G. Pellegrino, and R. Bojoi, "Parameter identification and self-commissioning in ac motor drives: A technology status review," *IEEE Trans. Power Electron.*, vol. 34, no. 4, pp. 3603–3614, Apr. 2019.

[65] S. Wiedemann and C. M. Hackl, "Simultaneous identification of inverter and machine nonlinearities for self-commissioning of electrical synchronous machine drives," *IEEE Trans. Energy Convers.*, vol. 38, no. 3, pp. 1767–1780, Sept. 2023.

[66] M. Seilmeier and B. Piepenbreier, "Identification of steady-state inductances of pmsm using polynomial representations of the flux surfaces," in *Proc. IEEE IECON*, pp. 2899–2904, 2013.

[67] S. Kuehl, P. Landsmann, and R. M. Kennel, "Bivariate polynomial approximation of cross-saturated flux curves in synchronous machine models," in *Proc. IEEE ENERGYCON*, pp. 219–224, 2012.

[68] K. Liu, J. Feng, S. Guo, L. Xiao, and Z.-Q. Zhu, "Identification of flux linkage map of permanent magnet synchronous machines under uncertain circuit resistance and inverter nonlinearity," *IEEE Trans. Ind. Informat.*, vol. 14, no. 2, pp. 556–568, Feb. 2018.

[69] W. Lee, J. Kim, P. Jang, and K. Nam, "On-line mtpa control method for synchronous reluctance motor," *IEEE Trans. Ind. Appl.*, vol. 58, no. 1, pp. 356–364, Jan./Feb. 2022.

[70] Z. Qu, T. Tuovinen, and M. Hinkkanen, "Inclusion of magnetic saturation in dynamic models of synchronous reluctance motors," in *Proc. IEEE ICEM*, pp. 994–1000, 2012.

[71] M. Hinkkanen, P. Pescetto, E. Mölsä, S. E. Saarakkala, G. Pellegrino, and R. Bojoi, "Sensorless self-commissioning of synchronous reluctance motors at standstill without rotor locking," *IEEE Trans. Ind. Appl.*, vol. 53, no. 3, pp. 2120–2129, May/June 2017.

[72] N. Bedetti, S. Calligaro, and R. Petrella, "Stand-still self-identification of flux characteristics for synchronous reluctance machines using novel saturation approximating function and multiple linear regression," *IEEE Trans. Ind. Appl.*, vol. 52, no. 4, pp. 3083–3092, July/Aug. 2016.

[73] A. Accetta, M. Cirrincione, M. Pucci, and A. Sferlazza, "Space-vector state dynamic model of synrm considering self- and cross-saturation and related parameter identification," *IET Electr. Power Appl.*, vol. 14, no. 14, pp. 2798–2808, Dec. 2020.

[74] T.-G. Woo, S.-W. Park, S.-C. Choi, H.-J. Lee, and Y.-D. Yoon, "Flux saturation model including cross saturation for synchronous reluctance machines and its identification method at standstill," *IEEE Trans. Ind. Electron.*, vol. 70, no. 3, pp. 2318–2328, Mar. 2023.

[75] B. Stumberger, G. Stumberger, D. Dolinar, A. Hamler, and M. Trlep, "Evaluation of saturation and cross-magnetization effects in interior permanent-magnet synchronous motor," *IEEE Trans. Ind. Appl.*, vol. 39, no. 5, pp. 1264–1271, Sept./Oct. 2003.

[76] L. Ortombina, F. Tinazzi, and M. Zigliotto, "Magnetic modeling of synchronous reluctance and internal permanent magnet motors using radial basis function networks," *IEEE Trans. Ind. Electron.*, vol. 65, no. 2, pp. 1140–1148, Feb. 2018.

[77] I. Boldea, Z. X. Fu, and S. A. Nasar, "Torque vector control (tvc) of axially-laminated anisotropic (ala) rotor reluctance synchronous motors," *Electric Machines and Power Systems*, vol. 19, pp. 533–554, 1991.

[78] R. Lagerquist, I. Boldea, and T. J. E. Miller, "Sensorless-control of the synchronous reluctance motor," *IEEE Trans. Ind. Appl.*, vol. 30, no. 3, pp. 673–682, May/June 1994.

[79] S. Wiedemann and A. Dziechciarz, "Comparative evaluation of dtc strategies for the synchronous reluctance machine," in *Proc. IEEE EVER*, pp. 1–5, 2015.

[80] L. Xu, X. Xu, T. Lipo, and D. Novotny, "Vector control of a synchronous reluctance motor including saturation and iron loss," *IEEE Trans. Ind. Appl.*, vol. 27, no. 5, pp. 977–985, Sept./Oct. 1991.

[81] T. Matsuo and T. A. Lipo, "Field oriented control of synchronous reluctance machine," in *Proc. IEEE PESC*, pp. 425–431, 1993.

[82] J. E. Fletcher, B. W. Williams, and T. C. Green, "Efficiency aspects of vector control applied to synchronous reluctance motors," in *Proc. IEEE IAS*, pp. 294–300, 1995.

[83] A. Kilthau and J. M. Pacas, "Appropriate models for the control of the synchronous reluctance machine," in *Proc. IEEE IAS*, pp. 2289–2295, 2002.

[84] I. Z. Petrić, A. Galassini, S. Wang, D. Prystupa, M. Degano, G. Buticchi, and C. Gerada, "A robust current controller design method for highly nonlinear synchronous reluctance motors," in *Proc. IET PEMD*, pp. 104–109, 2020.

[85] H. A. A. Awan, S. E. Saarakkala, and M. Hinkkanen, "Flux-linkage-based current control of saturated synchronous motors," *IEEE Trans. Ind. Appl.*, vol. 55, no. 5, pp. 4762–4769, Sept./Oct. 2019.

[86] H. W. de Kock, A. J. Rix, and M. J. Kamper, "Optimal torque control of synchronous machines based on finite-element analysis," *IEEE Trans. Ind. Electron.*, vol. 57, no. 1, pp. 413–419, Jan. 2010.

[87] R. Thike and P. Pillay, "Experimental investigation of mtpa trajectory of synchronous reluctance machine," in *Proc. IEEE PEDES*, pp. 1–6, 2018.

[88] V. Ketchedjian, A. Haspel, J. Haarer, and J. Roth-Stielow, "An open-loop control for the determination of the mtpv-trajectory of a synrm," in *Proc. IEEE IPEC*, pp. 2714–2720, 2022.

[89] A. Dianov, F. Tinazzi, S. Calligaro, and S. Bolognani, "Review and classification of mtpa control algorithms for synchronous motors," *IEEE Trans. Power Electron.*, vol. 37, no. 4, pp. 3990–4007, Apr. 2022.

[90] S. Bolognani, L. Peretti, and M. Zigliotto, "Online mtpa control strategy for dtc synchronous-reluctance-motor drives," *IEEE Trans. Power Electron.*, vol. 26, no. 1, pp. 20–28, Jan. 2011.

[91] R. Antonello, M. Carraro, and M. Zigliotto, "Maximum-torque-per-ampere operation of anisotropic synchronous permanent-magnet motors based on extremum seeking control," *IEEE Trans. Ind. Electron.*, vol. 61, no. 9, pp. 5086–5093, Sept. 2014.

[92] N. Bedetti, S. Calligaro, and R. Petrella, "Self-adaptation of mtpa tracking controller for ipmsm and synrm drives based on on-line estimation of loop gain," in *Proc. IEEE ECCE*, pp. 1917–1924, 2017.

[93] S. Calligaro, D. Marzona, R. Petrella, and A. Shahdadi, "Mtpa tracking algorithms for ipmsms and synrms: Accurate evaluation and adaptive tuning of real signal injection and virtual signal injection," in *Proc. IEEE ECCE*, pp. 6079–6086, 2020.

[94] C. Mademlis, "Compensation of magnetic saturation in maximum torque to current vector controlled synchronous reluctance motor drives," *IEEE Trans. Energy Convers.*, vol. 18, no. 3, pp. 379–385, Sept. 2003.

[95] S.-Y. Jung, J. Hong, and K. Nam, "Current minimizing torque control of the ipmsm using ferrari's method," *IEEE Trans. Power Electron.*, vol. 28, no. 12, pp. 5603–5617, Dec. 2013.

[96] S. M. Ferdous, P. Garcia, M. A. M. Oninda, and M. A. Hoque, "Mtpa and field weakening control of synchronous reluctance motor," in *Proc. IEEE ICECE*, pp. 598–601, 2016.

[97] J. Bonifacio and R. M. Kennel, "On considering saturation and cross-coupling effects for copper loss minimization on highly anisotropic synchronous machines," *IEEE Trans. Ind. Appl.*, vol. 54, no. 5, pp. 4177–4185, Sept./Oct. 2018.

[98] H. A. A. Awan, Z. Song, S. E. Saarakkala, and M. Hinkkanen, "Optimal torque control of saturated synchronous motors: Plug-and-play method," *IEEE Trans. Ind. Appl.*, vol. 54, no. 6, pp. 6110–6120, Nov./Dec. 2018.

[99] A. Accetta, M. Cirrincione, M. C. D. Piazza, G. L. Tona, M. Luna, and M. Pucci, "Analytical formulation of a maximum torque per ampere (mtpa) technique for synrms considering the magnetic saturation," *IEEE Trans. Ind. Appl.*, vol. 56, no. 4, pp. 3846–3854, July/Aug. 2020.

[100] A. K. Singh, R. Raja, T. Sebastian, A. Shrestha, M. Sariful Islam, and K. Rajashekara, "A novel control strategy to mitigate the parameter saturation problems in synchronous reluctance machines," in *Proc. IEEE IECON*, pp. 1–6, 2021.

[101] W.-T. Wu, T.-Y. Su, C.-W. Yang, C.-M. Liaw, C.-L. Chiang, Y.-G. Liu, and C.-C. Wang, "On a smr-fed synrm drive with real-time commutation tuning," *IEEE Access*, vol. 10, pp. 130 861–130 879, 2022.

[102] L. Horlbeck and C. M. Hackl, "Analytical solution for the mtpv hyperbola including the stator resistance," in *Proc. IEEE ICIT*, pp. 1060–1067, 2016.

[103] V. Manzolini, D. Da Rù, and S. Bolognani, "An effective flux weakening control of a syrm drive including mtpv operation," *IEEE Trans. Ind. Appl.*, vol. 55, no. 3, pp. 2700–2709, May/June 2019.

[104] N. Bianchi, S. Bolognani, M. D. Pre, and G. Grezzani, "Design considerations for fractional-slot winding configurations of synchronous machines," *IEEE Trans. Ind. Appl.*, vol. 42, no. 4, pp. 997–1006, July/Aug. 2006.

[105] A. M. EL-Refaie, "Fractional-slot concentrated-windings synchronous permanent magnet machines: Opportunities and challenges," *IEEE Trans. Ind. Electron.*, vol. 57, no. 1, pp. 107–121, Jan. 2010.

[106] S.-U. Chung, J.-W. Kim, Y.-D. Chun, B.-C. Woo, and D.-K. Hong, "Fractional slot concentrated winding pmsm with consequent pole rotor for a low-speed direct drive: Reduction of rare earth permanent magnet," *IEEE Trans. Energy Convers.*, vol. 30, no. 1, pp. 103–109, Mar. 2015.

[107] C. M. Spargo, B. C. Mecrow, J. D. Widmer, and C. Morton, "Application of fractional-slot concentrated windings to synchronous reluctance motors," *IEEE Trans. Ind. Appl.*, vol. 51, no. 2, pp. 1446–1455, Mar./Apr. 2015.

[108] C. M. Spargo, B. C. Mecrow, J. D. Widmer, C. Morton, and N. J. Baker, "Design and validation of a synchronous reluctance motor with single tooth windings," *IEEE Trans. Energy Convers.*, vol. 30, no. 2, pp. 795–805, June 2015.

[109] M. Gamba, G. Pellegrino, E. Armando, and S. Ferrari, "Synchronous reluctance motor with concentrated windings for ie4 efficiency," in *Proc. IEEE ECCE*, pp. 3905–3912, 2017.

[110] J. Kolehmainen, "Synchronous reluctance motor with form blocked rotor," *IEEE Trans. Energy Convers.*, vol. 25, no. 2, pp. 450–456, June 2010.

[111] C. Desai, H. R. Mehta, and P. Pillay, "Fabrication and assembly method for synchronous reluctance machines," *IEEE Trans. Ind. Appl.*, vol. 54, no. 5, pp. 4227–4235, Sept./Oct. 2018.

[112] E. Agamloh and S. Deb, "Performance comparison of transverse and axially laminated synchronous reluctance machines," in *Proc. IEEE ECCE*, pp. 1–7, 2022.

[113] M. J. Kamper and A. F. Volschenk, "Effect of rotor dimensions and cross magnetisation on ld and lq inductances of reluctance synchronous machine with cageless flux barrier rotor," *IEE Proc.-Electr. Power Appl.*, vol. 141, no. 4, pp. 213–220, July 1994.

[114] M. Ferrari, N. Bianchi, and E. Fornasiero, "Analysis of rotor saturation in synchronous reluctance and pm-assisted reluctance motors," *IEEE Trans. Ind. Appl.*, vol. 51, no. 1, pp. 169–177, Jan./Feb. 2015.

[115] C. Babetto, G. Bacco, and N. Bianchi, "Synchronous reluctance machine optimization for high-speed applications," *IEEE Trans. Energy Convers.*, vol. 33, no. 3, pp. 1266–1273, Sept. 2018.

[116] N. Bianchi, S. Bolognani, D. Bon, and M. Dai Pre, "Rotor flux-barrier design for torque ripple reduction in synchronous reluctance and pm-assisted synchronous reluctance motors," *IEEE Trans. Ind. Appl.*, vol. 45, no. 3, pp. 921–928, May/June 2009.

[117] E. Howard, M. J. Kamper, and S. Gerber, "Asymmetric flux barrier and skew design optimization of reluctance synchronous machines," *IEEE Trans. Ind. Appl.*, vol. 51, no. 5, pp. 3751–3760, Sept./Oct. 2015.

[118] C. Hackl, *Non-identifier Based Adaptive Control in Mechatronics*, vol. 466. Springer Cham, 2017.

[119] S. Wiedemann, S. Hall, R. M. Kennel, and M. Alaküla, "Dynamic testing characterization of a synchronous reluctance machine," *IEEE Trans. Ind. Appl.*, vol. 54, no. 2, pp. 1370–1378, Mar./Apr. 2018.

[120] S.-H. Hwang, J.-M. Kim, H. V. Khang, and J.-W. Ahn, "Parameter identification of a synchronous reluctance motor by using a synchronous pi current regulator at a standstill," *J. Power Electron.*, vol. 10, no. 5, pp. 491–497, Sept. 2010.

[121] R. Thike and P. Pillay, "Automated current control method for flux-linkage measurement of synchronous reluctance machines," *IEEE Trans. Ind. Appl.*, vol. 56, no. 2, pp. 1464–1474, Mar./Apr. 2020.

[122] J. Kullick and C. M. Hackl, "Nonlinear modeling, identification, and optimal feedforward torque control of induction machines using steady-state machine maps," *IEEE Trans. Ind. Electron.*, vol. 70, no. 1, pp. 211–221, Jan. 2023.

[123] G. Pellegrino, B. Boazzo, and T. M. Jahns, "Magnetic model self-identification for pm synchronous machine drives," *IEEE Trans. Ind. Appl.*, vol. 51, no. 3, pp. 2246–2254, May/June 2015.

[124] S. Wiedemann and R. M. Kennel, "Encoderless self-commissioning and identification of synchronous reluctance machines at standstill," in *Proc. IEEE ISIE*, pp. 296–302, 2017.

[125] J. A. Melkebeek and J. L. Willems, "Reciprocity relations for the mutual inductances between orthogonal axis windings in saturated salient-pole machines," *IEEE Trans. Ind. Appl.*, vol. 26, no. 1, pp. 107–114, Jan./Feb. 1990.

[126] D. Mingardi, M. Morandin, S. Bolognani, and N. Bianchi, "On the proprieties of the differential cross-saturation inductance in synchronous machines," *IEEE Trans. Ind. Appl.*, vol. 53, no. 2, pp. 991–1000, Mar./Apr. 2017.

[127] H. Gavin, "The levenberg-marquardt method for nonlinear least squares curve-fitting problems," *Department of Civil and Environmental Engineering, Duke University*, vol. 28, pp. 1–5, 2011.

[128] E. Armando, P. Guglielmi, G. Pellegrino, M. Pastorelli, and A. Vagati, "Accurate modeling and performance analysis of ipm-pmasr motors," *IEEE Trans. Ind. Appl.*, vol. 45, no. 1, pp. 123–130, Jan./Feb. 2009.

[129] Y. Peng, D. Vrancic, and R. Hanus, "Anti-windup, bumpless, and conditioned transfer techniques for pid controllers," *IEEE Control Syst. Mag.*, vol. 16, no. 4, pp. 48–57, Aug. 1996.

List of Figures

List of Tables